TUM

Technische Universität München

Fakultät für Chemie

Arbeitskreis für Synthese und Charaterisierung innovativer Materialien

---

Synthesis of Main Group Element Compounds and their Application in Batteries, Water Splitting and Photodetection

---

Claudia Ott

Vollständiger Abdruck der von der Fakultät für Chemie der Technischen Universität München zur Erlangung des akademischen Grades eines

Doktors der Naturwissenschaften (Dr. rer. nat.)

genehmigten Dissertation.

Vorsitzender: Prof. Dr. Thomas F. Fässler

Prüfer der Dissertation: 1. Prof. Dr. Tom Nilges
2. Prof. Dr. Dr. h.c. Bernhard Rieger

Die Dissertation wurde am 22.11.2018 an der Technischen Universität München eingereicht und durch die Fakultät für Chemie am 10.01.2019 angenommen.

"I don't believe that the ultimate theory will come by steady work along existing lines. We need something new. We can't predict what that will be or when we will find it because if we knew that, we would have found it already!"

Stephen Hawking

Danksagung

Ich möchte mich bei Allen bedanken, die mich während meiner Arbeit auf beiden Seiten des großen Teiches unterstützt haben. Ohne die Hilfe und Unterstützung dieser Personen wäre meine Arbeit niemals möglich gewesen. Mein besonderer Dank geht an:

- Meinen Doktorvater **Prof. Dr. Tom Nilges** für die Möglichkeit meine Promotion in seiner Arbeitsgruppe durchzuführen sowie einen Auslandsaufenthalt von einem halben Jahr im wunderschönen Alberta, Kanada zu verbringen. Außerdem bedanke ich mich für die Freiheiten bei der Themenwahl sowie Umsetzung, das mir entgegengebrachte Vertrauen, die vielen hilfreichen und interessanten Diskussionen und die herzliche Aufnahme in die Arbeitsgruppe.

- Prof. Dr. Karthik Shankar für die Möglichkeit meinen Auslandsaufenthalt in seiner Arbeitsgruppe der Fakultät "Chemical and Electrical Engineering" der University of Alberta zu verbringen. Ohne die Unterstützung trotz des ein oder anderen zerbrochenen Glases und die Erlaubnis meine Experimente in seinem Labor durchzuführen wäre diese Arbeit nicht möglich gewesen.

- den Organisatoren des ATUMS Projektes: Prof. Dr. Bernhard Rieger, Prof. Dr. Jonathan Veinot, Dr. Sergei Vagin und Leah Veinot

- Prof. Dr. Richard Weihrich, Prof. Dr. Rainer Pöttgen, Prof. Dr. Peter Müller-Buschbaum, Prof. Dr. Peer Schmidt, Prof. Dr. Leo van Wüllen, Prof. Dr. Lorenz Kienle, Prof. Dr. Alexander Holleitner, Dr. Gregor Kieslich, Dr. Dominik Daisenberger, Dr. Jeff Armstrong, Prof. Dr. Davide Donadio, Prof. Dr. Thomas Weitz, Prof. Dr. Feng Miao, Prof. Dr. Bilu Liu, Prof. Dr. Fengnian Xia für die vielen Kooperationen in verschiedensten Projekten.

- den Arbeitsgruppen Nilges und Fässler für das gute Arbeitsklima, die hilfreichen Diskussionen im Seminar sowie wundervolle gemeinsame Ausflüge.

- Unserer guten Seele Lucia, die immer ein offenes Ohr oder aufbauendes Wort hatte. Ohne sie wäre ich an der ganzen Bürokratie verzweifelt.

- mein besonderer Dank geht an meinen Freund Martin, der meine Launen ertragen musste und mich immer wieder aufgebaut hat, wenn mal was nicht so lief wie ich es mir vorgestellt habe. Er hat mir gezeigt, dass positive Gedanken auch über weite Strecken reisen können.

Kurzfassung

Die Suche nach neuen Verbindungen und reasisierbare neue Anwendungsmöglichkeiten spielen eine entscheidende Rolle in einer schnell-lebigen Welt wie unserer heutigen. In dieser Arbeit wurden verschiedene, neue Verbindungen mit Hauptgruppenelementen gefunden, phasenrein synthetisiert und deren Eigenschaften analysiert. Außerdem wurden realisierbare Anwendungsmöglichkeiten gesucht. Ein Hauptaugenmerk lag dabei auf erneuerbaren Eneergien und sogenannten "grünen" Technologien. Bei den neuen Verbindungen handelt es sich um La_2NiBi und SnIP. Bei ersterem handelt es sich um einen neuen, ternären Vertreter des Bi_3Ni-Strukturtyps. Die Verbindung kann mittels einer keramischen Festkörperreaktions aus den Elementen synthetisiert werden. Bei der zweiten neuen Verbindung handelt es sich um SnIP, die erste anorganische Doppelhelix auf atomarer Basis. Sie kann mittels einer Gasphasentransportreaktion aus den Elementen hergestellt werden. Mit dieser Verbindung ist es möglich eine Erniedrigung der Dimensionalität von einem 3D Bulkmaterial zu einem eindimensionalen Halbleiter mittels chamischer Delaminierung zu erreichen. Solch niedrig-dimensionale Materialien zeigen starke, strukturelle Anisotropieeffekte. Für die Verbindung als Hybridmaterial wurde die photoelektrochemische Wasserspaltung als neue Anwendungsmöglichkeit untersucht. Des weiteren wurden die bereits bekannten Stoffe schwarzer Phosphor (b-P) und schwarzes Arsen-Phosphor (b-AsP) auf neue Anwendungsgebiete hin erforscht. b-P wurde analysiert, um einen neuen und einfachen Zugang zu hochleistenden Natriumionen-Batterien (SIBs) zu finden. Außerdem wurde der Einfluss von Kupfer auf die Kapapzität und Zyklenstabilität solcher Batterien erforscht. b-AsP andererseits wurde als neues 2-dimensionales Material für Photodetektion im mittleren Infrarotbereich betrachtet.

Abstract

Finding new compounds and investigating possible new applications are crucial in a fast-living world like ours is today. In this work different new compounds containing main group elements were discovered, synthesized phase pure and analyzed. Possible applications with a focus on renewable energy sources and "green" technologies were investigated. The new compounds are La_2NiBi and SnIP. The first one is a ternary compound of the Bi_3Ni structure type. It can be synthesized via a ceramic solid state reaction of the elements. The second compound SnIP represents the first atom-scale inorganic double helix. It can be synthesized in an easy gasphase transport reaction from the elements. With this compound a decrease of dimensionality from a 3D material to an one-dimensional semiconductor can be achieved by chemical delamination. Such a low-dimensional material exhibits strong, structural anisotropy. This compound was investigated as a hybrid material in photoelectrochemical water splitting. Further work was done on new applications for the two already known compounds black phosphorous (b-P) and black arsenic-phosphorous (b-AsP). b-P in the context of finding a new and easy approach to high performance sodium-ion batteries (SIBs). Furthermore the influence of copper on the capacity and cycle stability was investigated. b-AsP on the other hand as a new 2-dimensional material for applications in the field of mid-infrared photodetection.

Contents

Abbreviations and Symbols

A	Active Area
AFM	Atomic Force Microscopy
B	Measuring Bandwidth
b-AsP	Black Arsenic Phosphorous
BS	Band Structure
c	Speed of Light
CNFCl	fluorine and chlorine co-doped C_3N_4
D^*	Specific Detectivity
DC	Direct Current
DFT	Density Functional Theory
DOS	Density of State
DSC	Differential Scanning Calorimetry
DTA	Differential Thermal Analysis
EDX	Energy Dispersive X-ray Spectroscopy
ELF	Electron Loclization Function
f	Frequency
FET	Field-effect Transistor
FPLO	Full Potential Local Orbital
HPPXRD	High Pressure Powder X-ray Diffraction
HR-TEM	High Resolution Transmission Elektron Microscopy
HR-XPS	High Resolution X-ray Photoelectron Spectroscopy
IR	Infrared
LIB	Lithium Ion Battery
λ	Wavelength
MIR	Mid-infrared
NEP	Noise Equivalent Power
PAW	Projector Augmented Wave
PBE functional	Perdew, Burke, Ernzerrhoff Functional

PCD	Pearson's Chrystallographic-database
PL	Photoluminescence
PMMA	Poly(methyl methacrylate)
PPMS	Physical Property Measurement System
PTE	Phototermoelectric
PVE	Photovoltaic Effect
PXRD	Powder X-ray Diffraction
R	Responsivity
resubl.	Resublimated
S	Seebeck Coefficient
SEI	Solid Electrolyte Interface
SEM	Scanning Electron Microscopy
SIB	Sodium Ion Battery
SOC	Spin-Orbit-Coupling
TEM	Transmission Electron Microscope
TRPL	Time Resolved Photoluminescence
V_{ds}	Source-Drain Voltage
vdW	Van Der Waals
V_{g}	Gate Voltage
XRD	X-ray Diffraction

1 Introduction

In modern times, we face urgent problems due to the increasing demand for cheap, fast, but still environmentally friendly energy sources. We must stray from fossil fuels like coal or crude oil because the resources are getting scarce and have radical consequences on our environment as highlighted in the media. To provide a healthy planet for our children, we have to abandon fossil fuels which destroy or poison the environment and move on to renewable energy sources. Big efforts are being made to find new materials that improve existing technologies. Of particular interest is hydrogen as an energy source and rechargeable batteries to store electrical energy over long periods of time or even open a new, effective way to transport it. It would be advantageous to store solar or wind energy, which can only be produced at specific times due to the periodic availability of sunlight and high winds. This would allow access to these "green" energies at times of high demand. Moreover, it would be beneficial to transport energy produced in this manner over far distances without excessive losses or detrimental effects on the environment.

In light of this increasing need for "green" energy sources and storage, we investigated new inorganic materials and examined possible applications. First, the innovative material black phosphorous is analyzed for application in lithium/sodium ion batteries. This could enable the more efficient and less space-consuming storage of energy and open a way to build smaller but more powerful devices. Second, SnIP, a compound with extraordinary structural features is discovered and investigated in terms of photocatalytical water splitting performance.

Another challenge for modern technologies is efficient and fast data storage and handling. The McKinsey Global Institute (MGI) predicts a rise of generated data by 40% every year.[1] To keep pace with the growing amounts of generated data, the progress in the field of semiconductor technologies cannot come to a halt. New materials exhibiting innovative features must be found or existing materials must be engineered to allow for a downscaling of dimensionality. Successes in this field were made with 2-dimensional materials like graphene, phosphorene, silicene or transition metal dichalcogenides.[2–6] Furthermore, a reduction in dimensionality of materials allows the utilization of structural anisotropy and changes in their electronic properties.[3] One-dimensional nanomaterials could be realized by growing CdSe-nanorods or delaminating SnIP crystals.[7,8] New materials with one-dimensional features have to be investigated in this

respect. [9]

Additionaly, the known compound black arsenic-phosphorous is probed for its ability and performance in the field of infrared photodetection. This is of special interest in space telecommunication, molecular "fingerprint" imaging or even optical radar. In the future this field will be of great interest not only for military applications but also for space exploration and therefore organizations like NASA or SpaceX.

1.1 Half-Cell Battery Fabrication Setup

In this work a new setup for the production of coin cell batteries was established and built from scratch. It was kept as simple and cost effective as possible but should still fulfill all the nesseccary requirements for battery testing. Three different steps had to be considered. First of all the active material had to be synthesized, characterized and scaled down to achieve a homogeneous particle size distribution of a few micrometers. Those procedures are described in chapter 2.2 of the "Materials and Methods" part on page 14 and following. Second the fabrication of the anodes had to be studied. The coating should exhibit a homogeneous particle distribution and film thickness. Slurry mixing could be performed using an agate mortar under inert conditions in a glovebox (see figure 1.1A, B). All used starting materials were synthesized or purchased in battery grade quality and dried using a Büchi glass oven at 400 K under vakuum before anode coating. To achieve the desired film thickness of 150 μm for the anodes a wire bar K Hand Coater Nr. 150 (Erichsen) was used (see figure 1.1C, D). This is an easy but effective way to accomplish a homogeneous film on a flat surface. The coatings can be dried under inert conditions at room temperature and punched to the desired diameter using a circular puncher (diameter 15 mm) on a soft Teflon® surface. To obtain the best possible contact within the anodes, they are pressed using a Maassen pellet press MP150 for 30 s at 3 to and again dried with a Büchi glass oven at 400 K under vakuum. The different coating steps are illustrated in figure 1.1A-I.
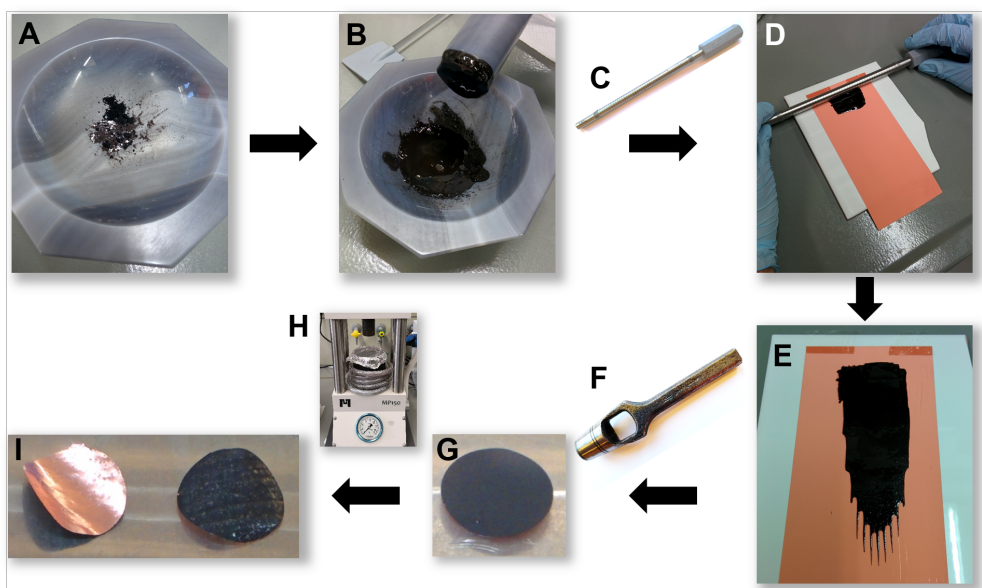
Figure 1.1: Coating procedure for black phosphorous anodes to be used in LIBs and SIBs. **A, B**: Slurry preparation in an agate mortar using black phosphorous powder, C_{65} (TimCal), PVDF (Polyvinyliden-fluoride, Kynar) and NMP (N-Methyl-2-pyrrolidone, 99%, Sigma); **C, D, E**: Coating on copper foil using a K Hand Coater Nr. 150 (Erichsen) wire bar; **F, G**: Punching of the anodes with a diameter of 15 mm; **H, I**: Pressing anodes to achieve best possible contact.

The last step before battery testing is the assembly of the half cell. The required coin cell components are shown in figure 1.2. Before assembly they were washed in a boiling ethanol/water mixture (40% Ethanol in DI water) to eliminate every organic contamination on the metal parts. Afterwards the components are dried in a Büchi glass oven at 400 K under vakuum to reduce the water content to a minimum before half cell assembly.
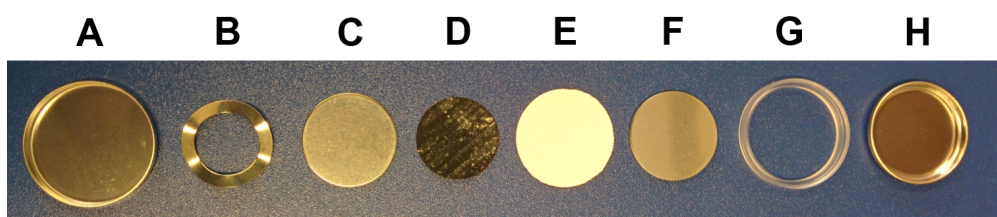
Figure 1.2: List of parts required to build a coin cell battery half cell. **A**: Stainless steel lid, **B**: Stainless steel spring, **C**: Stainless steel spacer, **D**: Anode prepared as described above, **E**: Glasfiber separator saturated with electrolyte, **F**: Lithium or sodium cathode, **G**: Gasket, **H**: Stainless steel bottom.

To assemble the coin cells the components shown in figure 1.2 have to be stacked and sealed airtight using a coin cell press. This press was designed and built in the course of this work with the help of the TUM precision engineering department. Figure 1.3 shows the engineering drawing of such a coin cell press and a picture of the final product. Additional drawings including all dimensions are added in the appendix on page 267. The press was fabricated using a commercially available product and modified to fulfil all neccessary requirements. An extrusion die was manufactured fitting the exact dimensions of CR2032 standard coin cells. Furthermore, the pressure exerted by the press was regulated to precisely seal the cells but not crush the whole setup or destoy the polymer gasket. A leak in the final coin cell would lead to decomposition in the battery and therefore to malfunction while cycling. The extrusion die was lined with Teflon® to prevent short-circuit while battery fabrication. That is also the reason why all assembly steps were carried out using plastic tweezers. Testing of the fabricated half-cell was conducted using a commercially available BioLogic VMP3 multichannel galvanostat as described in chapter 2.3 on page 30.
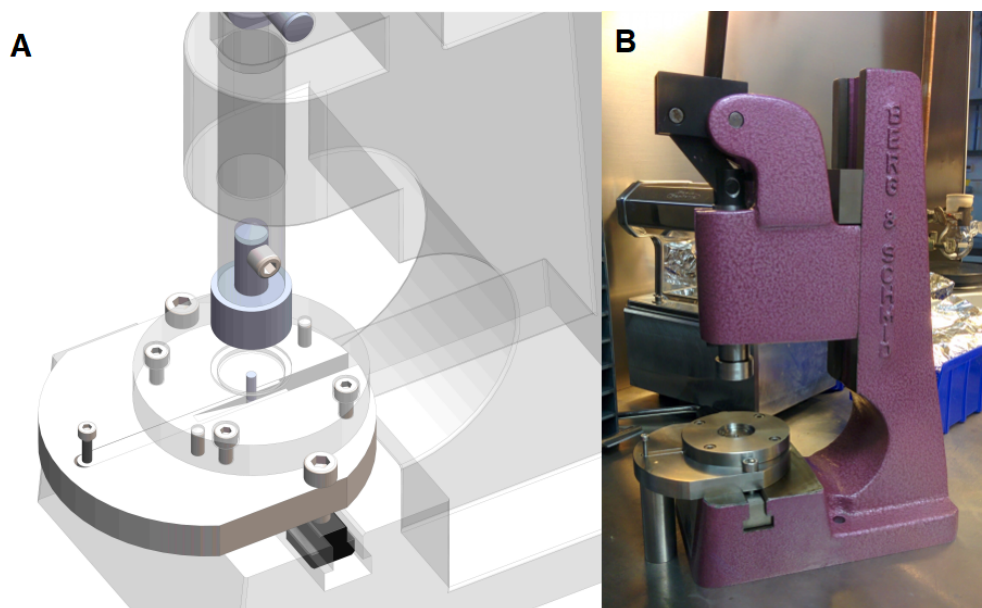
Figure 1.3: Engineering drawing (**A**) and photo (**B**) of the final coin cell press built in the course of this work.

1.2 Problems concerning Lithium-Ion-Batteries

New portable, electronic devices demand new batteries with high energy and power density to make them long-lasting but light and small.[10] Rechargeable lithium ion batteries (LIBs) have made a big impact on the development of high-end devices like phones, laptops, cameras and even cars. For LIBs, the commercially available anode material is graphite with a theoretical capacity of 372 mAh $\cdot$ g^{-1}.[11] Graphite can intercalate lithium between its layers but is limited to one lithium atom for every 6 carbon atoms. The theoretical capacity of a compound is calculated with Faraday's law ($Q_{\text{theoretical}} = (nF)/(3600 \cdot M)$ [mAh $\cdot$ g^{-1}] with F = Faraday constant 96485.33289(59) [C $\cdot$ mol^{-1}], n = number of moles and M = molecular weight [g $\cdot$ mol^{-1}]).[12] As the equation shows, the theoretical capacity is dependent on the number of moles for each intercalated lithium[13,14] and therefore is a specific property of a material and cannot be exceeded. It represents a big limiting factor in the development of new, more powerful batteries. Other compounds show a much higher theoretical capacity but cannot be applied in LIBs due to issues like an extreme volume expansion while charging.[15–17] This for instance is the case for silicon, the material with the highest theoretical capacity of 4200 mAh $\cdot$ g^{-1}. This value is more than ten times higher than for graphite.[15–17] The limiting factor here is the 400% volume increase during lithium insertion in the crystal structure.[15–17] Research groups around the world studied various compounds as a new possible anode material for lithium ion batteries.

Black phosphorous, a modification known since 1914, shows a similar layered crystal structure as graphite with condensed 6-rings.[18,19] In graphite those rings form stacked, planar layers, whereas in black phosphorous they are conjugated and show a chair conformation as illustrated in figure 1.4. The zig-zag layers of those condensed chairs again form 2-dimensional layers comparable with those of graphite. These structural similarities lead to the idea of using black phosphorous in LIBs (and SIBs) to substitute graphite as anode material.
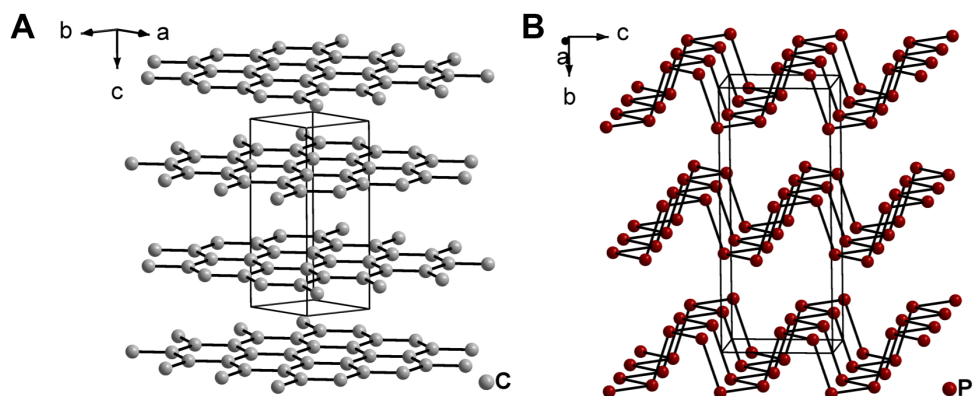
Figure 1.4: Crystal structures of graphite and black phosphorous. **A**: Illustration of graphite. The layered structure is built up by planar layers of condensed C_6-rings. **B**: Crystal structure of black phosphorous. The layered structure here is built up by condensed P_6-rings. However the layers are not planar but show a chair conformation.

In contrast to graphite, the theoretical capacity is notably higher (2596 mAh · g^{-1}).[10] Over the last years a great effort was made to study the application of black phosphorous as anode material in lithium ion batteries.[10,20–23] The higher theoretical capacity can be explained by the different lithiation and sodiation mechanisms of graphite and phosphorous. In graphite the alkali metal intercalates between the carbon layers up to a maximum composition of MC_6 (with M = Li, Na). This results in one lithium/sodium atom for each C_6-Ring. Black phosphorous on the other hand shows no intercalation mechanism but a conversion up to a composition of M_3P (with M = Li, Na).[22] This however means that the bonds between the phosphorous atoms have to be broken while discharging the battery and the crystal stucture can not be retained. The reaction mechanism can be simplified as:

$$P_{\text{black}} \xrightarrow{\text{M=Li, Na}} MP \xrightarrow{\text{M=Li, Na}} M_2P \xrightarrow{\text{M=Li, Na}} M_3P \,^{[20]}$$
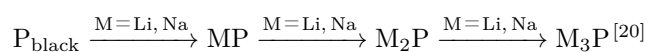
The high reactivity of the black phosphorous surface leads to a significant capacity loss in the first cycle due to the formation of the solid-electrolyte interface.[22] Other reasons for capacity decrease could be the loss of contact due to volume changes of the anode while cyclization.[20] As described above anode materials can undergo a big change in volume while cyclization. This leads to cracks in the material and electrode coating and therefore a possible loss of contact between the active material, the conductive carbon and the copper current collector. The volume increase

for phosphorous is not as extensive as in the case of silicone but not neglectible. Despite those limitations, capacities up to over 900 mAh · g^{-1} after 100 cycles could be achieved. [10,20,21,24] Quian *et al.* even report on capacities of 1900 to 2200 mAh · g^{-1} over 100 cycles. [25]

Stan *et al.* published a paper in 2013 concerning the influence of copper on the capacity and cycle stability of LIBs using black phosphorous as active anode material. [22] They proposed the active species in the lithiation process to be Cu_3P which spontaneously forms at the interface between the anode material and the copper current collector. [22] To prove that assumption, they coated the phosphorous particles with copper or a copper species in a solvothermal process using ethylenediamine. The copper reacts with the reactive surface atoms of the phosphorous particles forming a Cu_3P layer. Cyclization measurements showed an enhanced performance, which led to the conclusion that copper plays a crucial part in black phosphorous lithium battery systems. [22]

Unfortunately, there are also some issues to be taken into account in lithium ion battery research. LIBs are used in many portable devices which led to an excessive growth of the demand for lithium over the last decades and is likely to further increase. Hence the implementation of LIBs in portable electronics and especially in electric cars has to be reconsidered. Lithium is an abundant element but not with inexhaustible resources which could lead to a lithium shortage if the demand rises above the production level and therefore a large price increase. The biggest lithium mine contributing 27% to the worlds lithium reserve is located in the Atacama desert in Chile. The extraction in salt brines to obtain battery grade lithium uses up to two-thirds of the areas fresh drinking water. This causes a lot of pressure on the local agriculture and can lead to hunger crisis in dry seasons. Furthermore, working with lithium poses big health issues due to the build-up of fluid in the respiratory system after prolonged exposure to lithium dust. This affects the workers in lithium mines in less developed countries with lower security standards like Chile. [26]

The general demand for renewable, "green" but nevertheless low-cost energy systems is rising in society. With sodium being placed directly under lithium in the periodic table and the general chemical behaviour being related, there are already big efforts made to substitute lithium in batteries with sodium. [27–30] Sodium is a very common element in the earth crust and has large reserves like the salt (NaCl) in oceans. It could be extracted from sea water at large scale with less expensive and destructive ways than lithium is produced now.

Black phosphorous shows the same type of reactions with sodium as in the case of lithium. While cyclization Na_3P, equivalent to Li_3P in LIBs, is formed on the anode side. This reaction is not an intercalation as it is in graphite anodes but a conversion reaction. The "de-sodiation" is one of the main challenges in those kind of batteries. That leads to an extensive capacity loss after the first cycle caused by irreversible reactions of the active material and the formation of a SEI (solid electrolyte interface). This is a big issue in black phosphorous batteries but a stabilization of the system after the first cycle with a retained capacity of above 300 mAh $\cdot$ g^{-1} would still mean an improvement to the commercially available anode material graphite.

1.3   Compounds Containing One-dimensional Structural Feactures

Intermetallic Compounds: The first definition of intermetallic compounds was given by G. Schulze in 1967. He specified that intermetallics are compounds consisting of two or more metals which show a crystal structure that differs from the one exhibited by the elemental components.[31] Before that, materials included by this defination have already been known but were never summed up under one name. Examples are LAVES-, HUME-ROTHERY- or ZINTL-phases.[31] The former are named after the german chrystallographer Fritz Laves and are formed by to metals with the composition AB_2.[31] They represent the biggest group of intermetallic compounds and crystallize in either the cubic $MgCu_2$-type or the hexagonal types $MgZn_2$ and $MgNi_2$.[31,32] They exhibit high symmetry, coordination-numbers and density.[31] LAVES-compounds are hard and brittle but stable up to very high temperatures.[33,34] HUME-ROTHERY-phases on the other hand are defined by the ratio of valence electrons and metal cations.[32] Special values from this equation (3:2, 21:13 and 7:4) result in specific crystal structures. They are named after the british metallurgist William Hume-Rothery. The last mentioned intermetallic phases are named after the german chemist Eduard Zintl.[35] They describe compounds with highly polarized bonds formed by strongly electropositive metals (alkali and alkaline earth metals) and electronegative elements (11th-16th group of the periodic table).[31,32,36] Those phases form a crossover between metallic and ionic compounds and belong to the semi-metals.[32] In contrast to both former mentioned phases, the ZINTL-compounds show semiconductive behaviour with a small bandgap.[31,37]

Even in ancient cultures intermetallics played an important role as tools and weapons. In modern times they are applied as for example high-tensile, temperature-stable alloys or even superconductors. Characteristic for those phases is high temperature and corrosion resistance and brittleness.[36] Due to the importance of those materials great efforts should be made to find new representatives with interesting features like one-dimensional structural properties.

Zig-zag chains are an established feature in polymer and metalorganic-complex chemistry.[38–42] In carbon-free inorganic solid state chemistry comparable structure features are not as common. Ade *et al.* published a work in 2010 with a B_5 zig-zag chain fragement in the metal-rich ternary borides $Ni_{12}AlB_8$, $Ni_{12}GaB_8$ and $Ni_{10.6}Ga_{0.4}B_6$.[43] In other works infinite Ni-chains are one structural element in compounds like LaNi, GdNi, Bi_3Ni or La_2NiSb.[44–47]

LaNi was first synthesized by Dwight *et al.* in 1965. It can be described as a layered structure of alternating, parallel infinite nickel and lanthanum zig-zag chains running along the *b*-axis of the crystal lattice. Neighbouring layers are shifted by half a translation period along the *a*-axis.[44] Another compound showing this feature is GdNi, first synthesized by Baenzinger *et al.* in 1961. Here the infinite chains are surrounded trigonal prismatically by gadolinium forming a 3-dimensional network.[45]

The intermetallic phase Bi_3Ni was synthesized by Ruck *et al.* in 2006. The nickel zig-zag chains in this compound are surrounded trigonal-prismatically as in GdNi. Here however, the bismuth atoms in the surrounding first coordination sphere are not connected to neighbouring rods in any way and two opposite planes of each trigonal prism are capped by further bismuth atoms. Thus, forming the characteristic building blocks of the Bi_3Ni structure.[46] In 2014 Schäfer *et al.* published the first ternary version of the above described Bi_3Ni structure type. They substituted the bismuth atoms with lanthanum and antimony. Lanthanum occupies sites forming a hexagonal prismatic coordination of nickel and antimony occupies the capping positions.[47]

An interesting feature in the above described compounds are the varying Ni-Ni distances in the zig-zag chains. The 1:1 compounds show a distance decrease from 319 pm[44] in LaNi to 267 pm[45] in GdNi. The latter is surprisingly short and only slightly larger than the one of elemental, metallic nickel (250 pm).[48] In the 3:1 compounds the Ni-Ni distance decreases even further to 263 pm for Bi_3Ni and 259 pm in the case of La_2NiSb. Those values represent the shortest nickel-nickel distances in this structure type so far.

One-dimensional inorganic double helices: Double helices are a well known motive in organic and bio-chemistry.[49–52] The fundamental structure of all living organisms is arranged in a double helical way. This configuration of the so called desoxyribose nucleic acid (a compound known to every child as DNA) was first discovered by Watson and Crick in 1953.[49] The two strands forming the DNA double helix is built up by nucleobases pairs (cytosine-guanine [C]-[G] or adenine-thymine [A]-[T]), a sugar (desoxyribose) and a phosphate group as shown in figure 1.5.[49]
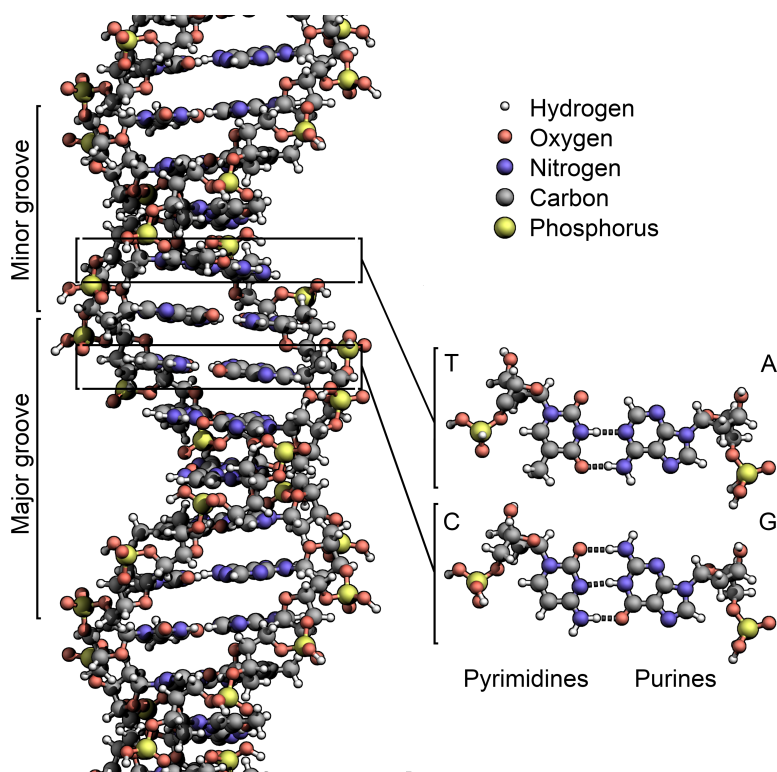
Figure 1.5: Crystal structure of desoxyribose acid (DNA).[49] Picture by Richard Wheeler, The Sir William Dunn School of Pathology, Oxford, United Kingdom.

Considering the importance of naturally occuring double helices, a great effort was made to artificially recreate similar structures.[53] There are different man-made helical and double-helical structures known in literature. Some are organic polymers like Teflon® (Poly-tetrafluoro-ethylene, PTFE)[54], others inorganic structures synthesized with the help of an organic template (e.g. DNA-templated gold nanoparticle arrays)[55,56]. Purely inorganic double helical compounds without any stabilizing organic ligands or template structures are barely known. Some can be

found as part of the crystal structure in solid state materials ($^1_\infty$[PbO$_2$-tetraeder in the poly-morph structure of PbO$_2$(C$_6$H$_5$COO)] or the helical polyanions $^1_\infty$X$_7^{1-}$ in LiX$_7$ and NaX$_7$ with X = P$_{0.5}$As$_{0.5}$ published by Schnering *et al.*).[57,58] Templating and self-assembly strategies are bottom-up approaches to single and double helix like structures containing CdS or GaN.[59,60] Another way to obtain such structures are top-down strategies commonly achieved via solution-based procedures as reported for the formation of Au/Ag-alloy nanowires[61] or based on Zintl precursors to form Si microtubes.[62]

As mentioned above, a synthesis of a carbon-free inorganic double helix could not be realized or just in negligible small yields. Ivanov *et al.* published new calculated Li$_x$P$_x$ structures and their stabilities in 2010.[63–66] They found the most stable structure for a compound with the composition Li$_7$P$_7$ to be a double helix on atomic level. However, an actual synthesis of this structure motive has not been realized to this day.

In this work a new inorganic double-helix on an atomic level could be realized with an easy and fast ampoule-synthesis using the non-toxic, abundant elements tin (Sn), iodine (I) and phosphorous (P) in a ratio of 1:1:1. The resulting dark brown/red needles are built up by double helices on an atomic level and can be exfoliated due to the weak van der Waals (vdW) interactions between the double helical strands. Another characteristic caused by the weak vdW interactions is the high flexibility of the needles. They can be bent to 180° without breaking or other visible degradation.

1.4   Infrared Photodetection

Photodetectors can generally be divided into three groups. The first generation photodetector or photoconductor, the second generation photodetector or photodiode and the third generation photodetector. First generation photodetectors were based on a simple scheme of applying metal electrodes to a thin layer (approx. 10 μm) of a n-type material like HgCdTe or PbSe.[67,68] A big downside of those photodetectors is their toxicity. Nevertheless, a high quantity of such devices was manufactured and are still in use to this day. The second generation of photodetectors can be described as a 2-dimensional array of photodiodes with a modest impedance of 10 Ωcm^2.[67,69] Over the last decades the setup of photodiodes was improved steadily due to new findings in

material and device processing studies. There are still some limitations in longer wavelength detection. This would be a crucial step in applications like monitoring the earth's atmosphere from space. The third generation of photodetectors is not well defined. There are some improvements in capabilities like more pixels, higher frame rates and such.[70,71] Other "third" generation infrared photodetectors are based on quantum-well and quantum-dot structures. These are built up by group III to V materials like for example GaAlAs superlattices published by Levine *et al.* in 1987.[72] Such devices show very high response speeds for long wavelength infrared light ($\lambda = 10.8 \ \mu$m).

The most commonly used commercially available materials for mid-infrared (MIR) photodetectors are HgCdTe and PbSe.[67,68] HgCdTe was first synthesized in 1959 by Lawson *et al.*[73] Middle wavelength infrared describes wavelengths between 3 and 50 μm (MIR) or wavelengths from 3 to 8 μm (MWIR). The formerly described materials are used due to their narrow-bandgap semiconductor properties with an adjustable direct band gap suitable for wavelengths between 0.7 and 25 μm.[67,68] To do so in the case of HgCdTe, different Hg to Cd ratios can be applied in the scheme of $Hg_{1-x}Cd_xTe$.

There are several major challenges in the field of midrange infrared photodetection like the challenging growth of large single crystals, environmentally hazardous aspects of the applied materials or the challenging formation of heterojunction devices. Operation usually requires a cryogenic environment with complex cooling facilities and therefore prohibits their usage in portable devices.[74]

Graphene was suggested as a promising alternative due to its easy fabrication method and possibility to be operated under room temperature.[5,75–77] It is limited by its very low light absorption and extremely small band gap which results in high dark current and noise level.[78] MIR photodetectors working under ambient conditions and with wavelengths of about 8 to 14 nm have yet to be established. Interesting new materials could include structures similar to graphene but exhibiting broader bandgaps like black phosphorous and black arsenic-phosphorous.

2   Materials and Methods

2.1   Starting Materials and Reactants

All reactants used in this work are listed in table 2.1 and are used without further purification steps. The oxygen or moisture sensitive compounds are stored under inert conditions in a glovebox (MBRAUN, MB200B, Ar-atmosphere, water and oxygen content below 0.1 ppm).

Table 2.1: Specifications of all reactants used in the synthesis, coating and device fabrication of this work.

Reactant	Shape	Purity [%]	Supplier
As (grey Arsenic)	Pieces 2x resubl.	99,9999	CHEMPUR
Au (Gold contacts)	50 nm layer	sputtered	n.a.
Bi (Bismuth)	pieces	99.999	ALFA AESAR
Cu	foil	99.99	MTI COOPERATION
EN (Ethylenediamine)	liquid	99+	ALFA AESAR
H_2O (Water (deionized))	liquid	deionized	n.a.
I_2 (Iodine)	Powder resubl.	99.8	CHEMPUR
La (Lanthanum)	powder	99.9	CHEMPUR
MeCN (Acetonitrile)	liquid	>99.8	VWR
Ni (Nickel)	powder	99.99	CHEMPUR
NMP	liquid	99	SIGMA
PbI_2 Lead-diiodide	Powder	98,5	ALPHA AESER
PE (Polyethylene)	Pieces	n.a.	n.a.
PEDOT:PSS (Poly(3,4-ethylenedioxy-thiophene)-Polystyrene-Sulfonate)	aq. solution	25% solution	SIGMA ALDRICH
PEO (Polyethylene Oxide)	Powder	n.a.	SIGMA-ALDRICH
P_{red} (red Phosphorous)	Pieces	99.999	CHEMPUR
PVDF (Polyvinylidene Fluoride)	Powder	99.9	KYNAR

(continue table 2.1)

PVP (Polyvinylpyrrolidone)	Powder	n.a.	n.a.
P$_{white}$ (white Phosphorous)	Powder	chrystal. phase pure	Own Production
P3HT (Poly(3-hexyl-thiophene-2,5-diyl))	Pieces	99.995	SIGMA ALDRICH
Si silicone	Wafer	n.a.	n.a.
SiO$_2$ Silicone-dioxide	Layer	n.a.	n.a.
Sn (Tin)	Shots	99.999	CHEMPUR
SnI$_4$ (Tintetraiodide)	Powder	chrystal. phase pure	Own Production
Super C65	powder		TIMCAL
Ti (Titanium)	5 nm layer	sputtered	n.a.
Toluene (Methylbenzene)	liquid	anhydrous	VWR

2.2 Synthesis and Fabrication Methods

Ceramic Synthesis: The starting materials for ceramic syntheses were mixed in an agate mortar under inert conditions in a glovebox (MBRAUN, MB200B, Ar-atmosphere, water and oxygen content below 0.1 ppm) and pressed to a pellet with a diameter of 6 mm in a hydraulic press (MAASSEN, MP150) with a pressure of 1 to for 10 min. The pellet was sealed in an evacuated silica tube and placed in a muffle furnace (NABERTHERM). The reaction mixture was heated according to the respective temperature program.
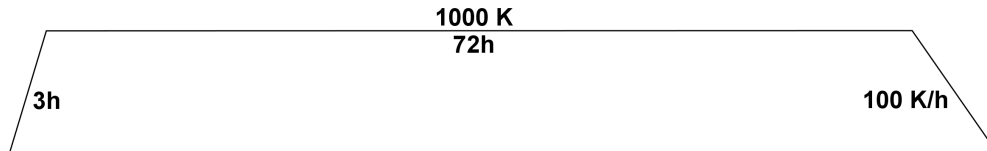
Figure 2.1: Exemplary temperature program for a ceramic synthesis shown for La$_2$NiBi. The reaction mixture was heated up to 1000 K in 3h, kept at this temperature for 72h and cooled down to room temperature with a rate of 100 K/h.

Gas-phase Transport Reaction: Nilges *et al.* published a slow pressure route to synthesize black phosphorous via a gas phase transport reaction using a mineralizator concept in 2014.[79] Other compounds like SnIP can be synthesized analogously. The starting materials (if nesseccary pressed to a pellet with a diameter of 10 mm (MAASSEN pellet press MP150, 1 to, 15 min)) were sealed into an evacuated silica glass ampoule (p < 10^{-3} mbar). The ampoule is placed into a NABERTHERM muffle furnace with the starting materials at the hot side (heating elements on the walls) and heated according to the respective temperature program.

Because needles form in the last step, meaning the cooling process, the length of the needles can be adjusted by different cooling rates. Furthermore, some compounds like SnIP can be obtained via ceramic as well as gas phase transport reactions resulting in needles of different lengths. Figure 2.2 shows a comparism between those two synthesis ways in case of SnIP.
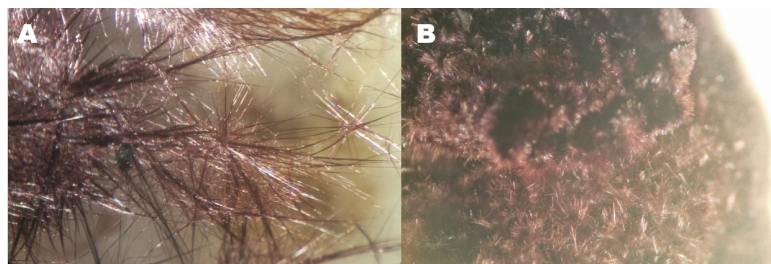
Figure 2.2: Different needle sizes in dependence of the synthesis way. **A:** Single crystals of SnIP can be achieved via a gasphase-transport-reaction when choosing a high reaction temperature. **B:** Bulk SnIP is yielded via a ceramic reaction choosing a lower reaction temperature.

Solvothermal Synthesis: The solvothermal synthesis described in the work of Tian *et al.* did not include all neccessary information to conduct the synthesis.[80]

Direct citation from Tian *et al.*[80]: "Few-layer BP nanosheets were synthesized by a directly solvothermal process in ethylenediamine system using white phosphorus as raw material. In a typical synthesis process, an amount of white phosphorus was added in ethylenediamine under magnetic stirring. Subsequently, the mixture was transferred to a 100-mL Teflon®-lined stainless autoclave followed by heating at 100°C for 12 h. After cooling to room temperature naturally, the precipitates were collected and washed with benzene, ethanol, and distilled water in sequence. The final product was dried in vacuum at 60°C overnight. Reaction temperature determines the

formation and thickness of BP nanosheets. Here we confirmed the temperature in the range of 60–140°C works for the preparation of fewlayer BP nanosheets. Moreover, the higher the temperature is, the higher the yield is."

To obtain black phosphorous in this work, 27 mL of dissolved white phosphorous in dry ethylenediamin (EN) were transferred under inert conditions to a Teflon$^{®}$ beaker. The container is sealed with a Teflon$^{®}$ lid and placed in a DAB-2 stainless steel pressure vessel (Berghof, 316 Ti, *i.e.* titanium stabilized CrNiMo stainless steel, V = 50 mL), which is placed in a pressure digestion system (digestec, Berghof, T_{max} = 523 K, ρ_{max} = 200 bar). After externally heating up the vessel to 400 K (DAH-412 heating block, capacity: 12 vessels, programmable BTC-3000 temperature control unit with NiCr-Ni temperature probe), it is kept at that temperature for 3 h and then swiched off to cool down to room temperature. A stirring of the reaction mixture while synthesis was not possible. The final product was transferred to a Schlenk tube and separated from the EN via a Whatman-filter-tube. The solid was washed with anhydrous ethanol and dried under vacuum. To obtain SnIP 1.0 mL of a 2.0 mol/L solution of white phosphorous in ethylendiamine (EN) is slowly added to a solution of SnI_4 (1.2526 g, 2.0 mmol, presynthesized according to literature[79,81]) in 10 mL EN and transferred to a Teflon$^{®}$ beaker. The external heating was set to 330-410 K and kept at that temperature for 12-168 h. The product was washed with toluene. The further synthesis procedure is conducted as described above.

The setup of the Berghof digestec pressure digestive system is schematically shown in figure 2.3 on page 17.
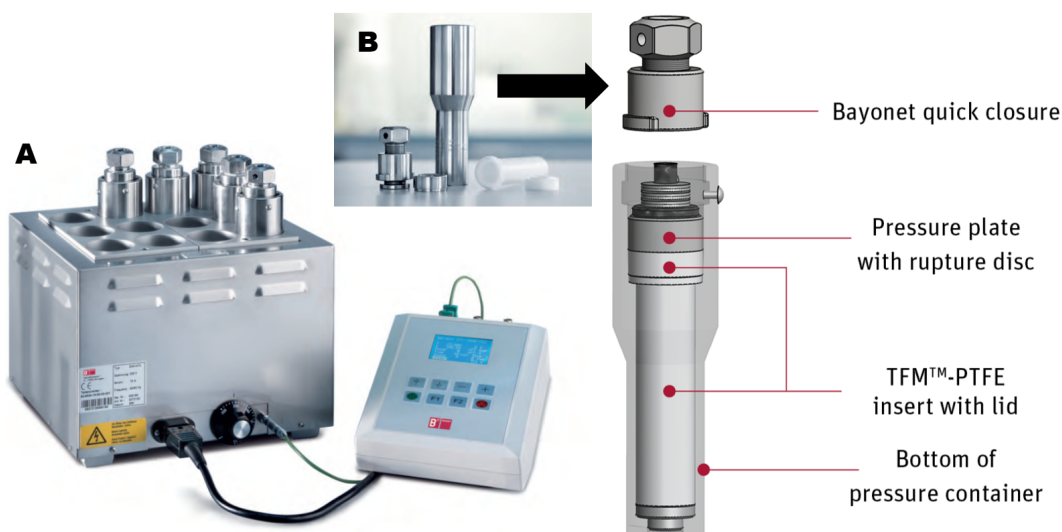
Figure 2.3:   A: DAH-412 heating block and programmable BTC-3000 temperature control unit. **B:** Schematic representation of a Berghof DAB-2 stainless steel pressure vessel (V = 50 mL, ρ_{max} = 200 bar) consisting of a bayonet quick closure, a pressure plate with rupture disc, a TFM^{TM}-PTFE insert with lid and the bottom part of the pressure container. Pictures taken from Berghof website (November 2018). [82]

Ball-milling Technique: The bulk material is manually broken up in an agate mortar and filled with about 200 tungsten-carbide balls (diameter 5.0 mm) into a 50 mL tungsten-carbide beaker under inert conditions. The container is sealed airtight and mounted into the ball mill. The milling procedure was set to be 250 rpm for 12 hours (10 min pause after every 10 min milling to avoid heat building up in the beaker). After the procedure is completed the homogeneous, fine powder was separated from the tungsten balls under inert conditions and stored in the glovebox.

Mechanical Delamination: Mechanical delamination can be achieved using adhesive tape (e.g. Lensguard 7568, Nitto). [83,84] The sample is placed between two stripes of tape, pressed together and pulled apart. By using this method multiple times nanocrystals smaller than 40 nm can be prepared.

Chemical Exfoliation: The bulk material was, as for the preparation by ball milling, broken up manually in an agate mortar and transferred to a high-walled glass beaker. Solvent was added as appropriate. The mixture was homogenized with an IKA T18 digital Ultra Turrax at 13000 rpm for 10 min. A 10 min treatment leads to the minimum particle size achieveable with this method. To achieve even smaller particle sizes the suspension was treated with a Sonoplus ultrasonic-homogenizer from Bandelin at 80% of the maximum power for 10 h. To avoid solvent evaporation, the suspension was cooled down in an ice bath. The suspension was dried under vakuum and transferred to a glovebox. Until further processing the powder was stored under inert conditions in the glovebox.

Thin Film Coating methods: The polymers are dissolved in an appropriate solvent and stirred for at least an hour before chemically delaminated SnIP is added. The mixture is stirred until a homogeneous suspension is obtained. Different coating methods were investigated and suitable substrates were chosen. The films were examined with optical light microscopy (Leica DM 1750 M, 10×100 magnification), scanning electron microscopy (SEM), Raman, UV-Vis and photoluminescence measurements.

Electrospinning: PEO (7.95 mmol, 0.35 g) is dissolved in 5 mL acetonitrile (VWR, >99.8, H_2O below 30 ppm) and stirred for 1 h under inert conditions. As in the case of film formation, chemically delaminated SnIP is added in different weight ratios and stirred until a homogeneous suspension is obtained. The suspension was electrospun as described by Freitag *et al.* in 2017 in a self-build apparatus.[85] A 0.9 mm (inner diameter) injector was used at a flow rate of 3.5 mL·min^{-1} and an acceleration voltage of 10.9 kV. To achieve different fiber orientations, two different collectors can be used. To achieve alligned fibers an aluminium collector consisting of two parallel, separately grounded, plates was used. Before analysis, the fibers were dried under vacuum.

SnIP-CNFCl hybrids: A hybrid suspension of 30 mg·mL^{-1} fluorine and chlorine co-doped C_3N_4 (CNFCl) was chemically delaminated. Different weight-percentages of SnIP in chlorobenzene were added and ultrasonicated for another 30 min. Afterwards the mixture was stirred for

24 h. This ensures the enwrapping of SnIP needles with CNFCl sheets. The obtained nanocomposite was dried in a vacuum before further characterization.

Anode Coating: To prepare the anode slurries 15 wt.-% of the respective phosphorous (ball milled, chemically exfoliated or hydrothermal synthesized), 65 wt.-% conductive carbon (carbon Super C65, Timcal) and 20 wt.-% PVDF (Solvay) are mixed in an agate mortar. NMP is added slowly until a homogeneous, honey-like texture is achieved. Copper foil is fixed to a flat surface like glass and dried at 350 K before transferring it to the glovebox (MBraun, MB200B, Ar-atmosphere, water and oxygen content below 0.1 ppm). The slurry is spread onto the copper foil and coated to a thickness of 150 μm using a doctor bar (Erichsen). The coating is dried at room temperature under inert conditions, punched into 14 mm diameter anodes and pressed at 3 to for 30 seconds. For the investigation of the influence of copper incorporation into the process, half of the anodes were coated with a saturated $CuSO_4$-solution. The excess liquid was removed and the anodes were dried under vakuum at 400 K in a glass oven B-585 Kugelrohr (Büchi) over night before transferring them to a glovebox and applying them in lithium ion battery applications.

Coin Cell Assembly: The anodes were preapred as described above. The assembly was carried out under inert conditions in a glovebox (MBraun, MB200B, Ar-atmosphere, water and oxygen content below 0.1 ppm). CR2032 coin cells with a 15 mm elemental sodium disc as couter electrode were used. As separator between the counter electrode and the anodes glass fiber separators (17 mm diameter, dried under vakuum at 400 K over night) and an electrolyte EC/EMC with 1 M $NaPF_6$ were employed.

Photodetector Fabrication: The mechnically delaminated flakes ($As_{0.83}P_{0.17}$, between 5-20 nm thickness) were transferred to a highly doped Si-wafer covered by a SiO_2 and if needed boron nitride protective layer (300 nm). The hight of the particles was measured with a Bruker MultiMode 8 atomic force microscope (AFM). The different layers are annealed (Ar/H_2 flow) at 600-900 K to eliminate polymer contamination resulting from the exfoliation technique.[84] All steps except the annealing under Ar/H_2 flow were conducted under inert conditions (glovebox,

MBRAUN, MB200B, Ar-atmosphere, water and oxygen content below 0.1 ppm). The contacts were defined with electron-beam lithography amd deposited with a Nano38 thermal evaporator. The schematical setups of this devices are given in figure 2.4 on page 20. The two different fabrication methods were carried out in the groups of Feng Miao (National Laboratory of Solid State Microstructures, School of Physics, Collaborative Innovation Center of Advanced Microstructures, Nanjing University, Nanjing 210093, China) and Fengnian Xia (Department of Electrical Engineering, Yale University, New Haven, Connecticut 06511, United States).
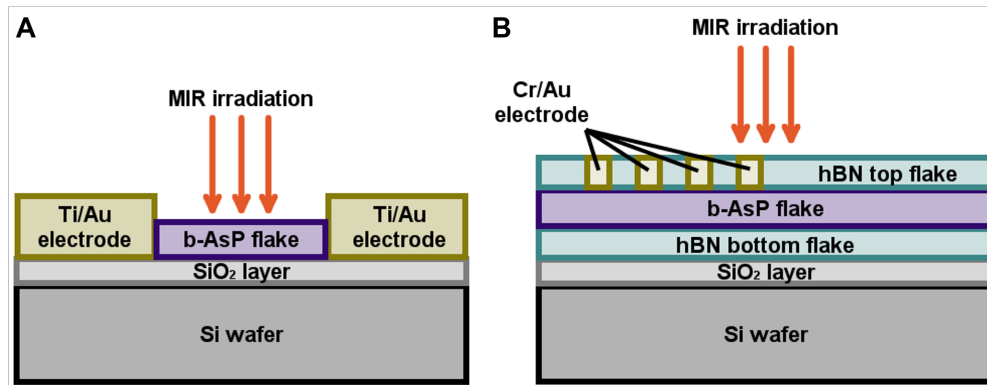
Figure 2.4: A: Schematic drawing of a black $As_{0.83}P_{0.17}$-phototransistor and **B:** a black hBN-$As_{0.83}P_{0.17}$-hBN-phototransistor for application in photodetection.

2.3 Characterization Techniques

Powder Diffraction: Phase analysis was conducted using powder X-ray diffraction (PXRD). The sample was ground in an agate mortar until an uniform powder was obtained, sealed airtight between two stripes of SCOTCH® *Magic*$^{\text{TM}}$, 810, 3M tape and placed in a flat sample holder. The powder diffraction measurements were conducted using Cu-$K_{\alpha 1}$ radiation ($\lambda = 1,54051$ Å, Ge(111) monochromator) on a STOE STADI P powder diffraction diffractometer equipped with a DECTRIS MYTHEN 1K detector.[86] An external calibration was applied using a silicon standard ($a = 5.43088$ Å). The measurements were conducted in a 2θ range between 5 and 80° within 15 minutes. The unit cell parameters were determined with the software WINXPOW of STOE and compared with the literature values taken from PEARSON'S CHRYSTALLOGRAPHIC-database (PCD).[87,88]

Single Crystal Diffraction: Single crystals were optically separated using a light microscope (Zeiss Stemi 508, 24x magnification). X-ray single crystal diffraction data sets were collected at room temperature using a Stoe IPDS-II image plate system (graphite monochromatized Mo-$K_{\alpha 1}$ radiation; $\lambda = 0.71073$ Å) in oscillation mode.

Structure Refinement from X-ray data: Determination of the cell parameters and reduction of the data set were conducted with the software suit X-Area.[89] A numerical absorption correction was applied to the data set. Structure solution was carried out with the software suit Jana2006, using the charge-flipping algorithm Superflip.[90,91] A separate refinement of the occupancy parameters did not show a deviation from the ideal composition. The final Fourier map showed no significant residual peaks.

Inelastic neutron scattering: The measurement was conducted in an aluminium bed cell of 4×4.8 cm^2 cross-sectional area. The measurements were conducted at low temperatures (10 K) at the inverted-geometry neutron spectrometer TOSCA at the ISIS Pulsed Neutron & Muon Source, Rutherford Appleton Laboratory, United Kingdom.[92]

High pressure synchrotron X-ray experiments: The measurements were performed at the beamline I15 at the Diamond Lightsource, UK, with a X-ray wavelength of 25.5 keV under the supervision of Dominik Daisenberger (Diamond Light Source Ltd. Harwell Science & Innovation Campus, Didcot, OX11 0DE, Great Britain). The experiments were conducted in Diamond Anvil Cells (750 μm diameter Diamonds) using Daphne oil 50 as pressure transmitting medium and ruby fluorescence as pressure calibrant (p = ambient - 4 GPa) or a self-built high-pressure cell (p = ambient - 0.4 GPa).[93] The DAC instrument is equipped with a 2D Mythen area detector, the self-build cell with a 2D PerkinElmer detector and the sample-to-detector distance was calibrated prior to the experiment with CeO$_2$ standard.

High pressure PXRD analysis: The evaluations of HPPXRD data were performed with the TOPAS academic v5 software. To aviod errors due to sample-to-detector distance changes while sample mounting, the data was initially calibrated against the V(p=ambient) volume of

the DAC experiments. The evolution of the full-width of half maximum (FWHM) was examined as a function of pressure. Based on the found phase transition of SnIP at 0.6 GPa only data below that value was used in the determination of the bulk modulus. It was obtained by fitting a Birch-Murnaghan equation of state to the compiled dataset. The analysis was conducted by Gregor Kieslich (Crystal Chemistry of Functional Materials group, Technical University Munich, Department of Chemistry, Lichtenbergstrasse 4, 85748 Garching, Germany).

Scanning Electron Microscopy (SEM) and Energy Dispersive X-Ray Spectroscopy (EDX): The compounds were analyzed with a scanning electron microscope (SEM) JCM-6000 NEOSCOP TM (JEOL, 5900LV, Si(Li) detector) using an integrated energy dispersive X-ray spectroscopy-unit (EDX). Further SEM/EDX measurements were conducted on a HR SEM JSM-7500F field emission scanning electron microscope (JEOL) equipped with an INCA X-Max analyzer (OXFORD INSTRUMENTS), a SH NVision40 (ZEISS), a ZEISS Sigma FESEM w/EDX&EBSD integrated with OXFORD AZtecSynergy system and an Ultra55Plus (ZEISS, Gemini, 5 kV). EDX data was generated using 15 kV acceleration voltage and avaraged over 3 random points on the sample surface with an integration time of 300 s.

Transmission Electrone Microscopy (TEM): The sample was eighter suspended in butanol or prepared dry. The samples were analysed with a JEM-2100 (JEOL, acceleration voltage 200 kV, LaB_6 cathode, spherical aberration coefficient $C_S = 1.0$ mm) with EDX detector (SDD, OXFORD), a field emission gun microscope TECNAI F30 G2 (FEI, 300 kV, $C_S = 1.2$ mm) with EDX detector (SiLi, EDAX) or a CM 30 ST microscope (PHILIPS, 300 kV, LaB_6, $C_S = 1.15$ mm) equipped with a spinning star device (allowing precession electron diffraction (PED) [94,95] and selected area electron diffraction (SAED)). Simulations of the PED and SAED patterns as well as the high resulution images were obtained with the JEMS software package. [96] Some analyzed samples were beam sensitive and decomposed during aquisition of high resolution images. The TEM measurements were conducted in the groups of Lorenz Kienle (Technische Fakultät Christian-Albrechts-Universität zu Kiel, Kaiserstr. 2, 24143 Kiel, Germany) and Karthik Shankar (Deaprtment of Electrical and Computer Engineering, University of Alberta, 11-384 Donadeo Innovation Centre For Engineering, Edmonton, Canada T6G 1H9).

High Resolution Transmission Electron Microscope Imaging: HR-TEM measurements were conducted using a FEI Tecnai F-30 instrument at a working voltage of 300 kV. The sample was coated with 6-10 nm amorphous carbon on the sample surface for conductivity increase via thermal evaporation. Elemental mapping was conducted using an electron energy loss spectroscopy (EELS) combined with a Gatan imaging filter (GIF). This resulted in energy-filtered TEM (EFTEM) images. EDX data was generated with a JEOL JEM-ARM200CF S/TEM equipped with STEM EDX detector, operating at an acceleration voltage of 200 keV. The HRTEM measurements were conducted in the group of Karthik Shankar (Deaprtment of Electrical and Computer Engineering, University of Alberta, 11-384 Donadeo Innovation Centre For Engineering, Edmonton, Canada T6G 1H9).

X-ray photoelectron spectroscopy (XPS): XPS measurements investigate the surface chemical nature and binding energy of diverse elements. A Kratos Analytical Axis-Ultra XPS-instrument equipped with monochromatic Al-Kα source (15 kV, 50 W) and photon energy of 1486.7 eV was used under ultrahigh vacuum (about 10^{-8} Torr). To identify the various elements carbon correction was applied. The measurements were conducted in the group of Karthik Shankar (Deaprtment of Electrical and Computer Engineering, University of Alberta, 11-384 Donadeo Innovation Centre For Engineering, Edmonton, Canada T6G 1H9).

Thermal Analysis (DSC/DTA): The thermal characteristics up to 623 K of the new compound were analyzed with a Netsch DSC (differential scanning calorimetry) 200 F3 Maia and above this temperature using a Netsch DSC 404 Pegasus up until 1273 K. The heating and cooling rates were set to 10 K·min^{-1}. For the low temperature-DTA (differential thermal analysis) experiments aluminum crucibles and for the high temperature DTA experiments, niobium crucibles were used. All thermal experiments were conducted under inert conditions. The DTA data was analyzed with the Proteus Thermal Analysis software.[97]

Thermogravimetry: Thermogravimetric experiments were conducted in a temperature range between 300 and 1273 K with a heating rate of 10 K·min^{-1} under nitrogen flow (flow rate: 100 mL·min^{-1}) on a STA 449 F3 Jupiter simultaneous thermal analyzer (Netsch). Experiments

to 1673 K were conducted under argon flow (flow rate: 100 mL·min⁻¹) on a STA 409 Luxx simultaneous thermal analyzer (Netsch). To analyze the intermediate products some experiments with slow heating rates (2 K·min⁻¹) were interrupted at 730 bzw. 743 K. The decomposition temperatures were determined from the onset values of the DTG signals. The intermediate products were analyzed via powder X-ray diffraction (Bruker D2 X-ray diffractometer, accelerating voltage: 30 kV, filament current: 10 mA, Cu-K_α radiation, reflection mode, LynxEye detector). The measurements were conducted in the group of Peer Schmidt (BTU Cottbus-Senftenberg, Großenhainer Str. 57, 01968 Senftenberg, Germany).

High-Temperature Gas Balance: An advanced high-temperature gas balance (HTGB) is used investigate the thermal decomposition behaviour of a material under it's own equilibrium vapour pressure.[98] The compound is sealed in a silica-ampoule so the equilibrium gas phase is in permanent contact with the solid phase. While evaporation and condensation a different leverage impacts the horizontal balance support which causes the signal. A heating/cooling rate of 10 K·h⁻¹ up to 1123 K/ down to room temperature is applied. The HTGB measurements were conducted in the group of Peer Schmidt (BTU Cottbus-Senftenberg, Großenhainer Str. 57, 01968 Senftenberg, Germany).

Impedance Measurement: Impedance spectroscopy was used to measure the electrical conductivity in the range of 10^5 to 1 Hz and an amplitude of 20 mV. The new compound was pressed to a pellet (6 mm diameter, 79% theoretical density) and analyzed at 293 K with a RHD Instruments TSC standard cell with a Methrom Autolab B.V. PGSTAT204 potentiostat and a FRA32 unit. An Arrhenius-type representation where the logarithm of the conductivity was plotted against the inverse temperature 1/T was applied to calculate the activation energy and the slope of the graph was determined. In further measurements Mott-Schottky plots were assessed from impedance-potential values and Nyquist plots were prepared by electrochemical impedance spectroscopy (EIS) (3 electrode configuration).

Seebeck Coefficient Measurements: A pellet of the new compound (diameter 15 mm, 81% of the theoretical density) was pressed using a Massen GmBH MP150 hydraulic press of

the type 15T, at a temperature of 373 K and pressure of 10 bar. The Seebeck coefficient was obtained with a NETSCH SBA 458 Nemesis in a temperature range between 273 and 873 K. Due to device specifications, the electrical conductivity is always determined before a Seebeck-coefficient measurement is conducted. The sample was suffering from decomposition after a DC (direct current) current was applied and therefore this value was set to be as low as possible (0.1 mA) and the structure of the compound analyzed via PXRD analysis to ensure its integrity.

Magnetic Measurements: Magnetic measurements were performed on a PPMS (physical property measurement system) system (QUANTUM DESIGN PPMS Modell 6000, equipped with an Evercool-System). The sample powder was weighed and sealed in a polyethylene capsule. The sample was cooled in zero external field and the susceptibility was measured at 10 kOe in the temperature range from 3 to 300 K. The low-temperature regime (2.1-6 K) was additionally measured at 20 Oe to test for superconductivity. Measurements were conducted in the group of Rainer Pöttgen at the Institute for Inorganic and Analytical Chemistry at the University of Münster.

Young's modulus determination: The Young's modulus was determined with an atomic-force microscope (AFM) in nanoindenation mode. SnIP was deposited onto a Si-wafer with a SiO_2 surface layer. Beforehand the SiO_2 layer was etched 500 nm deep ($25 \times 25 \ \mu m^2$ wide trenches) via reactive ion etch using a TEM grid as a shadow mask. Needles bridging an etched trench were identified with an optical microscope. The experiments were conducted in the group of Thomas Weitz (Physics of Nanosystems, Department of Physics, Ludwig-Maximilians-University Munich, Amalienstrasse 54, 80799 Munich, Germany / Center for NanoScience (CeNS) and Nanosystems Initiative Munich (NIM), Schellingstrasse 4, 80799 Munich, Germany).

[119]Sn-Mössbauer Spectroscopy: For [119]Sn-Mössbauer spectroscopy a $Ca^{119m}SnO_3$ source was used. SnIP was enclosed in a small thin-walled polymethyl metacrylate (PMMA) container resulting in a Sn thickness of 13 mg·cm^{-3}. A 0.05 mm thick palladium foil captures the concurrently emitted Sn K X-rays. Samples were analyzed at room temperature and in a liquid nitrogen bath under transmission geometry. The data sets were evaluated using the Normos-90 program

package. [99] Measurements were conducted in the group of Rainer Pöttgen at the Institute for Inorganic and Analytical Chemistry at the University of Münster.

^{31}P Nuclear Magnetic Resonance (^{31}P-NMR): Solid state ^{31}P-NMR studies were performed on a AVANCE III spectrometer (BRUKER) at 7 T and a resonance frequency of 121.53 MHz. A BRUKER 1.3 mm probe was used for Magic-Angle-Spinning (MAS) measurements (spinning frequency: 30 kHz, RF amplitudes: 122 kHz). All shifts were referenced to 85% H_3PO_4 with ammonium dihydrogen phosphate as external standard. Spectra with 300 s repetition time were evaluated with the DMFIT software. [100] The homonuclear magnetic dipole coupling between the ^{31}P nuclei and therefore the connectivity between the phosphorous atoms was analyzed with a 2D ^{31}P-RFDR-NMR (radio frequency-driven dipolar recoupling NMR, saturation comb, repetition time: 30 s, mixing time: 1.6 ms). [101] Measurements were conducted in the group of Leo van Wüllen at the Institute for Physics at the University of Augsburg.

Raman Spectroscopy: Raman spectra were recorded on a SENTERRA spectrometer (BRUKER OPTICS) with a 785 nm laser and a power of 1 mW. Five measurements with an integration time of 30 s each were added to obtain the spectrum. The laser was focused using a 50× magnification (slide 50× 1000 μm, zoom lens 50 long distance).

Diffuse Reflectance UV-Vis: For this measurement on bulk and single crystal samples a AVASPEC 2048 spectrometer (AVANTES) with a deuterium/halogen leight source (AVALIGHT-DH-S-BAL) connected with a reflection probe (FCR-7UV200-2-ME) and a custom-made sample holder (depth: 5 mm) was used. The diffuse reflectance UV-Vis spectrum was plotted using the Kubelka-Munk equation which is defined as follows (equation 1 with $R = R_S/R_T$, R_S: reflectance of sample, R_T: reflectance of PTFE reference). [102]

$$F(R) = (1 - R)^2 \cdot (2R)^{-1} \tag{1}$$

The bandgap was calculated using a Tauc-plot $[F(R)h\nu]^x$ (indirect band-gap: x = 0.5; direct band-gap: x = 2). [103,104] The measurements were conducted in the group of Karthik Shankar

(Deaprtment of Electrical and Computer Engineering, University of Alberta, 11-384 Donadeo Innovation Centre For Engineering, Edmonton, Canada T6G 1H9).

Photoluminescence (PL) Spectroscopy: Photoluminescence measurements were conducted at room temperature using a Princton Instruments PyLoN LN Digital CCD Spectroscopy System on SnIP needles with single gating of 1,800 1 mm^{-1}. A linear polarized He/Ne-laser exitation laser (633 nm, 86 μW) is used and the spectra were integrated for 120 s using a 100$\times$ LD EC Epiplan-Neofluar objective (Zeiss). The measurements were conducted in the groups of Alexander Holleitner (Walter Schottky and Physics Department, Technical University of Munich, Am Coulombwall 4a, 85748 Garching, Germany) and Karthik Shankar (Deaprtment of Electrical and Computer Engineering, University of Alberta, 11-384 Donadeo Innovation Centre For Engineering, Edmonton, Canada T6G 1H9).

Photoelectrochemical experiments: For substrate preparation, a FTO glass was covered with a 60 nm thick TiO_2 layer using a solution of titanium isopropoxide. $C_3N_4(F, Cl)$ and SnIP-CNFCl hybrids were suspended (30 mg·mL^{-1}) in a film forming agent (α-terpineol), dropcoated onto the substrate and dried at 520 K. To conduct the photoelectrochemical experiments a circular surface area (1-inch diameter) of the films was exposed while the rest was sealed with a Surlyn sheet. This device was used as the working electrode (photoanode) in a 3 electrode system water-splitting setup with Pt and Ag/AgCl as counter (cathode) and reference electrode. The setup was placed in a 0.1 M Na_2SO_4 solution and irradiated with simulated sunlight (AM 1.5 G) with an intensity of 100 mW·cm^{-2}. UV-light was filtered out with an UV cut off filter. Linear sweep voltammetry (-0.8 to +0.8 V) was conducted to analyze the photoresponse of the prepared samples (photocurrent density vs applied voltage). Further experiments were conducted with specific wavelength irradiation and in the dark. The measurements were conducted in the group Karthik Shankar (Deaprtment of Electrical and Computer Engineering, University of Alberta, 11-384 Donadeo Innovation Centre For Engineering, Edmonton, Canada T6G 1H9).

Electronic Property Measurements: The electrical conductivity of SnIP needles was determined by transferring it to a silicon substrate with a silicon dioxide layer (300 nm) and contacting it via nano-wires attached by optical lithography and e-beam evaporation (3 nm Ti/30 nm Au). These steps were performed using the AZ 5214E photoresist and AZ 351 B developer (AZ ELECTRONIC MATERIALS GmbH), a maskaligner (KARL SÜSS GmbH&Co) and a custom-build evaporator. The contacts were used to measure a two-terminal current–voltage characteristic using a DL INSTRUMENTS 1211 current preamplifier ($10\text{-}9$ A·V^{-1}) and an Agilent 34410A digital multimeter (KEYSIGHT TECHNOLOGIES). To apply a bias between -5 and +5 V a DC source (Model 7651, YOKOGAWA ELECTRIC CORPORATION) was used. To measure the electron beam induced current (EBIC) a bundle of SnIP needles was contacted by a tungsten tip attached to a micromanipulator (KLEINDIEK NANOTECHNIK). The measurement was performed with a NVision40 scanning electron microscope (ZEISS) using a DL Systems 1211 current preamplifier ($10\text{-}9$ A·V^{-1}), sampled by a PXI-DAQ system (NATIONAL INSTRUMENTS), along with the signal of the SEM in-lens detector. The measurements were conducted in the group of Alexander Holleitner (Walter Schottky and Physics Department, Technical University of Munich, Am Coulombwall 4a, 85748 Garching, Germany).

Electrical and Photoresponse Measurements: The measurements were performed at ambient conditions with a Keithley 2636A dual-channel digital source meter. Wavelength-dependent photoresponse was analyzed with a custom-built wavelength-tunable multichannel MIR-laser source in the group of Feng Miao. The investigated spectrum reached from 2 to 8.05 μm. The spot size in the wavelength range between 2 and 4.3 μm was about 0.43 mm^2 and in the range of 5.3 to 8.05 μm about 9 mm^2 (50 mW power). The lasers were focused using an integrated Hyperion 2000 microscope. The total incident power reached from 30 to 100 μW depending on the used laser. For all measurements the devices are placed in a thoroughly screened metal box to ensure complete darkness and minimize environmental noise. Noise spectra were acquired using a spectrum analyzer (STANFORD Research System SR770, 100 kHz bandwidth) at different biases. The two different fabrication methods were carried out in the groups of Feng Miao (National Laboratory of Solid State Microstructures, School of Physics, Collaborative Innovation Center of Advanced Microstructures, Nanjing University, Nanjing 210093, China) and

Fengnian Xia (Department of Electrical Engineering, Yale University, New Haven, Connecticut 06511, United States).

Polarized Infrared Extinction Measurements: The polarized infrared extinction measurements were conducted with the same microscope used for the electrical and photoresponse measurements. The polarization of the IR-light was controlled with an infrared polarizer. The measurements were carried out in the group of Fengnian Xia (Department of Electrical Engineering, Yale University, New Haven, Connecticut 06511, United States).

Quantum Chemical Calculations: Band structure (BS) and density of state (DOS) calculations were performed in the framework of density functional theory (DFT) applying Perdew, Burke, Ernzerrhoff (PBE) functionals[105] with the full potential local orbital (FPLO) package.[106,107] To reach sufficient accuracy a k-grid mesh of $8 \times 8 \times 8$ was applied.

Further calculations were performed in the framework of DFT within the all-electron local orbital approach with the Schlegel algorithm as implemented in CRYSTAL14.[108] PBE functional models with and without Grimme's D2 correction for van der Waals interactions were investigated.[109] In pressure dependent calculations effective core pseudopotential (ECP) and all electron valence basis sets [Pascale 2005] were used for the contemplated elements. To simulate pressure respective unit cell axis lengths were shortened in steps of 2% of the axis length.

The electronic band structures were calculated with HSE06 functionals.[110,111] To determine the energy versus volume curves, the implemented EOS (equation of state) functions were used. All electron Gaussian type basis sets for phosphorous (AE-531151d1*)[112], tin (AE-976631311d1*)[113] and a valence basis set for iodine (HW-1111111*)[114] were applied for all calculations (DOS, tin Fermi contact density, IR- and Raman frequencies). All calculations were converged to k-point shrinking of $2 \times 2 \times 2$ to $8 \times 8 \times 8$. Xcrysden was used to obtain graphical representations.[115] Data from single crystal structure determination was used for both the 1D-polymer and the single strand SnIP calculations. In case of the single strand calculations distances of 8.3 Å were used to assume interactions between the rods as neglectible. For the 1D-polymer all crystal symmetry was removed that just one repetative rod remained in the unit cell and translation was allowed in rod-direction. Compounds isotypic to SnIP were derived

from DFT calculations. The expected lattice parameters are obtained from SnIP by linear interpolation to the respective compound for full substitution estimating Vegard's law for partial substitution. The applied method (DFT-LDA) slightly underestimates bond lengths and lattice parameters by 1 to 3%.

Electron Localization Function (ELF) Calculations: The electron localization function was developed by Becke and Savin et al. to analyze the electronic structure in direct space. [116,117] The calculations were conducted as implemented in the vasp4.6 code with PAW potentials and PBE functionals for exchange and correlation comparable to the quantum chemical calculations (bandstructure calculations). [118–121] The figures were generated with the software Vesta. [122] The ELF calculations were carried out by Richard Weihrich (Institut für Materials Resource Management, Universität Augsburg, Universitätsstraße 1, 86159 Augsburg, Germany).

Battery Testing: The half cells were analyzed with a BioLogic VMP3 multichannel galvanostat. The cyclization was conducted in a voltage range between 2.0 and 0.2 eV and a scan rate of 0.05 mV·s^{-1} for 10 cycles. The specific capacities were evaluated with the software EC-Lab (version V10.40) and calculated on basis of the active material content in each anode.

3 Results

3.1 Structure and Bonding of La$_2$NiBi

Claudia Ott[1], Max Baumgartner[1], Konrad Schäfer[1,3], Franziska Baumer[1], Katharina Freitag[1], Lavinia Scherf[1], Lukas Heletta[3], Richard Weihrich[2], Rainer Pöttgen[3] and Tom Nilges[1]

[1] Technische Universität München, Department Chemie, Synthese und Charakterisierung innovativer Materialien, Lichtenbergstraße 4, 85748 Garching

[2] Institut für Materials Resource Management, Universität Augsburg, Universitätsstr. 1, 86159 Augsburg, Germany

[3] Universität Münster, Institut für Anorganische und Analytische Chemie, Corrensstraße 30, 48149 Münster

The article "Structure and bonding of La$_2$NiBi" was submitted in June 2018 to the "Zeitschrift für Allgemeine und Anorganische Chemie" and published online in September 2018. The main results were presented by Claudia Ott at the 6th Energy Colloquium in Munich, Germany in 2016, the Annual ATUMS meeting 2016 in Raitenhaslach, Germany and the 11th IGSSE Forum in Raitenhaslach, Germany in 2017.

The object of this work was the synthesis of a new compound in the Bi$_3$Ni structure type. As described in chapter 1.3 on page 8 one ternary representative in this system was already published by Schäfer *et al.* in 2014.[47] The new ternary version of this structure type was synthesized via a ceramic solid state reaction. The compound crystallizes in the space group *Pnma* with the unit cell parameters $a = 838.88(6)$ pm, $b = 455.61(11)$ pm, $c = 1210.4(2)$ pm and a cell volume of V $= 0.46261(14)$ nm^3.

The crystal structure is comparable to the one of La$_2$NiSb and Bi$_3$Ni.[46,47] Each nickel atom is surrounded by six lanthanum atoms in a slightly distorted trigonal prismatic way. Two

rectangular faces of such a prism are connected to adjacent prisms. This leads to rod like structures stacked along the crystallographic *b*-axis. Within these rods the nickel atoms form zig-zag chains. The free rectangular side of the earlier described prism is in contrast to the structure published by Schäfer *et al.* capped with not an antimony but a bismuth atom. Thus tracing back to the original binary compound (Bi_3Ni) where this crystallographic position is occupied by a bismuth atom as well. The here observed nickel coordination number of 9 can be frequently observed in related intermetallic compounds. Notable is that the Ni-Ni distance within the zig-zag chains is surprisingly short and close to the one of elemental nickel.[48] It represents the shortest distance reported in any compound containing Ni-Ni zig-zag chains to this date.[44–47]

The chemical composition derived from the single crystal measurement was verified via semi-quantitative EDX analysis. The melting point was analyzed with DTA measurements. Electronic properties of this new compound were investigated by quantum chemical and ELF calculations as well as impedance and Seebeck measurements. The compound decomposed under DC current and higher temperatures and displays metallic behaviour with no signs of anisotropy. Magnetic measurements showed that La_2NiBi is a weak Pauli paramagnet. The compound shows no distinct nickel impurities at the grain boundaries. Measurements at the low temperature regime (2.1-6 K) resulted in no signs of superconductivity.

Author contributions: C.O. synthesized the new compound and conducted all XRD, SEM as well as EDX measurements, C.O. and K.S. solved the structure using the software XArea and JANA, M.B. did low temperature DSC measuremts and quantumchemical calculations, F.B. conducted Seebeck measurements, K.F. impedance measurements, L.S. measured high temperature DSC, L.K. and R.P. investigated the magnetic properties of the samples, ELF calculations were conducted by R.W., C.O., T.N. wrote the manuscript. All authors discussed the results and revised the manuscript.

Structure and Bonding of La$_2$NiBi

Claudia Ott,[a] Max Baumgartner,[a] Konrad Schäfer,[a,c] Franziska Baumer,[a] Katharina Freitag,[a]
Lavinia Scherf,[a] Lukas Heletta,[c] Richard Weihrich,[b] Rainer Pöttgen,*[c] and Tom Nilges*[a]

Dedicated to Prof. Dr. T. F. Fässler on the Occasion of his 60th Birthday

Abstract. La$_2$NiBi was synthesized by heating a cold pressed pellet of the elements in a sealed and evacuated silica tube at 1070 K. The structure was determined via powder and single crystal X-ray diffraction. La$_2$NiBi crystallizes orthorhombically, in the space group *Pnma*: a = 838.88(6), b = 455.61(11), c = 1210.4(2) pm and V = 0.46261(14) nm^3 (wR = 0.1002, 1001 F^2 values, 26 variables, Z = 4). La$_2$NiBi represents a higher congener of La$_2$NiSb and adopts a ternary ordered version of the Bi$_3$Ni structure type. Similar to La$_2$NiSb, the nickel atoms form infinite zigzag chains (259 pm Ni–Ni) with trigonal-prismatic lanthanum coordination. One rectangular face of the lantha-

num prism is capped by a bismuth atom (333.08–364.74 pm La–Bi, 281.18 pm Ni–Bi). These zigzag chains run along the *b* axis. DFT based band structure calculations and DOS representations suggest metallic behavior. This was confirmed via temperature dependent impedance spectroscopic measurements. A Seebeck coefficient of –10 µV·K^{-1} in the temperature range up to 873 K substantiates this finding. Thermal analyses show that the compound is stable up to 873 K under inert gas conditions and degrades at higher temperatures. The magnetic measurements show almost no grain boundary nickel impurities characterizing La$_2$NiBi as a weak Pauli paramagnet.

Introduction

Compounds with nickel chains attracted interest in the past due to their remarkable structural properties.[1–3] Such compounds like LaNi or GdNi, synthesized and characterized by *Dwight* et al. and *Baenzinger* et al. contain nickel atoms which are organized in infinite zigzag chains.[1,2] In LaNi the Ni chains are located parallel to each other and they are separated by La chains. The Ni and La subunits form layers stacked along the *b* axis. Neighbored layers are shifted by half a translation period along the *a* axis and form the 3D structure.[1] The nickel zigzag chains are oriented parallel to each other. In contrast, in GdNi the Gd atoms form a three-dimensional substructure where nickel zigzag chains tend to fill suitable channels formed by gadolinium.[2] In this case the zigzag chains of Ni are arranged alternatingly to each other like the iodine molecules in elemental iodine (herringbone pattern). The Ni–Ni distances differ significantly from each other in

both compounds. While for LaNi the distance is 319 pm, it is reduced to 267 pm in GdNi.[1,2] The latter Ni–Ni distance is surprisingly short and only slightly larger than in elemental, metallic nickel (250 pm).[8] The characteristic Ni chains are not very common in solid state materials and therefore not many of such compounds are known.

We now turn to the bismuth-rich phase Bi$_3$Ni. This 3:1 compound shows a different Ni substructure compared with the 1:1 ones.[4] Zigzag chains of Ni are still present, but the next coordination sphere differs significantly. Each Ni chain is surrounded by Bi atoms to from a comparable first coordination sphere like in the case of LaNi (see Figure 1). In addition, each of these subunits is capped at two opposite sides with further bismuth atoms to form the characteristic building block as shown in Figure 1c. In Bi$_3$Ni, the Ni–Ni distance is about 263 pm, even smaller than in GdNi.[2,4]

According to *Ruck* et al. Bi$_3$Ni shows a 1D structure with short Ni–Ni distances of 263 pm[4] and Ni–Bi distances of 273 pm in Bi$_7$ prisms around each Ni atom. Both distances indicate strong intermetallic bonding and they are even shorter than in other intermetallic compounds like e.g. Bi$_2$Ni$_3$S$_2$ with d(Ni–Ni) = 273 pm and d(Bi–Ni) = 277–296 pm.[5] Interesting properties were found such as superconductivity below T = 10 K, co-existing ferromagnetism, and mechanical elasticity.[6,7] Bonding analysis indicated stronger Ni–Bi than Ni–Ni bonds within the chains.

If two Bi atoms in Bi$_3$Ni are substituted by La the title compound La$_2$NiBi is realized, whereas an additional substitution of the remaining Bi by Sb results in La$_2$NiSb.[3] In the latter compound, the capping bismuth atoms in Bi$_3$Ni were substituted by Sb atoms and Bi atoms who form the trigonal prismatic first coordination sphere in Bi$_3$Ni are replaced by La. This results in independent infinite rods running along the

* Prof. Dr. R. Pöttgen
E-Mail: pottgen@uni-muenster.de
* Prof. Dr. T. Nilges
E-Mail: tom.nilges@tum.de
[a] Synthese und Charakterisierung innovativer Materialien
Departement Chemie
Technische Universität München
Lichtenbergstraße 4
85748 Garching, Germany
[b] Institut für Materials Resource Management
Universität Augsburg
Universitätsstraße 1
86159 Augsburg, Germany
[c] Institut für Anorganische und Analytische Chemie
Universität Münster
Corrensstraße 30
48149 Münster, Germany
Supporting information for this article is available on the WWW under **http://dx.doi.org/10.1002/zaac.201800237** or from the author.
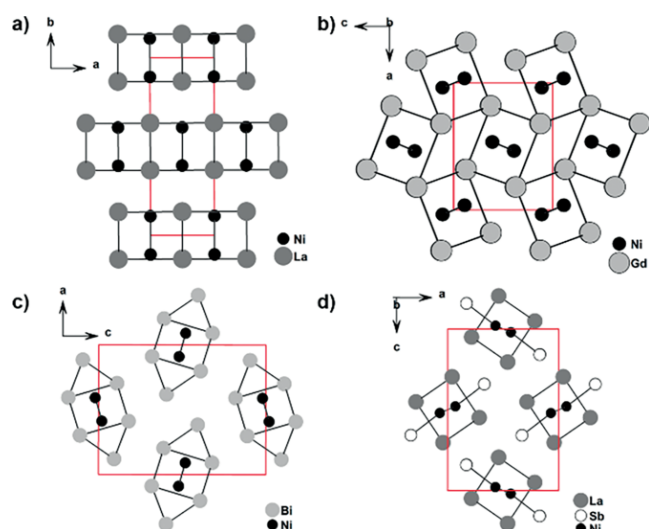
Figure 1. Projections of different rare earth and main group element nickel intermetallics (a) LaNi,[1] (b) GdNi,[2] (c) Bi$_3$Ni,[4] (d) La$_2$NiSb.[3] In all cases infinite nickel zigzag chains are present, embedded within a rare earth or main group element substructure. In going from the 1:1 to the 3:1 compounds, the rare earth and main group metal substructures becomes more and more diversified. This Figure is in part adapted from references[1–4] and a 3D representation is given in Figure S1 (Supporting Information).

b axis. The Ni–Ni distance is about 259 pm, which is the shortest one in the set of compounds discussed. A brief structural overview is given in the oncoming section. Coming back to the bonding analysis of ordered La$_2$NiSb, significant charge transfer was found from La to Sb as well as multi center bonds between the metals. In contrast to metallic Bi$_3$Ni, the electronic band structure of La$_2$NiSb indicated a state between metal and insulator.[3]

Herein, we report on the synthesis, crystal structure, and selected physical properties of La$_2$NiBi, a new representative adopting the Bi$_3$Ni structure type, with infinite nickel zigzag chains. The properties and effects on the electronic structure and bonding are analyzed by DFT calculations.

Results and Discussion

Crystal Chemistry

The synthesis of La$_2$NiBi from the elements resulted in a mixture of the title compound being the main fraction and an additional side phase (Figure 2, marked with *). The preparation of La$_2$NiBi is only possible in a small temperature window between 1000 K and the decomposition point (see below). If the synthesis temperature is lowered too much La$_2$NiBi does not even form. Single crystals of La$_2$NiBi were selected from the bulk phase and used for crystal structure analysis. Indexing and refinement of single-crystal X-ray diffraction data led to space group *Pnma* and lattice parameters of *a* = 838.88(6) pm, *b* = 455.61(11) pm and *c* = 1210.4(2) pm for La$_2$NiBi (Table 1).
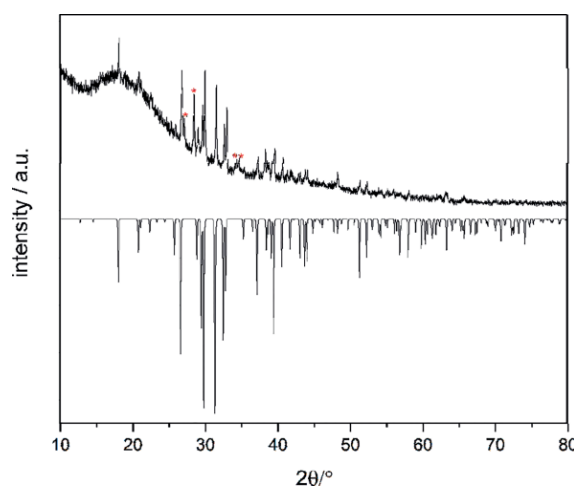
Figure 2. Powder diffraction pattern of La$_2$NiBi. Positive intensity: black: experimental powder diffraction pattern of a bulk sample, red: reflections of an unknown by-product; negative intensity: calculated powder diffraction pattern using the single crystal data.

Table 1. Selected crystallographic data and measurement parameters for La$_2$NiBi, space group *Pnma*, Z = 4, *T* = 293 K.

	La$_2$NiBi
Diffractometer type	IPDS-II
Pearson symbol	oP16
Space group	*Pnma*
Formula weight /g·mol^{-1}	545.5
Unit cell dimensions (*Guinier*-data)	
a /pm	838.88(6)
b /pm	455.61(11)
c /pm	1210.4(2)
Cell volume /nm^3	0.46261(14)
Calculated density /g·cm^{-3}	7.83
Transmission (max; min)	0.1751, 0.0706
Absorption coefficient /mm^{-1}	59.8
F(000)	900
θ range /°	2.95–35.25
Range in *hkl*	±13; ±7; ±19
Total number of reflections	12744
Independent reflections; R_{int}	1001 / 0.3961
Reflections with $I \geq 3\sigma(I)$; $R\sigma$	465 / 0.0844
Data / parameter	1001 / 26
Goodness-of-fit on F^2	1.18
R_1 / wR_2 [$I > 3\sigma(I)$]	0.0521 / 0.0766
R_1 / wR_2 (all data)	0.1474 / 0.1002
Extinction coefficient	172(19)
Largest diff. peak and hole /e·Å^{-3}	3.96 / –4.72

La$_2$BiNi represents a ternary and ordered variant of the Bi$_3$Ni structure type and is isotypic with La$_2$NiSb.[3,4] The crystal structure of La$_2$NiBi along with the characteristic building units is presented in Figure 3. Each nickel atom is coordinated in a slightly distorted trigonal prismatic way by six lanthanum atoms. The Ni–La distances lie between 282.0 and 317.2 pm. Two rectangular faces of each lanthanum prism are connected with adjacent prisms, leading to a rod running parallel to the crystallographic *b* axis. The nickel atoms within these prisms form a zigzag chain running in the same direction. The remaining rectangular faces of the lanthanum prisms are capped with a bismuth atom (Bi–La distance: 333.1–

364.7 pm). This leads to a nickel coordination in form of a tri-capped (two adjacent Ni, one Bi atoms) trigonal prism (coordination number 9), which is frequently observed in related intermetallic compounds.[9]
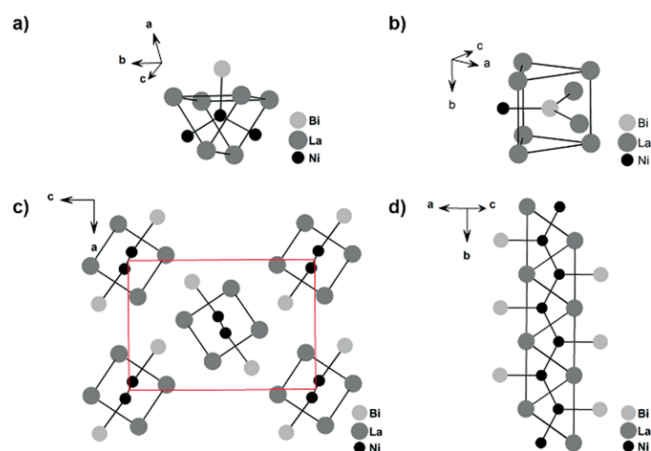
Figure 3. (Top) Tri-capped trigonal prismatic coordination sites of (a) nickel and (b) bismuth in La_2NiBi. (Bottom) Infinite chains in the La_2NiBi crystal structure. (c) Top view of a crystal structure section projected along the a and c axis, (d) nickel zigzag chain along the b axis.

The coordination sphere of the bismuth atoms in La_2NiBi is shown in Figure 3b. Similar to nickel, also bismuth has a coordination number of 9 in form of a slightly distorted tri-capped trigonal prism.

The fundamental building unit of the La_2BiNi structure is shown in Figure 3d. These units are arranged in form of a distorted hexagonal rod packing (Figure 3c). The Ni–Ni distance in La_2NiBi of 256 pm is even shorter than in La_2NiSb (259 pm),[3] and is close to elemental nickel[8] (250 pm). La_2NiBi and La_2NiSb are isopointal to Bi_3Ni.[3]

The composition derived from the single crystal structure determination was verified by a semi quantitative EDX analysis. A composition of 50 ± 2 at.-% La; 19 ± 3 at.-% Ni; 30 ± 4 at.-% Bi was found, averaged from ten independent measurements. Considering the accuracy of the method, this result is close to the ideal composition of La:Ni:Bi = 50:25:25 at%. No impurity elements heavier than sodium (detection limit of the instrument) could be observed.

Due to the small impurity found in the X-ray phase analysis it has to be stated at this point that the ongoing characterization and the determination of the physical properties were performed with this sample. Data reported in the following are maybe influenced by this fact and have to be handled with care. Therefore, the absolute values of the conductivity, Seebeck coefficient and susceptibility might be different if phase pure La_2NiBi will be available in the future.

Physical Properties

La_2NiBi melts incongruently at 1045 K as shown in Figure 4. A small effect at approx. 950 K is caused by the sealing procedure of the niobium ampoule and partial decomposition of the sample due to radiated heat. Also a thermal effect caused

by the non-identified side phase is possible. There is only a very small temperature window around 1000 K, in which La_2NiBi is formed.
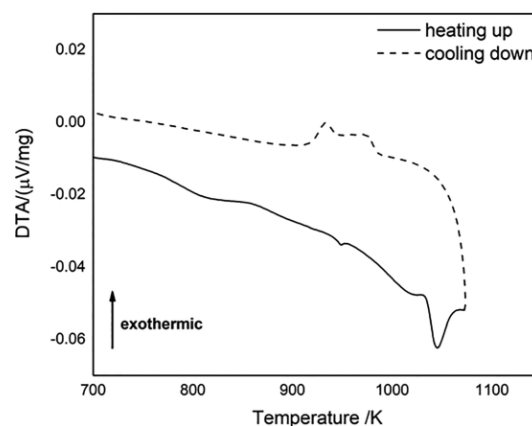
Figure 4. DTA measurement of La_2NiBi performed in a niobium crucible.

The electronic properties of La_2NiBi were determined by quantum chemical calculations as well as conductivity measurements. At room temperature a total conductivity of 1.65×10^{-2} S·cm^{-1} was found from impedance spectroscopy. La_2NiBi is characterized as a compound being on the borderline between a metallic and an insulating state, as also observed for La_2NiSb. The low conductivity characterizes it as a bad metal, which is in good accordance with the theoretical calculations (vide infra). Seebeck coefficient measurements were also performed in a temperature range of 300 to 900 K. La_2NiBi shows a Seebeck coefficient between -5 and -11 µV·K^{-1} in this temperature interval (Figure 5). These values are typical for a metallic compound. In the whole temperature range, the electrical conductivity, measured in parallel to the Seebeck coefficient was in the order of 10^{-1} S·cm^{-1}. No clear temperature dependency was detected, classifying La_2NiBi as a semimetal, which is consistent with the low conductivity values. Unfortunately, La_2NiBi tends to decompose under the applied DC current at higher temperatures and therefore no exact conductivity values are given.
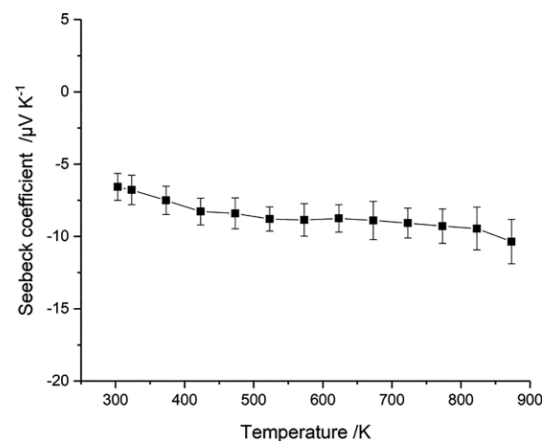
Figure 5. Seebeck coefficient measurement of a La_2NiBi pellet (density 81%).

In order to verify and substantiate the measured electronic properties, we conducted quantum chemical DFT calculations. Figure 6 shows the band structure and Figure 7 the electron localization functions (ELF) of La_2NiBi.

Schäfer et al. proposed a semi one-dimensional conductivity pathway for their La_2NiSb compound and therefore a strongly anisotropic electrical conductivity.[3]

Indeed, the electronic structure is characterized by intriguing features related to the crystal structure. At first sight metallic behavior is found from band structure calculations (Figure 6a, see Supporting Information for Brillouin zone), similar to La_2SbNi.[3] However, using relativistic calculations with spin-orbit-coupling (SOC) several gaps and pseudo gaps open along various k-points and paths (X, S, Z-U-R) at or close to the Fermi level. Here, valence (VB) and conduction band (CB) like states overlap as also seen for SiP_2.[29] According to further studies the respective gap positions are also sensitive to lattice distortions. As shown from the subsequent analyses, the formation of the bands at E_F is the result of interactions of Ni-4s, Ni-3d, Bi-6p, and La-5d orbitals.

For a deeper insight into the bonding situation of the Ni chains, we studied the orbital contributions to the band structure (Figure 6b–d). In contrast to e.g. Ni^0 in ternary sulfides[10,11] strong Ni-4s bands are found for La_2BiNi in the range of –3 and –4.5 eV. Ni-3d states mainly contribute to bands from –2.5 to –0.5 eV and to a lower degree to unoccupied states at and above the Fermi energy (E_F). Consequently, high orbital occupation numbers are found for Ni-4s (1.0 e), Ni-4p (0.4 e) Ni-3d (9.0 e) that indicate negatively charged Ni chains with a charge of $Q = -0.4$ per Ni atom. Ni orbital contributions to bands around E_F are due to bonding to neighboring Bi and La atoms. Bi-6s-bands are located below –10 eV in line with lone pair behavior (not shown in Figure 6c, see Supporting Information). We conclude on bonding of Bi-6p orbitals to Ni-3d and Ni-4sp, as indicated by major contributions to bands from –0.5 to –4 eV (Figure 6b). Again, high orbital occupation of 4.2 e for Bi-6p leads to negatively charged Bi atoms ($Q = -1.2$ e). The La atoms act as positively charged ($Q_{La1} = 0.76$, $Q_{La2} = 0.79$) donors. Respective band contributions of La-5d orbitals are mainly found for *anti*-bonding bands above E_F with weaker contributions below E_F. The given picture coincides with the one given for La_2NiSb with negatively charged Sb and positive La. It underlines the role of polarized metal–metal bonds that are also found for Laves phases and shandites.[10] The given analysis points out the exceptional bonding situation of Ni. Its orbital occupation differs and does not signal a localized Ni^0-$4s^2 3d^8$ or $4s^0 d^{10}$ state. The found orbital occupation $4s^1 4p^{0.4} 3d^9$ is in accordance with subsequently described multi-center metal bonding in the Ni chains, metal bonding to Bi and La, and partially occupied bands.

The given picture is complemented by analysis of the electron localization function (ELF)[12,13] in direct space. Figure 7a shows a 3D plot of ELF at the isovalue 0.37. Accordingly, the ELF maxima and rings as also found between each pair of Ni atoms for La_2NiSb, which evolve to a dominant bonding system of Ni-3d orbitals along the Ni chains in La_2NiBi. At lower
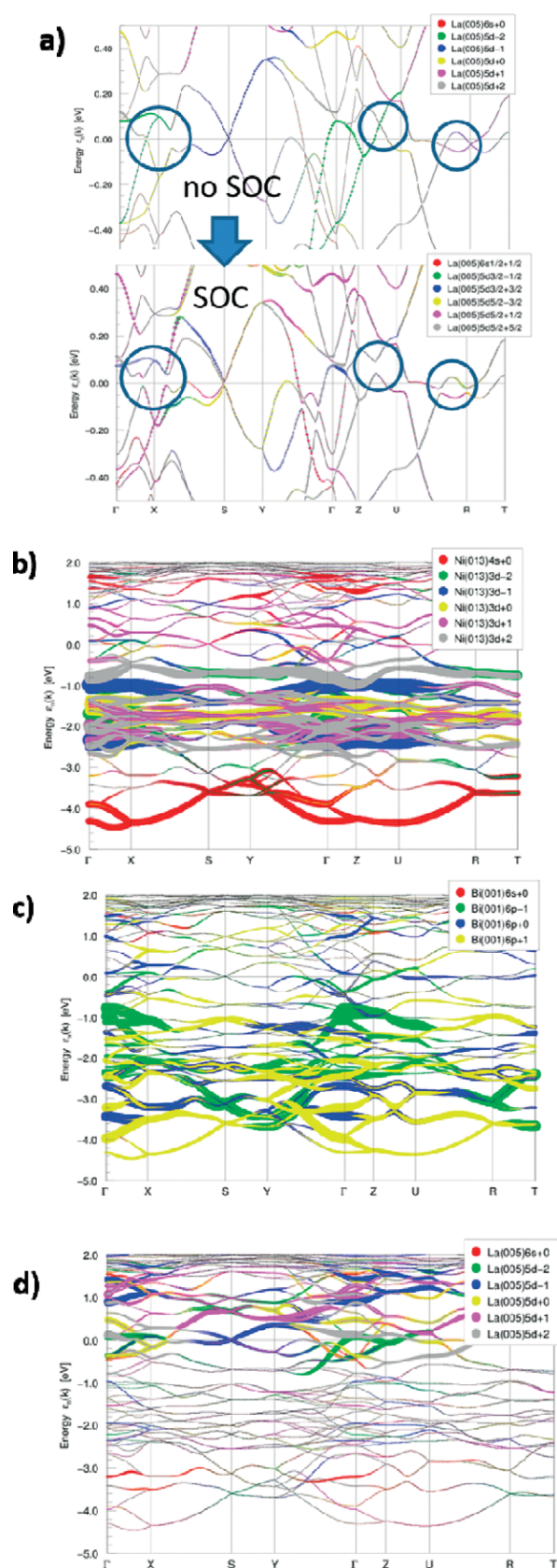
Figure 6. Calculated band structure of La_2NiBi with (a) pseudo gap opening upon SOC; (b–d) fat band projections on Ni-4s and Ni-3d (b), Bi-6sp (c), La-6s and 5d (d).
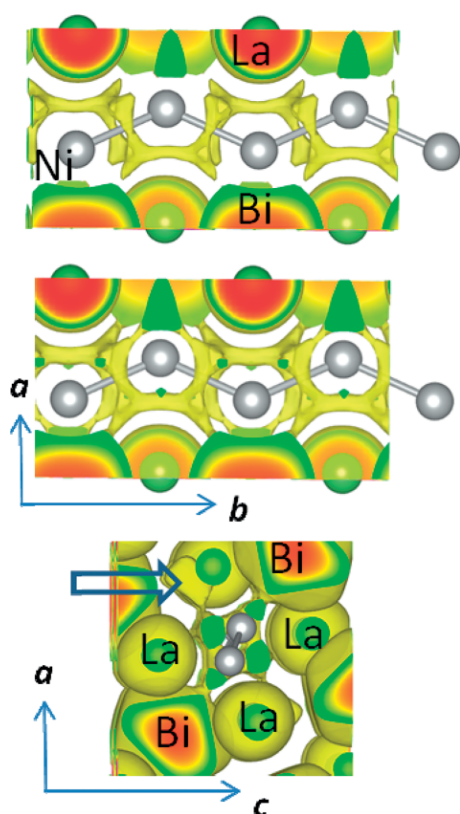
Figure 7. Views on 3D plots of isosurfaces of the electron localization functions ELF. (a) View on the Ni chain along crystallographic *c* axis iso value 0.37, (b) ELF = 0.35, (c) view along the *b* axis (the arrow marks an ELF maximum between La atoms).

ELF values (< 0.35) the surfaces interconnect Ni chains to neighboring Bi atoms. Interstitial ELF maxima are also identified between the La atoms (marked by an arrow in Figure 7c) similar to La_2NiSb. They are due to multi-center bonds and can be found in intermetallic compounds like Laves phases[14] or shandites[10,11]. The given analyses underline the strong intermetallic bonding system along the chains in La_2NiBi. It results from electron transfer of La to Bi and Ni.

Magnetic Measurements

The temperature dependence of the magnetic susceptibility of La_2NiBi, measured at 10 kOe is presented in Figure 8. La_2NiBi is a weak Pauli paramagnet with a susceptibility of $3.5(1) \times 10^{-4}$ emu·mol^{-1} at 300 K. The small upturn below ca. 80 K is due to trace amounts of paramagnetic impurities. The La_2NiBi sample shows no pronounced nickel impurities at the grain boundaries as it was observed for the isotypic antimonide.[3] The low-temperature regime (2.1–6 K) was additionally measured at the much lower flux density of 20 Oe. We observed no superconductivity for La_2NiBi. The negative susceptibility (Figure 8, insert) measured at low field results from less than 3% (*Meissner* contribution) of an unkown superconducting impurity phase.
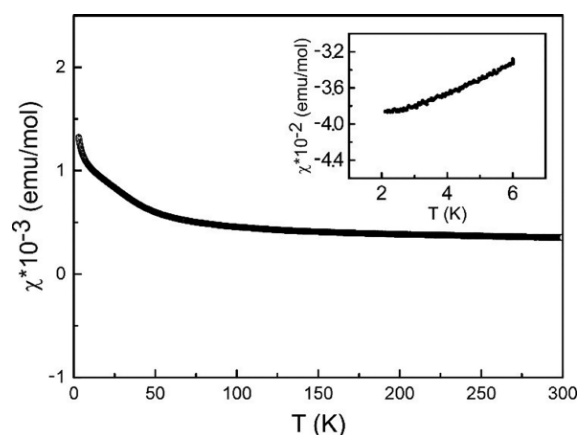
Figure 8. Temperature dependence of the magnetic susceptibility of La_2NiBi measured at 10 kOe. The insert shows the low-temperature regime measured at 20 Oe.

Conclusions

La_2NiBi is a ternary ordered variant of the Bi_3Ni structure type. It was synthesized from the elements in a very small temperature window using an evacuated silica ampoule at 1000 K. La_2NiBi crystallizes orthorhombically, in space group *Pnma*, as a structure variant of Bi_3Ni. An electron transfer from La to Ni and Bi occurs, which results in polarized metal–metal bonds for the chain-like Ni substructure. ELF calculations substantiate this feature showing a defined bonding system of Ni-3d-orbitals along the chains. With a combined set of different physical property measurements including DFT calculations it was shown that incongruently melting La_2NiBi is a bad metal with an electric conductivity of about 10^{-1} S·cm^{-1}. Magnetic measurements indicate that La_2NiBi is a weak Pauli paramagnet. In accordance with the electronic properties the Seebeck coefficient is expectedly small being located in the range of metals.

Experimental Section

Ceramic Synthesis: La_2NiBi was synthesized similar to the already known lanthanum rich antimonide La_2NiSb.[3] Lanthanum powder (CHEMPUR, 99.9%), nickel powder (CHEMPUR, 99.99%) and bismuth powder (ALPHA AESER, 99.95+%) were mixed in an agate mortar in a glove box. The mixture was pressed to a pellet of 6 mm diameter at room temperature and sealed in an evacuated silica tube. Afterwards, the ampoule was placed in a muffle furnace (NABERTHERM), heated to 1000 K within 3 h, and kept at this temperature for 72 h. Subsequently, the furnace was cooled to room temperature at a rate of 100 K·h^{-1}. The resulting compound is dark grey and stable at air for a few days before slow hydrolysis starts. At temperatures below 920 K and above 1045 K no formation of La_2NiBi can be observed.

Powder Diffraction: Phase analysis was conducted using X-ray powder diffraction. The unit cell parameters were determined via the software suite STOE WINXPOW.[15] Crystal parameters of La_2NiSb were taken from Pearson's Crystallographic database (PCD).[16] The product was ground in an agate mortar, placed between two stripes of Scotch® MagicTM 810, 3 M tape and fixed onto a flat sample holder. The mea-

ZAAC
Journal of Inorganic and General Chemistry
Zeitschrift für anorganische und allgemeine Chemie

ARTICLE

Table 2. Atomic coordinates, anisotropic and equivalent isotropic displacment parameters /pm^2 for La$_2$NiSb. All atoms lie on Wyckoff sites 4c (x, 1/4, z). The anisotropic displacement factor exponent takes the form: $-2\pi^2[(ha^*)^2U_{11} + \dots + 2hka^*b^*U_{12}]$. $U_{12} = U_{23} = 0$. U_{eq} is defined as one third of the trace of the orthogonalized U_{ij} tensor.

Atom	x	z	U_{11}	U_{22}	U_{33}	U_{13}	U_{eq}
Bi1	0.33376(11)	0.15824(9)	0.0153(4)	0.0140(5)	0.0174(4)	−0.0024(4)	0.0156(2)
La1	0.21905(17)	0.44890(13)	0.0149(7)	0.0160(7)	0.0180(6)	−0.0024(5)	0.0163(2)
La2	0.45913(18)	0.70141(13)	0.0150(6)	0.0156(7)	0.0171(7)	−0.0012(5)	0.0159(4)
Ni1	0.0646(4)	0.0198(3)	0.0214(17)	0.0160(17)	0.0214(17)	−0.0038(13)	0.020(1)

surement was conducted using Cu-$K_{\alpha1}$ radiation [λ = 1.54051 Å, Ge(111) monochromator] with a STOE Stadi-P powder diffraction diffractometer, equipped with a DECTRIS MYTHEN 1 K detector.[17] The measurement was conducted in a 2θ range of 5 to 80° within 15 min.

Single Crystal Diffraction: A suitable single crystal of the La$_2$NiBi sample was separated and a data set was collected at room temperature using a STOE IPDS-II image plate system (graphite monochromatized Mo-$K_{\alpha1}$ radiation; λ = 71.073 pm) in oscillation mode. A numerical absorption correction was applied to the data set. All relevant crystallographic data and details on the data collection and evaluation are listed in Table 1.

Structure Refinement: The cell parameter determination and the reduction of the data set were conducted via the software suite X-Area.[18] A structure solution was carried out with the software suite JANA2006, using the charge-flipping algorithm of SUPERFLIP.[19,20] Systematic extinctions were compatible with space group *Pnma*. The structure solution resulted in the Pearson code oP16 with Wyckoff sequence c^4. Pearson's Crystallographic database (PCD)[16] indicates an isotypism with Bi$_3$Ni and La$_2$NiSb.[3,4] The structure was refined with anisotropic displacement parameters for all atoms. No deviation from the ideal composition could be observed from a separate refinement of the occupancy parameters. The final Fourier synthesis displayed no significant residual peaks (Table 1). All relevant atomic parameters and interatomic distances are listed in Table 2 and Table 3.

Table 3. Interatomic distances /pm calculated with the powder lattice parameters of La$_2$NiBi. All distances within the first coordination spheres are listed. Standard deviations are all equal or less than 0.3 pm.

La1	1	Ni	292.3	Ni1	2	Ni	256.8
	2	Ni	303.6		1	Bi	281.2
	2	Bi	343.6		1	La2	282.0
	1	Bi	348.3		1	La1	292.3
	1	Bi	364.7		2	La1	303.6
	1	La2	366.0		2	La2	317.2
	2	La2	397.3				
La2	1	Ni	282.0				
	2	Ni	317.2				
	2	Bi	333.1				
	2	Bi	339.1				
	1	La1	366.0				
	2	La1	397.3				

SEM/EDX: The sample was analyzed by X-ray diffraction with a scanning electron microscope JCM-6000 NEOSCOP TM (JEOL, 5900LV, Si(Li) detector) with integrated EDX unit.

Thermal Analysis: A thermal analysis was conducted with a NETZSCH DSC 200 F3 Maia up to 623 K and a NETZSCH DSC 404 Pegasus up to 1273 K. Both, the heating and cooling rate was 10 K·min^{-1}. For the low temperature-DSC experiment an aluminum

crucible, and for the high temperature DSC, a niobium crucible was used. The samples were sealed under inert conditions.

Impedance Measurement: The electrical conductivity was measured by impedance spectroscopy in the range between 10^5–1 Hz and an amplitude of 20 mV. The sample was pressed to a pellet with a diameter of 6 mm and 79 % of the theoretical density. A RHD Instruments TSC standard cell with a METHROM Autolab B.V. PGSTAT204 potentiostat and a FRA32 unit was used to perform the measurements at 293 K. To calculate the activation energy, an Arrhenius-type representation, using the logarithm of the conductivity plotted against the inverse temperature 1/T was applied and the slope of the graph was determined.

Seebeck Coefficient: Part of the La$_2$NiBi sample was pressed to a pellet with a diameter of 15 mm using a MASSEN GmBH MP150 hydraulic press of the type 15 T, at a temperature of 373 K and pressure of 10 bar. The density of the pellet was calculated to be 81 % of the theoretical density. Seebeck-coefficients of La$_2$NiBi were measured with a NETZSCH SBA 458 Nemesis in a temperature range between 273 and 873 K. Device-specifically, the electrical conductivity is always determined in parallel to the Seebeck coefficient measurement. As we observed a decomposition of the sample due to the applied DC current we set this value as low as possible to 0.1 mA.

Quantum Chemical Calculations: The band structure and Density of States (DOS) calculations were performed in the framework of Density Functional Theory (DFT), applying the Perdew, Burke, Ernzerhof (PBE) functional[21] with the full potential local orbital (FPLO) package.[22,23] A k-grid mesh of $8 \times 8 \times 8$ was applied to reach sufficient accuracy.

ELF Calculations: The electronic structure was analyzed in direct space from the electron localization function (ELF), as developed by *Becke*, *Savin* et al.[12,13] It was calculated as implemented in the vasp4.6 code[24–27] with PAW potentials and PBE functionals for exchange and correlation similar to the band structure calculations. Visualization was performed with the vesta software.[28]

Magnetic Measurements: The measurements were performed with a PPMS system (QUANTUM DESIGN PPMS Modell 6000, equipped with an Evercool-System). The La$_2$NiBi powder (29.006 mg) was weighed in a polyethylene capsule. The sample was cooled in zero external field and the susceptibility was measured at 10 kOe in the temperature range from 3 to 300 K. To test for superconductivity, the low-temperature regime (2.1–6 K) was additionally measured at 20 Oe.

Supporting Information (see footnote on the first page of this article): Additional quantum chemical data, partial charges and fat band projections are given in the supplement.

ARTICLE

References

[1] A. E. Dwight, R. A. Conner, J. W. Downey, *Acta Crystallogr.* **1965**, *18*, 835.

[2] N. C. Baenziger, J. L. Moriarty, *Acta Crystallogr.* **1961**, *14*, 946.

[3] K. Schäfer, A. Isaeva, M. Ruck, B. Gerke, C. Schwickert, R. Pöttgen, *Z. Naturforsch. B* **2014**, *69*, 1097.

[4] M. Ruck, T. Söhnel, *Z. Naturforsch. B* **2006**, *61*, 785.

[5] R. Weihrich, S. F. Matar, V. Eyert, F. Rau, M. Zabel, M. Andratschke, I. Anusca, Th. Bernert, *Prog. Solid State Chem.* **2007**, *35*, 309.

[6] A. Grigas, M. Heise, T. Herrmannsdörfer, A. Isaeva, S. Kaskel, D. Köhler, M. Ruck, R. Skrotzki, J. Wosnitza, *Z. Anorg. Allg. Chem.* **2012**, *638*, 2035.

[7] T. Herrmannsdörfer, R. Skrotzki, J. Wosnitza, D. Köhler, R. Boldt, M. Ruck, *Phys. Rev. B* **2011**, *83*, 140501.

[8] J. Donohue, *The Structures of the Elements*, Wiley, New York, **1974**.

[9] O. L. Sologub, P. S. Salamakha, in *Handbook on the Physics and Chemistry of Rare Earths* (Eds.: K. A. Gschneidner Jr., J.-C. G. Bünzli, V. K. Pecharsky), vol. 33, Elsevier Science B. V., Amsterdam, **2003**, chapter 212, pp. 35.

[10] R. Weihrich, W. Yan, J. Rothballer, Ph. Peter, S. M. Rommel, S. Haumann, F. Winter, Ch. Schwickert, R. Pöttgen, *Dalton Trans.* **2015**, *44*, 15855.

[11] R. Weihrich, I. Anusca, I. M. Zabel, *Z. Anorg. Allg. Chem.* **2005**, *631*, 1463.

[12] A. D. Becke, K. E. Edgecombe, *J. Chem. Phys.* **1990**, *92*, 5397.

[13] B. Silvi, A. Savin, *Nature* **1994**, *371*, 683.

[14] O. Osters, T. Nilges, M. Schöneich, P. Schmidt, J. Rothballer, F. Pielnhofer, R. Weihrich, *Inorg. Chem.* **2012**, *51*, 8119.

[15] WinXPOW, volume Version 3.05. Stoe & Cie GmbH, Materials Park, ASM International, Ohio, USA, **2003**.

[16] P. Villars, K. Cenzual, *Pearson's Crystal Data – Crystal Structure Database for Inorganic Compounds* (release 2017/18), ASM International, Materials Park, Ohio, USA **2017**.

[17] https://www.dectris.com/products/mythen2/mythen2-r-for-laboratory/details/ mythen2-r-1k, Mai **2018**.

[18] Stoe & Cie GmbH. X-area, Version 1.56. **2011**.

[19] V. Petříček, M. Dušek, L. Palatinus, *Z. Kristallogr.* **2014**, *229*, 345.

[20] L. Palatinus, G. Chapuis, *J. Appl. Crystallogr.* **2007**, *40*, 786.

[21] J. P. Perdew, K. Burke, M. Ernzerhof, *Phys. Rev. Lett.* **1996**, *77*, 3865.

[22] K. Koepernik, H. Eschrig, *Phys. Rev. B* **1999**, *59*, 1743.

[23] K. K. I. Opahle, H. Eschrig, *Phys. Rev. B* **1999**, *60*, 14035.

[24] G. Kresse, J. Hafner, *J. Phys.: Condens. Matter* **1994**, *6*, 8245.

[25] G. Kresse, J. Furthmüller, *Comput. Mater. Sci.* **1996**, *6*, 15.

[26] G. Kresse, J. Furthmüller, *Phys. Rev. B* **1996**, *54*, 11169.

[27] P. E. Blöchl, *Phys. Rev. B* **1994**, *50*, 17953.

[28] K. Momma, F. Izumi, *J. Appl. Crystallogr.* **2011**, *44*, 1272.

[29] F. Bachhuber, J. Rothballer, F. Pielnhofer, R. Weihrich, *J. Chem. Phys.* **2001**, *135*, 124508.

C. Ott, M. Baumgartner, K. Schäfer, F. Baumer, K. Freitag, L. Scherf, L. Heletta, R. Weihrich, R. Pöttgen,* T. Nilges* **1–8**

Structure and Bonding of La$_2$NiBi
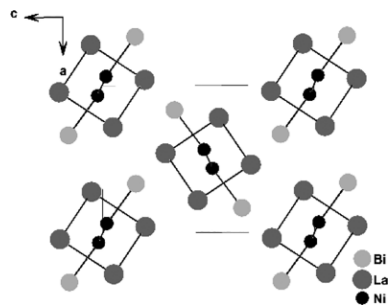
SUPPORTING INFORMATION

Title: Structure and Bonding of La$_2$NiBi
Author(s): C. Ott, M. Baumgartner, K. Schäfer, F. Baumer, K. Freitag, L. Scherf, L. Heletta, R. Weihrich, R. Pöttgen,* T. Nilges*
Ref. No.: z201800237

Structure and bonding of La$_2$NiBi

Claudia Ott, Max Baumgartner, Konrad Schäfer, Franziska Baumer, Katharina Freitag, Lavinia Scherf, Lukas Heletta, Richard Weihrich, Rainer Pöttgen, Tom Nilges
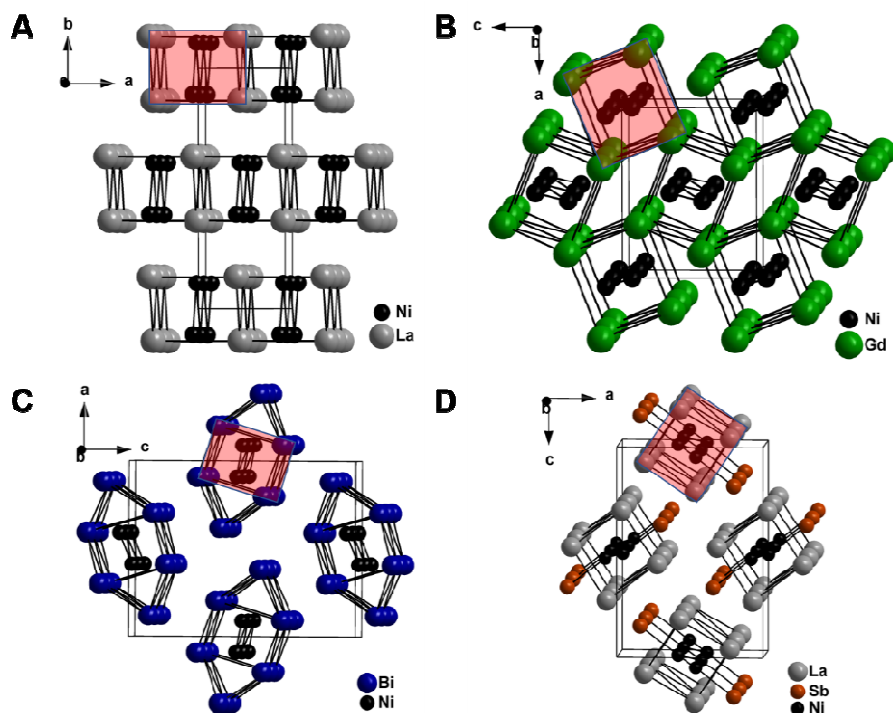
Figure S1: Projections of different rare earth and main group element nickel intermetallics (a) LaNi [1], b) GdNi [2], c) Bi$_3$Ni [5], d) La$_2$NiSb [3] in 3-dimensional representation. This Figure is as the 2-dimensional representation in part adapted from [1, 2, 3, 5].

Table S1: Atomic positions after optimization of the cell a =8.40 Å, b = 4.58 Å, c = 12.104 Å for La_2NiBi.

	x	y	z
Bi1	0.3327	¼	0.1595
La1	0.2185	¼	0.4503
La2	0.4610	¼	0.7009
Ni1	0.0619	¼	0.0165

Table S2: Calculated Orbital Occupation Numbers (DFT-PBE, net and gross values) for La_2NiBi.

	Orbital	5d	6s	7s	6d	6p	7p	charge	
Bi	N_net	9.996	1.873	0.008	0.011	3.648	0.028	23.596	
Bi	N_gross	9.990	1.886	0.000	0.088	4.168	0.029	24.174	-1.174
	Orbital	6s	7s	5d	6d	6p	4f		
La1	N_net	0.181	0.001	0.956	0.016	0.008	0.095	9.436	
La1	N_gross	0.412	-0.006	1.633	0.026	0.066	0.145	10.243	+0.757
	Orbital	6s	7s	5d	6d	6p	4f		
La2	N_net	0.139	0.001	0.965	0.016	0.006	0.094	9.438	
La2	N_gross	0.336	-0.009	1.703	0.018	0.049	0.147	10.203	+0.797
	Orbital		4s	5s	3d	4d	4p		
Ni	N_net		0.748	0.004	8.646	0.052	0.085	17.582	
Ni	N_gross		1.001	-0.004	8.844	0.129	0.405	18.380	-0.380

Table S3: Electron numbers and charges from density analysis for La_2NiBi.

Atomic no.	Atomic site	e/Atom	nuclear charge Z	Q/e
1	Bi	-84.4	+83	-1.37
8	La1	-56.0	+57	+0.96
9	La2	-56.0	+57	+1.03
13	Ni	-28.7	+28	-0.62

Table S4: Orbital analysis (net and gross values), relativistic DFT-PBE-calculation with SOC for La_2NiBi.

		5d	6s	7s	6d	6p	7p	total	Q/e
Bi	N_net	9.995	1.878	0.008	0.011	3.364	0.020	23.283	
Bi	N_gross	9.989	1.887	-0.001	0.089	3.968	0.011	23.944	-0.944
		6s	7s	5d	6d	6p	4f		
La	N_net	0.197	0.001	0.992	0.016	0.009	0.095	9.479	
La	N_gross	0.439	-0.004	1.673	0.040	0.070	0.145	10.328	+0.672
		6s	7s	5d	6d	6p	4f		
La	N_net	0.157	0.001	1.011	0.014	0.006	0.095	9.486	
La	N_gross	0.378	-0.006	1.755	0.038	0.056	0.147	10.327	+0.673
		4s	5s	3d	4d	4p			
Ni	N_net		0.764	0.004	8.645	0.052	0.087	17.598	
Ni	N_gross		1.017	-0.002	8.843	0.130	0.409	18.401	-0.401

Table S5: Density analysis Relativistic DFT-PBE-calculation with SOC for La$_2$NiBi.

Atomic no.	Atomic site	e/Atom	nuclear charge Z	Q/e
1	Bi	-84.2	+83	-1.17
5	La	-56.1	+57	+0.88
9	La	-56.1	+57	+0.92
13	Ni	-28.6	+28	-0.64
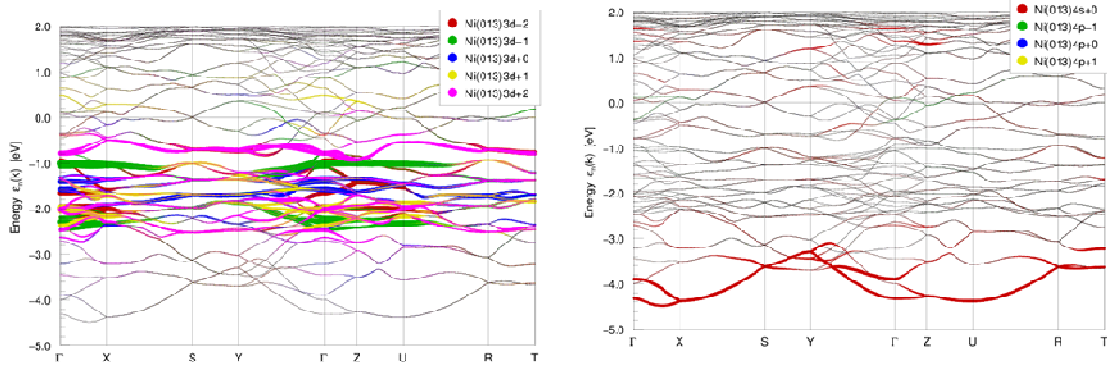
Figure S2: Fat band projections on Ni-4s (left), Ni-3d (right) and Ni-4p (left).
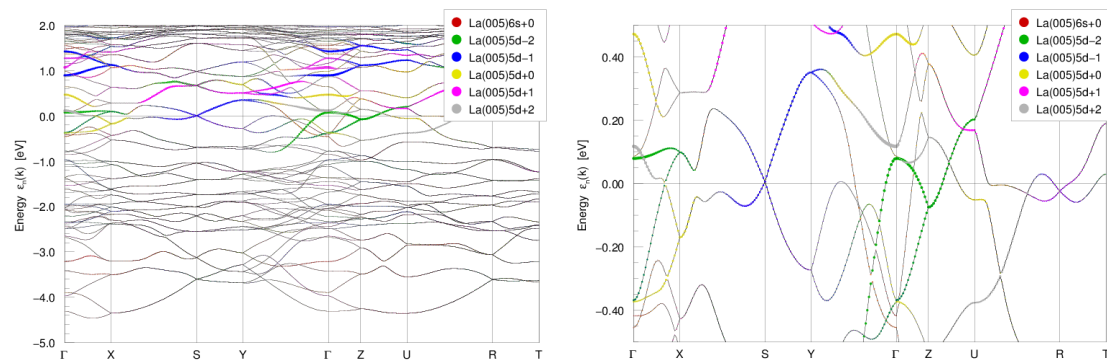
Figure S3: Fat band projections on La-6s and La-5d (left). Detailed representation of the Fermi level (right).
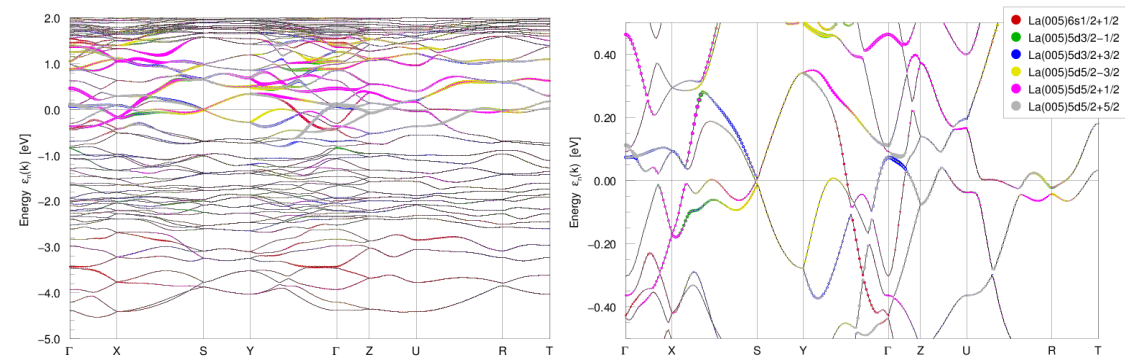
Figure S4: Fat band projections on La-6s1/2 and La-5d3/2 and La-5s5/2 (left). Detailed representation of the Fermi level (right).
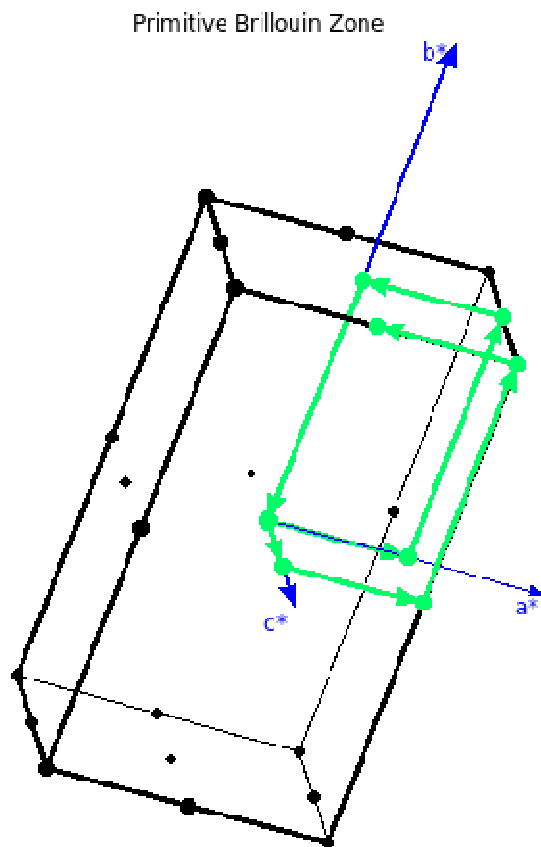
Figure S5: Brillouinzone for the band structure calculations of La_2NiBi with the k-points path
Γ (000) - X (½,0,0) - S(½, ½,0) - Y (0, ½, 0) - Γ (0,0,0)- Z (0,0,½) - U (½,0,½) - R (½,½,½) -
T (0, ½,½)

3.2 Influence of Copper on the Capacity of Phosphorus-Anodes in Sodium-Ion-Batteries

Claudia Ott, Annabelle Degg, Patrick Walke, Felix Reiter and Tom Nilges

Technische Universität München, Department Chemie, Synthese und Charakterisierung innovativer Materialien, Lichtenbergstraße 4, 85748 Garching

This work focuses on a simpler fabrication process of black phosphorous anodes for sodium ion battery half cells, the effects of crystallinity, particle size and the surface coating of black phosphorous with copper ions. Three different preparation methods of black phosphorous active material for SIBs were investigated (2 top-down methods: ball milling and chemical delamination and 1 bottom-up method: solvothermal synthesis[80]). The characteristics are listed in table 3.1 on page 48. Furthermore an easy method to apply a copper coating to the active material surface was developed and capacity changes were investigated.

Ball milled samples of black phosphorous active material show the least crystallinity but small particle sizes. The observed capacities were the smallest compared to the other samples. Solvothermal synthesized material shows a medium grade crystallinity but large agglomerated particles. The higher crystallinity on the other hand, shows an enhancing effect on the reached capacities, which could still be improved by particle size reduction in further studies.

Powder diffraction pattern prove that the chemically delaminated black phosphorous active material exhibits the highest crystallinity of all investigated samples and exceeds all previous described materials in regard of their performance in sodium ion half cells. The following trend can be derived from our results:

ball milled (BM, (a)) < solvothermal (ST, (b)) < ultrasonicated (US, (c))

Table 3.1: Crystallinity, particle size and cycling capacity of differently prepared black phosphorous active material samples.

	preparation method		
	ball milled (a)	solvothermal (b)	ultrasonicated (c)
abbreviation	BM	ST	US
crystallinity	amorphous	medium	high
particle size [μm]	0.1 - 101	4 - 680	0.5 - 59
	(mode: 0.6)	(mode: 262)	(mode: 0.7)
capacity after 10th cycle [mAh $\cdot$ g^{-1}]	$\sim$ 470	$\sim$ 570	$\sim$ 690
Improvement after Cu coating [mAh $\cdot$ g^{-1}]	$\sim$ +100	$\sim$ +100	$\sim$ +150

After a simple coating process of the anodes using copper sulfate solution (dip-coating, washing and drying), EDX element mapping confirmed the presence of phosphorous and copper on the anode surface as well as the absence of sulfur. This suggests the reaction of copper with phosphorous. The copper coating resulted in an capacity improvement of the examined system by 7 to 13%. The initial coulombic efficiencies (ICEs) on the other hand show a different picture. In all cases we found a decrease of the ICEs after applying the copper coating. This means a faster degradation of the active material during cyclization. Copper can also be introduced into the anode through current collector degradation while operating a battery. Therefore, battery research using copper as current collector and phosphorous as active material must be critically reflected based on these results.

Author contributions: C.O. prepared and characterized the starting materials, developed coating techniques and conducted the fabrication as well as the electrochemical evaluations of the battery systems. P.W. helped with the evaluation of the results and realization of the particle size distribution measurements, F.R. conducted parts of SEM and EDX measurements, A.D. prepared solvothermal sythesized black phosphorous. C.O. and T.N. wrote the manuscript. All authors discussed the results and reviewed the manuskript.

Influence of Copper on the Capacity of Phosphorus-Anodes in Sodium-Ion-Batteries

Claudia Ott, Annabelle Degg, Patrick Walke, Felix Reiter, Tom Nilges[*]

Address

Synthesis and Characterization of Innovative Material, Department of Chemistry, Technical University Munich (TUM), Lichtenbergstraße 4, 85747 Garching, Germany

Email: Claudia.ott@mytu.de; Annabelle.degg@mytum.de; Patrick.walke@tum.de, felix.reiter@tum.de, tom.nilges@tum.de

Abstract

Copper is a common current collector at the anode side in rechargeable batteries. The reactivity of copper is often neglected in battery applications which becomes a problem if the active material is highly reactive as well. Corrosion and compound formation results. Here, we report on the influence of the synthesis method and the role of copper on the electrochemical performance of black phosphorus anodes for sodium ion batteries. Two top-down and one bottom-up approaches were applied to prepare different samples. An easy dip coating process was developed to apply copper prior to usage significantly increasing the capacity of the system.

Keywords: Sodium ion batteries, black phosphorus, anodes, copper coating, capacity improvement

Highlights

- Black phosphorus half cells were tested as anodes for sodium ion batteries
- Copper coating negatively influences the performance in sodium ion batteries
- ~10% increase in capacity but ~15% decrease of coulombic efficiency occurs
- Copper can be provided by current collector corrosion during battery operation

1. Introduction

Black phosphorus amongst other element allotropes[2018 Nilges] is a well-studied anode material for the use in rechargeable lithium ion batteries (LIBs).[2012 Sun, 2007 Park, 2011 Marino, 2013 Stan, 2014 Nitta] The high theoretical capacity of 2596 mAh/g would suite the growing demand for high energy and power density in the lithium-ion battery industry.[2012 Sun] Lithium itself is a limited resource and with the increasing demand in lithium-ion batteries for computers, phones and especially cars it's price could rise drastically over the next few years. With the globally uneven distribution of lithium and the uncertain price politics, the lithium supply might be significantly shortened in the next few years. Furthermore, new developments arose substantiating the demand for "green" technology without the usage of sparse elements like lithium. Therefore, an alternative to lithium should be investigated. The abundant element sodium is located right below lithium in the periodic table and its chemical behavior is closely related. Sodium has been successfully used in rechargeable batteries replacing lithium as shown in recent studies [2013 Qian, 2013 Kim, 2014 Yabuuchi_1, 2014 Yabuuchi_2] In contrast to lithium, sodium is widespread and easy accessible in the upper earth crust, for instance in big reservoirs like the ocean or in salt stocks. With approx. 2.8 weight-% it represents the 6th most abundant element of the earth's crust. [1967 Parker]

Black phosphorus reacts to Na_3P in sodium ion batteries (SIBs) and it therefore shows the same theoretical capacity as lithium in LIBs.[2013 Qian, 2013 Kim, 2014 Yabuuchi_2] Due to the almost identical cell volume of the fully-lithiated and sodificated M_3P (space group $P6_3/mmc$) species[2005 Dong, 2007 Dong] the volume expansion is comparable and relatively low for both systems.[2011 Chevrier, 2014 Yabuuchi_1] This qualifies sodium as an excellent candidate to replace lithium in future battery technology.

One of the main problems in LIBs and SIBs with phosphorus as anode is the exceptionally reactive phosphorus surface and a high rate of electrolyte-decomposition at the formed solid-electrolyte-interface (SEI).[2014 Yabuuchi_1, 2014 Yabuuchi_2] Beside these aspects another important feature seemed to be overlooked in the electrochemical investigations of Na-P chemistry so far, that is the influence of copper, present in the current collector, and its corrosion, reactivity and dissolution during operation. In a previous work Stan *et al.* reported, that copper itself has a positive influence on the electrochemical properties of black phosphorus in LIBs. They identified copper phosphide, which has been formed during the lithiation/delithiation process within the electrode, as an important component capable to increase the electrochemical performance of the system. Cu_3P formed on black phosphorus lead to a 43 % improvement of the capacity compared with non-Cu_3P coated material in LIBs.[2013 Stan]

Our intension of this work is to examine the influence of copper ions and formed copper species on the electrochemical performance of black phosphorus anodes used for SIBs, and to develop an easy and effective way to provide copper ions capable to react with the active phosphorus material to copper phosphides. In addition, we investigate the influence of different preparation methods of the black phosphorus active material in order to evaluate the influence of size and synthesis history on the overall electrochemical performance.

2. Material and methods

2.1 Synthesis and battery half-cell assembly

2.1.1. Synthesis of bulk black phosphorus

Black phosphorus was synthesized via the low pressure route published by Nilges *et al.* in 2014. [2014 Köpf] Sn (20.0 mg, 99,999%; CHEMPUR), SnI$_4$ (10.0 mg, pre-synthesized according to literature)[1], and red phosphorus (500.0 mg, ultrahigh grade, 99.999+%, CHEMPUR) were sealed into an evacuated silica glass ampoule (p<10^{-3} mbar) and placed into a NABERTHERM muffle furnace with the starting materials pointing towards the heating elements at the side of the furnace. The ampoule was heated up to 923 K in 8h, kept at that temperature for 5h, cooled down to 773 K with a rate of 20 K·h^{-1}. After that the furnace was switched off.

2.1.2. Synthesis of white phosphorus

Red phosphorus (200.0 mg, ultrahigh grade, 99.999+%, CHEMPUR) was sealed in a slightly bend, 15 cm long, evacuated silica glass ampoule. The end of the ampoule containing the red phosphorus was placed in a three zone tube furnace applying a final temperature of 673 K at the position of the red phosphorus. The other end of the tube was placed in such a way that it exits the oven where temperature does not exceed 300 K. The reaction can be stopped if all white phosphorus is condensed at the cold end of the ampoule. After cooling the whole ampoule down to room temperature it was opened in a protective gas atmosphere. The whole oven must be placed in a fume hood and special care must kept on safety and fire regulations. In the case of a failure of the ampoule, common sand can be used to extinguish burning phosphorus. Pieces of white phosphorus should be covered with water and destroyed by aqueous copper sulfate solution. Caution: White phosphorus is toxic and should therefore be handled

with care. Due to the low melting point of 317 K a relatively large partial pressure is present even at room temperature. On air it can ignite at spontaneously at 307 K in a dry and pure from. White phosphorus should be exclusively handled in a fume cupboard and cooling is sometimes necessary to keep white phosphorus in the solid state. White phosphorus can be reacted to copper phosphide using saturated (or at least 10 wght-% containing) copper sulfate solution. If white phosphorus is handled, such a saturated aqueous solution should always be available prior to the start of the experiment.

2.1.3. Ball milling of black phosphorus (BM)

Black phosphorus synthesized according to 2.1.1. was mechanically ground in an agate mortar and after that homogenized to a fine powder via ball milling. 10.0 mg ground black phosphorus and 200 tungsten-carbide balls (diameter 5.0 mm) were placed into a 50 mL tungsten-carbide beaker, sealed under inert gas conditions (Argon 99.998%) and milled at 250 rpm for 12 hours. The milling procedure was paused after every 10 min for 10 min to avoid heat building up inside the beaker. The beaker was opened under inert conditions and the final product is stored in a glovebox (MBRAUN, Ar-atmosphere, water and oxygen content below 0.1 ppm). The material is called BM in the following.

2.1.4. Solvothermal synthesis of few-layer black phosphorus (ST)

The solvothermal synthesis of few-layer black phosphorus (in the following called ST) was conducted as described in literature.[2018 Tian] White phosphorus (1.24 g, 40 mmol) prepared according to 2.1.2. was solved under stirring in 20 mL dry ethylene diamine under inert conditions (glovebox, MBRAUN, Ar-atmosphere, water and oxygen content below 0.1 ppm) in a Teflon beaker. The Teflon beaker was sealed and transferred to a high-pressure steel vessel. The steel cylinder was heated up to 400 K for 12 hours. After cooling down to room temperature, the reaction mixture was filtered via a nylon membrane filter (0.45 µm pore size, MERCK MILLIPORE) and washed three times with toluene, ethanol and deionized water. The obtained black powder was dried under vacuum, analyzed via an optical light microscope from LEICA DM 1750 M (10 × 100 magnification), powder diffraction and scanning electron microscopy. Before further processing the powder is stored in a glovebox (MBRAUN, Ar-atmosphere, water and oxygen content below 0.1 ppm). Caution advices see white phosphorus synthesis section!

2.1.5. Chemical exfoliation and ultrasonication of black phosphorus (US)

Pre-synthesized black phosphorus was mechanically ground in an agate mortar and suspended in Dimethylformamide (DMF) or Dimethylsulfoxide (DMSO). The mixture was treated with an IKA T18 digital ULTRA TURRAX at 13000 rpm for 10 min to achieve smaller particles. Afterwards, the suspension was treated with a SONOPLUS ultrasonic-homogenizer from BANDELIN for 10h. The suspension was dried under vacuum to obtain a homogeneous powder. To verify the quality of the product a selected fraction was analyzed via an optical light microscope from LEICA DM 1750 M (10 × 100 magnification), powder diffraction and scanning electron microscopy. The final product was stored in a glovebox (MBRAUN, Ar-atmosphere, water and oxygen content below 0.1 ppm) and is called (US) in this article.

2.1.6. Preparation of phosphorus anodes

The slurries were prepared by mixing 15 wt.-% of black phosphorus samples (BM, ST, US), 65 wt.-% conductive carbon (carbon Super C65, TIMCAL) and 20 wt.-% PVDF (SOLVAY) in an agate mortar under inert conditions. NMP was added to form a homogenous, honey like texture. The resulting ink was transferred onto a copper current collector (99.99%, MTI COOPERATION) using a doctor bar (150 µm, ERICHSEN), to form a homogeneous film with a thickness of 150 µm. The film was dried under inert conditions at room temperature, punched into anodes with a diameter of 14 mm and pressed at 3 to for 30 sec.

Half the amount of the anodes prepared were dip-coated with a saturated $CuSO_4$ solution in water for 30 seconds. After the coating process, the excess solution was removed from the surface of the anode after washing with deionized water until no sulfate was detectable and filter paper. The anode was processed afterwards by drying in a vacuum glass oven (B-585, BÜCHI) at 120°C for 12 h before transferring them to the glovebox (MBRAUN, Ar-atmosphere, water and oxygen content below 0.1 ppm) to assemble the coin cells. An elemental analysis after the drying cycle (see main text) was performed to evaluate the amounts of copper and sulfur present in the anode after this process. While copper was detected on the surface of the electrode, no hints for significant amounts of sulfur were found.

2.1.7. Battery coin cell assembly

The prepared anodes are built into CR2032 coin cells (HOHSEN CORP.) using a 15 mm disc of elemental sodium (99,95%, SIGMA ALDRICH) as counter electrode and glass fiber separators (691, VWR, 17 mm diameter) saturated with 1:1 (w/w) EC/DMC with 1 M $NaPF_6$ as electrolyte (EC: 99%, SIGMA ALDRICH, DMC: >99%, SIGMA ALDRICH, $NaPF_6$: 98%, ALFA AESER).

2.2. Methods

2.2.1. Powder diffraction

Phase analysis of the black phosphorus crystals and powders was conducted using X-ray powder diffraction. The unit cell parameters were determined with the software suit STOE WINXPOW.[2003 WINXPOW] The crystal parameters of the orthorhombic black phosphorus were taken from literature.[2007 Lange] All analyzed samples were ground in an agate mortar (if needed), placed between two stripes of SCOTCH® MagicTM 810, 3M tape and fixed into a flat sample holder. The measurements were conducted using Cu-K$_{\alpha 1}$ radiation (λ = 1.54051 Å, Ge(111) monochromator) on a STOE Stadi-P powder diffraction diffractometer, equipped with a DECTRIS MYTHEN 1K detector. All were conducted in a range between 5 and 90° 2θ within 15 min.

2.2.2. Scanning electron microscopy (EM) and energy dispersive X-ray spectroscopy (EDX)

The sample was analyzed via EM using a scanning electron microscope JCM-6000 NEOSCOP TM (JEOL, 5900LV, Si(Li) detector) with integrated EDX unit. The acceleration voltage was set to 15 kV. Copper and aluminum were used as an external standard.

2.2.3. Battery testing

The battery half cells were tested with a BIOLOGIC VMP3 multichannel galvanostat, in a voltage range between 2.0 and 0.2 eV, and a scan rate of 0.05 mV/s for 10 cycles. Specific capacities were evaluated with the software EC-Lab V10.40 and calculated on basis of the active material content in the anode.

2.2.4. Particle size distribution measurement

The particle size distribution of the differently prepared black phosphorous active materials (BM, ST and US) were analyzed via light scattering using a Particle Sizer LA-950V2 (RETSCH) equipped with a 650 nm laser and a 405 nm LED light source. The sample was suspended in DI water and ultrasonicated 1 min before measurement. Data are summarized in Table 1.

3. Results

3.1 Synthesis and characterization of three different black phosphorus active materials

In a first set of experiments, the influence of particle size and crystallinity of the black phosphorus active material on the electrochemical performance was investigated. Differently synthesized and treated black phosphorus samples were used as active material to assemble black phosphorus anodes. Three different active material blends were fabricated (see Experimental section): a) As-synthesized black phosphorus was ball milled to achieve a homogeneous amorphous powder (BM). b) A second sample, was prepared by a bottom-up solvothermal process recently published by Tian *et al.* in 2018.[2018 Tian] This route resulted in small particles with a medium-grade of crystallinity (ST). c) Finally, a third batch of black phosphorus was chemically delaminated from a bulk sample using DMSO as a solvent. Route c resulted in very thin black phosphorus sheets (~100 nm estimated from SEM measurements) with a recent grade of crystallinity (US, see Figure 1, SEM images of black phosphorus active material prepared via route a) to c), same magnification). Material from route a) is characterized by a rather inhomogeneous particle size distribution and spherically agglomerated particles. The second example b) displays a more uniform size distribution, but they still do not show the expected layered morphology of black phosphorus. Finally, c) shows the desired sheet-like morphology and nicely-shaped crystals with low grade of agglomeration and beneficial properties for slurry preparation. In all cases (see Table 1), the size of the agglomerated particles and crystals is rather large compared with the capacity-optimized samples reported in literature.[2013 Qian, 2013 Kim, 2014 Yabuuchi_1, 2014 Yabuuchi_2]

Table 1. Particle size distribution of the investigated black phosphorus samples (mode, minimum and maximum measured particle sizes).

Synthesis/Delamination method of black phosphorus	Mode (µm)	Minimum particle size (µm)	Maximum particle size (µm)
Ball milled (BM)	0.6	0.1	101
Solvothermal (ST)	262	4	680
Ultrasonicated (US)	0.7	0.5	59

This average particle size is the main reason for the observed low capacities in this study which are approximately half the value from optimized systems reported so far. Large particles are non-beneficial for an effective diffusion, the sodium reactivity throughout the entire particle, and the volume expansion

during the sodification/desodification process. Our intention was to keep the synthesis and particle reduction step as effective, less time-consuming, and easy as possible due to two reasons: a) to be as close as possible to a realizable industrial process and b) to verify the influence of copper on the properties in more realistic and non-optimized samples. Only for large particles the bulk to surface ratio is high and the amount of copper species on the surface after the coating process does not significantly contribute to the overall capacity of the electrode.
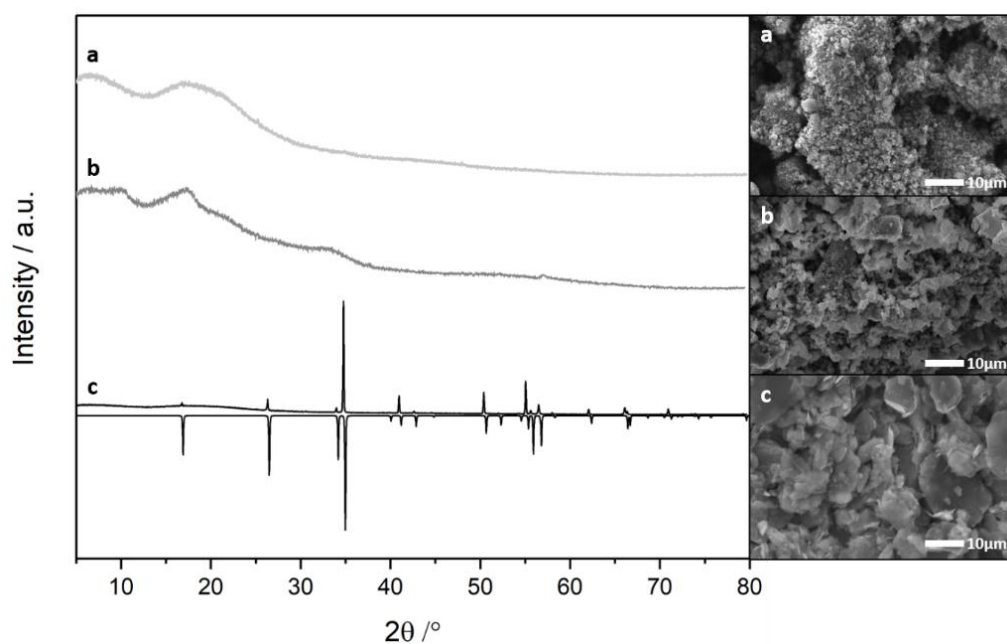
Figure 1. Powder X-ray diffraction pattern of different black phosphorus samples from route a) to c), and the corresponding SEM pictures. a) ball-milled black phosphorus (BM, milling time 12 h) b) solvothermal black phosphorus (ST). c) chemically-delaminated black phosphorus (US). Negative intensity: black phosphorus diffractogram calculated from literature data.[2007 Lange] Differences in intensity are due to texture effects of the plate-like crystals.

Figure 2 summarizes a copper/phosphorus /sulfur EDX mapping on an exemplary copper coated anode and the electrochemical performance measured in sodium half cells. The capacities are average values of at least 20 analyzed coin cells.

Ball milled almost amorphous black phosphorus (BM, see Figure 1a) displays the lowest crystallinity and also the lowest capacity of all investigated samples. This is surprising because it also shows a small particle size and size distribution which points towards the fact that the morphology and crystallinity plays a certain role for the electrochemical performance.

Black phosphorus produced via the solvothermal route (ST, Figure 1b) shows an enhanced crystallinity but very large (4-680 μm) and agglomerated particles (see Table 1). Each agglomerated particle is porous which allows access for the sodium ions via the electrolyte. Particles of more than ~100 μm in size are non-beneficial for an effective and fast transformation of phosphorus to Na_3P during the sodification process, due to the long diffusion lengths of Na through the material. Compared to the previously analyzed ball-milled material a), the applied bottom-up process b) offers a slightly higher grade of periodicity illustrated by gradually more defined reflections in the X-ray powder pattern. It outperforms the ball milled sample by approx. 100 mAh/g, despite the very large particle sizes. A reduction of the particles by a factor of 10 might be beneficial for an enhanced performance.

Chemically delaminated and ultra-sonicated black phosphorus (US, Figure 1c) shows a comparable average size and slightly smaller maximum-sized particle as the ball milled sample a) discussed so far. (see Table 1). The thickness of the sheets was estimated from SEM measurements to approximately hundred nanometers. Differences between the calculated and measured diffraction pattern are due to texture effects of the plate-like crystals. Chemical delamination is a mild way to break-down big particles which leads to a highly crystalline sample with almost no amorphous content. We found an improvement of the capacity by another 150 mA/g in comparison to the solvothermal material. Whether the significantly improved crystallinity (Figure 1) compared with the ball-milled (BM) sample or the smaller particle size (taking the maximum sized ones into account) are responsible for that results remains not clear at this stage.
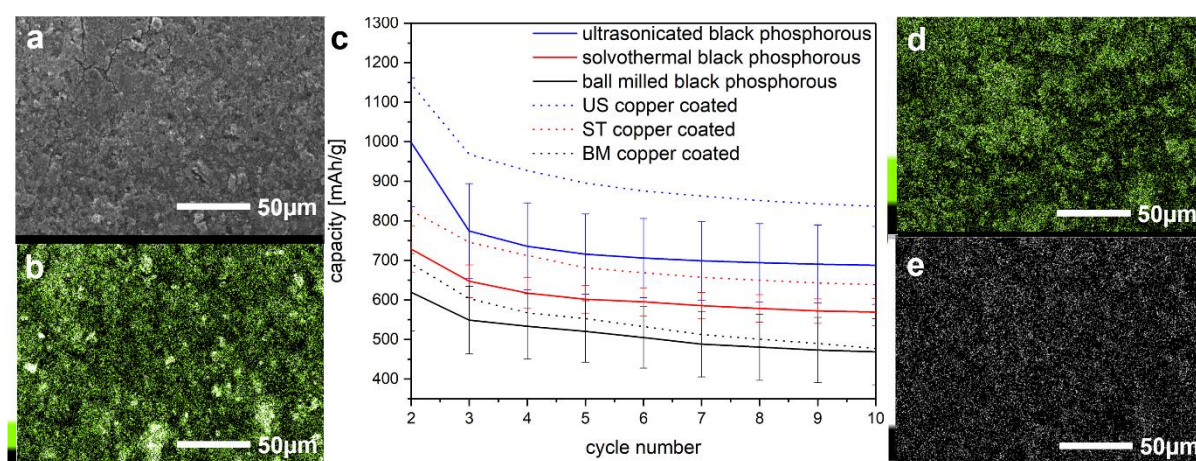
Figure 2. a) Scanning electron microscope image of a black phosphorus anode where a copper sulfate solution was used to supply copper ions and to form copper species on the active material. EDX element mapping of the same anode, b) illustrating the phosphorus, d) the copper and e) the sulfur distribution within the electrode. The color gradient is given on the left side of each image; c) Electrochemical

performance of various black phosphorus-sodium metal half cells (BM, ST and US; solid lines); Black phosphorus samples with a copper coating on the surface of the anode (dotted lines). Black: ball milled (BM) black phosphorus, red: solvothermal approach (ST) to black-phosphorus nano-crystals and blue: chemically delaminated black phosphorus (US). All CR2032 coin cells were cycled between 2.0 and 0.2 V with a rate of 0.05 mV/s for 10 cycles. For each phosphorus sample at least 20 different cells were analyzed. Due to SEI formation, capacities of the first cycle for each sample are not shown (Figure S1 in the supplement show all error bars and the first cycles).

The capacity of pure black phosphorus is strongly affected by the particle size, synthesis way and crystallinity of the utilized black phosphorus (solid lines in Figure 2c). In all cases we saw a pronounced drop of the initial capacity after the first cycle (not shown) which is likely due to SEI formation (as discussed in the introduction section), followed by a gradual and comparable capacity loss in the upcoming cycles. According the capacity value of the pure, non-coated electrodes we see a clear trend:

ball milled (BM, route a) < solvothermal (ST, route b) < ultrasonicated (US, route c)

which is not related to the lateral size but rather correlated with the crystallinity and the smallest realized thickness of the particles.

3.2 Electrochemical characterization of copper-modified phosphorus active materials

In order to verify the influence of copper incorporation on the electrochemical performance of black phosphorus we conducted a series of measurements for all investigated phosphorus samples. To achieve best-possible comparability we used anodes punched out from the same anode coatings analyzed before and applied the copper ion coating to the already-prepared electrodes prior to the cycling measurements. The copper ion coating was performed by dip-coating the entire fully assembled anode in a saturated aqueous $CuSO_4$ solution and adding a full drying process (see anode coating section 2.1.6. for further details) afterwards. We performed an EDX mapping to check if copper and sulfur (or sulfate) is incorporated in the electrode. Sulfur and copper EDX-mappings were conducted at the same spot and the with same accumulation time (see Figure 2e). While copper is found at the place where the phosphorus particles are located (Figure 2b and d), an area EDX scan shows almost no presence of sulfur on the anode. These experiments confirm our previous assumption that copper ions reacted with black phosphorus to copper species and sulfate ions were effectively removed from the electrode after the coating procedure. Note, copper sulfate solution is used frequently to react white

phosphorus into non-toxic copper phosphides [1995 Walsh] or phosphates (including oxygen from the atmosphere). [2001 Chou] The same reaction can take place with less-reactive black phosphorus on the surface of the particles where dangling bonds and highly reactive sites are present.

After electrochemical sodification and de-sodification we observed a significant increase of the capacity by ~100-150 mAh/g for all copper coated samples (compare Figure 2c, dotted lines) which seems to be beneficial on a first glance.

Another important aspect beside the capacities are the initial coulombic efficiencies (ICE) before and after copper coating. In Figure 3 the ICEs for all three systems are denoted for the first 10 cycles.
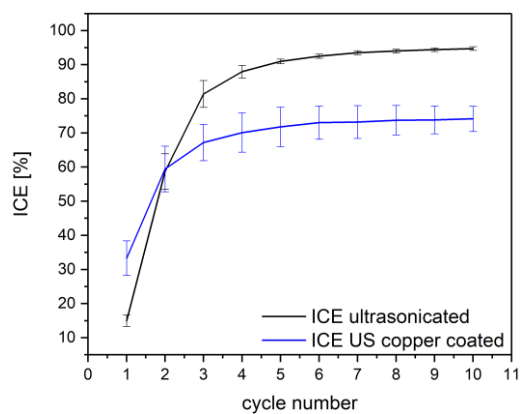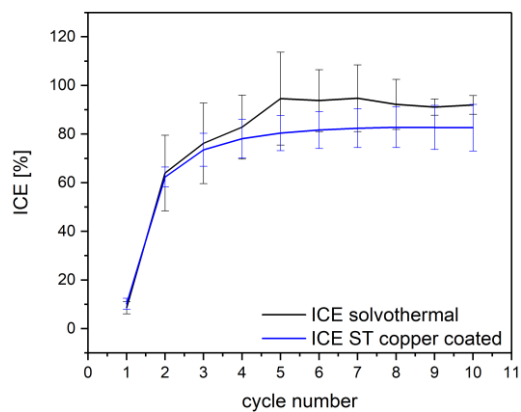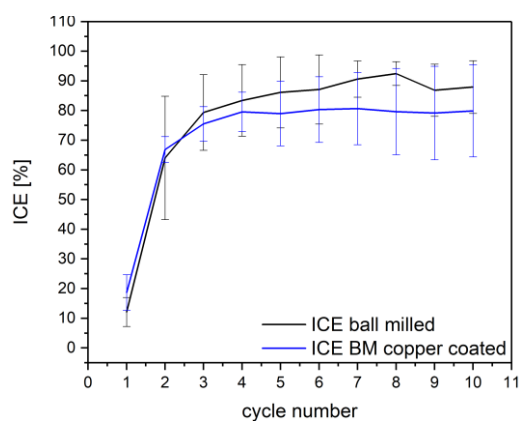
Figure 3. Initial coulombic efficiencies (ICE) in percent of black phosphorus-sodium half cells with a) ball milled (BM), b) solvothermally prepared (ST) and c) ultrasonicated (US) black phosphorous without (black) and after copper coating (blue). Error bars are based on 8-15 different measurements.

In all cases the ICE goes down from approximately 90% to values of between 70 to 80%, dependent on the system. It is obvious that such a copper coating process provided to the electrodes has a destabilizing effect on the electrochemical performance in all cases. A much faster degradation of the active material takes place for copper-coated electrodes than for the non-coated ones.

4. Discussion

The enhancing effect of copper on the cycle stability and capacity was already discussed by Stan *et al.* in 2013 for the black phosphorus/lithium system.[2013 Stan] In this study, black phosphorus active material was coated with Cu_3P by an solvothermal process using $CuCl_2$ in an ethylene diamine solution prior to the anode fabrication. Cu_3P was identified as the main source and the important compound for the performance increase during lithium ion battery operation. In order to reduce the synthesis requirements and to optimize the copper coating process we developed a dip coating routine where copper ions are introduced to the system in a one-step procedure and for already fabricated anodes. This procedure simplifies the fabrication process drastically and the usage of toxic solvents is avoided. In order to evaluate if a coating of the active material prior to the electrode assembly makes any difference we also coated the active material prior to the anode fabrication by applying the same coating procedure. We did not see any significant difference in the electrochemical performance using this procedure.

Usually, in lithium and sodium battery systems with phosphorus as active anode material, Cu is supplied via corrosion of the current collector during battery operation. It has been shown in LIBs, that a preformation of Cu_3P on the active materials in the case of lithium can reduce the irreversible capacity loss during the first battery cycles. The same effect can be observed in the present case where lithium is replaced by sodium. If copper is supplied to the phosphorus/sodium electrodes we observe a significant increase of the capacity of 12.4% for US, 7.4% for ST and 9.4% for BM phosphorus (after the 10th cycle) as illustrated in Figure 2. In the first cycles this improvement is even higher, in some cases up to 20%. Obviously, the incorporation of copper is of benefit and it improves the capacity but it decreases the coulombic efficiency as shown by the reduction of the ICE (Figure 3). This study shows that if a Cu current collector corrosion process occurs during battery operation this will have a negative

influence on the battery performance. Due to the reactivity of phosphorus – it reacts with almost every element of the periodic table including Cu[2018 Nilges] – a certain reaction cannot be neglected under battery operation conditions. This feature needs to be considered for each phosphorus allotrope, not only for the black one examined in this study. Therefore, a Cu current collector corrosion can pose a significant degradation process which should be tested in each sodium ion battery.

If the current collector corrosion itself will be reduced or avoided by a copper coating procedure prior to usage of the electrodes is an open question and still under investigation. Further experiments are necessary to substantiate this assumption. Each report where phosphorus (or any other allotrope) was used and copper corrosion was not taken into account must be reconsidered based on the results of this report.

Ex situ investigation of the cycled anodes after usage were performed in order to prove the formation of copper phosphides or other copper species, for instance like the most probable one Cu_3P. The amount of weight gain after the coating process and effective drying of the electrode lies below 0.1 mg which translates to an incorporation of copper to the active material of below 0.6 mass-% (assuming Cu_3P formation). We were not able to detect any crystalline additional phases by X-ray diffraction phase analysis. Two possible reasons for that are the low amount of copper species on the surface or the low-temperature coating process used may lead to amorphous copper phosphides or related compounds instead. Nevertheless, EDX mapping confirmed the presence of copper on the anode.

This fact shows the high impact of even small amounts of copper ions on the capacity of the investigated active material, which cannot be explained by the additional capacity delivered from an electrochemically active species like ($Cu_3P + Li \rightarrow Cu + Li_3P$).

5. Conclusion

This work investigated the influence of the preparation method of black phosphorus active material for the application in sodium ion batteries and verified the influence of copper to the anode performance. Different synthesis ways were tested to find an easy and fast route to relatively small particles with the highest possible crystallinity. Chemical delamination in DMSO amongst ball milling and a bottom-up synthesis of black phosphorus in ethylene diamine resulted in the best crystallinity and smallest particles. Furthermore, the effect of coating of the active material with a copper solution was

investigated. Copper is able to enhance the capacity in SIBs significantly, in accordance with the findings for LIBs. Copper sulfate, acting as a soluble copper source and a simple dip coating procedure, offers a straightforward way to form beneficial copper compounds on the surface of the active material. Sulfur or Sulfate from the coating process was successfully removed from the anode prior to the electrode cycling, as verified by EDX mapping. The amount of copper species formed was negligible low compared to the loading with active material. In sum, copper is beneficial for the capacity in SIBs and due to the simple and effective coating process it offers a simple way to improve the performance of a SIBs and might offer a step towards practical applications in the future.

Associated content

Supporting Information contains additional information concerning the electrochemical characterization of the half cells.

Author information

Corresponding author: *tom.nilges@tum.de

Acknowledgement

References

[1967 Parker] R. L. Parker in Data of Geochemistry, 6th ed. Ed. M. Fleischer, Chapter D, US Geol. Survey, 1967, p. D13.

[1995 Walsh] M. E. Walsh, C. M. Collins, C. Racine, in Persistence of White Phosphorus Particles in Sediment, CREL Report 95-23, US Army Corps of Engineers, 1995, p. 4.

[2001 Chou] T.-D. Chou, T.-W. Lee, S.-L. Chen, Y.-M. Tung, N.-T. Dai, S.-G. Chen, C.-H. Lee, T.-M. Chen, H.-J. Wang, The management of white phosphorus burns, Burns 27 (2001) 492-497. https://doi.org/10.1016/S0305-4179(01)00003-1

[2003 WinXPOW] WinXPOW, volume Version 3.05. Stoe & Cie GmbH, Materials Park, ASM International, Ohio, USA, 2003.

[2005 Dong] Y. Dong, F. J. DiSalvo, Reinvestigation of Na_3P based on single-crystal data, Acta Cryst. E61 (2005) i223. DOI:10.1107/S1600536805031168

[2007 Park] C. M. Park, H. J. Sohn, Black Phosphorus and its Composite for Lithium Rechargeable Batteries, Adv. Mater. 19 (2007) 2465. DOI:10.1002/adma.200602592.

[2007 Lange]   S. Lange, P. Schmidt, T. Nilges; Au_3SnP_7@Black Phosphorus: An Easy Access to Black Phosphorus, Inorg. Chem. 46 (2007) 4028. DOI:10.1021/ic062192q.

[2007 Dong] Y. Dong, F. J. DiSalvo, Reinvestigation of trilithium phosphide, Li_3P, Acta Cryst. E63 (2007) i97. DOI:10.1107/S1600536807008422.

[2011 Marino] C. Marino, A. Debenedetti, B. Fraisse, F. Favier, L. Monconduit, Activated-phosphorus as new electrode material for Li-ion batteries, Electrochemistry Commun. 13(4) (2011) 346. DOI: 10.1016/j.elecom.2011.01.021.

[2011 Chevrier] V. L. Chevrier, G. Ceder, Challenges for Na-ion Negative Electrodes, J. Electrochem. Soc. 158(9) (2011) A1011. DOI:10.1149/1.3607983.

[2012 Sun] L. Q. Sun, M. J. Li, K. Sun, S. H. Yu, R. S. Wang, H. M. Xie, Electrochemical Activity of Black Phosphorus as an Anode Material for Lithium-Ion Batteries, J. Phys. Chem. C 116 (2012) 14772. DOI:10.1021/jp302265n.

[2013 Stan] M. C. Stan, J. von Zamory, S. Passerini, T. Nilges, M. Winter, Puzzling out the origin of the electrochemical activity of black P as a negative electrode material for lithium-ion

Batteries, J. Mater. Chem. A 1 (2013) 5293. DOI:10.1039/c3ta10380c.

[2013 Qian] J. Qian, X. Wu, Y. Cao, X. Ai, H. Yang, High capacity and rate capability of amorphous phosphorus for sodium ion batteries. Angew. Chem. 125 (2013) 4731. DOI: 10.1002/anie.201209689.

[2013 Kim] Y. Kim, Y. Park, A. Choi, N. S. Choi, J. Kim, J. Lee, J. H. Ryu, S. M. Oh, K. T. Lee, An Amorphous Red Phosphorus/Carbon Composite as a Promising Anode Material for Sodium Ion Batteries, Adv. Mater. 25 (2013) 3045. DOI:10.1002/adma.201204877.

[2014 Köpf] M. Köpf, N. Eckstein, D. Pfister, C. Grotz, I. Krüger, M. Greiwe, T. Hansen, H. Kohlmann, T. Nilges, Access and in situ growth of phosphorene-precursor black phosphorus, J. Crystal Growth 405 (2014) 6. DOI:10.1016/j.jcrysgro.2014.07.029.

[2014 Nitta] N. Nitta, G. Yushin, High-Capacity Anode Materials for Lithium-Ion Batteries: Choice of Elements and Structures for Active Particles, Part. Part. Syst. Charact. 31 (2014) 317. DOI: 10.1002/ppsc.201300231.

[2014 Yabuuchi_1] N. Yabuuchi, Y. Matsuura, T. Ishikawa, S. Kuze, J. Y. Son, Y. T. Cui, H. Oji, S. Komaba, Phosphorus Electrodes in Sodium Cells: Small Volume Expansion by Sodiation and the Surface-Stabilization Mechanism in Aprotic Solvent, ChemElectroChem. 1 (2014) 580. DOI: 10.1002/celc.201300149.

[2014 Yabuuchi_2] N. Yabuuchi, K. Kubota, M. Dahbi, S. Komaba, Research Development on Sodium-Ion Batteries, Chem. Rev. 114 (2014) 11636. DOI:10.1021/cr500192f.

[2018 Nilges] T. Nilges, P. Schmidt, R. Weihrich, Phosphorus: The Allotropes, Stability, Synthesis, and Selected Applications in: D. Attwood (Ed) Encycl. Inorg. Bioinorg. Chem. 2018. https://doi.org/10.1002/9781119951438.eibc2643.

[2018 Tian] B. Tian, B. Tian, B. Smith, M. C. Scott, Q. Lei, R. Hua, Y. Tian, Y. Liu, Facile bottom-up synthesis of partially oxidized black phosphorus nanosheets as metal-free photocatalyst for hydrogen evolution, PNAS 115(17) (2018) 4345. DOI: 10.1073/pnas.1800069115.

Graphical abstract
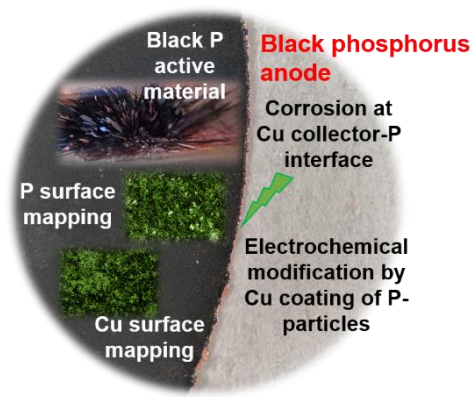
Black phosphorus anode for sodium ion batteries after soft-chemical

Cu-coating process

Supplement

Influence of Copper on the Capacity of

Phosphorus-Anodes in Sodium-Ion-Batteries

Claudia Ott, Annabelle Degg, Patrick Walke, Felix Reiter, Tom Nilges[*]
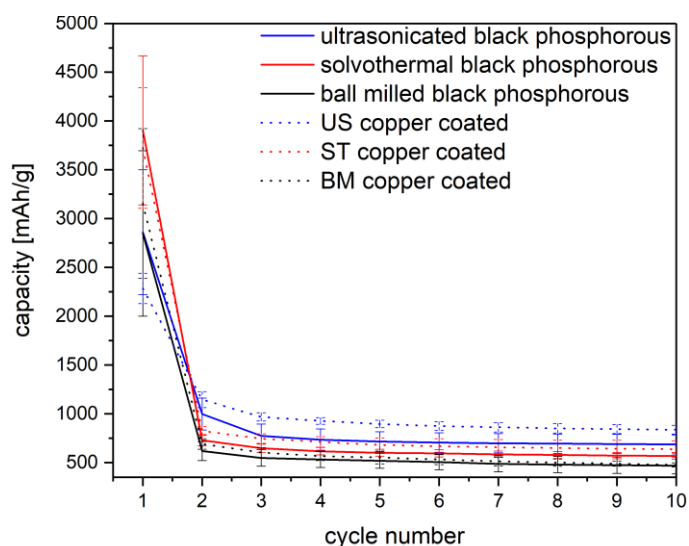
Figure S1. Electrochemical performance of different black phosphorus electrodes cycled against sodium metal. Solid lines: Comparison of coin cells using different samples of black phosphorous as active anode material in half cells; dotted lines: same black phosphorous samples with a copper coating on the surface of the anode. Black: Ball milled black phosphorous (BM), red: solvothermal approach to black-phosphorous nano-crystals (ST) and blue: chemically delaminated black phosphorous (US). All CR2032 coin cells were cycled between 2.0 and 0.2 V with a rate of 0.05 mV/s for 10 cycles. For each phosphorous sample at least 20 different cells were analyzed.

Influence of Copper on Capacity and Cycling Stability of Phosphorous-Anodes in Sodium-Ion-Batteries

Claudia Ott, Annabelle Degg, Patrick Walke, Felix Reiter, Tom Nilges
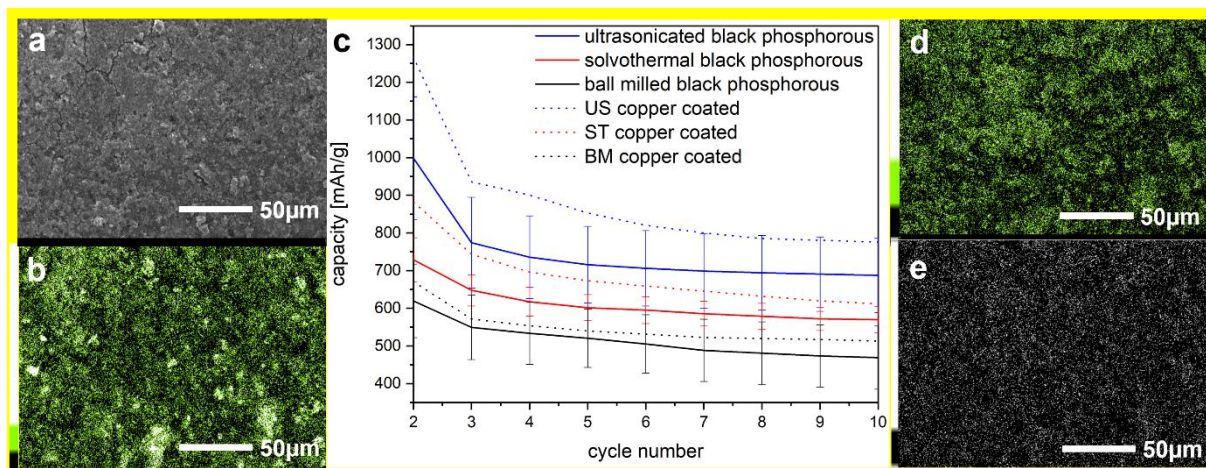
Figure S1: Figure 2: a) Scanning electron microscope image a black phosphorous anode where black phosphorus particles are coated with copper species. EDX element mapping of the same anode, illustrating the phosphorous b), the copper d) and the sulfur distribution e) on the particles. The color gradient is given on the left side of each image; c) solid lines: Comparison of coin cells using different samples of black phosphorous as active anode material in half cells; dotted lines: same black phosphorous samples with a copper coating on the surface of the anode. Black: ball milled black phosphorous, red: solvothermal approach to black-phosphorous nano-crystals and blue: chemically delaminated black phosphorous. All CR2032 coin cells were cycled between 2.0 and 0.2 V with a rate of 0.05 mV/s for 10 cycles. For each phosphorous sample at least 20 different cells were analysed. Due to SEI formation, capacities the results of the first cycle were left out.
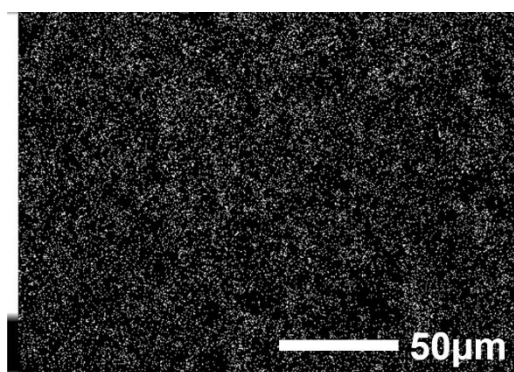
Figure S2: EDX element mapping of the same anode and the same integration time as depicted in Figure 2 of the main paper, illustrating the sulfur distribution on the particles which can is neglectibly low compared to the other elements.

3.3   Inorganic Double Helices in Semiconducting SnIP

Daniela Pfister, Konrad Schäfer, **Claudia Ott**, Birgit Gerke, Rainer Pöttgen, Oliver Janka, Maximilian Baumgartner, Anastasia Efimova, Andrea Hohmann, Peer Schmidt, Sabarinathan Venkatachalam, Leo van Wüllen, Ulrich Schürmann, Lorenz Kienle, Viola Duppel, Eric Parzinger, Bastian Miller, Jonathan Becker, Alexander Holleitner, Richard Weihrich and Tom Nilges

[1] Department of Chemistry, Technical University of Munich,Lichtenbergstr. 4, 85748 Garching b. München, Germany

[2] Institut für Anorganische und Analytische Chemie, Westfälische Wilhelms-Universität Münster, Corrensstr. 30, 48149 Münster, Germany

[3] BTU Cottbus-Senftenberg, Großenhainer Str. 57, 01968 Senftenberg, Germany

[4] Institut für Physik, Universität Augsburg, Universitätsstr. 1, 86159 Augsburg, Germany

[5] Technische Fakultät, Christian-Albrechts-Universität zu Kiel, Kaiserstr. 2, 24143 Kiel, Germany

[6] Max-Planck-Institut für Festkörperforschung, Heisenbergstraße 1, 70569 Stuttgart, Germany

[7] Walter Schottky and Physics Department, Technical University of Munich, Am Coulombwall 4a, 85748 Garching, Germany

[8] Institut für Materials Resource Management, Universität Augsburg, Universitätsstr. 1, 86159 Augsburg, Germany

The article "Inorganic Double Helices in Semiconducting SnIP" was submitted in June 2016 to the Journal "Advanced Materials" and published online in September 2016. The main results were presented by Daniela Pfister at the Gordon Conference 2016, New-London, USA and by Claudia Ott at the Annual ATUMS meeting 2016 in Raitenhaslach, Germany.

Phase pure bulk SnIP can be obtained via a simple solid state reaction. It crystallizes mono-clinically in space group *P2/c* (No. 17) with cell parameters of $a = 7.934(2)$ Å, $b = 9.802(3)$ Å, $c = 18.439(9)$ Å and $\beta = 110.06(5)°$. One unit cell consists of two enantiomeric SnIP double helices which each consist of an inner $^1_\infty[\text{P}^-]$ and an outer $^1_\infty[\text{SnI}^+]$ helix. One single double helix has a calculated diameter of 0.98 nm (9.8 Å). The enantiomers in the unit cell can be de-scribed as one left (*M*-helix, Herrmann-Mauguin notation $\not\perp 7_3 2$) and one right handed (*P*-helix, Herrmann-Mauguin notation $\not\perp 7_4 2$) double helix with a distance between the two single strands of 3.738(3) Å. Density functional theory (DFT) calculations show a van der Waals interaction of $25\,\text{kJ} \cdot \text{mol}^{-1}$. The direct and indirect band gaps were calculated and measured with UV/Vis and photoluminescence measurements (indirect: 1.80 eV, direct: 1.86 eV). Calculations of a single strand of SnIP result in a bandgap of 2.28 eV and therefore just an increase of about 0.5 eV, which is surprisingly low. For comparison, by delamination of black phosphorous a bandgap increase of almost 1.2 eV was observed. [123]

Electron localization function (ELF) analysis shows the covalent character of the P-P bonds and strong polarization of the Sn lone-pair to form a dative interaction between the outer and the inner helix. The good interaction between the helices and the aforementioned van der Waals interactions lead to a high mechanical flexibility. It is possible to bend SnIP needles 180° without visual disintegration. ^{119}Sn-Mössbauer spectroscopy characterizes SnIP as an electron precise diamagnetic compound. DTA measurements on SnIP revealed that it is stable up to 600 K prior to decomposition. SnIP can be mechnically and chemically delaminated into crystals with a diameter of below 50 nm within hours or even minutes if ultrasonication is applied. TEM-images show residual crystallinity even in a needle with just 15 nm diameter. Raman spectroscopy showed no significant difference between the spectrum of a single rod or bulk material which shows that stacking is not influencing the vibrational modes of a double helix. The conductivity of a small SnIP bundle was analyzed with electron beam induced current (EBIC) and found to be comparable to non-doped GaAs. [124] Nanostructured rod-like materials can be a valuable starting materials in inorganic-polymer solar cells. As SnIP is a 1.86 eV non-toxic semiconductor using abundant, inexpensive elements and can be delaminated, it shows promising properties for quantum dot solar cells. It even shows a more suitable bandgap than commonly used CdSe, as it is rather close to the efficiency maximum of single junction solar cells. [125]

Author contributions: C.O. and D.P. found and characterized the new compound, K.S. helped solve the structure, C.O., D.P., A.E., A. Hohmann, and P.S. conducted the analytical and thermoanalytical measurements, M.B. and R.W. conducted the quantumchemical calculations, B.G. and R.P. measured the Mössbauer spectra, L.v.W. the Solid State NMR spectra, O.J. and R.P. conducted the magnetic measurements, U.S., L.K., and V.D. performed the TEM experiments, E.P. and A. Holleitner measured the photoluminescence spectra and E.P., B.M., J.B., and A.Hol. the electrical conductivity, T.N. wrote the manuscript with feedback from D.P. and C.O, all authors discussed about the findings and commented on the manuskript.

Inorganic Double Helices in Semiconducting SnIP

Daniela Pfister, Konrad Schäfer, Claudia Ott, Birgit Gerke, Rainer Pöttgen, Oliver Janka, Maximilian Baumgartner, Anastasia Efimova, Andrea Hohmann, Peer Schmidt, Sabarinathan Venkatachalam, Leo van Wüllen, Ulrich Schürmann, Lorenz Kienle, Viola Duppel, Eric Parzinger, Bastian Miller, Jonathan Becker, Alexander Holleitner, Richard Weihrich, and Tom Nilges*

Double helices are one of the most fascinating structures in nature.[1] The discovery of the structure of DNA by Watson and Crick in 1953 inspired scientists to manufacture and examine (double) helical structures of various compounds and almost all classes of materials.[2,3] In polymer science, a helical arrangement can be found for instance in polytetrafluoroethylene (PTFE), being a commonly used material nowadays.[4] Obviously, the (double) helix is a prominent building block frequently realized in organic and living systems, but a pure carbon free and atomic scale pendant in the inorganic world is unknown. Recently, theoretical calculations predicted the existence of a simple atomic chain double helix for LiP but such an arrangement has not been realized yet.[5a] LiP reported in the 1980s only contains a P-helix coordinated by lithium.[5b]

D. Pfister, Dr. K. Schäfer, C. Ott, M. Baumgartner,
Prof. T. Nilges
Department of Chemistry
Technical University of Munich
Lichtenbergstr. 4, 85748 Garching b. München, Germany
E-mail: tom.nilges@lrz.tum.de

Dr. B. Gerke, Dr. O. Janka, Prof. R. Pöttgen
Institut für Anorganische und Analytische Chemie
Westfälische Wilhelms-Universität Münster
Corrensstr. 30, 48149 Münster, Germany

Dr. A. Efimova, A. Hohmann, Prof. P. Schmidt
BTU Cottbus-Senftenberg
Großenhainer Str. 57, 01968 Senftenberg, Germany

Dr. S. Venkatachalam, Prof. L. van Wüllen
Institut für Physik
Universität Augsburg
Universitätsstr. 1, 86159 Augsburg, Germany

Dr. U. Schürmann, Prof. L. Kienle
Technische Fakultät
Christian-Albrechts-Universität zu Kiel
Kaiserstr. 2, 24143 Kiel, Germany

V. Duppel
Max-Planck-Institut für Festkörperforschung
Heisenbergstraße 1, 70569 Stuttgart, Germany

E. Parzinger, B. Miller, J. Becker, Prof. A. Holleitner
Walter Schottky and Physics Department
Technical University of Munich
Am Coulombwall 4a, 85748 Garching, Germany

Prof. R. Weihrich
Institut für Materials Resource Management
Universität Augsburg
Universitätsstr. 1, 86159 Augsburg, Germany

Several approaches have been tested to prepare inorganic double helical materials. Double helical selenium was found in traces using double-walled carbon nanotubes as a template.[6] On a nonatomistic nanometer to micrometer scale, helical arrangements of semiconductors such as CdTe/CdS[7,8] or metals as gold templated by DNA[9] have been realized. A more complex double helical compound composed by metal-oxo species such as $[(CH_3)_2NH_2]K_4[V_{10}O_{10}(H_2O)_2(OH)_4(PO_4)_7]\cdot 4H_2O$ is known.[10] Materials adopting an inorganic double helical structure promise excellent mechanical, electrical, and optical properties.[2] A double helical arrangement will lead to an improved strength or strain compared to linear chains or single helices and secondary attractive interactions between the two helices in a double helix can be the origin of interesting electronic properties. Despite of an intensive research for more than 60 years, a nontemplated, carbon-free double helical inorganic structure on an atomic scale did not exist so far.

Bulk SnIP was prepared phase pure (Figure S1, Supporting Information) on a gram scale in a fast and simple solid state annealing reaction from tin, phosphorus and tin tetraiodide. In order to systemize the description of SnIP we discuss the determination of bulk and nanosized properties separately. SnIP crystallizes monoclinically, in space group $P2/c$ (No. 13) containing $Z = 14$ units in the unit cell and lattice parameters of $a = 7.934(2)$ Å, $b = 9.802(3)$ Å, $c = 18.439(9)$ Å, and $\beta = 110.06(5)°$ (**Figure 1**). Two substructures of different elemental composition, a helical $\frac{1}{\infty}[P^-]$ chain of phosphorus and a second helical $\frac{1}{\infty}[SnI^+]$ chain are forming SnIP double helices of 0.98 nm diameter.

The single rods are either left (*M*-helix) or right-handed (*P*-helix) and thus have opposite chirality. Both sets of double helices are assembled in a pseudo-hexagonal arrangement of rods along the *a*-axis. Seven SnIP units per two chain windings are present in each rod resulting in a 7/2 helix.[11,12] In Herrmann–Mauguin notation, the symmetry of a separate *P*-helix fulfills the rod group $\not{p}7_42$ in very good approximation, while that of an *M* helix corresponds to $\not{p}7_32$. Rods of a given chirality are arranged in rows along the *b*-direction. Bond lengths within the helices of $d(Sn-I) = 3.060(2)$ to $3.288(3)$ Å for the tin-iodide helix and of $d(P-P) = 2.170(5)$ to $2.211(5)$ Å for the phosphorus helix are common and comparable to distances in 3D-bulk compounds such as $Sn_{24}P_{19.3}I_8$ or binary compounds.[13]

In order to understand the structure and physical properties of SnIP we examined the electronic structure and chemical
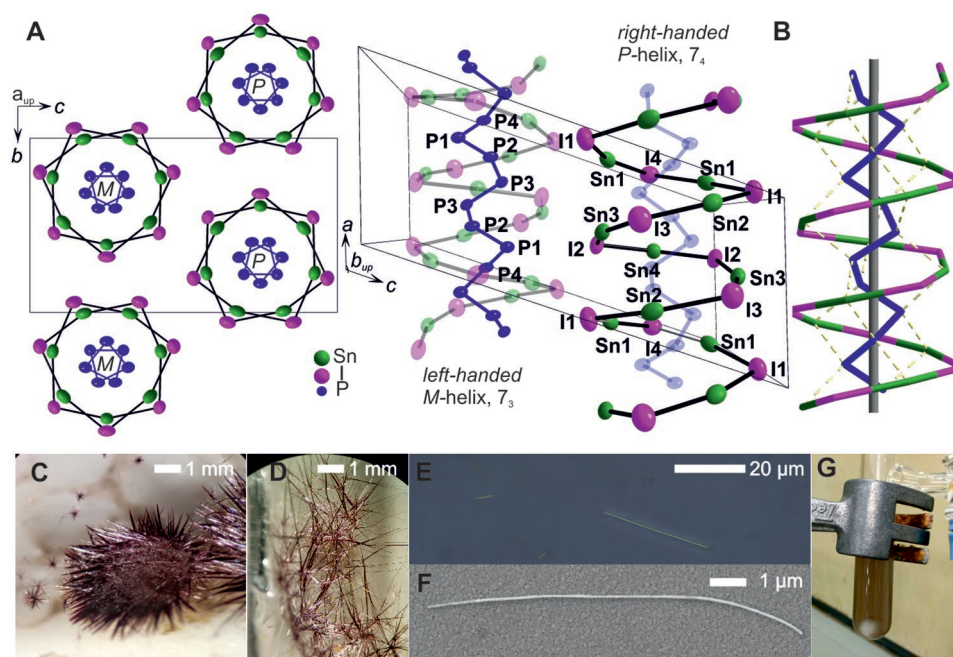
Figure 1. Bulk and nanosized crystals of double helical SnIP. A) Crystal structure sections projected along the *a* and *b* axis of SnIP. [SnI] and [P] helices are forming a double helical SnIP strand. B) Schematic representation of the double helix arrangement and the intrahelical Sn–P interaction. C,D) As-grown crystals of SnIP. E) Mechanically exfoliated SnIP on ITO presents different color shading under microscope dependent on thickness. F) Scanning electron microscopy (SEM) image of exfoliated SnIP on ITO with diameter 68 to 85 nm which indicates that it consists of multiple rods. G) Suspension of SnIP in chloroform.

bonding within and between the double helices in more detail (**Figure 2**). Quantum chemical calculations within the framework of DFT[14] were performed to envision the band structure and density of states (DOS) of SnIP. A graphical representation is given in Figure 2A,C.

Different functionals were applied for geometry optimization and energy calculations (see Supporting Information). GGA functionals with D2 correction for dispersion interactions have been selected as the best possible functional approach, based on previous observations on covalently bonded phosphorus allotropes[15] and 2D-layered materials[16] to describe all interactions including the weak van der Waals interactions in SnIP. Optimized[17] structure parameters are close to the observed ones with deviations smaller than 2% for the lattice parameters and of 3.5% for the cell volume. SnIP shows a calculated indirect band gap (hse06 functional) of 1.79 eV (between D_1 and Y_1 point) and a direct one of ≈1.81 eV (D_1 point). The indirect and direct optical band gap of SnIP have been determined experimentally by diffuse reflectance UV–vis spectroscopy as well as photoluminescence experiments (Figure 2G,H). We found an indirect band gap of 1.80 and a direct one of 1.86 eV for as-prepared bulk SnIP by UV–vis spectroscopy and 1.86 eV by photoluminescence. The calculated band gaps for bulk SnIP are in good agreement with the experimental ones. All calculations and experiments are fully consistent pointing toward an almost identical indirect and direct band gap.

To display the chemical bonding we performed an electron localization function (ELF) analysis of SnIP (see Figure 2F). The ELF shows two main features, the covalent character of the P–P bonds within the *P*-helices and the strong polarization of

the Sn lone-pair, pointing toward the outer sphere of each SnI helix. A dative ionic interaction between the two helices can be assumed between the Sn and P atoms. Two lone pairs of phosphorus are pointing toward the tin positions resulting in bond lengths of $d(Sn–P) = 2.669(3)$ to $2.708(3)$ Å.

The closest distance between the two SnIP double helices form two iodide ions with 3.738(3) Å. These attractive interactions between the single SnIP double helices are weak van der Waals (vdW) forces, which has direct consequences on the material properties. A binding energy of 25 kJ mol^{-1} was derived from density functional theory (DFT) calculations with D2 corrections taking van der Waals-like dispersion interactions (Figure S2, Supporting Information) into account. This rather weak interaction, significantly larger than in vdW systems like black P (7 kJ mol^{-1})[18] and H-bonding systems like in DNA, has consequences on the mechanical properties of SnIP. Bulk crystals with diameters of several micrometers can be bent 180° without visible disintegration (see Movie 1, Supporting Information). A more quantitative determination of the mechanical properties, like Young's modulus, are interesting and will be reported soon. We are optimistic that SnIP can be used in semiconductor-based applications like flexible optical devices due to its high mechanical flexibility, but one has to keep in mind that upon stress and strain the electronic properties can be affected. Obviously, the vdW interaction is strong enough to preserve the beneficial flexibility of double helices even in large scale crystals. On the other hand, the vdW interactions are weak enough to provide a certain cleavage tendency which was used for the fabrication of SnIP nanorods (see later on).
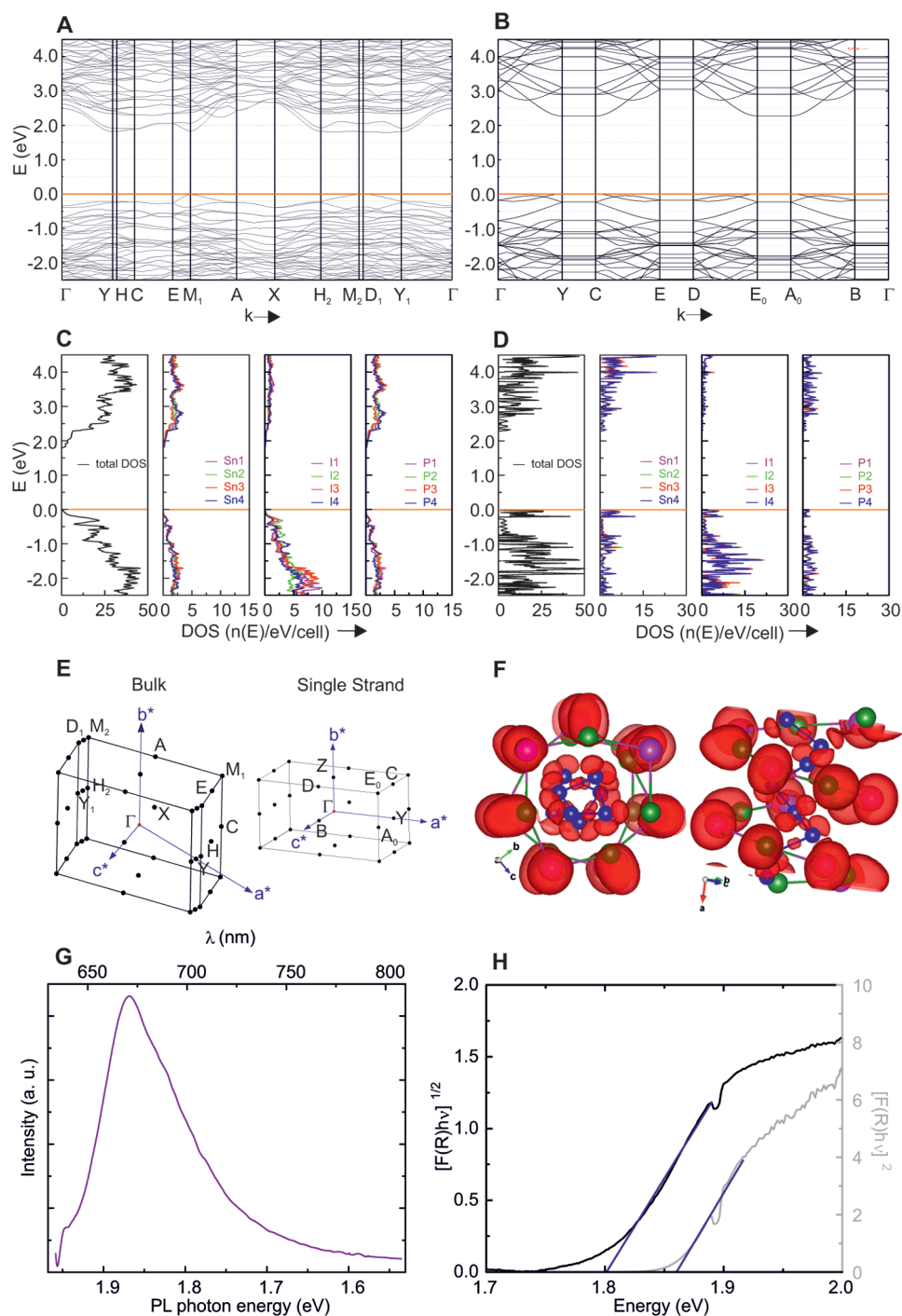
Figure 2. Electronic structure, density of states (DOS) and electronic properties of SnIP. A,C) Quantum chemical calculations within the DFT framework were performed for bulk and B,D) single rod SnIP. (A) The bulk and (B) the single rod band structure of SnIP. Band gaps are 1.79 and 2.27 eV, respectively. (C,D) The total DOS and partial DOS for 3D-bulk and single-rod SnIP. E) Corresponding Brillouin zones used for DFT calculations. F) Electron localization function (ELF) along and perpendicular to the rods show the covalent bonding between P, the dative, ionic Sn–P interaction and the polarized Sn(II) lone pair pointing toward the outside of the rod. G) Room temperature photoluminescence measurement on a SnIP needle featuring a minimum recombination energy of 1.86 eV with a shoulder at 1.8 eV. H) Diffuse reflectance UV–vis spectroscopy of micro crystalline SnIP. The Kubelka–Munk transformation was applied to determine the indirect band gap by extrapolation of $[F(R)h\nu]^{1/2}$ and direct band gap $[F(R)h\nu]^2$, respectively, versus the photon energy to zero absorption. The Tauc plot shows an indirect band gap of 1.8 eV and a direct band gap of 1.86 eV.

Additional structural, chemical, and physical properties of SnIP have been determined by various spectroscopic methods (Figures S3–S6, Supporting Information). ^{31}P-MAS-NMR and

2D-^{31}P RFDR (radio frequency driven recoupling) spectroscopy on 3D-bulk SnIP corroborate the P4-P1-P2-P3-P3-P2-P1-P4 connectivity pattern derived from single crystal structure

determination. Using ^{119}Sn Mößbauer spectroscopy the expected formal oxidation states of Sn^{2+}, I^-, and P^- were substantiated characterizing SnIP as an electron precise and diamagnetic compound. Measured Raman spectra show the characteristic vibration modes of P–P, Sn–P, and Sn–I bonds. We have assigned the modes to inter- and intrarod modes by the aid of quantum chemical calculations.[19]

SnIP starts to decompose at temperatures above 600 K by evaporation of $SnI_4(g)$ and $P_4(g)$ followed by $SnI_2(g)$ to form the bulk residue (Figure S7b, Supporting Information). Only liquid tin remains after heating to 1000 K, and β-Sn was ultimately obtained as the solid phase after recrystallization. When tightly enclosed under its own vapor pressure, SnIP decomposes peritectically at 740(2) K with formation of $Sn_{24}P_{19.3}I_8$. A detailed phase diagram and a measurement of the equilibrium gas pressures above SnIP is given in the Supporting Information (Figure S7a,c, Supporting Information). The electrical conductivity was measured for a 500 nm crystal which will be reported in the oncoming nanosize part of the paper.

In the following we briefly discuss the preparation and properties of SnIP nanorods. As stated earlier on the inter-rod interactions of the SnIP double helices are weak enough to provide a cleavage tendency in bulk crystals. Bulk-SnIP can be mechanically and chemically delaminated into nanorods with large aspect ratios. Applying a commonly used Scotch-tape approach, crystals with micrometer diameters of bulk-SnIP (see Figure 1C,D) can be exfoliated down to ≈50 nm crystals within minutes. Representative crystals prepared by this approach are given in Figure 1E,F. Dependent on the number of shells coordinated around a single SnIP rod, different diameters can be expected (**Figure 3**A).

A single nanorod will show a diameter of 0.98 nm increasing to 9 nm for a rod surrounded by 4 shells (see Figure 3B). Bulk-SnIP can be suspended in different organic solvents such as toluene, N-methyl-2-pyrrolidone or chloroform; in the latter solvent within hours—if ultrasonication is applied, within minutes. The ability to suspend SnIP in organic solvents opens up perspectives for the fabrication of thin-layer devices with SnIP nanorods of variable lengths and diameters. As-prepared fibrous SnIP and nanosized rods are shown in Figures 1C,D and 3. SEM pictures (Figure 3C) illustrate the pronounced polymer-like morphology of SnIP. Aspect ratios larger than 500 were realized after successful delamination of bulky micrometer-sized SnIP crystals into nanometer rods. The thinnest rods observable by means of transmission electron microscopy (TEM) have a diameter of 15 nm (Figure 3B). Only the inner part of around 5 nm (or four SnIP shells) shows hereby residual crystallinity. The amorphous shell and the rounded shape of the rod end indicate the sensitivity of the material to the electron beam. Precession electron diffraction patterns (zone [010] in Figure 3D, and further in Figure S8, Supporting Information) coincide with the simulated patterns (Figure 3E) resulting from the suggested structure. High resolution images recorded in the same zone [010] at different focus values are shown in Figure 3F. The insets depict the simulation of the high resolution contrast and emphasize the agreement with the experimental data. An overlay of the structure in the high resolution simulation indicates the arrangement of the SnIP helices in the presented zone [010] and demonstrate the relation between contrast and structure (Figure 3G).
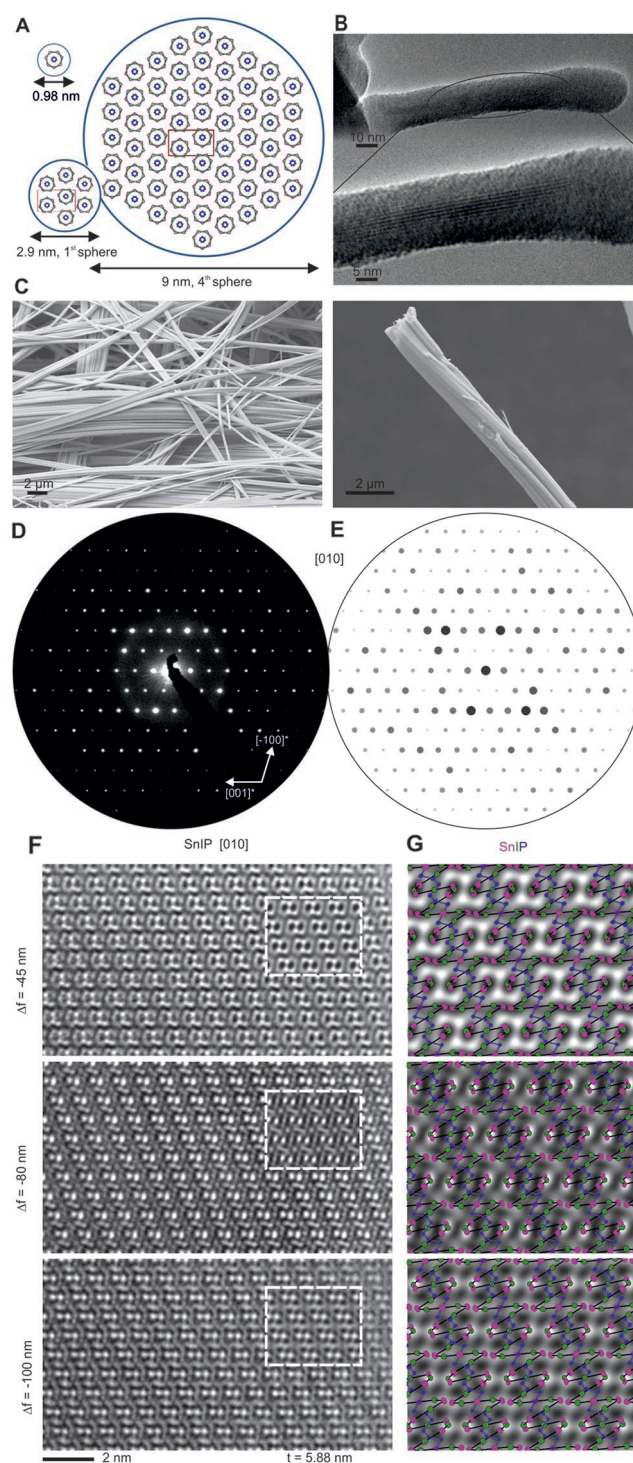
Figure 3. SnIP nanorods of different sizes and length scales. A) Schematic representation of SnIP nanorods starting from a single-rod to a four shell nanorod. B) TEM image of a thin rod with a diameter of 15 nm. C) SEM images of the SnIP rods. D) Precession electron diffraction (PED) pattern of the [010] zone with corresponding simulation (E). F) High resolution TEM images (zone [010]) at different focus values and insets showing simulations of the high resolution contrast. G) Overlay of the high resolution contrast simulations with the SnIP structure.

Materials
Views
www.MaterialsViews.com

ADVANCED
MATERIALS
www.advmat.de

COMMUNICATION
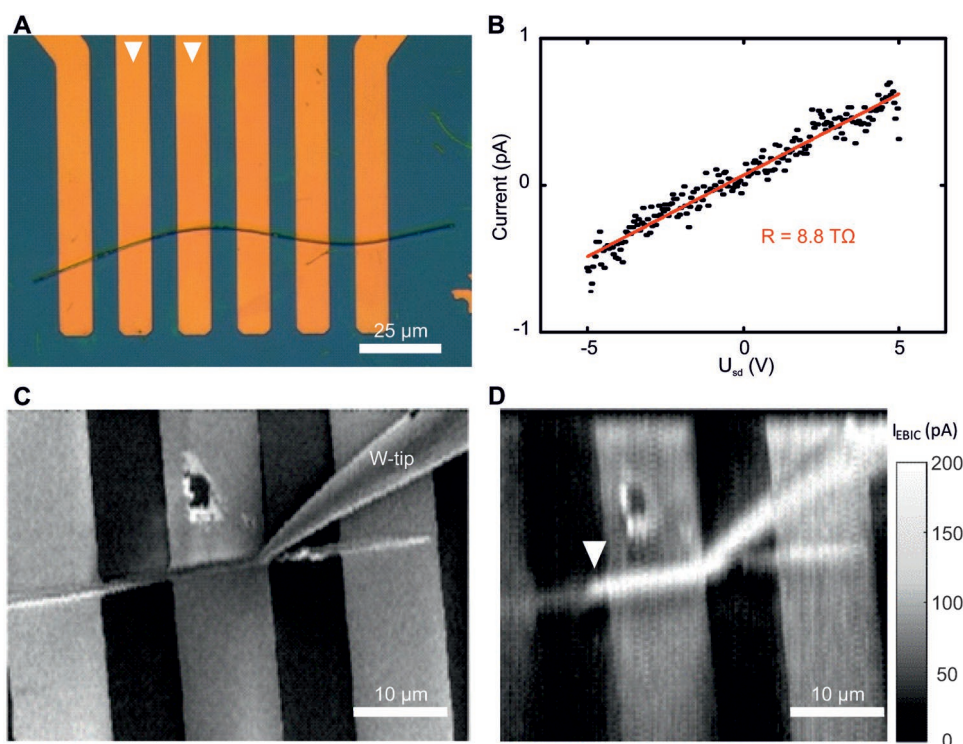
Figure 4. Electronic property measurements of SnIP. A) Optical microscope image of a SnIP-bundle contacted by six Ti/Au strips. The bundle is deposited on a Si/SiO$_2$-substrate. The SiO$_2$ (Ti/Au) has a thickness of 300 nm (3 nm/30 nm). B) Two-terminal current–voltage characteristic measured at the two strips highlighted by triangles in (A) with a preamplifier having an input resistance of 10 kΩ. C) Scanning electron microscope image of a similar SnIP-bundle which is additionally contacted by a tungsten tip (W-tip). The tip is positioned on top of the SnIP-bundle with the help of piezopositioners, and it is electronically connected to the current–voltage amplifier. Hereby, the electron beam induced current (EBIC) can be measured versus the position of the electron-beam. D) A corresponding EBIC-map at an acceleration voltage of 15 keV verifies that the current flow occurs across the contacted SnIP-bundle (e.g., triangle).

We also performed quantum chemical calculations for one double helical SnIP nanorod in order to evaluate the properties in more detail. After a geometry optimization and structure relaxation the structure remains almost unchanged (Figure S9, Supporting Information). Neither atomic distances nor the overall geometry change significantly going to the single nanorod. We calculated a band gap of 2.28 eV for a single SnIP nanorod which is larger than the value of 1.79 eV for the bulk material. Compared with a 2D-material like phosphorene where the 0.3 eV band gap of bulk black phosphorus is enlarged to >1.5 eV,[20] the band gap increase for bulk SnIP to single SnIP rod is only moderate. The small change of 0.49 eV from is in coincidence with the relative rigidity of the electronic structure. According our calculations, a quantum confinement has no drastic influence on the double helical SnIP structure itself. This finding is also substantiated by Raman spectroscopy. We found no significant differences in the calculated SnIP mode positions between bulk SnIP and a single nanorod (Figure S6, Supporting Information) which indicates an almost unaffected and noninfluenced stacking of single rods in the bulk material.

The conductivity of SnIP was estimated by electron beam induced current (EBIC) measurements (**Figure 4**) for a 500 nm SnIP crystal. A representative single crystal was mounted on a chip and contacted carefully. The crystal was bent several times prior to the conductivity measurement which resulted in a curved morphology. We observed an electronic conductivity of 2.5(5) µS m^{-1} which is comparable to 1 µS m^{-1} reported for non-doped GaAs.[21]

SnIP in its nanosized form can be regarded as a quantum confined semiconductor. Such semiconductors are widely used in energy science and technology. Examples are perovskite-based or all solid state dye-sensitized CsSnI$_3$ based solar cells which reach efficiencies larger than 10%.[22–25] Nanorod-polymer solar cells based on CdSe have been already produced underlining the potential of nanostructured semiconductors for energy conversion.[26] Furthermore, in most quantum dot applications of such kind toxic, less abundant, expensive elements, and often complex nanostructuring are needed to realize efficient materials. Bulk-SnIP as a 1.86 eV semiconductor contains nontoxic and abundant elements, which can be successfully delaminated mechanically and chemically to nanorods within minutes by state of the art techniques.[27] Even better, the measured direct band gap is relatively close to the efficiency maximum of single junction solar cells.[28] In the case of effective doping we are optimistic that the conductivity of SnIP can be optimized to make this material applicable.

The structural chemistry of double-helical SnIP is unique. While a 1:1:1 composition is the most prominent one in intermetallic systems such a composition is uncommon in main group chemistry. The general building principle of combining metal halides and complex building blocks can be found for the combination of copper halides and neutral polyphosphide

units[29] or bismuth polycations[30] in metal halide environments. Copper halide phosphorus adducts have been used as precursor compounds for the isolation of new phosphorus allotropes. One may ask the question if the single helices in SnIP might be separated from each other comparable with the neutral polyphosphide strands in the copper halide adducts. In contrast to the copper halide adducts both helices in SnIP are charged (see Table S2 of the Supporting Information for details) and it is therefore unlikely that both helices can be separated in an easy mechanical or chemical way.

The existence of double helical SnIP is unexpected and unusual but as novel prototype structure it offers perspective in nanoscience and related technologies. Double helical assemblies can be easily fabricated from organic substances due to their variable shapes and complex interactions while the inorganic counterpart is much more difficult to realize. The lack of directed inter and intramolecular interactions in the case of simple atom chains renders a self-assembly to pure inorganic double helices more challenging. On a larger scale, a double helical arrangement becomes more and more stable due to the increasing possibility of stabilization by secondary interactions. Several examples are known and only a small fraction will be discussed herein. Examples amongst others are silicon microtubes[31] or carbon nanotubes (CNT)[32] which show diameters of 10–50 µm and 4–6 nm (inner diameter of double-walled CNT), respectively. In the case of double helical CNT's,[33] a large quantity of unwanted byproducts (single helical or noncoiled rods) often disfavors such materials for applications. A combination of both strategies led to the formation of a double-helical Se rod in a double-walled CNT.[6,32] Templating or nanomolding[34] are widely used principles for materials design as shown for chiral Au-nanoparticle helices.[35] Glancing angle deposition were used to fabricate helical hollow Si nanotubes with 30 nm inner diameter.[36] Magnetite nanocubes can be arranged in helical superstructures on a post-atomic scale by an interplay of van der Waals and magnetic dipole–dipole interactions.[37] None of given examples are a purely inorganic carbon-free atomic double helix materials capable to be produced in a defined gram scale synthesis.

With SnIP, the first prototype representative of an atomic-scale double helical structure featuring a phosphorus $^1_\infty[P^-]$ and $^1_\infty[SnI^+]$ helix interpenetrating each other exists. A racemic mixture of left and right handed double helices is arranged parallel to each other, only bond by weak van der Waals interactions. As bulk material and as nanorods, SnIP shows an extraordinary flexibility and photoluminescence making it a promising candidate for semiconductor applications like flexible devices or in energy conversion processes. It can be synthesized phase pure in a simple process from the elements on a gram scale. Complex synthesis procedures or templating routes are not necessary and therefore up-scaling is possible. Due to the electronic and mechanical properties of SnIP a wide range of applications can be addressed in semiconductor science.[38] The pronounced 1D-character of SnIP and the simple production process of nanorods from bulk material defines a new and easily accessible 1D-substance class beside the well-established 2D-materials such as the molybdenum dichalcogenides, graphene or phosphorene. From a topological point of view the bonding situation of SnIP is comparable to the H-bond system in DNA.[39]

Experimental Section

Synthesis of Bulk and Nanostructured SnIP: SnI_4 was synthesized according to literature procedures.[40] A mixture of Sn (107.8 mg, 99,999%; Chempur), SnI_4 (189.6 mg, presynthesized as stated above), and red phosphorus (37.5 mg, ultrahigh grade, 99.999+%, Chempur) was pressed into a pellet (diameter 10 mm, 25 MPa for 15 min) and sealed in a silica glass ampoule under vacuum ($p < 10^{-3}$ mbar). The ampoule was placed in a Nabertherm muffle furnace (L3/11/330) with the starting materials located in the hot zone at 673 K. The melt was cooled down to room temperature within 75 h at the rate of 5 K h^{-1}. Single crystals were obtained by heating up to 923 K followed by slower cooling at the rates of 2 K h^{-1} to 773 K (holding period 15 h) and of 1 K h^{-1} to room temperature. The product has formed during cooling. SnIP can also be synthesized by heating the stoichiometric mixture of Sn, I_2, and red P in an evacuated ($p < 10^{-3}$ mbar) silica glass ampoule at 673 K for 10 h. The same cooling procedure was applied as described above. Bulk SnIP can be nanostructured either mechanically using tape (*Lensguard* 7568 by Nitto) or chemically by using chloroform, *N*-methyl-2-pyrrolidone or toluene. We used an ultrasonic bath with 45 kHz (80 W) for durations from 10 min to 10 h. The latter approach yields in nanorods with diameters smaller than 25 nm. The exfoliated products were examined with an optical light microscope from LEICA DM 1750 M (10 × 100 magnification).

Structure Determination: X-ray powder data were collected on a Stoe Stadi P diffractometer (Cu-K$_{\alpha1}$ radiation, $\lambda = 1.54051$ Å, Ge-monochromator) using a Mythen 1 K detector (Fa. Dectris). An external calibration was performed using Si ($a = 5.43088$ Å). Phase analysis and indexing was performed with the program package Stoe Winxpow.[41]

Single crystal data were measured with a Stoe IPDS II, equipped with Mo-K$_\alpha$ radiation ($\lambda = 0.71073$ Å) and a graphite monochromator. For SnIP, the absorption was corrected numerically, on the basis of symmetry equivalent reflections, after optimization of the crystal shape, using the Stoe X-red and X-shape programs.[42] The structure was solved by the Superflip routine[43] implemented in the Jana2006 program suite.[44]

Crystal Structure of SnIP: Stoe IPDS II diffractometer (MoK$_\alpha$ radiation, $\lambda = 0.71069$ Å), $T = 293$ K, crystal dimensions 0.03 × 0.05 × 0.3 mm^3, monoclinic, space group $P2/c$ (No. 13), lattice parameters $a = 7.934(2)$ Å, $b = 9.802(3)$ Å, $c = 18.439(9)$ Å, $\beta = 110.06(5)°$, $V = 1347.0(9)$ Å^3, $Z = 14$. ρ(calc.) = 4.77 g cm^{-3}, μ(MoK$_\alpha$) = 14.8 mm^{-1}, numerical absorption correction[30], full matrix least squares refinement on F^2 using Jana2006 (32), 6796 reflections, 3567 unique ones, θ max = 29.13°, 98 parameters, R_{int} 0.086, $R1(1651Fo >3\sigma(Fo)) = 0.0407$, wR2 = 0.0840, *GoF* = 1.01, residual electron density +1.88/−1.98 e Å^{-3}.

Further details of the crystal structure investigation(s) may be obtained from the Fachinformationszentrum Karlsruhe, 76344 Eggenstein-Leopoldshafen (Germany), on quoting the depository number CSD-430054.

Scanning Electron Microscopy (SEM) and Energy Dispersive X-Ray Spectroscopy (EDS): SEM images and EDS were performed using a Jeol HR SEM JSM-7500F field emission scanning electron microscope with an Oxford Instrument Inca X-Max analyzer a Zeiss SII NVision40, and a Zeiss Ultra55Plus (Gemini, 5 kV). The EDS results were averaged from three different points selected randomly on the crystal surface. The acceleration voltage was set to 15 kV. The measured composition is in good agreement with the composition calculated from the structure refinement and by quantitative chemical analysis. No other impurities were detected.

Transmission Electron Microscopy: The SnIP needles suspended in butanol respectively prepared dry, were distributed onto grids and studied with different transmission electron microscopes: A Jem-2100 from Jeol (acceleration voltage 200 kV, LaB$_6$, spherical aberration coefficient C_S = 1.0 mm) with EDS detector (SDD, Oxford), a field emission gun microscope Tecnai F30 G2 from Fei (300 kV, C_S = 1.2 mm) with EDS detector (SiLi, Edax), and a Philips CM 30 ST microscope (300 kV, LaB$_6$ cathode, C_S = 1.15 mm) equipped with a spinning star device enabling the use of precession electron diffraction (PED)[45,46]

in addition to selected area electron diffraction (SAED). Simulations of the SAED and PED pattern and the high resolution images were obtained with the JEMS software package.[47] The SnIP crystals grow as needles with different diameters. The analyzed crystals are beam sensitive. During recording of high resolution images the structure and morphology has changed. EDS measurements before and after recording of the images with focused beam longer than 1 min show also the change in the stoichiometry from the given Sn:I:P ratio of 1:1:1 to almost 3:1:3.

Quantum Chemical Calculations: All quantum chemical calculations were performed in the framework of DFT within the all-electron local orbital approach with the Schlegel algorithm as implemented in CRYSTAL14.[14] For all structure optimizations on bulk (3D periodic) and single polymer (1D periodic) models the PBE functional with and without Grimme's D2 correction for vdW interactions[16] was performed. Electronic band structures were calculated with HSE06 functionals.[48,49] Energy versus volume curves were computed with the implemented EOS (equation of state) function. For all calculations including DOS, Sn Fermi contact density, and IR- and Raman frequencies all electron Gaussian type basis sets were applied for P (AE-531151d1*)[50] and Sn (AE-976631311d1*),[51] and a valence basis set for I (HW-1111111*).[52] All calculations were converged to k-point shrinking of 2 × 2 × 2 to 8 × 8 × 8. Graphical representations were created with Xcrysden.[53]

For the description of the SnIP rods we used two different models, a single strand and 1D-polymer. For both models we used the data from structure determination. For the single strand model the distance between the rods was increased to 8.3 Å. At this distance dispersion interactions between the SnIP rods are vanished. For the 1D-model the smallest building block of one strand in the unit cell was taken as repetitive unit and all crystal symmetry was removed. A translation was allowed in rod-direction only.

Thermal Analysis: Differential scanning calorimetry (DSC) was conducted on a DSC 404 *Pegasus* instrument (NETZSCH). About 80 mg of the sample were sealed in a cylindrical niobium crucible by arc-welding in an argon-filled glovebox. An empty sealed crucible served as a reference. The measurements were performed under an argon flow of 60–70 mL min⁻¹ with the heating rate of 10 mL min⁻¹ up to 973 and 1273 K, respectively. The DSC data were processed with the Proteus Thermal Analysis software.[54]

Thermogravimetry (TG): The presented thermogravimetric data were recorded in the range from the ambient temperature to 1273 K with the heating rate of 10 K min⁻¹ under nitrogen with the flow rate of 100 mL min⁻¹ using a simultaneous thermal analyzer (STA 449 F3 Jupiter) manufactured by NETZSCH. Additional experiments under argon atmosphere were performed using a simultaneous thermal analyzer STA 409 Luxx from NETZSCH with the flow rate of 100 mL min⁻¹ from ambient to 1673 K. In order to analyze the intermediate products of thermal decomposition, measurements from ambient to 730 and 743 K, respectively, were carried out on a STA 449 F3 Jupiter instrument with the heating rate of 2 K min⁻¹ (end temperature: 730 K) and 10 K min⁻¹ (end temperature: 743 K). The masses of SnIP taken for various measurements were ≈21 mg. The reported decomposition temperatures were determined at the onset of the differential thermogravimetry (DTG) curve of the respective thermal effect. In order to identify crystalline products of thermal decomposition, powder X-ray diffraction patterns were collected on a BRUKER D2 X-ray diffractometer using the accelerating voltage of 30 kV and the filament current of 10 mA. The patterns were recorded with CuK_α radiation in the reflection mode by a LynxEye detector.

High Temperature Gas Balance: Thermal decomposition behavior of SnIP under its own equilibrium vapor pressure was analyzed using an advanced high-temperature gas balance (HTGB).[55] In this method, the vapor phase is enclosed in a silica ampoule and thus forms the equilibrium gas phase in permanent contact with the solid phase. The measured signal is evoked by the change of the leverage of the horizontal balance support during evaporation and condensation. Application of the HTGB method enables analysis of the solid–gas equilibria in the working range from 0.01 till 15 bars at temperatures up

to 1373 K. For the present measurements the total mass of 199.5 mg of starting material SnIP was sealed in evacuated silica ampoules ($V = 16$ cm³) and heated up with the rate of 10 K h⁻¹ up to 1123 K, then and cooled down to ambient with the rate of 10 K h⁻¹.

Spectroscopic Studies: A Ca¹¹⁹ᵐSnO₃ source was used for the ¹¹⁹Sn Mößbauer spectroscopic investigations. The sample was enclosed in a small thin-walled polymethyl metacrylate (PMMA) container at a thickness of about 13 mg Sn cm⁻². A palladium foil of 0.05 mm thickness was used to reduce the tin K X-rays concurrently emitted by this source. The measurement was conducted in the usual transmission geometry at ambient and liquid nitrogen temperature (bath cryostat). The Mößbauer source was kept at room temperature. Fitting of the data was done by using the Normos-90 program package.[56]

Raman Spectroscopy: Raman spectra were measured using a SENTERRA Spectrometer (BRUKER OPTICS GmbH) equipped with a 785 nm laser and 1 mW power. The spectrum was gained by adding five separate measurements with an integration time of 30 s each and a magnification of 50× (slide 50 × 1000 μm, zoom lens 50 long distance).

³¹P Nuclear Magnetic Resonance: Solid state ³¹P NMR experiments were performed employing a BRUKER AVANCE III spectrometer operating at 7 T at a resonance frequency of 121.53 MHz. MAS was performed using a Bruker 1.3 mm probe at spinning frequencies of 30 kHz, employing RF amplitudes of 122 kHz for ³¹P. Chemical shifts are referenced to 85% H₃PO₄ with ammonium dihydrogen phosphate as an external standard. The ³¹P-MAS-NMR spectrum of SnIP, obtained using a repetition time of 300 s, was deconvoluted with the help of the DMFIT software.[57] A 2D ³¹P RFDR-NMR experiment,[58] which measures the homonuclear magnetic dipole coupling between the ³¹P nuclei, was performed to trace the connectivity's between the P atoms present in the structure. For this experiment, a saturation comb (repetition time 30 s) was used for the excitation, the mixing time was set to 1.6 ms.

Diffuse-Reflectance UV–vis: Diffuse-reflectance UV–vis measurements of powdered and crystalline SnIP samples were performed with an AVANTES AVASPEC 2048 spectrometer and a deuterium/halogen light source (AVALIGHT-DH-S-BAL) connected via a reflection probe (FCR-7UV200-2-ME) using a home-made sample holder (depth: 5 mm). DR UV–vis spectrum is plotted in the form of Kubelka–Munk[59] function defined as $F(R) = (1-R)^2 (2R)^{-1}$ with $R = R_S/R_T$, where R_S is the reflectance of the sample and R_T is the reflectance of PTFE used as a reference. A Tauc plot ($[F(R)h\nu]^x$ with x = 0.5 for an indirect and x = 2 for a direct band gap) was used to derive the bandgap.[60,61]

Photoluminescence Spectroscopy: Photoluminescence on a SnIP needle was measured at ambient temperature on a PRINCTON INSTRUMENTS PyLoN LN Digital CCD Spectroscopy System with single grating of 1,800 1 mm⁻¹. A linear polarized He/Ne-laser (633 nm, 86 μW) is used to excite the SnIP wires. The spectrum was gained by integrating for 120 s using a 100x ZEISS LD EC Epiplan-Neofluar objective.

Magnetic Properties: SnIP was used either as a polycrystalline powder or as a compact piece. The polycrystalline sample was packed in PE capsules and attached to the sample holder rod of a vibrating sample magnetometer unit (VSM) for measuring the magnetization M(T) in a quantum design physical-property-measurement-system (PPMS). The compact piece was attached to the sample holder rod using Kapton foil. The samples were investigated in the temperature range of 3–300 K with magnetic flux densities up to 10 kOe.

Electronic Property Measurements: For the conductance measurements, SnIPs were transferred onto silicon substrates with a silicon dioxide layer of 300 nm on top. The contacts to the nanowires were made by optical lithography and e-beam evaporation of 3 nm Ti and 30 nm Au using the AZ 5214E photoresist and AZ 351 B developer provided by AZ Electronic Materials GmbH and a maskaligner from Karl Süss GmbH&Co. The evaporator is custom-built. The two-terminal current–voltage characteristic was measured at the two contacts highlighted by triangles in Figure S12A of the Supporting Information. A Yokogawa Electric Corporation DC source (Model 7651) was used to apply a bias between −5 and +5 V. The current was measured using a DL INSTUMENTS 1211 current preamplifier (10−9 A/V) together with an Agilent 34410A digital multimeter (Keysight Technologies). The electron

beam induced current (EBIC) measurement was performed using a Zeiss NVision40 scanning electron microscope. One end of the SnIP bundle was contacted by a tungsten tip attached to a micromanipulator from kleindiek nanotechnik. The current in and out of the probe tip was converted to voltage by a DL Systems 1211 current preamplifier (10–9 A/V) and sampled by a National Instruments PXI-DAQ system, along with the signal of the SEM in-lens detector. All data acquisitions were synchronized to the SEM scanning pattern by a dedicated timing module.

SnIP: mp 740 K (peritectic decomposition); ^{31}P Solid State NMR (121.53 MHz, 85% H_3PO_4, δ): 39.0 (P4), 25.3 (P1, P2), 10.5 (P3); Raman (785 nm laser): ν = 460 (w), 450 (w), 446 (w), 439 (w), 351 (w), 339 (w), 218 (w), 180 (vw), 129 (s), 109 (w), 101 (w), 90 (m), 85 (m), 74 (w), 67 (m), 63 (m); Analytical calculation for SnIP (in at%): Sn 33.3, I 33.3, P 33.3; found (EDS): Sn 34(1), I 33(1), P 33(1).

Supporting Information

Supporting Information is available from the Wiley Online Library or from the author.

Acknowledgements

[1] J. D. Watson, F. H. Crick, *Nature* **1953**, *171*, 737.

[2] M.-Q. Zhao, Q. Zhang, G.-L. Tian, F. Wei, *Nanoscale* **2014**, *6*, 9339.

[3] C. Zeng, Y Chen, C. Liu, K. Nobusada, N. L. Rosi, R. Jin, *Sci. Adv.* **2015**, *1*, e1500425.

[4] C. W. Bunn, E. R. Howells, *Nature* **1954**, *174*, 549.

[5] a) A. S. Ivanov, A. J. Morris, K. V. Bozhenko, C. J. Pickard, A. I. Boldyrev, *Angew. Chem., Int. Ed.* **2012**, *51*, 8330; b) W. Hönle, H. G. von Schnering, *Z. Kristallogr.* **1981**, *155*, 307.

[6] T. Fujimori, R. B. dos Santos, T. Hayashi, M. Endo, K. Kanek, D. Tománek, *ACS Nano* **2013**, *7*, 5607.

[7] Z. Tang, Z. Zhang, Y. Wang, S. C. Glotzer, N. A. Kotov, *Science* **2006**, *314*, 274.

[8] S. Srivastava, A. Santos, K. Critchley, K. S. Kim, P. Podsiadlo, K. Sun, J. Lee, C. Xu, G. D. Lilly, S. C. Glotzer, N. A. Kotov, *Science* **2010**, *327*, 1355.

[9] J. Sharma, R. Chhabra, A. Cheng, J. Brownell, Y. Liu, H. Yan, *Science* **2009**, *323*, 112.

[10] V. Soghomonian, Q. Chen, R. C. Haushalter, J. Zubieta, C. J. O'Connor, *Science* **1993**, *259*, 1596.

[11] U. Müller, *Symmetry Relationships Between Crystal Structures: Applications of Crystallographic Group Theory in Crystal Chemistry*, Oxford University Press, UK **2013**.

[12] M. I. Aroyo, *International Tables for Crystallography, Volume A: Space Group Symmetry*, 6th ed., Springer, Germany **2016**.

[13] M. M. Shatruk, K. A. Kovnir, A. V. Shevelkov, I. A. Presniakov, B. A. Popovkin, *Inorg. Chem.* **1999**, *38*, 3455.

[14] R. Dovesi, R. Orlando, A. Erba, C. M. Zicovich-Wilson, B. Civalleri, S. Casassa, L. Maschio, M. Ferrabone, M. De La Pierre, P. D'Arco, Y. Noel, M. Causa, M. Rerat, B. Kirtman, *Int. J. Quantum Chem.* **2014**, *114*, 1287.

[15] a) F. Bachhuber, J. von Appen, R. Dronskowski, P. Schmidt, T. Nilges, A. Pfitzner, R. Weihrich, *Angew. Chem.* **2014**, *126*, 11813; b) F. Bachhuber, J. von Appen, R. Dronskowski, P. Schmidt, T. Nilges, A. Pfitzner, R. Weihrich, *Angew. Chem., Int. Ed.* **2014**, *53*, 11629.

[16] a) O. Osters, T. Nilges, R. Weihrich, F. Bachhuber, F. Pielnhofer, M. Schöneich, P. Schmidt, *Angew. Chem.* **2012**, *124*, 3049; b) O. Osters, T. Nilges, R. Weihrich, F. Bachhuber, F. Pielnhofer, M. Schöneich, P. Schmidt, *Angew. Chem., Int. Ed.* **2012**, *51*, 2994.

[17] K. Doll, R. Dovesi, R. Orlando, *Theor. Chem. Acc.* **2005**, *115*, 354.

[18] F. Bachhuber, J. von Appen, R. Dronskowski, P. Schmidt, T. Nilges, A. Pfitzner, R. Weihrich, *Z. Kristallogr.* **2015**, *230*, 107.

[19] C. M. Zicovich-Wilson, F. J. Torres, F. Pascale, L. Valenzano, R. Orlando, R. Dovesi, *J. Comput. Chem.* **2008**, *29*, 2268.

[20] L. Li, Y. Yu, G. J. Ye, Q. Ge, X. Ou, H. Wu, D. Feng, X. H. Chen, Y. Zhang, *Nat. Nanotechnol.* **2014**, *9*, 372.

[21] K. Terashima, T. Katsumata, F. Orito, T. Kikuta, T. Fukuda, *Jpn. J. Appl. Phys.* **1983**, *22*, L325.

[22] M. Graetzel, R. A. J. Janssen, D. B. Mitzi, E. H. Sargent, *Nature* **2012**, *488*, 304.

[23] W. Chen, Y. Wu, Y. Yue, J. Liu, W. Zhang, X. Yang, H. Chen, E. Bi, I. Ashraful, M. Grätzel, L. Han, *Science* **2015**, *350*, 944.

[24] W. Nie, H. Tsai, R. Asadpour, J. C. Blancon, A. J. Neukirch, G. Gupta, J. J. Crochet, M. Chhowalla, S. Tretiak, M. A. Alam, H. L. Wang, A. D. Mohite, *Science* **2015**, *347*, 522.

[25] I. Chung, B. Lee, J. He, R. P. H. Chang, M. G. Kanatzidis, *Nature* **2012**, *485*, 486.

[26] W. U. Huynh, J. J. Dittmer, A. P. Alivisatos, *Science* **2002**, *295*, 2425.

[27] J. N. Coleman, M. Lotya, A. O'Neill, S. D. Bergin, P. J. King, U. Kha, K. Young, A. Gaucher, S. De, R. J. Smith, I. V. Shvets, S. K. Arora, G. Stanto, H.-Y. Kim, K. Lee, G. T. Kim, G. S. Duesberg, T. Hallam, J. J. Boland, J. J. Wang, J. F. Donegan, J. C. Grunlan, G. Moriarty, A. Shmeliov, R. J. Nicholls, J. M. Perkins, E. M. Grieveson, K. Theuwissen, D. W. McComb, P. D. Nellist, V. Nicolosi, *Science* **2011**, *331*, 568.

[28] W. Shockley, H. J. Queisser, *J. Appl. Phys.* **1961**, *32*, 510.

[29] A. Pfitzner, *Chem. Eur. J.* **2000**, *6*, 1891.

[30] E. Ahmed, M. Ruck, *Coord. Chem. Rev.* **2011**, *255*, 2892.

[31] H. Morito, H. Yamane, *Angew. Chem., Int. Ed.* **2010**, *49*, 3638.

[32] Q. Zhang, M.-Q. Zhao, D.-M. Tang, F. Li, J.-Q. Huang, B. Liu, W.-C. Zhu, Y.-H. Zhang, F. Wei, *Angew. Chem., Int. Ed.* **2010**, *49*, 3642.

[33] S. Iijima, T. Ichihashi, *Nature* **1993**, *363*, 603.

[34] W. Sun, E. Boulais, Y. Hakobyan, W. L. Wang, A. Guan, M. Bathe, P. Yin, *Science* **2014**, *346*, 1258361.

[35] A. Kuzyk, R. Schreiber, Z. Fan, G. Pardatscher, E. M. Roller, A. Högele, F. C. Simmel, A. O. Govorov, T. Liedl, *Nature* **2012**, *483*, 311.

[36] Z. Huang, K. D. Harris, M. J. Brett, *Adv. Mater.* **2009**, *21*, 2983.

[37] G. Singh, H. Chan, A. Baskin, E. Gelman, N. Repnin, P. Král, R. Klajn, *Science* **2014**, *345*, 1149.

[38] D. Pfister, C. Ott, M. Baumgartner, K. Schäfer, R. Weihrich, T. Nilges, *EP15176311.7*, **2015**.

[39] N. Narayana, M. A. Weiss, *J. Mol. Biol.* **2009**, *385*, 469.

[40] a) S. Lange, P. Schmidt, T. Nilges, *Inorg. Chem.* **2007**, *46*, 4028; b) M. Köpf, N. Eckstein, D. Pfister, C. Grotz, I. Krüger, M. Greiwe, T. Hansen, H. Kohlmann, T. Nilges, *J. Cryst. Growth* **2014**, *405*, 6.

[41] *Stoe Winxpow, Version 3.0.2.1*, Stoe & Cie GmbH, Darmstadt, Germany **2011**.

[42] a) Stoe Xarea, version 1.56, Stoe & Cie GmbH, Darmstadt, Germay **2011**; b) X-Red32, Version 1.53, Stoe & Cie GmbH, Darmstadt, Germany **2009**; c) X-shape, Version 2.1, Stoe & Cie GmbH, X-Red32, Darmstadt, Germany **2009**.

[43] L. Palatinus, G. Chapuis, *J. Appl. Crystallogr.* **2007**, *40*, 786.

[44] V. Petříček, M. Dušek, L. Palatinus, *Z. Kristallogr.* **2014**, *229*, 345.

[45] U. Schürmann, V. Duppel, S. Buller, W. Bensch, L. Kienle, *Cryst. Res. Technol.* **2011**, *46*, 561.

[46] R. Vincent, P. A. Midgley, *Ultramicroscopy* **1994**, *53*, 27.

[47] P. A. Stadelmann, *Ultramicroscopy* **1987**, *21*, 131.

[48] J. P. Perdew, Y. Wang, *Phys. Rev. B* **1992**, *45*, 13244.

[49] A. V. Krukau, O. A. Vydrov, A. F. Izmaylov, G. E. Scuseria, *J. Chem. Phys.* **2006**, *125*, 224106.

[50] A. J. Karttunen, T. F. Fässler, M. Linnolahti, T. A. Pakkanen, *Inorg. Chem.* **2011**, *50*, 1733.

[51] J. Rothballer, F. Bachhuber, F. Pielnhofer, S. M. Schappacher, R. Pöttgen, R. Weihrich, *Eur. J. Inorg. Chem.* **2013**, 248.

[52] K. Doll, H. Stoll, *Phys. Rev. B* **1998**, *57*, 4327.

[53] A. Kokalj, *J. Mol. Graphics Modell.* **1999**, *17*, 176.

[54] *Netzsch Proteus Thermal Analysis V4.8.2*, Netzsch-Gerätebau GmbH, Selb, Germany **2006**.

[55] P. Schmidt, M. Schöneich, M. Bawohl, T. Nilges, R. Weihrich, *J. Therm. Anal. Calorim.* **2011**, *110*, 1511.

[56] R. A. Brand, *Normos 90-Mößbauer Fitting Program*, Universität Duisburg, Duisburg, Germany **2007**.

[57] D. Massiot, F. Fayon, M. Capron, I. King, S. Le Calvé, B. Alonso, J.-O. Durand, B. Bujoli, Z. Gan, G. Hoatson, *Magn. Reson. Chem.* **2002**, *40*, 70.

[58] A. E. Bennett, R. G. Griffin, J. H. Ok, S. Vega, *J. Chem. Phys.* **1992**, *96*, 8624.

[59] P. Kubelka, F. Munk, *Z. Tech. Phys.* **1931**, *12*, 593.

[60] J. Tauc, R. Grigorovici, A. Vancu, *Phys. Status Solidi* **1966**, *15*, 627.

[61] J. Tauc, *J. Mater. Res. Bull.* **1968**, *3*, 37.

ADVANCED MATERIALS

Supporting Information

Inorganic Double Helices in Semiconducting SnIP

Daniela Pfister, Konrad Schäfer, Claudia Ott, Birgit Gerke, Rainer Pöttgen, Oliver Janka, Maximilian Baumgartner, Anastasia Efimova, Andrea Hohmann, Peer Schmidt, Sabarinathan Venkatachalam, Leo van Wüllen, Ulrich Schürmann, Lorenz Kienle, Viola Duppel, Eric Parzinger, Bastian Miller, Jonathan Becker, Alexander Holleitner, Richard Weihrich, and Tom Nilges*

Supplementary Materials for

Inorganic Double Helices in Semiconducting SnIP

By Daniela Pfister, Konrad Schäfer, Claudia Ott, Birgit Gerke, Rainer Pöttgen, Oliver Janka, Maximilian Baumgartner, Anastasia Efimova, Andrea Hohmann, Peer Schmidt, Sabarinathan Venkatachalam, Leo van Wüllen, Ulrich Schürmann, Lorenz Kienle, Viola Duppel, Eric Parzinger, Bastian Miller, Jonathan Becker, Alexander Holleitner, Richard Weihrich, Tom Nilges[*]

Correspondence to: tom.nilges@lrz.tum.de

Other Supplementary Materials for this manuscript includes the following:

> Movie S1: Bending of SnIP crystals
> Movie S2: Suspending and reemerging of SnIP

Crystallographic structure data of SnIP

Crystal structure data tables, atomic coordinates and selected interatomic distances for SnIP are given in Table S1-S4. Data are collected at 298 K from single crystals.

Thermoanalytic investigations on SnIP

Thermochemical behavior of SnIP is related to the phase relations within the ternary Sn/P/I phase diagram. According to the latter, SnIP can form equilibria with the ternary clathrate phase $Sn_{24}P_{19.3}I_8$ [13,62], the binary tin iodides SnI_2 and SnI_4 and elemental phosphorus, Figure S7a. Depending on temperature the volatile compounds melt already below 500 K ($T_m(SnI_4) = 418$ K [63]) and start to sublime above 600 K ($T_b(SnI_4) = 626$ K; $T_b(P_{red}) = 703$ K [63]). The resultant heterogeneous solid-gas equilibria of SnIP can be observed at different steps of thermal decomposition in high-temperature DSC experiments and in the measurements using simultaneous thermal analysis (TG-DTA).

Differential Scanning calorimetry (DSC)

The first DSC experiment that was performed in the range between 123 K and 423 K (no figure) revealed no thermal effects. In order to evaluate the thermal stability and to infer the best synthesis conditions, high-temperature DSC experiments were performed in sealed niobium ampoules up to 973 K (Figure S7b A), and up to 1273 K (Figure S7b B)**,** up to 973 K shown).

The results of the DSC measurements differ with the end temperature of the heating run. The measurement of the SnIP thermal behavior up to 973 K shows almost completely reversible melting and re-crystallization processes (Figure S7b A), while the DSC run up to 1273 K shows irreversible decomposition of SnIP (Figure S7b B). At the first heating round, all samples of initial composition of SnIP show two endothermic effects with the onset temperatures at 740(2) K and 873(2) K. Thus it is concluded, that SnIP decomposes peritectically in a first heating cycle forming the *Shevelkov* phase

$Sn_{24}P_{19.3}I_8$ [13,62] and a melt. The second effect represents the melting process of the complex ternary mixture (with $Sn_{24}P_{19.3}I_8$ as the main phase). The very sharp signal at 873 K indicates a well-defined melting point, most likely, a ternary eutectic point. (The very first endothermic effect at about 600 K can be assigned to a small residue of SnI_2 which maybe originates from grinding or sealing of the tube).

The same effects reappear in the reverse order as exothermic ones in the cooling run down from the end temperature $T = 973$ K (Figure S7b A). The sharp crystallization peak of the complex ternary mixture with $Sn_{24}P_{19.3}I_8$ as the main phase occurs with a thermal hysteresis of about 90 K ($T_{cryst} = 780(5)$ K). Peritectic re-crystallization of SnIP is observed with a hysteresis of about 30 K ($T_{cryst} = 710(5)$ K). Due to the incongruent character of the peritectic melting and re-crystallization, a noticeable amount of liquid SnI_2 remains and solidifies at 590(5) K. Likewise, the second cycle up to 973 K shows reversible occurrence of the characteristic effects in the heating and cooling runs. However, due to the incongruent processes of melting and crystallization, temperatures and peak shapes slightly differ.

During the cooling run of the measurement up to 1273 K no reversible re-crystallization was observed (Figure S7a C). One very small exothermic effect is present at 710(5) K, followed by two strong exothermic effects at 595(5) and 505(5) K. The observed thermal effects can be attributed to the re-crystallization of the system components SnIP, SnI_2 ($T_m = 593$ K [63]), and Sn ($T_m = 505$ K [63]). Only two effects at 595 and 505 K can still be observed in the second cycle. These two sharp peaks can be assigned to the melting and crystallization of the system components Sn ($T_m = 505$ K [63]), and SnI_2 ($T_m = 593$ K [63]) with almost no hysteresis. Two different mechanisms can cause the non-reversible behaviour: 1st) Free volume of the measurement ampoule is sufficient for evaporation of large amounts of system components Sn, SnI_2, SnI_4, and P_4 (with several bar). Condensation of different species at different temperatures and within small temperature gradients of the ampoule leads to separation and non-homogeneous mixtures. Finally, the formation of SnIP is subjected to kinetic restraints. 2nd) The system components SnI_4 and phosphorus are able to oxidize niobium (the ampoule material) at higher temperatures to form binary and/or ternary niobium phases. Thereby, the composition of the initial mixture "SnIP" has distinctly changed and a reversible reaction is barred.

Thermogravimetry-Differential thermal analysis (TG-DTA)

The thermal stability of SnIP additionally has been investigated applying simultaneous thermal analysis (TG-DTA, Figure S7b). Irreversible decomposition of SnIP starting slightly above 600 K was observed both in nitrogen and argon atmosphere. Some TG experiments offered a small effect of mass increase (up to 1 %) due to oxidation of the sample. For these samples small amounts of SnO could be detected in the residual by powder XRD.

A total mass loss of 73(2) % can be assigned to the heterogeneous decomposition reaction forming the gaseous products tin(IV) iodide, tin(II) iodide, and phosphorus besides β-tin as the residual.

$$SnIP(s) \rightarrow 0.63\ Sn(s,l) + 0.13\ SnI_4(g) + 0.24\ SnI_2(g) + 0.25\ P_4(g)$$

Differentiation and quantification of single steps failed, since the respective decomposition reactions interfered. Most certainly, the first effect occurs from the release of both - SnI_4 and phosphorus. The cationic clathrate phase $Sn_{24}P_{19.3}I_8$ is formed as the main product besides SnI_2. $Sn_{24}P_{19.3}I_8$ and SnI_2 could be isolated as intermediate products in separate TG experiments up to 730 K. Nonetheless, $Sn_{24}P_{19.3}I_8$ [13,62] has immediately degraded towards liquid tin. The decomposition process is dominated here by evaporation of SnI_2 and phosphorus, respectively.

$$SnIP(s) \rightarrow 0.03\ Sn_{24}P_{19.3}I_8(s) + 0.18\ SnI_2(l) + 0.10\ SnI_4(g) + 0.10525\ P_4(g)$$

$$0.03\ Sn_{24}P_{19.3}I_8(s) + 0.18\ SnI_2(l) \rightarrow 0.63\ Sn(s,l) + 0.03\ SnI_4(g) + 0.24\ SnI_2(g) + 0.14475\ P_4(g)$$
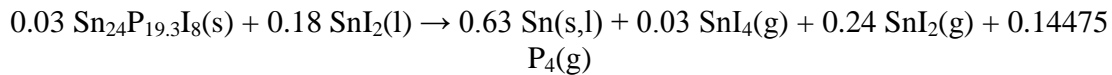
The stepwise dominance of different gaseous species was substantiated by thermogravimetric measurements using the high-temperature gas-balance (HTGB) approach [63]. Thus the first decomposition step in Figure S7c shows a course slightly higher than the calculated mass loss of evaporation of phosphorus. Thus the mass loss results from evaporation of a mixture of $SnI_4(g)$ and $P_4(g)$. Thereby, the decomposition vapor pressure of SnIP is almost the same as of pure phosphorus. The second step runs under release of SnI_2 and P_4 as the dominating gas species. The basically two-step mechanism of decomposition of SnIP can be confirmed: While SnIP decomposes above 600 K under formation of $Sn_{24}P_{19.3}I_8(s)$ and $SnI_2(l)$, the second step ($T > 800$ K) describes the decomposition of $Sn_{24}P_{19.3}I_8$ and evaporation of additional SnI_2 (see reaction formula above).

^{119}Sn Mößbauer spectroscopy

^{119}Sn Mößbauer spectra of SnIP have been recorded at 298 and 77 K. Two signals with an isomer shift of $3.37(1)$ mm·s^{-1} (85 % intensity) and $2.76(1)$ mm·s^{-1} (15 % intensity) have been observed (Figure S4a). According the crystal structure, we expect four different Sn signals for the atoms sitting 3× on $4g$ and 1× on $2f$ sites. The observed values are compared to a selection of tin, tin phosphides and tin iodides as given in Table S5.

Due to the almost identical first and second coordination sphere and our calculations (see Table S6) we assign the 3.37 mm·s^{-1} signal to the four different Sn species in SnIP. The signal at 2.76 mm·s^{-1} is due to a SnO impurity. This assignment is underlined from DFT calculations.

A measurement of an independently synthesized second sample showed identical results.

In ^{119}Sn Mößbauer spectroscopy, the energy $\mathit{\Delta}E$ of the nuclear spin transition is proportional to the electron density $\rho(0)$ at the given tin core (Fermi contact density). Any change in $\rho(0)$ in a sample S can thus be detected with respect to a reference R that contains Sn(+IV) like $CaSnO_3$ $BaSnO_3$ or SnO_2. Experimentally, the Doppler-effect is used to measure an isomer shift

$$\delta = A[\rho R(0) - \rho S(0)] = A \cdot \Delta\rho\ (0)$$

3

For the interpretation of ^{119}Sn Mößbauer data by DFT calculations two approaches are applied:

(1st) According to the relation $\delta = A \cdot \Delta\rho(0)$ the Fermi contact density is calculated for reference compounds to relate isomer shifts and bonding states. This method requires an all electron approach and avoids problems related to orbital occupation numbers that depend very much on applied methods, potentials and/or basis sets.

(2nd) According to earlier work [64-67] isomer shifts of Sn can be related to valence orbital contributions with major Sn-5s effects, which causes a non-vanishing charge density at the core positions. With carefully or automatically optimized basis sets this method delivers good results, too.

For the first method (1) the Fermi contact density was calculated within an all electron approach as implemented in CRYSTAL14. A correlation of experimentally determined isomer shift and contact density is found along various Sn compounds with different charge and oxidation states (see Table in Figure S4a D) and Table S6). Therein, all Sn positions in SnIP are found in the range of Sn(+II) compounds, but clearly separated from SnCl$_2$ and SnO at the same δ and $\rho°$ values. Each of the four Sn atoms on different sites show similar Fermi contact values leading to the conclusion that the Sn sites in SnIP cannot be distinguished from isomer shifts in ^{119}Sn Mößbauer spectroscopy.

Within the second approach (2) orbital occupation numbers were calculated with the full potential local orbital code FPLO14 [68,69]. The integrated total valence and orbital separated occupation numbers are given in Figure S4b. FPLO optimizes outer shell parameters automatically that reduces the basis set dependency. As seen in Figure S4a C) again, the Sn-5s orbital occupation follows, to a first approximation, a linear dependency with the isomer shift for various Sn compounds. To the contrary, the Sn-5p orbital occupation or the number of electrons N, can change unsystematically and depends on the overall bonding situation. The same is found for the total orbital occupation. As shown for α-Sn and β-Sn, the total number of valence electrons is 4, but the distribution between 5s and 5p orbitals differs due to the differences in local bonding. One has to point out, that the orbital occupation for all compounds is higher than expected from the ionic model. The reason for this is a covalent bonding contribution even in Sn(+IV) compounds. The same reason explains the low but not vanishing occupation of Sn-5d orbitals.

According to both computational approaches the Sn atoms in SnIP are found in a typical region for Sn(+II) states as also found in SnS and Sn$_2$S$_3$. For both approaches it becomes clear, that the origin of the 2.8 mm·s^{-1} signal cannot be SnIP, but might be SnO.

Structure Chemistry of SnIP

The structure principle of interpenetrating charged helices is unique for SnIP. Nevertheless, some similarities can be found to existing materials. Compounds containing neutral metal halide and neutral pnicogen substructures have been reported by *Pfitzner et al.* for copper(I) halide phosphorus adducts [29]. Neutral phosphorus polymers or neutral phosphorus-chalcogen molecules and polymers are embedded in a copper halide matrix [29]. In the case of (CuI)$_3$P$_{12}$ [70] and (CuI)$_2$P$_{14}$ [71] the adduct character has been proven by the synthesis of new phosphorus allotropes, dissolving the copper halides in suitable solvents [72].

Heavy pnicogen elements like Bi also realize related structural chemistry where homoatomic and heteroatomic polycations in various compositions can be stabilized in a metal halide environment [30,73]. One compound containing a homoatomic bismuth polycation is $(Bi_9^{5+})_2[Sn_7Br_{24}^{10-}]$ [74], where $[Bi_9]^{5+}$ cations are separated by bromidostannate(II) groups. Two heteroatomic examples are $[Ru_2Bi_{14}Br_4](AlCl_4)_4$ [75] or $[Ru(Te_9)](InCl_4)_2$ [76], where either $[AlCl_4]^-$ or $[InCl_4]^-$ are coordinating complex bismuth or tellurium containing polycations.

Magnetic Properties of SnIP

The temperature dependence of the magnetic susceptibility (χ) of two samples of SnIP were measured at 10 kOe (Figure S5). Both samples show diamagnetic behavior above 10 K, the measurement of the compact piece shows Pauli-paramagnetic behavior at low temperatures ($< 6K$), most likely due to trace impurities. The susceptibility at 300 K exhibits values of $-40(1) \times 10^{-6}$ emu·mol^{-1} (polycrystalline powder) and $-71(1) \times 10^{-6}$ emu·mol^{-1} (compact piece) respectively. The observed diamagnetism is in line with no localized electrons. The values of the observed susceptibilities are close to the calculated ones ($\sim -93 \times 10^{-6}$ emu mol^{-1}) using the diamagnetic increments ($Sn^{2+} = -20 \times 10^{-6}$ emu·mol^{-1}; $I^- = -50.6 \times 10^{-6}$ emu·mol^{-1}; P^- estimated to be -22.4×10^{-6} emu·mol^{-1}) listed in [77]. The deviations from the ideal values can be explained by traces of paramagnetic impurities.

Electronic properties

The EBIC measurements unambiguously show that SnIP-bundles are electronically conductive (cf. Figure 4). Assuming a length of 3 µm between the contacting metal contacts and a bundle diameter of about 400-500 nm, we can estimate an electronic conductivity in the order of 2-3 µS/m. This naive estimate does not consider any specific transport morphology within the SnIP-bundle. We note that the SnIPs have a bandgap of about 1.8 eV with a Fermi-energy most likely mid-gap. We are very positive that doping will increase the electronic conductivity.

References for supplement only

[62]   V. V. Novikov *et al.*, *J. Alloys Compd.* **2012**, *520*, 174.

[63]   I. B. O. Knacke, *Thermochemical properties of inorganic substances*. Springer, Berlin, Heidelberg, Budapest, Stahleisen, ed. 2nd, **1991**.

[64]   P. Lippens, *Phys. Rev. B* **1999**, *60*, 4576.

[65]   L. Häggström, J. Gullman, T. Ericsson, R. Wäppling, *J. Solid State Chem.* **1975**, *13*, 204-207 (1975).

[66]   A. Svane, N. E. Christensen, C. O. Rodriguez, M. Methfessel, *Phys. Rev. B* **1997**, *55*, 12572.

[67]   R. Weihrich, S. Lange, T. Nilges, *Solid state Sci.* **2009**, *11*, 519.

[68]   R. Weihrich *et al.*, *Dalton Trans.* **2015**, *44*, 15855.

[69]   K. Koepernik, H. Eschrig, *Phys. Rev. B* **1999**, *59*, 1743.

[70]   A. Pfitzner, E. Freudenthaler, *Angew. Chem. Int. Ed.* **1995**, *34*, 1647.

[71]   A. Pfitzner, E. Freudenthaler, *Z. Natrufosrch. Sect. B.* **1997**, *52*, 199.

[72] A. Pfitzner, M. F. Bräu, J. Zweck, G. Brunklaus, H. Eckert, *Angew. Chem. Int. Ed.* **2004**, *43*, 4228.
[73] M. Ruck, F. Locherer, *Coord. Chem. Rev.* **2015**, *285*, 1.
[74] B. Wahl, M. Ruck, *Z. Anorg. Allg. Chem.* **2010**, *636*, 337.
[75] M. F. Groh, A. Isaeva, M. Ruck, *Chem. Eur. J.* **2012**, *18*, 10886.
[76] A. Günther, A. Isaeva, A. I. Baranov, M. Ruck, *Chem. Eur. J.* **2011**, *17*, 6382.
[77] G. A. Bain, J. F. Berry, *J. Chem. Educ.* **2008**, *85*, 532.
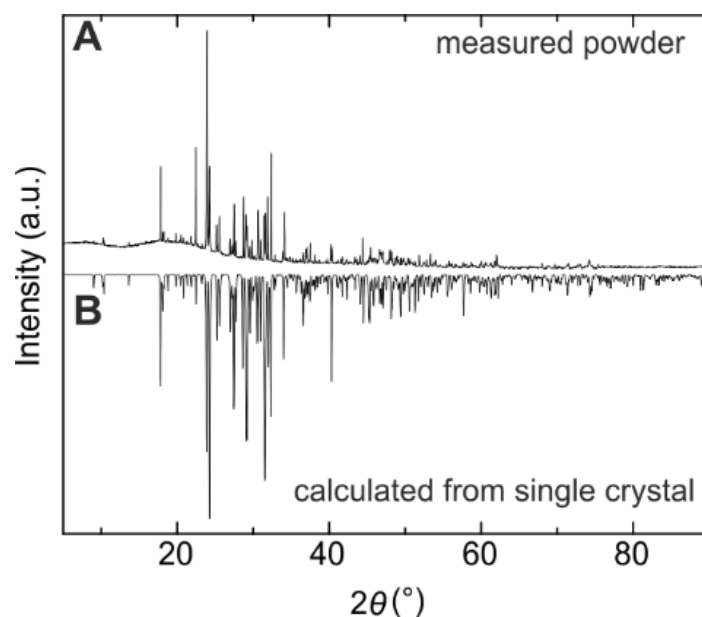
Figure S1. Powder X-ray diffractogram of phase pure SnIP recorded at room temperature. A) Diffractogram of crystalline SnIP. B) Calculated powder diffractogram based on the single crystal structure data is plotted with negative intensities for comparison. Results from EDX analyses in at.-% are: Sn:I:P = 34(3):33(1):33(1) (calc. 33.3:33.3:33.3).
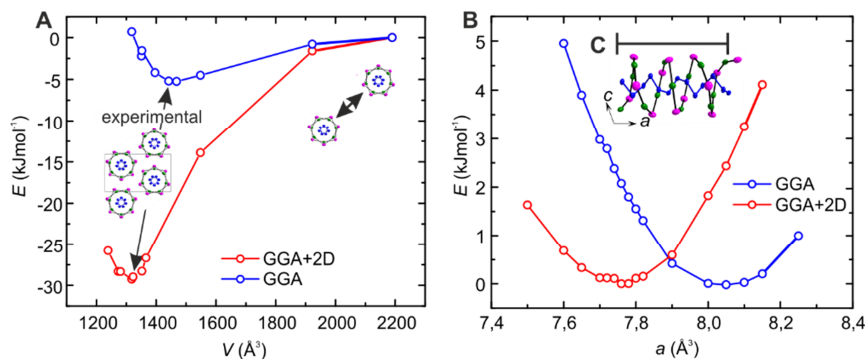
Figure S2. Results from quantum chemical calculations on SnIP. Van der Waals (vdW) interactions have been determined by varying the inter-rod distance and calculating the energy volume potential curves using GGA (blue curve, no vdW interactions) and GGd+D2 (red curve, including vdW interactions) functionals. An arrow marks the experimental cell volume of SnIP. According our calculations, A) vdW inter-rod interaction of 25 kJ·mol^{-1} was found. B) Attractive intra-rod interactions are also present in SnIP. The rod distance as shown in C) is significantly shortened if vdW interactions are taken into account.
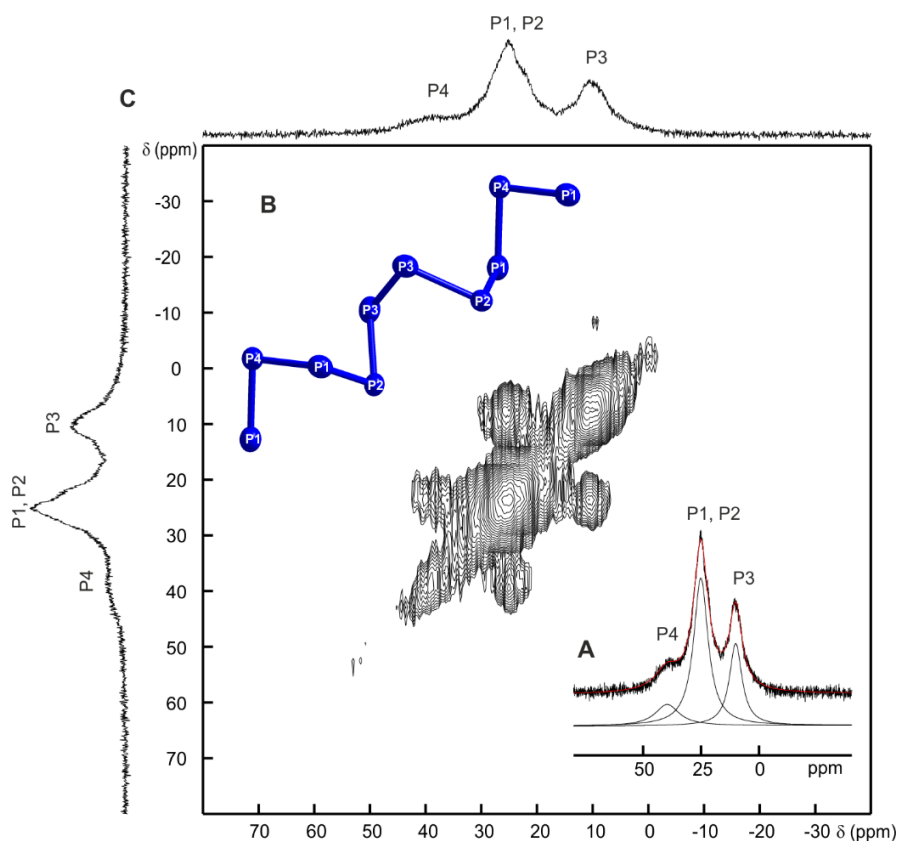
Figure S3. ^{31}P-MAS-NMR investigations on SnIP. A) In the ^{31}P-MAS-NMR spectrum, three different signals can be identified, which may be deconvoluted with the help of the DMFIT software into signals at 39.0 ppm, 25.3 ppm and 10.5 ppm with relative fractions of 0.13, 0.58 and 0.29. The signal at 39 ppm has to be assigned to P4. C) The two-dimensional ^{31}P RFDR-NMR experiment [58], which measures the homo-nuclear magnetic dipole coupling between the ^{31}P nuclei traces the connectivities between the P atoms present in the structure. With the assignment of the 25.3 pm signal to P1, P2 and the 10.5 ppm signal to P3 the connectivity pattern as found in the RFDR spectrum (P4 – P1,P2, P4 - P1,P2 – P3, P1,P2, - P3) proves to be in good agreement with the result of the X-ray structure determination B).

A

Sn1: 3.171(2) Å — 3.184(2) Å (I4, I1); 2.673(4) Å, 2.678(4) Å (P2, P1)

Sn2: 3.119(2) Å — 3.288(2) Å (I1, I3); 2.664(4) Å, 2.681(3) Å (P3, P4)

Sn3: 3.215(2) Å — 3.062(2) Å (I2, I3); 2.713(4) Å, 2.682(4) Å (P1, P2)

Sn4: 3.060(2) Å — 3.060(2) Å (I3, I2); 2.710(4) Å, 2.710(4) Å

B relative transmission; 5%; 78 K; velocity (mm·s⁻¹)

C δ (mms⁻¹) vs $\Delta\rho(0)$ (e/au³)

D

	δ (mms⁻¹)	$\Delta\rho(0)$ (e/au³)
BaSnO$_3$	0.0	0.0
SnO$_2$	0.0	0.2
SnS$_2$	1.3	4.1
α-Sn	2.0	7.4
Sn$_2$Co$_3$S$_2$	2.2	8.0
β-Sn	2.6	9.6
SnO	2.7	10.5
SnS	3.3	14.2
SnIP_1	3.3	14.0
SnIP_2	3.3	13.9
SnIP_3	3.3	14.1
SnIP_4	3.3	14.0
SnCl$_2$	4.0	17.7
SnCl$_2$	4.0	17.9

Figure S4a. ^{119}Sn Mößbauer spectroscopic investigations on SnIP. A) Four different Sn sites are present in SnIP featuring an almost identical first coordination sphere. B) Fermi contact densities $\Delta\rho(0)/(e/au^3)$ have been calculated with an all electron approach as implemented in CRYSTAL14 (*16*) for different Sn compounds, see C), and the four sites in SnIP. The contact density for Sn is mainly determined by the Sn-5s orbital occupation that is in the ideal orbital picture 5s^0 for Sn(+IV), 5s^1 for Sn(0), and 5s^2 for Sn(II). Therefore a linear correlation was analyzed for the experimentally determined isomer shift (IS) to the difference in contact density for a sample ($\rho(r°)$s) with respect to a Sn(+IV) reference ($\rho(r°)$ref): IS = k*|($\rho(r°)$ref-$\rho°(r°)$s)|. According our calculations almost identical and non-resolvable Mößbauer isomer shifts δ (mm s^{-1}) are expected for the different Sn sites and the Sn(+II) valence state is confirmed. According to a comparison in D) to typical systems for Sn(+IV) (SnO$_2$, BaSnO$_3$), Sn(0) (α-Sn, β-Sn), both isomer shift and calculated contact density of Sn in SnIP are found in the typical region for Sn(+II) (SnS, SnCl$_2$). Deviations are however due to different degrees of covalent and ionic bonding contributions.

9
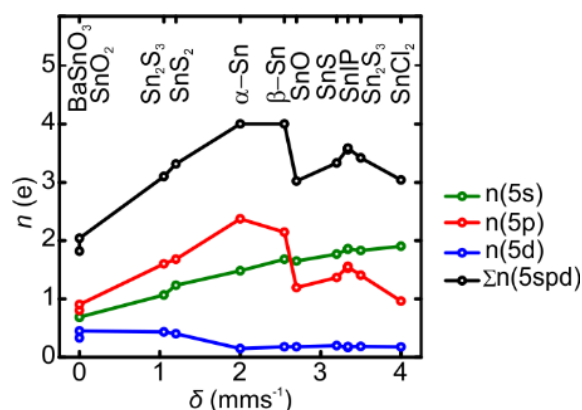
Figure S4b. Integrated total valence and orbital separated occupation numbers (FPLO14 [70, 78]) for Sn-5s, 5p, and 5d orbitals as a function of the [119]Sn Mößbauer isomer shift δ in various Sn compounds. A linear trend was found for the 5s electron occupancy n (e) at the nucleus vs. the isomer shift δ.
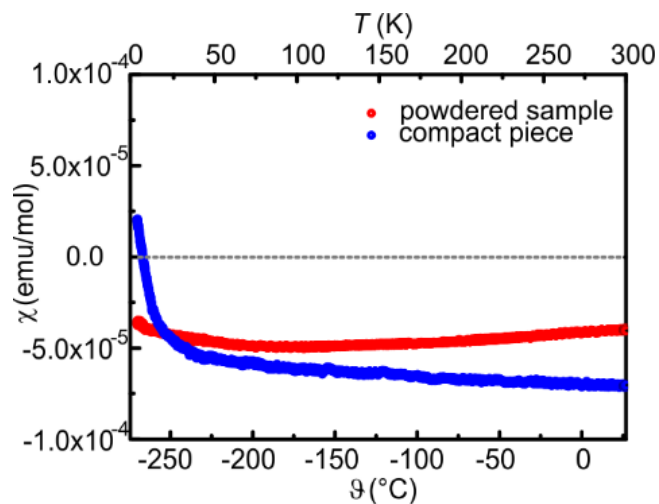
Figure S5. Susceptibility measurements of SnIP. Magnetic measurements on a compact piece and powdered SnIP. Diamagnetic behavior was observed in both cases. A small paramagnetic impurity was present in the compact sample.
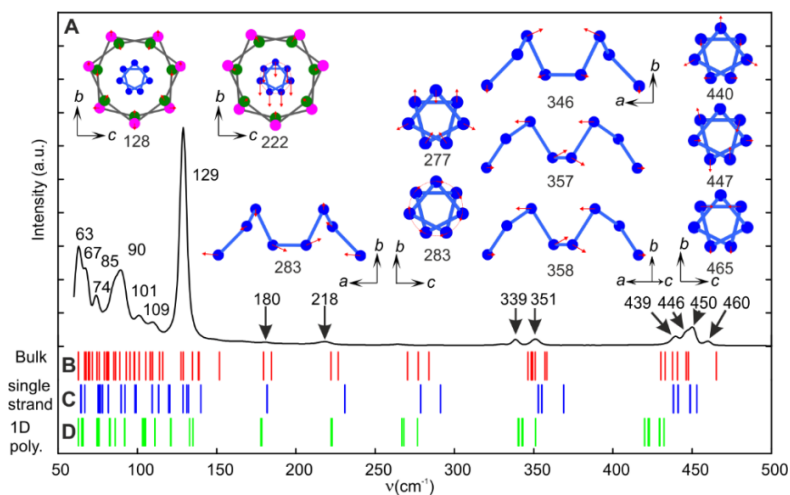
Figure S6. Results from Raman spectroscopy on SnIP. A) Raman spectrum of SnIP measured at room temperature. Modes of SnIP have been calculated after structure optimization, based on GGA-D2 functionals within the framework of DFT theory. Modes for B), 3D bulk-SnIP (red lines), C) a single strand of SnIP (blue), and D) a 1D polymer nano-rod (green) are given. Selected modes including wavenumbers and their atomic movement are shown above. No significant shifts can be observed for both models compared with the experimental data.
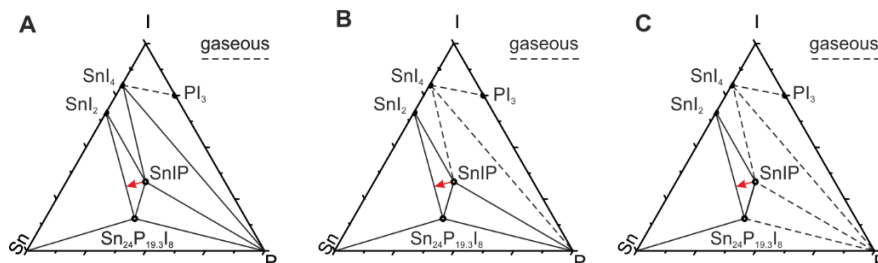
Figure S7a. Phase diagram of the ternary system Sn/P/I and phase relations of SnIP at different temperatures: A) $T \geq 500$ K, B) $T \geq 626$ K, C) $T \geq 703$ K.
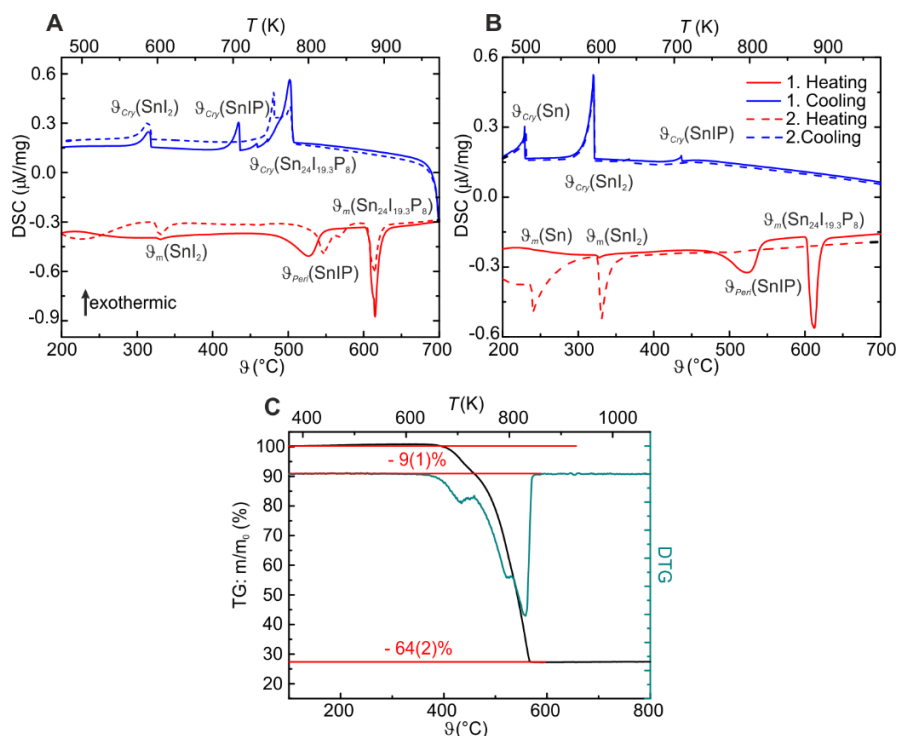
Figure S7b. Thermal analysis of SnIP. A) and B), Differential scanning calorimetry of SnIP in the temperature range from ambient temperature to A) 973 K and B) 1273 K (relevant temperature range extracted up to 973 K) showing the peritectic decomposition of SnIP at 740(2) K forming $Sn_{24}P_{19.3}I_8$ and melt of $Sn_{24}P_{19.3}I_8$.at 873(2) K. C) Differential thermal analysis combined with thermogravimetry was performed for SnIP. SnIP decomposes incongruently slightly above 600 K according to the brutto formula: $SnIP(s) \rightarrow 0.63\ Sn(s,l) + 0.13\ SnI_4(g) + 0.24\ SnI_2(g) + 0.25\ P_4(g)$. β-Sn remains as solid residue after this treatment.
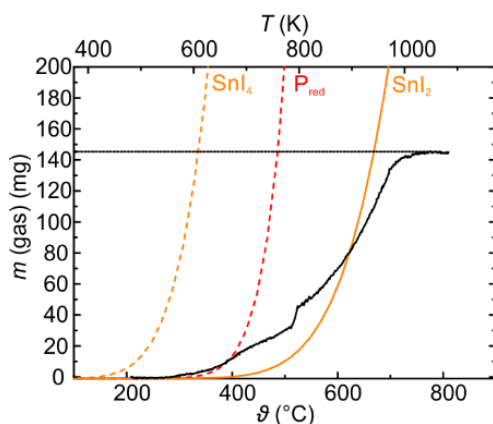
Figure S7c. High temperature gas phase balance measurement of SnIP (black line), in comparison with the theoretical mass loss of SnI_4 (orange dotted line), red phosphorus (red dotted line) and SnI_2 (solid orange line), calculated from the respective equilibrium pressures of gaseous species and under assumption of an ideal gas behavior within the defined measurement ampoule volume. The gas mass above the solid residue is plotted against the temperature.
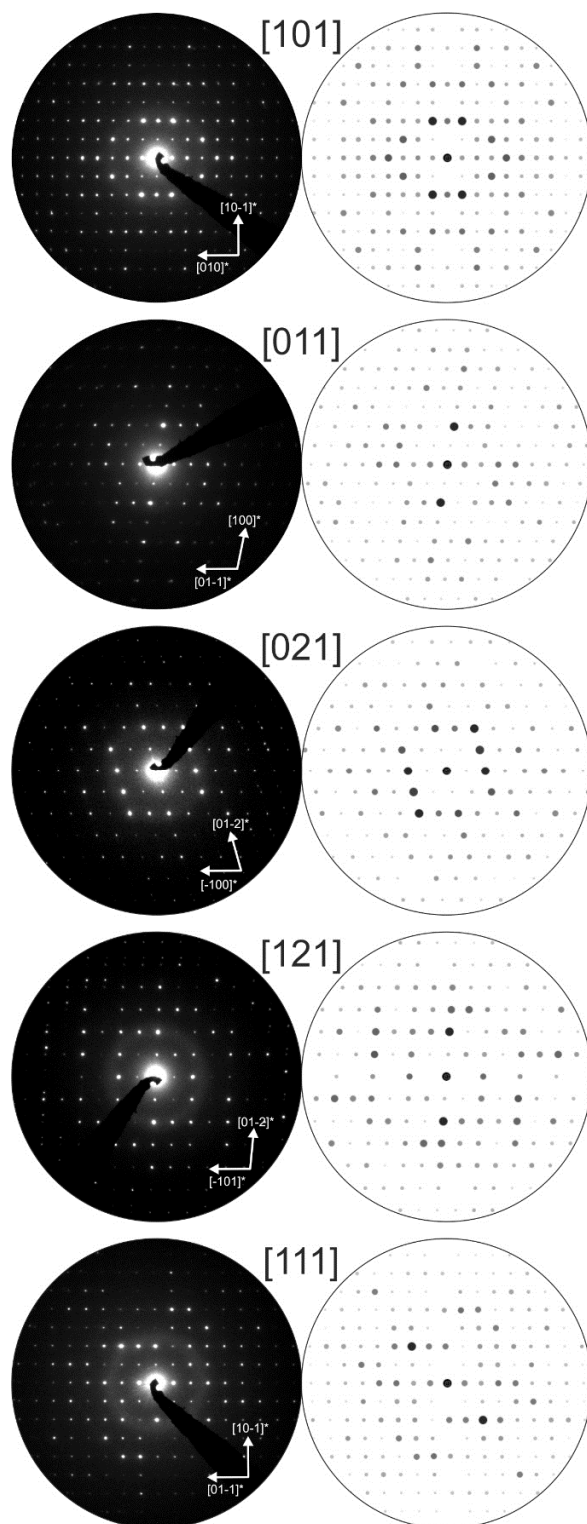
Figure S8. Precession electron diffraction patterns with the zone axis of [101], [011], [021], [121] and [111] (left) and the calculated intensities of the respective pattern (right).
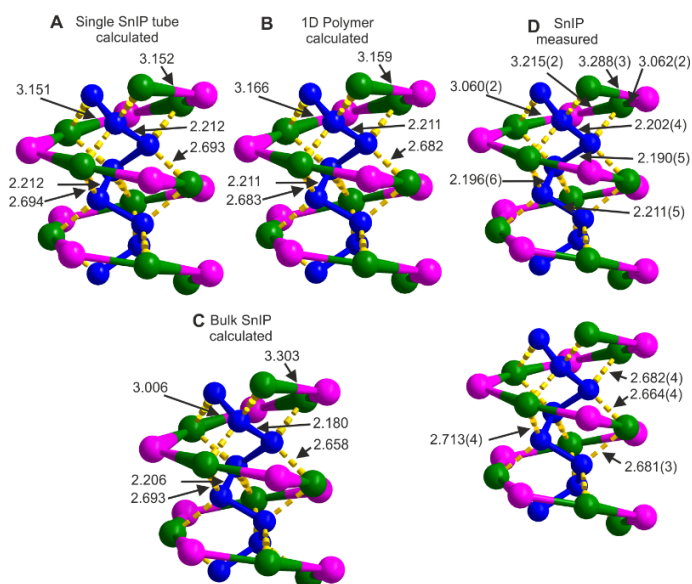
Figure S9. Double helical structure sections of SnIP. Data are presented for 3D-bulk, a single strand SnIP and a 1D polymer of the SnIP helix, derived from DFT calculations after structure optimization. Structure optimization is based on the HSE06 functional. Selected calculated bond lengths (Å) are given for single-rod SnIP A), a 1D model of the SnIP helix B), the calculated bulk SnIP C), and the experimental 3D-bulk SnIP D). Calculated values of bond length do not differ significantly from experimentally found values.
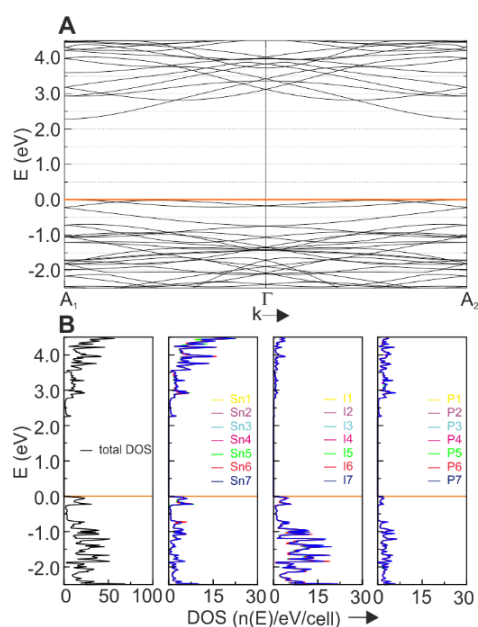
Figure S10. Band structure and DOS of the 1D Polymer model of SnIP (HSE06). The band gap is 2.28 eV which is in perfect agreement to the value found for the single strand

model as shown in Figure 2 B) and D). The path above is along the direction of the helix being the only possible way in a one-dimensional model.

Table S1. Crystallographic data, measurement and refinement parameters of SnIP crystal at 298 K. $Z = 14$.

Empirical formula	SnIP
Data collection	IPDS-2T
Pearson Symbol	mP42
Space group	$P2/c$ (13)
Formula weight [g mol^{-1}]	276.6
Crystal shape	Needle
Crystal colour	Black, dark red
Unit cell dimensions [Å]	$a = 7.934(2)$
	$b = 9.802(3)$
	$c = 18.439(9)$
	$\beta = 110.06(5)$
Cell Volume [nm^3]	1.347
Calculated density [g cm^{-3}]	4.77
Crystal size [µm^3]	$3 \times 5 \times 300$
Transm. ratio [max / min]	1.69
Detector distance [mm]	100
Exposure time [s]	120
ω range; increment [°]	0 - 180°, 0.5°
Integr. Param. [A, B, EMS]	22.1, -2.1, 0.044
Absorption coefficient [mm^{-1}]	14.8
F(000)	1652
θ range for data collection [°]	2.1 - 29.1
Range in *hkl*	±10, ±13, 0 - 25
Total no. Reflections	6769
Independent reflections / R_{int}	3567 / 0.086
Reflections with $I \geq 3\sigma(I)$ / R_σ	1651 / 0.111
Data / parameters	3567 / 98
Goodness-of-fit on F^2	1.01
$R1$ / $\omega R2$ for $I > 3\sigma(I)$)	0.0407 / 0.0769
$R1$ / $\omega R2$ (all data)	0.1021 / 0.0840
Extinction coefficient	150(30)
Largest diff. peak / hole [e Å^{-3}]	1.88 / -1.98

Table S2. Atomic coordinates, isotropic displacement parameters and Mulliken population analysis data (MPA) of SnIP.

Atom	*Wyckoff*	x (a)	y (b)	z (c)	U_{eq} [Å²]	MPA
Sn1	4*g*	0.03676(13)	0.48355(11)	0.39057(6)	0.0259(4)	0.47
Sn2	4*g*	0.16001(14)	0.00706(11)	0.17477(6)	0.0253(4)	0.49
Sn3	4*g*	0.49338(13)	0.22508(11)	0.07377(5)	0.0235(3)	0.51
Sn4	2*f*	1/2	0.61069(15)	1/4	0.0218(5)	0.48
I1	4*g*	0.01956(15)	0.19522(11)	0.46722(6)	0.0335(4)	-0.32
I2	4*g*	0.41459(14)	0.54599(11)	0.07876(5)	0.0278(4)	-0.31
I3	4*g*	0.61321(15)	0.05777(11)	0.64272(6)	0.0347(4)	-0.33
I4	2*e*	0	0.68160(14)	1/4	0.0303(5)	-0.32
P1	4*g*	0.1978(5)	0.3164(4)	0.31971(19)	0.018(1)	-0.17
P2	4*g*	0.2607(5)	0.4030(3)	0.22211(19)	0.017(1)	-0.16
P3	4*g*	0.3836(5)	0.2179(4)	0.19604(18)	0.017(1)	-0.16
P4	2*e*	0	1/6	1/4	0.018(2)	-0.16

U_{eq} is defined as one third of the trace of the orthogonalised U_{ij} tensor.

Table S3. Anisotropic displacement parameters of SnIP [Å²].

Atom	U_{11}	U_{22}	U_{33}	U_{12}	U_{13}	U_{23}
Sn1	0.0221(5)	0.0262(6)	0.0270(5)	0.0015(4)	0.0052(4)	−0.0089(4)
Sn2	0.0290(6)	0.0172(5)	0.0340(5)	−0.0049(4)	0.0165(4)	−0.0057(4)
Sn3	0.0262(5)	0.0271(6)	0.0188(5)	−0.0033(4)	0.0096(4)	−0.0025(4)
Sn4	0.0250(8)	0.0172(7)	0.0232(7)	0	0.0082(6)	0
I1	0.0401(6)	0.0302(6)	0.0252(5)	−0.0057(5)	0.0046(4)	0.0010(4)
I2	0.0389(6)	0.0250(6)	0.0211(5)	0.0026(4)	0.0123(4)	0.0031(4)
I3	0.0446(7)	0.0206(6)	0.0365(6)	−0.0031(5)	0.0107(5)	0.0038(4)
I4	0.0350(8)	0.0165(7)	0.0407(8)	0	0.0148(7)	0
P1	0.017(12)	0.017(2)	0.023(2)	0.002(2)	0.009(2)	−0.001(1)
P2	0.015(2)	0.013(2)	0.024(2)	−0.001(1)	0.010(1)	0.001(1)
P3	0.018(2)	0.017(2)	0.019(2)	−0.003(2)	0.009(1)	0.0003(1)
P4	0.016(3)	0.014(3)	0.027(3)	0	0.012(2)	0

Table S4. Interatomic distances [Å] for the first coordination shell of SnIP. Standard deviations are given in parentheses.

Sn1	P2	1x	2.673(4)	I2	Sn4	1x	3.060(2)	P1	P2	1x	2.197(6)
	P1	1x	2.678(4)		Sn3	1x	3.215(2)		P4	1x	2.211(5)
	I4	1x	3.171(2)		P2	1x	3.558(4)		Sn1	1x	2.678(4)
	I1	1x	3.184(2)		I2	1x	3.713(2)		Sn3	1x	2.713(4)
					Sn1	1x	3.738(3)				
Sn2	P3	1x	2.664(4)		P1	1x	3.752(4)	P2	P3	1x	2.170(5)
	P4	1x	2.681(3)		Sn3	1x	3.858(2)		P1	1x	2.197(6)
	I1	1x	3.119(2)		Sn1	1x	3.861(2)		Sn1	1x	2.673(4)
	I3	1x	3.288(3)		P3	1x	3.930(4)		Sn4	1x	2.710(0)
					P2	1x	3.949(4)				
Sn3	P3	1x	2.682(4)					P3	P2	1x	2.190(5)
	P1	1x	2.713(4)	I3	Sn3	1x	3.062(2)		P3	1x	2.202(4)
	I3	1x	3.062(2)		Sn2	1x	3.288(3)		Sn2	1x	2.664(4)
	I2	1x	3.215(2)		P3	1x	3.580(4)		Sn3	1x	2.682(4)
					P4	1x	3.742(3)				
Sn4	P2	2x	2.710(4)		Sn2	1x	3.891(2)	P4	P1	2x	2.211(5)
	I2	2x	3.060(2)		P1	1x	3.933(4)		Sn2	2x	2.681(3)
					I4	1x	3.961(2)		P2	2x	3.263(5)
I1	Sn2	1x	3.119(2)						P3	2x	3.547(5)
	Sn1	1x	3.184(2)	I4	Sn1	2x	3.171(2)				
	P3	1x	3.569(4)		P2	2x	3.568(4)				
	P1	1x	3.667(5)		Sn2	2x	3.863(2)				
	Sn3	1x	3.887(2)		P1	2x	3.943(4)				
	P4	1x	3.965(2)		I3	2x	3.961(2)				
	P2	1x	3.994(4)								

Table S5. [119]Sn Mößbauer spectroscopic data for tin and tin phosphides. Standard deviations are given in parentheses.

Compound	Isomer shift δ [mm·s^{-1}]	Line width Γ [mm·s^{-1}]	Quadrupole splitting ΔE_Q [mm·s^{-1}]	T [K]	Reference
β-Sn	2.6				(*65*)
SnP	2.7				(*65*)
SnP$_3$	2.43(3), 2.59(3)	0.78(2)	0.68	298	(*66*)
Sn$_4$P$_3$	2.30(3), 2.65(3), 2.83(3), 2.97(3)	0.79	0.80	298	(*66*)
Sn$_3$P$_4$	1.62(3), 1.70(3), 2.06(3), 2.34(3), 2.96(3), 3.13(3)	0.77(2)	0.99	298	(*66*)
SnI$_4$	1.5				(*65*)
SnI$_2$	3.9				(*65*)
SnIP	3.25(1)		1.30(1)	298	This work
SnIP	3.37(1)		1.37(1)	77	This work

Table S6. Calculated shifts in the Fermi contact density $\Delta\rho(0)$ for experimentally known [119]Sn isomer shifts for some Sn containing compounds.

	δ [mm·s^{-1}]	$\Delta\rho(0)$/[e/au^3]	Reference
BaSnO$_3$	0	0.0	(*65*)
SnO$_2$	0	0.2	(*65*)
SnS$_2$	1.3	4.1	(*65*)
α-Sn	2	7.4	(*65*)
Sn$_2$Co$_3$S$_2$	2.2	8.0	(*69*)
β-Sn	2.6	9.6	(*65*)
SnO	2.8	10.5	(*65*)
SnIP-1	3.4	14.0	This work
SnIP-2	3.4	13.9	This work
SnIP-3	3.4	14.1	This work
SnIP-4	3.4	14.0	This work
SnS	3.2	14.2	(*65*)
SnCl$_2$	4.0	17.7	(*65*)
SnCl$_2$	4.0	17.9	(*65*)

Table S7. Predicted lattice parameters from DFT-LDA calculations for completely substituted compounds *MXQ* for *M* = Pb, Sn, Ge, Si, *X* = F, Cl, Br, I, *Q* = P. An error of +/- 5 % for each value must be taken into account.

	distances helix *Q* [Å]				distances helix *MX* [Å]						
	*Q*3-*Q*3	*Q*2-*Q*3	*Q*1-*Q*2	*Q*4-*Q*1	*X*3-*M*2	*M*3-*X*3	*M*3-*X*2	*M*4-*X*2	*M*2-*X*1	*M*1-*X*1	*M*1-*X*4
PbIP	2.16	2.18	2.18	2.20	3.21	3.15	3.21	3.11	3.20	3.22	3.21
SnIP	2.20	2.19	2.20	2.21	3.29	3.06	3.21	3.06	3.12	3.18	3.17
GeIP	2.18	2.20	2.20	2.21	3.06	2.89	3.03	2.89	2.95	2.99	3.01
SiIP	2.19	2.21	2.21	2.21	3.07	2.78	3.00	2.82	2.82	2.97	2.91
PbBrP	2.16	2.17	2.18	2.19	3.09	2.98	3.03	2.96	3.01	3.04	3.03
SnBrP	2.17	2.18	2.19	2.19	2.98	2.88	2.97	2.89	2.93	2.94	2.98
GeBrP	2.18	2.18	2.19	2.19	2.92	2.69	2.89	2.73	2.74	2.85	2.82
SiBrP	2.20	2.20	2.20	2.20	3.18	2.49	2.94	2.65	2.47	3.04	2.61
PbClP	2.17	2.17	2.17	2.18	2.99	2.85	2.92	2.86	2.87	2.95	2.90
SnClP	2.17	2.17	2.18	2.18	2.88	2.75	2.85	2.79	2.79	2.83	2.86
GeClP	2.17	2.17	2.19	2.19	2.54	2.66	2.70	2.64	2.95	2.49	2.95
SiClP	2.16	2.18	2.20	2.21	2.27	2.75	2.44	2.58	3.35	2.24	3.03
PbFP	2.18	2.18	2.17	2.15	2.92	2.55	2.87	2.38	2.29	3.50	2.35
SnFP	2.19	2.18	2.17	2.16	2.51	2.49	2.90	2.39	2.15	3.24	2.39
GeFP	2.19	2.16	2.17	2.18	1.88	3.40	2.01	2.33	3.55	1.86	3.06
SiFP	2.18	2.17	2.18	2.18	1.67	3.47	1.82	2.28	3.62	1.66	3.23

Movie S1. Bending of SnIP crystals (30MB max Quicktime movie *.mov)
As prepared single crystals of SnIP were bend with a needle observed by a common light microscope. The crystal has a length of approx. 1500 μm and a thickness of 10 μm. (Film link here)

Movie S2. Reappearance of SnIP crystals from suspension (30MB max Quicktime movie *.mov). SnIP can be suspended in selected solvents.

3.4   Inorganic Semiconducting Compounds

Tom Nilges, Daniela Pfister, **Claudia Ott**, Konrad Schäfer, Maximilian Baumgartner and Richard Weihrich

[1] Department of Chemistry, Technical University of Munich, Lichtenbergstr. 4, 85748 Garching b. München, Germany

[2] Institut für Materials Resource Management, Universität Augsburg, Universitätsstr. 1, 86159 Augsburg, Germany

The patent "Inorganic Semiconducting Compounds" was filed in October 2015 by the Technical Univerity of Munich and published in January 2017.

The invention in this patent concerns a class of double helical semiconductors that can be synthesized without the need for an external template or complex precursors. The described compounds consist of a 1:1:1 ratio of group 14 : group 15 : group 17 elements or doped variants of those. This can be summarized in an easy compound formula 2 or a more advanced variant of it 3

$$M_{1-x}^A M_x^B X_{1-y}^A X_y^B Q_{1-z}^A Q_z^B \tag{2}$$

$$(M_{1-x}^A M_x^B)_{1-3m} M_{2m}^D X_{1-y}^A X_y^B (Q_{1-z}^A Q_z^B)_{1-2n} Q_n^D \tag{3}$$
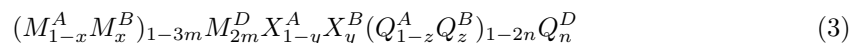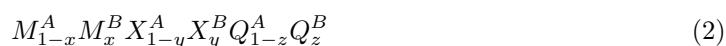
With M^A, M^B, M^D, X^A, X^B, Q^A, Q^B, Q^D, x, y, z, n and m defined as follows:

M^A	Si, Ge, Sn or Pb
M^B	Si, Ge, Sn or Pb or combinations thereof (not containing M^A)
x	0 - 0.50, prefereably 0 - 0.15, more prefereably 0 - 0.05

X^A	F, Cl, Br or I
X^B	F, Cl, Br or I or combinations thereof (not containing X^A)
y	0 - 0.50, prefereably 0 - 0.15, more prefereably 0 - 0.05
Q^A	P, As, Sb or Bi
Q^B	P, As, Sb or Bi or combinations thereof (not containing Q^A)
z	0 - 0.50, prefereably 0 - 0.15, more prefereably 0 - 0.05
M^D	Al, Ga or In or combinations thereof
Q^D	S, Se or Te or combinations thereof
m	0 - 0.03, prefereably 0 - 0.01, more prefereably 0 - 0.005
n	0 - 0.1, prefereably 0 - 0.05, more prefereably 0 - 0.01, most preferably 0 - 0.005

The patent further concerns nanomaterials built up by the described compounds, the process of preparation and its applications. Described compounds are arranged on a molecular level in form of double helices. The negatively charged inner helix $^1_\infty[Q^{A\text{-}}]$ is surrounded by a second but positively charged helix $^1_\infty[(M^A X^A)^+]$ to form a double helical nanotube, nanowire or nanofiber. A single double helix exhibits a diameter in the range of 1 to 10 nm. Attractive forces in between those structures were determined as weak van der Waals interactions, which allow easy and efficient delamination. The aspect ratio of a needle built up by an arrangement of double helices can be described as the ratio of the nanowire-length and its diameter. Here described compounds usually show aspect ratios in the order of several hundreds. Mechanical or solvent assisted delamination of such needles allows the formation of thin films either on a substrate or self-supporting.

Calculations showed the compounds to be semiconductors with different bandgaps for bulk and single non-coordinated nanotubes in the magnitude of around 2 eV.

Weak van der Waals interactions between the double helices account for high mechanical flexibility and elasticity while showing extraordinary stability. This allows SnIP to be used in any kind of flexible devices such as (quantum-dot) solar cells, thermoelectric materials/devices, inorganic-organic hybrid thermoelectrical materials/devices, sensor applications, optical devices and photocatalysts (eg. for water splitting). Compared to the materials used in such devices the

new material class is comparatively abundant, cheap, easy to synthesize and less toxic.

The synthesis and delamination techniques are described in chapter 2.2 on page 14, characterization techniques in chapter 2.3 on page 20.

Author contributions: C.O. and D.P. found and characterized the new compound, K.S. helped solve the structure, M.B. and R.W. conducted the quantumchemical calculations, C.O., D.P. and T.N. delivered data to write the claim. All authors discussed about the findngs and the claim.

Vossius & Partner
Patentanwälte Rechtsanwälte mbB
Siebertstr. 4
81675 München

New EP patent application
Technische Universität München
Our ref.: Y1784 EP

Inorganic Semiconducting Compounds

The invention concerns a new class of semiconducting inorganic compounds which, due to the arrangement of their constituting atoms in the form of a double helix, can be advantageously provided as nanomaterials, such as nanowires. The inorganic semiconducting compounds can be used in a variety of applications, in particular in semiconductive devices for the conversion of energy, including solar cells or thermoelectric devices, in sensor devices, for the provision of displays, or as photocatalysts.

With a view to the efficient provision of nanoscale materials, the synthesis of helical structures is of substantial interest because of the useful physical and electronic properties that can be expected of materials showing such structures (Zhao, M. Q., et al., *Nanoscale* 2014, 6, 9339). However, while the synthesis of double helical assemblies from organic substances has been shown to be feasible due to the variable shapes and complex interactions of such substances, corresponding inorganic structures are much more difficult to accomplish. The lack of directed inter- and intramolecular interactions in the case of simple atoms renders a self-assembly into purely inorganic double helices more challenging. In the case of carbon-based inorganic materials with (double) helical structures like carbon nano tubes (Iijima, S. et al., *Nature* 1993, 363, 603), a large quantity of unwanted byproducts (single helical or non-coiled fibers) renders a characterization rather challenging. A complex carbon containing inorganic double helix system $[(CH_3)_2NH_2]K_4[V_{10}O_{10}(H_2O)_2(OH)_4-(PO_4)_7]\cdot 4H_2O$, has been reported (Soghomonian et al., *Science* 1993, 259, 1596), where a double helix is formed by metal oxo species. Structures containing simple atomic helices are predicted for Li and P (Ivanov, A. S., et al., *Angew. Chem. Int. Ed.* 2012, 51, 8330). For the preparation of micro-sized and even more complicated nano-sized inorganic, carbon-free helical structures in bottom-up and top-down approaches, significant efforts are required (Zhao, M. Q., et al., *Nanoscale* 2014, 6, 9339; Liu, L. et al., *Nanoscale* 2014, 6, 9355). Molecular self-assembly or nano-particle self-assembly strategies or templating are bottom-up strategies which allowed for instance the preparation of helical structures containing CdS or GaN (Sone, E.D. et al., *Small* 2005, 1, 694; Goldberger, J. et al., *Nature* 2003, 422, 599). In none of the mentioned cases a single-atomic helical chain is realized. Top-down strategies were reported based on solution-chemical procedures e.g. for the formation of alloyed Au/Ag nanowires (Wang, Y., *JACS* 2011, 133, 20060), or based on the use of Zintl compound

precursors like NaSi to form Si microtubes (Morito, H., *Angew. Chem. Int. Ed.* 2010, 49, 3628).

Particularly challenging is the design and the preparation of nanoparticles in the sub-5nm-regime. A DNA nano-casting approach has been proposed to prepare 3D inorganic nanostructures with predefined dimensions, shapes and surfaces (Sun, W. et al., *Science* 2014, 346, 6210). Here, linear fragments of DNA are used to provide predefined molds wherein nanoparticles are formed.

Quantum confined semiconductors with dimensions on a nanometer scale are widely used. Solar cells, thermoelectric devices, optical devices and sensors are key applications where semiconducting materials of sizes significantly smaller than 50 nm are implemented (Graetzel, M., et al., *Nature* 2012, 488, 304; Boukai, A. I.et al., *Nature* 2008, 451, 168). A recent all solid state dye-sensitized $CsSnI_3$ based solar cell reached efficiencies larger than 10% (Chung, I. et al., *Nature* 2012, 485, 486). Furthermore, thermoelectric devices with a figure of merit larger than 2, realized by nano-sized precipitates of lead telluride based compounds were reported (Biswas, K., et al., *Nature* 2012, 489, 414). However, in both cases toxic, less abundant, and/or expensive elements and complex nano-structuring are needed to provide efficient nano-structured materials for such applications.

The present invention provides a class of semiconducting compounds showing a structure wherein the constituting atoms arrange themselves in the form of a double helix without the need for an external template, or for complex precursor structures. These compounds combine one or more elements of group 14, one or more elements of group 15 and one or more elements of group 17 of the periodic table in (molar) amounts such that the resulting stoichiometry can be schematically represented as (group 14 element(s)): (group 15 element(s)):(group 17 element(s)) = 1:1:1. However, changes in the electronic properties of these compounds via incorporation of dopant elements of group 13 or 16 are also encompassed by the invention. Compounds of group 14/15/17 elements with other stoichiometries, i.e. $Ge_{38}E_8I_8$ with E=P, As, Sb (von Schnering, H.G. et al., *Angew. Chem.* 1972, 84, 30, and von Schnering, H.G., *Z. Anorg. Chem.* 1973, 395, 223), $Sn_{24}P_{19.3}I_8$ and $Sn_{24}As_{19.3}I_8$ (Shatruk M. M., et al., *Inorg. Chem.* 1999, 38, 3455) had been reported as taking the form of a type I clathrate.

Thus, in a first embodiment, the invention provides a compound of formula (Ia):

$$M^A_{1-x} M^B_x X^A_{1-y} X^B_y Q^A_{1-z} Q^B_z \qquad \text{(Ia)},$$

wherein:

M^A is an element selected from Si, Ge, Sn, and Pb,

M^B is an element selected from Si, Ge, Sn, and Pb and from combinations thereof such that M^B is not the same as M^A and does not contain M^A, and

x is 0 to 0.50;

X^A is an element selected from F, Cl, Br and I,

X^B is an element selected from F, Cl, Br and I and from combinations thereof such that X^B is not the same as X^A and does not contain X^A, and

y is 0 to 0.50;

Q^A is an element selected from P, As, Sb and Bi,

Q^B is an element selected from P, As, Sb and Bi and from combinations thereof such that Q^B is not the same as Q^A and does not contain Q^A, and

z is 0 to 0.50.

In a further embodiment, the invention provides a compound which represents a doped variant of the compound of formula (Ia), and which further contains:

(i) an element M^D, selected from Al, Ga, In and from combinations thereof, in a maximum amount of 10 mol% based on the total molar amount of M^A and M^B, which element M^D may partially replace M^A and/or M^B in formula (Ia); and/or

(ii) an element Q^D, selected from S, Se, Te and from combinations thereof, in a maximum amount of 10 mol% based on the total molar amount of X^A, X^B, Q^A and Q^B, which element Q^D may partially replace X^A, X^B, Q^A and/or Q^B in formula (Ia).

As further preferred aspects, the present invention provides nanomaterials, such as a nanowire, comprising or consisting of the compound in accordance with the invention.

Still further aspects concern processes for the preparation of the compound of the invention or of the above nanomaterials.

Finally, the invention concerns the application of the compounds or the nanomaterials in accordance with the invention in particular as semiconductors in electrical, electronic, optical or optoelectronic devices, or as catalysts, in particular photocatalysts.

The compounds in accordance with the invention are either compounds of formula (Ia), or doped variants thereof. Thus, unless indicated otherwise in specific context, any reference herein to a compound or compounds in accordance with the invention encompasses the compounds of formula (Ia), the doped variants thereof and the preferred embodiments of the compounds of formula (Ia) and of the doped variants that will be illustrated below.

The compounds in accordance with the invention are provided in crystalline form, and it has been surprisingly found that the atoms constituting these compounds are arranged in the form of a double helix. Characteristics of this double helix structure will also be discussed in further detail below.

Essential components of the compounds in accordance with the invention are the elements M^A, X^A and Q^A.

M^A is an element of group 14 of the periodic table, which is selected from Si, Ge, Sn and Pb, which is preferably selected from Ge, Sn and Pb, and which is more preferably Sn. As further indicated in formula (Ia), it is also possible in the compounds in accordance with the invention that more than one element of group 14 is present, i.e. an element M^A selected from Si, Ge, Sn and Pb or its preferred embodiments, and an element M^B selected from Si, Ge, Sn and Pb and from combinations thereof, preferably selected from Ge, Sn and Pb and from combinations thereof. It will be apparent that in this case M^B is not the same as M^A, or, if M^B represents a combination of elements, that the combination does not contain M^A. Thus, in the preferred case where M^A is Sn, it is also preferred that M^B, if present, is selected from Si, Ge, Pb, and from a combination thereof, more preferred that M^B, if present, is selected from Ge, Pb, and from a combination of the two, and most preferably M^B is Pb. As will be understood by the skilled reader, the optional element(s) M^B replace the element M^A in the compounds in accordance with the invention by occupying sites in the crystal structure which would be occupied by M^A in the absence of M^B. The ratio of the optional element(s) M^B is defined by the index x in formula (Ia), which is 0 (i.e. element(s) M^B are absent) to 0.50 (i.e. a maximum of 50 % of the sites in the crystal structure which would be occupied by the element M^A can be occupied by M^B). Preferably, x is 0 to 0.15, more preferably 0 to 0.05.

X^A is an element of group 17 of the periodic table, which is selected from F, Cl, Br and I, preferably from Br and I, and which is particularly preferably I. As further indicated in formula (Ia), it is also possible in the compounds in accordance with the invention that more than one element of group 17 is present, i.e. an element X^A selected from F, Cl, Br and I or its preferred embodiments, and an element X^B selected from F, Cl, Br and I, and from

combinations thereof, preferably form Br and I. It will be apparent that in this case X^B is not the same as X^A, or, if X^B represents a combination of elements, that the combination does not contain X^A. Thus, in the particularly preferred case where X^A is I, it is preferred that X^B, if present, is selected from F, Cl, and Br and from combinations thereof. As will be understood by the skilled reader, the optional element(s) X^B replace the element X^A in the compounds in accordance with the invention by occupying sites in the crystal structure which would be occupied by X^A in the absence of X^B. The ratio of the optional element(s) X^B is defined by the index y in formula (Ia), which is 0 (i.e. element(s) X^B are absent) to 0.50 (i.e. a maximum of 50 % of the sites in the crystal structure which would be occupied by the element X^A can be occupied by X^B). Preferably, y is 0 to 0.15, more preferably 0 to 0.05.

Q^A is an element of group 15 of the periodic table, which is selected from P, As, Sb and Bi, preferably from P and As, and which is particularly preferably P. As further indicated in formula (Ia), it is also possible in the compounds in accordance with the invention that more than one element of group 15 is present, i.e. an element Q^A selected from P, As, Sb and Bi or its preferred embodiments, and an element Q^B selected from P, As, Sb and Bi, and from combinations thereof, preferably from P and As. It will be apparent that in this case Q^B is not the same as Q^A, or, if Q^B represents a combination of elements, that the combination does not contain Q^A. Thus, in the particularly preferred case where Q^A is P, it is preferred that Q^B, if present, is selected from As, Sb and Bi, and from combinations thereof. As will be understood by the skilled reader, the optional element(s) Q^B replace the element Q^A in the compound in accordance with the invention by occupying sites in the crystal structure which would otherwise be occupied by Q^A in the absence of Q^B. The ratio of the optional element(s) Q^B is defined by the index z in formula (Ia), which is 0 (i.e. element(s) Q^B are absent) to 0.50 (i.e. a maximum of 50 % of the sites in the crystal structure which would be occupied by the element Q^A can be occupied by Q^B). Preferably, z is 0 to 0.15, more preferably 0 to 0.05.

Thus, in the compounds in accordance with the invention, it is generally preferred that x, y and z are 0 to 0.15, and more preferred that x, y and z are 0 to 0.05. Moreover, it is generally preferred that at least one of x, y and z is 0 (i.e. at least one of M^B, X^B and Q^B is absent), and more preferred that at least two of x, y and z are 0. Most preferably, y and z are 0.

As noted above, the present invention also provides compounds containing elements from group 13 or 16 of the periodic table as dopant elements which are present in small amounts to modify the electronic structure, e.g. to increase the mobility of the charge carriers of the compound of formula (Ia). Thus, the invention also provides a doped variant of the compound of formula (Ia), which further contains:

5

(i) an element M^D, selected from Al, Ga, In and from combinations thereof, in a maximum amount of 10 mol% based on the total molar amount of M^A and M^B, which element M^D may partially replace M^A and/or M^B in formula (Ia); and/or

(ii) an element Q^D, selected from S, Se, Te and from combinations thereof, in a maximum amount of 10 mol% based on the total molar amount of X^A, X^B, Q^A and Q^B, which element Q^D may partially replace X^A, X^B, Q^A and/or Q^B in formula (Ia).

To that extent, the doped variants of the compound of formula (Ia) provided by the present invention can be represented by the following formula (Ib):
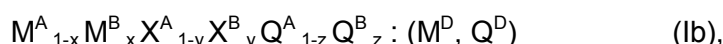
$$M^A_{1-x}M^B_xX^A_{1-y}X^B_yQ^A_{1-z}Q^B_z : (M^D, Q^D) \qquad \text{(Ib)},$$

wherein M^A, M^B, X^A, X^B, Q^A, Q^B, M^D, Q^D, x, y and z, and the amount of M^D and of Q^D are as defined above, including all preferred embodiments, and the notation of M^D and Q^D in brackets after the colon in the formula indicates that either M^D, or Q^D, or a combination of M^D and Q^D are present as dopant in the compound of the formula $M^A_{1-x}M^B_xX^A_{1-y}X^B_yQ^A_{1-z}Q^B_z$.

The doped variant of the compound of formula (Ia) consists of M^A, optionally M^B, X^A, optionally X^B, Q^A, and optionally Q^B, together with M^D and/or Q^D. It is preferred for the doped variant that M^D and Q^D are not present simultaneously in the same compound, i.e. that either M^D or Q^D is contained. These preferred doped variants can be represented by formulae (Ic) and (Id):
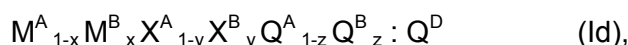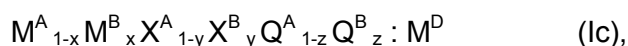
$$M^A_{1-x}M^B_xX^A_{1-y}X^B_yQ^A_{1-z}Q^B_z : M^D \qquad \text{(Ic)},$$

$$M^A_{1-x}M^B_xX^A_{1-y}X^B_yQ^A_{1-z}Q^B_z : Q^D \qquad \text{(Id)},$$

wherein M^A, M^B, X^A, X^B, Q^A, Q^B, M^D, Q^D, x, y and z, and the amount of M^D and of Q^D are as defined above, including all preferred embodiments.

In terms of a convenient synthesis of the compounds in accordance with the invention, it is preferred that M^B and M^D are not present simultaneously in the doped variant of the compound in accordance with the invention, i.e. that x is 0 when M^D is present. Similarly, it is preferred that X^B or Q^B and Q^D are not present simultaneously, i.e. that y and z are 0 when Q^D is present.

It is more preferred for the doped variant that M^B, X^B and Q^B are not present. Thus, particularly preferred as the doped variant of the compound in accordance with the invention are a compound consisting of M^A, X^A, Q^A and M^D and a compound consisting of M^A, X^A, Q^A and Q^D. These particularly preferred doped variants can be represented by formulae (Ie) and (If):

$$M^A X^A Q^A : M^D \qquad \text{(Ie)},$$

$$M^A X^A Q^A : Q^D \qquad \text{(If)},$$

wherein M^A, X^A, Q^A, M^D, and Q^D are as defined above, including all preferred embodiments.

In the doped variant of the compound in accordance with the invention, it is preferred that M^D, if present, replaces M^A and/or M^B in the compound of formula (Ia) by occupying sites in the crystal structure of the compound of formula (Ia) which would be occupied by M^A and optionally M^B in the absence of M^D. Similarly, it is preferred that Q^D, if present, replaces X^A, X^B, Q^A, and/or Q^B in the compound of formula (Ia) by occupying sites in the crystal structure of the compound of formula (Ia) which would be occupied by X^A, X^B, Q^A and/or Q^B in the absence of Q^D. Such a replacement is also preferred for the compounds of formulae (Ib) to (If), where M^D would replace sites occupied by M^A and/or M^B in the structure indicated before the colon, and/or Q^D would replace sites occupied by X^A, X^B, Q^A and/or Q^B in the structure indicated before the colon.

The element M^D is present in a maximum amount of 10 mol% based on the total molar amount of M^A and M^B in the doped variant of the compound of formula (Ia), including the preferred formulae of the doped variant illustrated above. Preferably, M^D is present in a maximum amount of 5 mol%, and more preferably in a maximum amount of 1 mol%. The element Q^D is present in a maximum amount of 10 mol% based on the total molar amount of X^A, X^B, Q^A and Q^B in the doped variant of the compound of formula (Ia), including the preferred formulae of the doped variant illustrated above. Preferably, Q^D is present in a maximum amount of 5 mol%, and more preferably in a maximum amount of 1 mol%.

In a preferred embodiment, the compounds in accordance with the present invention are compounds of the following formula (II). As will be appreciated, formula (II) encompasses compounds of formula (Ia) as well as doped variants thereof.

$$(M^A_{1-x} M^B_x)_{1-3m} M^D_{2m} X^A_{1-y} X^B_y (Q^A_{1-z} Q^B_z)_{1-2n} Q^D_n \qquad \text{(II)},$$

In formula (II) M^A, M^B, X^A, X^B, Q^A, Q^B, M^D, Q^D, x, y and z are defined as for formula (Ia) and for the doped variant thereof, including all preferred definitions, i.e.:

M^A is an element selected from Si, Ge, Sn, and Pb, ,

M^B is an element selected from Si, Ge, Sn, and Pb and from combinations thereof, such that M^B is not the same as M^A and does not contain M^A, and

x   is 0 to 0.50, preferably 0 to 0.15, and more preferably 0 to 0.05;

X^A is an element selected from F, Cl, Br and I,

X^B is an element selected from F, Cl, Br and I and from combinations thereof such that X^B is not the same as X^A and does not contain X^A, and

y   is 0 to 0.50, preferably 0 to 0.15, and more preferably 0 to 0.05;

Q^A is an element selected from P, As, Sb and Bi,

Q^B is an element selected from P, As, Sb and Bi and from combinations thereof such that Q^B is not the same as Q^A and does not contain Q^A,

z   is 0 to 0.50, preferably 0 to 0.15, and more preferably 0 to 0.05;

M^D is an element selected from Al, Ga and In and from combinations thereof,

Q^D is an element selected from S, Se and Te and from combinations thereof,

and

m   is 0 to 0.03, preferably 0 to 0.01, and more preferably 0 to 0.005; and

n   is 0 to 0.1, preferably 0 to 0.05, more preferably 0 to 0.01, and most preferably 0 to 0.005.

Also for the compounds of formula (II), it is preferred that M^A is selected from Ge, Sn and Pb, and is more preferably Sn. M^B, if present, is preferably selected from Ge, Sn and Pb and from combinations thereof, and is more preferably Pb. X^A is preferably selected from Br and I, and is particularly preferably I. X^B, if present, is preferably selected from Br and I. Q^A is preferably selected from P and As, and is particularly preferably P. Q^B, if present, is preferably selected from P and As.

Thus, in the compounds in accordance with the invention, it is generally preferred that x, y and z are 0 to 0.15, and more preferred that x, y and z are 0 to 0.05. Moreover, it is generally

preferred that at least one of x, y and z is 0 (i.e. at least one of M^B, X^B and Q^B is absent), and more preferred that at least two of x, y and z are 0. Most preferably, y and z are 0.

Also for the compounds of formula (II), it is generally preferred that at least one of x, y and z is 0 (i.e. at least one of M^B, X^B and Q^B is absent), and more preferred that at least two of x, y and z are 0. Most preferably, y and z are 0.

Preferably, m and n should not both be > 0 in the same compound, i.e. at least one of m and n should be 0. However, it may be beneficial for certain applications if different compounds in accordance with the invention are combined, e.g. to form separate regions within a device, wherein m > 0 and n = 0 and wherein n > 0 and m = 0.

Moreover, in terms of a convenient synthesis of the compounds in accordance with the invention, it is preferred that M^B and M^D are not present simultaneously, i.e. that at least one of m and x in formula (II), and where applicable in the preferred formulae, is 0. Similarly, it is preferred that Q^B and Q^D are not present simultaneously, i.e. that at least one of n and z in formula (II), and where applicable in the preferred formulae, is 0.

As will be understood by the skilled reader, the indices 1-x, x, 1-y, y, 1-z, z, 1-3m, m, 1-2n, and n indicate the stoichiometry of the elements in the concerned compound. Thus, if a value of 0 is indicated for x, y, z, m or n, the element carrying the concerned index is not contained in the compound. In the compounds of the invention which do not contain a dopant element M^D or Q^D, the stoichiometric ratio of component M^A (and optionally M^B), component X^A (and optionally X^B), and component Q^A (and optionally Q^B), respectively, is 1:1:1. Thus, equimolar amounts of the components may be determined, typically within a deviation of not more than ± 10%, preferably not more than ± 5% for each component, taking into account the error margins resulting from unavoidable practical limitations in the precision of synthetic and analytic techniques. This stoichiometric ratio may be shifted to values of < 1 for M^A (and optionally M^B) if M^D is present and partially replaces M^A and/or M^B, or to values < 1 for X^A (and optionally X^B) and/or values < 1 for Q^A (and optionally Q^B) if Q^D is present and partially replaces X^A and optionally X^B and/or Q^A and optionally Q^B.

In line with the above and in accordance with preferred embodiments, the present invention provides compounds of formulae (IIIa), (IIIb), (IIIc) or (IIId):

$$M^A_{1-3m}M^D_{2m}X^A(Q^A_{1-z}Q^B_z)_{1-2n}Q^D_n \qquad \text{(IIIa),}$$

$$M^A_{1-3m}M^D_{2m}X^A_{1-y}X^B_yQ^A_{1-2n}Q^D_n \qquad \text{(IIIb)},$$

$$(M^A_{1-x}M^B_x)_{1-3m}M^D_{2m}X^AQ^A_{1-2n}Q^D_n \qquad \text{(IIIc)},$$

$$M^A_{1-3m}M^D_{2m}X^AQ^A_{1-2n}Q^D_n \qquad \text{(IIId)},$$
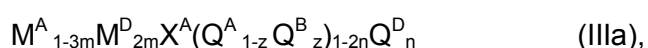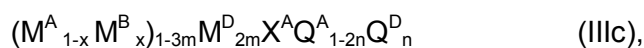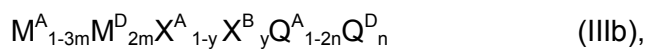
wherein M^A, M^B, M^D, X^A, X^B, Q^A, Q^B, x, y, z, m and n are defined as for formula (II), including the preferred embodiments.

In accordance with additional preferred embodiments, the present invention provides compounds of formulae (IVa), (IVb), (IVc) or (IVd):
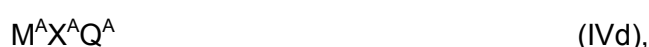
$$M^AX^A(Q^A_{1-z}Q^B_z) \qquad \text{(IVa)},$$

$$M^A(X^A_{1-y}X^B_y)Q^A \qquad \text{(IVb)},$$

$$(M^A_{1-x}M^B_x)X^AQ^A \qquad \text{(IVc)},$$

$$M^AX^AQ^A \qquad \text{(IVd)},$$

wherein M^A, M^B, X^A, X^B, Q^A, Q^B, x, y, and z are defined as for formula (II), including the preferred embodiments.

Preferred specific compounds in accordance with the invention can be selected from GeIP, GeBrP, GeClP, GeFP, GeIAs, GeBrAs, GeClAs, GeFAs, SnIP, SnBrP, SnClP, SnFP, SnIAs, SnBrAs, SnClAs, SnFAs, SnISb, SnBrSb, SnClSb, SnFSb, PbIP, PbBrP, PbClP, PbFP, PbIAs, PbBrAs, PbClAs, PbFAs, PbIBi, PbBrBi, PbClBi, and PbFBi, and more preferred specific compounds from GeIP, GeIAs, SnIP, SnBrP, SnClP, PbIP, PbBrP and PbClP. Particularly preferred is SnIP.

As indicated above, the compounds in accordance with the present invention are characterized by a crystal structure wherein the constituting atoms are arranged in the form of a double helix. In particular, two substructures can be identified in the crystalline compounds in accordance with the invention: a first, inner helical chain formed by a plurality of atoms of the element Q^A is surrounded by a second helical chain formed by a plurality of alternating atoms M^A and X^A. The first inner helix can also be described as $^1_\infty[Q^{A-}]$, the second helical chain as $^1_\infty[(M^AX^A)^+]$. This structure is illustrated in Fig. 1a and b for the

10

exemplary compound SnIP. Formal oxidation states of $(M^A)^{2+}$, $(X^A)^-$ and $(Q^A)^-$ can be assigned, such that the two helices are attracted to each other by the formal negative charges of the inner helix and the positive (net) charges of the surrounding helix. The resulting structure can also be referred to as a nanotube, with the double helix forming the tube wall. As explained above, the optional elements M^B, M^D, X^B, Q^B and/or Q^D can be incorporated to replace a part of the corresponding elements M^A, X^A and/or Q^A at their respective position in the double helix.

The diameter of the double helix or nanotube of the compounds in accordance with the invention is in the nanometer range, typically in the range of 0.5 to 10 nm, preferably 0.9 to 3 nm, and has been determined as 0.98 nm for the exemplary compound SnIP. The attractive bonds between the nanotubes have been found to be relatively weak van der Waals like bonds, such that the single nanotubes, or nanobundles combining a number of nanotubes, e.g. 2 or more, preferably 5 or more, and 100 or less, preferably 70 or less, can be conveniently provided. The convenient and efficient delamination of the compounds in accordance with the invention resulting from the double-helix structure, is a pronounced advantage since the provision of materials in the nanometer range usually involves laborious separation processes after synthesis.

As a result, the compounds of the present invention can be advantageously used to provide micro- or preferably nanomaterials. A micro- or nanomaterial in accordance with the invention comprises, and preferably consists of a compound in accordance with the invention. In this context, the term "micromaterial" refers to a material in a form where the smallest dimension is in the micrometer range. As an example, a microfiber can be mentioned, with a diameter in the micrometer range and a length of up to several mm, such as up to 5 mm. The term "nanomaterial" refers to a material in a form where at least one dimension is in the nanometer range. Preferred nanomaterials in the context of the invention are nanotubes or nanowires which comprise, or preferably consist of a compound in accordance with the invention. The term "nanowire" as a generic term is intended to encompass single nanotubes as well as bundles of nanotubes with an overall diameter in the nanometer range. For a nanowire, the diameter as the smallest dimension will be in the nanometer range, whereas the length of the nanowire can be substantially larger. With a view to their shape, the nanowires can alternatively be referred to as "nanofibers". However, due to the electronic properties of the compounds in accordance with the invention, and their suitability as semiconducting materials, the term "nanowire" was given preference. Further nanomaterials comprising or preferably consisting of one or more compounds in accordance with the invention are nanoparticles, where all dimensions are in the nanometer range.

Unless indicated otherwise in a specific context, the micrometer range as referred to herein is typically the range of > 100 nm to 100 µm, preferably 500 nm to 100 µm. Unless indicated otherwise in a specific context, the nanometer range as referred to herein is typically the range of 0.5 to 100 nm, preferably 0.7 to 50 nm.

Thus, in a particularly preferred aspect the present invention provides nanowires as elongated structures with a diameter in the nanometer range of typically 0.5 to 100 nm, preferably 0.7 to 50 nm, more preferably 0.7 to < 20 nm and most preferably 0.7 to < 10 nm, and a length of typically more than 100 nm, preferably more than 1 µm, and more preferably more than 10 µm. The upper limit of the length is not particularly restricted, but for most applications a length of up to 1 mm will be sufficient. In this context, it will be understood that the reference to the diameter of the nanowire relates to the diameter perpendicular to the longest axis of the nanowire, which diameter can be determined, e.g., from microphotographs. The nanowires provided in the context of the invention generally show uniform diameters, such that the diameter of a nanowire in accordance with the invention typically remains in the nanometer range along the whole length of the nanowire. If nevertheless a certain variation in the diameter is observed, the maximum diameter should be used as the representative value for the diameter, e.g. for the calculation of the aspect ratio. The aspect ratio, i.e. the ratio of the length of the nanowire to the diameter of the nanowire, is typically more than 100, and preferably more than 500. The upper limit of the aspect ratio is not particularly restricted, and nanowires with aspect ratios of up to 5000 can be conveniently provided using the synthetic methods described herein. However, generally an aspect ratio of 2000 or less, for most applications an aspect ratio of 1000 or less will be sufficient for the nanowires in accordance with the invention. The nanowires comprise a compound in accordance with the invention, and preferably consist of a compound in accordance with the invention, i.e. the compound is provided in the form of a nanowire.

Also encompassed as micro- or nanomaterials by the present invention are films comprising or consisting of the nanotubes or nanowires or both in accordance with the invention. The films are preferably nanofilms, i.e. films with a thickness in the nanometer range. The films can be supported by a carrier, but can also be self-supporting.

The compounds of the invention provide electronic properties which allow them to be used as semiconductors. For example, quantum chemical calculations on the exemplary compound SnIP yielded a band gap of 1.22 eV for the bulk material and a band gap of 1.29 eV for a single, non-coordinated nanotube. It will be understood that the electronic

properties of the compounds of the invention can be tailored for diverse applications using different starting materials and/or dopants. Thus, the compounds and the micro- or nanomaterials of the invention can be advantageously used in electrical, electronic, optical, or optoelectronic devices, or as photocatalysts.

Moreover, the compounds in accordance with the invention have been found to yield materials with extraordinary stability in terms of a high mechanical flexibility and elasticity. Even a crystalline microfiber formed from a compound in accordance with the invention and having a length of 1-2 mm and a thickness of several µm could be bent by 180° and returned to its original shape without visible deformation. Without wishing to be bound by theory, it is assumed that this is the result of the double-helix structure assumed by the constituting atoms of the compounds in accordance with the invention. Due to this flexibility, the compounds and the micro- or nanomaterials of the invention can be advantageously used in flexible devices, in particular flexible electrical, electronic, optical, or optoelectronic devices, such as solar cells, displays or sensors.

It will be appreciated that the definitions of the elements M^A, M^B, X^A, X^B, Q^A, Q^B, M^D and Q^D from which the compounds in accordance with the invention are formed encompass elements with little or no toxicity such as Sn, I or P, which may also be an advantage in applications of these compounds.

The properties discussed above can be exploited in a variety of applications of the compounds or of the micro- or nanomaterials in accordance with the invention, in particular of the nanowires. Thus, the invention also encompasses the use of a compound or of a micro- or nanomaterial, in particular a nanowire, in accordance with the invention as a semiconductor, in particular as a semiconductor in an electrical, electronic, optical, or optoelectronic device. It also encompasses an electrical, electronic, optical, or optoelectronic device comprising a compound or a micro- or nanomaterial, in particular a nanowire, in accordance with the invention. As noted above, the device may advantageously be a flexible device, or at least comprise a flexible part in which in the compound or the micro- or nanomaterial, in particular the nanowire, in accordance with the invention is present.

Preferred as an electrical, electronic, optical, or optoelectronic device are devices for the conversion of energy, in particular the conversion of electromagnetic waves in the UV, visible or infrared region into electric energy, e.g. a solar cell, or a thermoelectric device. Further preferred devices are a sensor, or a display or screen.

Solar cells commonly used for energy conversion are typically based on polycrystalline silicon. The compounds or the micro- or nanomaterials in accordance with the invention, such as SnIP, are particularly useful e.g. for the provision of linear nanostructured solar cells (cf. X. Wang, K. L. Pey, C. H. Yip, E. A. Fitzgerald, D. A. Antoniadis, *J. Appl. Phys.* 2010, 108, 124303; or D. T. Moore, B. Gaskey, A. Robbins, T. Hanrath, *J. Appl. Phys.* 2014, 115, 054313) or quantum-dot solar cells (G. Konstantatos, E. H. Sargent, Colloidal Quantum Dot Optoelectronics and Photovoltaics, Cambridge press, ISBN 978-0-521-19826-4). As explained above, the compounds in accordance with the invention can be used e.g. to fabricate thin film and flexible devices. Preferred are nanowires with diameters of < 10 nm and providing high aspect ratios of e.g. more than 1000. By self-assembling processes, a high aspect ratio can be of benefit to assemble thin film solar cells with parallel or random arrangement of such wires. For example SnIP, with a band gap of 1.2 – 1.3 eV (1.2 eV as microcrystalline material and 1.3 eV for nanowires) can provide solar cells with an extraordinary efficiency.

In thermoelectric materials and devices, a commonly used strategy for the optimization of the performance is the reduction of thermal conductivity by the generation or incorporation of phonon scattering, nanostructured materials. The efficiency of such systems can be systematically increased by such a process (B. Sothmann, R. Sánchez, A. N. Jordan, Nanotechnology 2015, 26, 032001 (23p)). Figure of merits larger than 2 have been achieved, pushing the efficiency of such systems in applicable regions. Due to the flexible adjustment of sizes for the compounds in accordance with the invention from micrometers down to 1 nm, an effective phonon scattering is possible. This feature can significantly increase the figure of merit of thermoelectrics. Thus, using the compounds or the micro- or nanomaterials in accordance with the invention, such as SnIP with a defined nanostructure < 10 nm, performances in the same region or even better can be expected. For example, self-organized bulk and thin layer devices are possible, representing high-quality quantum structures. Moreover, the compounds or the micro- or nanomaterials in accordance with the invention can be used in organic-inorganic hybrid thermoelectric materials and devices. For this purpose, the compounds in accordance with the invention, in particular in the form of nanowires, can be embedded in an electrically conductive polymer (e.g. a thiophen-based polymer) in different dimensions within the diameter range of 1 nm (e.g. single nanotubes) to 100 nm (e.g. bundles of nanotubes or nanowire). Consequently, the efficient phonon scattering based on the known panoscopic principle found with PbTe@Na@SrTe (K. Biswas, et al., Nature 2012, 489, 414–418) is possible due to scattering on particles of different sizes.

As far as sensors are concerned, the continuous reduction of size down to the nanoscale leads to an increase in efficiency in sensor applications. The present invention provides a simple and effective strategy to implement nanoscale structures in the form of the nanomaterials discussed herein, including sizes at the lower end of the nanometer range (e.g. 1 to 10 nm). State of the art approaches for the formation of particles in this size range, such as template syntheses, e.g. for the formation of GaN nanotubes, for senor applications (J. Goldberger, R. Fan, P. Yang, *Acc. Chem. Res.* 2006, 39, 239) are considerably more complex. Moreover, nanoparticular gold and silver are proposed for heavy metal detection (S. Su, W. Wu, J. Gao, J. Lu, C. Fan, *J Mater. Chem.* 2012, 22, 18101). The compounds in accordance with the invention are comparatively abundant and cheap elements.

Optical devices are known based on systems containing Zn, Cd, Pb and Hg-Selenides. One-dimensional nanotubes formed by CdTe are produced by a so called capping synthesis (Z. Tang, N. A. Kotov, M. Giersing, Science 2002, 297, 237-240). Nano imprinting is a method for the fabrication of metallic glasses down to 10 nm diameter and large aspect ratios (G. Kumar, H. X. Tang, J. Schroers, Nature 2009, 457, 868-872). The compounds in accordance with the invention make smaller nanomaterials accessible (down to 1 nm) with comparable or larger aspect ratios.

Furthermore, the invention also encompasses the use of a compound or of a micro- or nanomaterial in accordance with the invention as a photocatalyst, such as a photocatalyst for the splitting of water into hydrogen or oxygen. The compounds of the invention are water stable, and can be provided in the form of semiconductors with a band gap suitable for photocatalysis (e.g. SnIP). Their size can be suitably adjusted on the micrometer or nanometer scale, and elements can be used for which no environmental problems or issues in a recycling procedure will arise.

The present invention also provides a process for the preparation of the compounds in accordance with the invention, and a method for the preparation of the micro- or nanomaterials in accordance with the invention.

The compounds in accordance with the invention can be conveniently synthesized by reacting suitable starting materials in an annealing reaction. Such a reaction is carried out at high temperatures, and the reactions conditions will be discussed in further detail below. The starting materials can be selected, e.g., from (i) the elements contained in the compound, i.e. M^A, optionally M^B, X^A, optionally X^B, Q^A, optionally Q^B, optionally M^D and optionally Q^D in elemental form, (ii) precursor compounds formed from two or more of these elements, e.g.

metal halogenides formed from M^A, M^B, or M^D, and Q^A, Q^B, or Q^D, and (iii) from combinations of (i) and (ii). Prior to the reaction, the starting materials are typically mixed in the desired stoichiometric amounts. After mixing, they may be compressed to facilitate the reaction. Subsequently, the mixed starting materials are typically sealed in a vessel, e.g. a silica glass vessel such as an ampoule. The vessel should be dried, e.g. by keeping it at temperatures above 100°C. Where necessary, it can be washed prior to being charged with the starting materials, e.g. with an organic solvent having a low boiling point like acetone. During the reaction, the starting materials are kept in an inert atmosphere, i.e. an atmosphere not containing gases that could react with the starting materials under the desired reaction conditions. As used herein, an inert atmosphere includes a vacuum as a preferred option, typically with a pressure of less than 1 Pa.

The reaction of the starting materials is carried out under heat, e.g. at temperatures in the range of 623 to 1073 K. For compounds wherein M^A and, if present M^B, is Ge, Sn, and/or Pb, the temperature is preferably 643 to 923 K, more preferably 653-793 K. For compounds containing Si, reaction temperatures in the range of 823-1073 K are preferred. Reaction times are typically in the range of hours to days, such as 5 h to 18 days. For compounds wherein M^A and, if present M^B, is Ge, Sn, and/or Pb, the reaction time is preferably 5 h to 5 days, more preferably 5 h to 15 h for Sn and Pb compounds and of 3 to 5 days for Ge compounds. For compounds containing Si, longer reaction times may be useful, e.g. from 15 to 18 days. If the compounds contain, in addition to M^A, also M^B, and/or M^D, or if the compounds contain, in addition to Q^A, also Q^B, and/or Q^D, the preferred reaction temperatures are the same as for the non-substituted phases, but longer reaction times e.g. in the range of 6-8 days may be useful.

After the reaction, the cooling rate can be controlled to control the growth of crystals of the compounds in accordance with the invention. For example, cooling rates in the range of 5 K/h to 1 K/h may be applied, generally until the product reaches room temperature.

In order to obtain the micro- and nanomaterials in accordance with the invention, in particular the nanowires discussed above, the material yielded by the reaction (also referred to as "bulk material") can be exfoliated, i.e. crystalline entities of the desired size can be separated from the bulk material. The exfoliation can be accomplished e.g. by mechanical or chemical means. Preferred approaches are the removal of crystalline entities, e.g. as single nanotubes or bundles of nanotubes, from the surface of the bulk material via adhesion to an adhesive surface, such as an adhesive tape. Chemical methods may involve the dispersion of the bulk

material in a solvent, such as chloroform, dichloromethane, N-methylpyrrolidone or toluene. The dispersion may be assisted by an ultrasonic bath or ultra turrax®.

Important aspects of the invention are summarized in the following items.

1.   A compound of formula (Ia):

$$M^A_{1-x}M^B_xX^A_{1-y}X^B_yQ^A_{1-z}Q^B_z \qquad \text{(Ia)},$$

wherein:

M^A is an element selected from Si, Ge, Sn, and Pb,

M^B is an element selected from Si, Ge, Sn, and Pb and from combinations thereof, such that M^B is not the same as M^A and does not contain M^A, and

x is 0 to 0.50;

X^A is an element selected from F, Cl, Br and I,

X^B is an element selected from F, Cl, Br and I and from combinations thereof such that X^B is not the same as X^A and does not contain X^A, and

y is 0 to 0.50;

Q^A is an element selected from P, As, Sb and Bi,

Q^B is an element selected from P, As, Sb and Bi and from combinations thereof such that Q^B is not the same as Q^A and does not contain Q^A,

z is 0 to 0.50;

or a compound which is a doped variant of the compound of formula (Ia), and which further contains:
an element M^D, selected from Al, Ga, In and from combinations thereof, in a maximum amount of 10 mol% based on the total molar amount of M^A and M^B, which element M^D may partially replace M^A and/or M^B in formula (Ia); and/or
an element Q^D, selected from S, Se, Te and from combinations thereof, in a maximum amount of 10 mol% based on the total molar amount of X^A, X^B, Q^A and Q^B, which element Q^D may partially replace X^A, X^B, Q^A and/or Q^B in formula (Ia).

2.   The compound in accordance with item 1, which is a compound of formula (II):

$$(M^A_{1-x}M^B_x)_{1-3m}M^D_{2m}X^A_{1-y}X^B_y(Q^A_{1-z}Q^B_z)_{1-2n}Q^D_n \qquad (II),$$

wherein

M^A is an element selected from Si, Ge, Sn, and Pb,

M^B is an element selected from Si, Ge, Sn, and Pb and from combinations thereof, such that M^B is not the same as M^A and does not contain M^A, and

x is 0 to 0.50;

X^A is an element selected from F, Cl, Br and I,

X^B is an element selected from F, Cl, Br and I and from combinations thereof such that X^B is not the same as X^A and does not contain X^A, and

y is 0 to 0.50;

Q^A is an element selected from P, As, Sb and Bi,

Q^B is an element selected from P, As, Sb and Bi and from combinations thereof such that Q^B is not the same as Q^A and does not contain Q^A,

z is 0 to 0.50;

and wherein

M^D is an element selected from Al, Ga and In and from combinations thereof,

Q^D is an element selected from S, Se and Te and from combinations thereof,

m is 0 to 0.03; and

n is 0 to 0.10.

3.   The compound in accordance with item 2, which is a compound of formula (IIIa), (IIIb), (IIIc) or (IIId):

$$M^A_{1-3m}M^D_{2m}X^A(Q^A_{1-z}Q^B_z)_{1-2n}Q^D_n \qquad (IIIa),$$

$$M^A_{1-3m}M^D_{2m}X^A_{1-y}X^B_yQ^A_{1-2n}Q^D_n \qquad (IIIb),$$

$$(M^A_{1-x}M^B_x)_{1-3m}M^D_{2m}X^AQ^A_{1-2n}Q^D_n \qquad (IIIc),$$

$$M^A_{1-3m}M^D_{2m}X^AQ^A_{1-2n}Q^D_n \qquad (IIId),$$
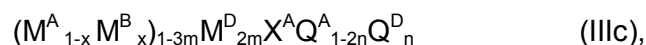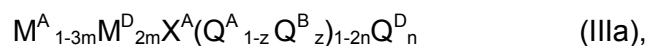
wherein M^A, M^B, M^D, X^A, X^B, Q^A, Q^D, x, y, z, m, and n are defined as in item 2.

4. The compound in accordance with item 2, which is a compound of formula (IVa), (IVb), (IVc) or (IVd):

$$M^A X^A Q^A_{1-z} Q^B_z \qquad \text{(IVa)},$$

$$M^A X^A_{1-y} X^B_y Q^A \qquad \text{(IVb)},$$

$$M^A_{1-x} M^B_x X^A Q^A \qquad \text{(IVc)},$$

$$M^A X^A Q^A \qquad \text{(IVd)},$$

wherein M^A, M^B, X^A, X^B, Q^A, Q^B, x, y and z are defined as in item 2.

5. The compound in accordance with any of items 1 to 4, wherein M^A is selected from Ge, Sn and Pb, and is preferably Sn,

6. The compound in accordance with any of items 1 to 5, wherein M^B, if present, is selected from Ge, Sn and Pb and from combinations thereof, and is preferably Pb,

7. The compound in accordance with any of items 1 to 6, wherein X^A is selected from Br and I, and is preferably I.

8. The compound in accordance with any of items 1 to 7, wherein X^B, if present, is selected from Br and I,

9. The compound in accordance with any of items 1 to 8, wherein Q^A is selected from P and As, and is preferably P.

10. The compound in accordance with any of items 1 to 9, wherein Q^B, if present, is selected from P and As,

11. The compound in accordance with any of items 1 to 10, wherein x, in formulae (Ia), (II), (IIIc) and (IVc) is 0 to 0.15, preferably 0 to 0.05.

12. The compound in accordance with any of items 1to 11, wherein y, in formulae (Ia), (II), (IIIb) and (IVb), is 0 to 0.15, preferably 0 to 0.05.

13. The compound in accordance with any of items 1 to 12, wherein z, in formulae (Ia), (II), (IIIa) and (IVa), is 0 to 0.15, preferably 0 to 0.05.

14. The compound in accordance with any of items 1, 2, and 5 to 13, wherein, in formulae (Ia) and (II), at least one of x, y and z is 0.

15. The compound in accordance with any of items 1, 2, and 5 to 14, wherein, in formulae (Ia) and (II), at least two of x, y and z are 0.

16. The compound in accordance with any of items 1, 2, and 5 to 15, wherein, in formulae (Ia) and (II), y and z are 0.

17. The compound in accordance with any of items 2, 3 and 5 to 16, wherein m, in formulae (II), (IIIa), (IIIb), (IIIc) and (IIId), is 0 to 0.01, preferably 0 to 0.005.

18. The compound in accordance with any of items 2, 3 and 5 to 17, wherein n, in formulae (II), (IIIa), (IIIb), (IIIc) and (IIId), is 0 to 0.05, preferably 0 to 0.01 and more preferably 0 to 0.005.

19. The compound in accordance with any of items 2 and 5 to 18, wherein, in formula (II), at least one of x and m is 0 and at least one of z and n is 0.

20. The compound in accordance with any of items 2, 3 and 5 to 19, wherein, in formulae (II) and (IIIa), at least one of z and n is 0.

21. The compound in accordance with any of items 2, 3 and 5 to 20, wherein, in formulae (II) and (IIIc), at least one of x and m is 0.

22. The compound in accordance with any of items 2, 3 and 5 to 21, wherein, in formulae (II), (IIIa), (IIIb), (IIIc) and (IIId), at least one of m and n is 0.

23. The compound in accordance with any of items 1 to 22, wherein M^A is Sn.

24. The compound in accordance with any of items 1 to 23, wherein X^A is I.

25. The compound in accordance with any of items 1 to 24, wherein Q^A is P.

26.   The compound in accordance with item 1, which is selected from GeIP, GeBrP, GeClP, GeFP, GeIAs, GeBrAs, GeClAs, GeFAs, SnIP, SnBrP, SnClP, SnFP, SnIAs, SnBrAs, SnClAs, SnFAs, SnISb, SnBrSb, SnClSb, SnFSb, PbIP, PbBrP, PbClP, PbFP, PbIAs, PbBrAs, PbClAs, PbFAs, PbIBi, PbBrBi, PbClBi, and PbFBi.

27.   The compound in accordance with item 1, which is selected from GeIP, GeIAs, SnIP, SnBrP, SnClP, PbIP, PbBrP and PbClP.

28.   The compound in accordance with item 1, which is SnIP.

29.   The compound in accordance with any of items 1 to 28 which is in the form of a nanowire.

30.   A process for the production of the compound in accordance with item 29, comprising the steps of:
a) reacting starting materials selected from (i) elements contained in the compound, (ii) precursor compounds formed from elements contained in the compound, and (iii) combinations of (i) and (ii) under heat in an inert atmosphere;
b) exfoliating the obtained material to prepare the compound in the form of a nanowire.

31.   A solar cell, comprising the compound in accordance with any of items 1 to 29.

32.   A thermoelectric device, comprising the compound in accordance with any of items 1 to 29.

33.   A sensor, comprising the compound in accordance with any of items 1 to 29.

34.   Use of a compound in accordance with any of items 1 to 29 as a semiconductor in an electrical, electronic, optical, or optoelectronic device.

35.   Use of a compound in accordance with item 34, wherein the device is selected from a solar cell, a thermoelectric device, or a sensor.

36.   Use of a compound in accordance with any of items 1 to 29 as a photocatalyst.

37.   Use of a compound in accordance with item 36 for the photocatalysed splitting of water into hydrogen and oxygen.

Examples

Synthesis of SnIP:

Microcrystalline SnIP was prepared either by reaction of the elements in stoichiometric amounts or by the reaction of Sn, SnI_4 and P in evacuated silica ampoule at 673 K. All glassware has been dried at 105° in an oven over night. Each ampoule was washed with acetone prior to the usage. The temperature program is as following: 0.8 K/min heating to 673 K, holding for 10 h and cooling with 5 K/h. Single crystals were prepared by heating Sn, SnI_4 and red P (20 mg, 10 mg and 500 mg) up to 923 K (1.3 K/min) in an evacuated silica tube and holding for 5 h. The cooling was done stepwise first with 2 K/h to 773 K, after 15 h it was cooled down to room temperature with a cooling rate of 1.2 K/h. A SEM picture of the obtained microcrystals is shown in Fig. 2.

By exfoliation with common tape, nanosized crystals with a diameter smaller than 40 nm and an aspect ratio of >1000 (aspect ratio: quotient of length to diameter) were prepared. The tape method was applied previously for other 2D materials as graphene. Nano wires of even smaller diameters down to single strand wires were prepared by optimized exfoliation (with tape e.g. "Lensguard 7568" by Nitto) or by dispersing in chloroform.

Chemical Analysis:

Elemental analysis shows Sn:P:I 40.0 : 11.26 : 44.2 wt.-%. The theoretical values are: 42.92 : 11.2 : 45.88. Energy dispersive X-ray spectroscopy (EDX) has been performed leading to a composition of SnIP of Sn 33(1): P 34(2): I 33(1) at.-%. Theoretical values: 33:33:33 at.-%.

Structure determination:

The crystal structure of SnIP (see Figure 1a and 1b) has been determined from a single crystal by X-ray diffraction and has been substantiated by X-ray powder diffraction of a microcrystalline sample. Lattice parameters and selected crystallographic data are: The crystal structure of SnIP: Stoe IPDS II diffractometer, MoK$_\alpha$ radiation, λ = 0.71069 Å, T = 293 K, crystal dimensions 0.01 x 0.01 x 0.2 mm^3, monoclinic, space group *P*2/*c* (No. 13), lattice parameters a = 7.934(2) Å, b = 9.802(3) Å, c = 18.439(9) Å, β= 110.06(5)°, V = 1347.0(9) Å^3, Z = 14. ρ (calc.) = 4.772 g cm^{-3}, μ (MoK$_\alpha$) = 14.81 mm^{-1}, numerical absorption

correction, crystal description using X reflections, full matrix least squares refinement on F^2 using Jana2006 [Petricek, V., et al., *Z. Kristallogr.* 2014, 229, 345.], 6796 reflections, 3567 unique ones, θ max = 29.13°, 98 parameters, R_{int} 0.0859, $R1$ (1651Fo >3σ(Fo)) = 0.0407, w$R2$ = 0.0840, GoF = 1.02, residual electron density +1.88/-1.98 e $Å^3$.

Bond distances within the helices of d(Sn-I) = 3.060(2) to 3.288(3) Å for the tin-iodide helix and of d(P-P) = 2.170(4) to 2.211(5) Å for the phosphorus helix were determined. Each chiral single tube is either left or right handed and stacked in an hexagonal rod packed arrangement along the *a* axis. Tubes of a given chirality are arranged in rows, stacked along the *b* axis.

Electron localization function (ELF) analysis of SnIP showed the covalent character of the P-P bonds and the strong polarization of the Sn lone pair towards the outer sphere of the tubes. A dative ionic interaction between the two helices can be assumed from the ELF between the Sn and P atoms. Two lone pairs of P are pointing towards the Sn positions creating bond lengths of d(Sn-P) = 2.669(3) to 2.708(3) Å. This interaction is comparable to the H-bond system in Deoxyribose Nucleic Acid (DNA),

The purity was substantiated by comparing the single crystal structure data and the measured powder diffractogram (see Figure 3).

Spectroscopic characterization:
Solid State NMR spectroscopy, Mössbauer spectroscopy and magnetic measurements have been performed, substantiating the crystal structure and oxidation states of Sn in SnIP. It contains Sn^{2+}, I^- and P^- (see Figures 4 to 7)

Exfoliation and dispersion of SnIP:
Double-helical tubes of SnIP are attracted to each other by van der Waals interactions and can therefore be exfoliated to provide nanotubes or bundles of nanotubes. SnIP was mechanically exfoliated to small bundles of nanotubes by the scotch tape approach. SnIP was fixed between two Nitto "Lensguard 7568" tape foils, the two foils were pressed together and separated afterwards. This process was repeated up to the point when the demanded thickness of the bundles of nanotubes was reached. White light interferometry was used to determine the thickness or diameter of such mechanically exfoliated nanotubes.

Also SnIP nanotubes or bundles of nanotubes were separated via dispersion in organic solvents by the aid of an ultrasonic bath to accelerate the separation process. A summary is given in Table 1. SnIP is not soluble in water.

Table 1: Solubility of SnIP in different solvents. All solutions have been tested for the occurrence of iodide by silver nitrate (formation and crystallization of AgI). + positive; - negative

	solubility (coloring of solution)	Iodide present	$AgNO_3/HNO_3$
Water	-	-	-
Aceton	+ (yellow/brown)	+	+
Acetonitril	+ (yellow)	+	+
Isopropanol	+ (pale yellow)	+	+
DMF	+ (pale yellow)	+	+
DMSO	- (pale yellow)	-	-
NMP	+ (grey, suspension)	-	-
Toluol	+ (grey, some yellow)	-	-
Ethanol	+ (yellow)	+	+
Chloroform	+ (brown suspension)	-	-
Dichloromethane	+ (brown suspension)	-	-

Bundles of nanotubes prepared by these methods are shown in Figs 8a to 8c, showing high resolution SEM pictures of exfoliated SnIP crystals. 8a: Mechanically (tape method) delaminated crystals of 30 nm diameter of SnIP. 8b: Chemically exfoliated SnIP crystal of the same size prepared on a copper grid. 8c: SnIP exfoliated and suspended in chloroform. Coils of SnIP nano tubes with diameters between 5 to 10 nm are provided after evaporation of the solvent.

Mechanical properties of SnIP:

Crystals of SnIP show a very high mechanical flexibility and elasticity. Even large crystals of 1-2 mm length and a thickness of some μm can be bent by 180°. Afterwards, the crystals rearrange without any visible deformation to their original position. This experiment has been performed using a conventional light microscope.

Electronic properties

Quantum chemical calculations were performed in the framework of density functional theory (DFT) with LDA and PBE-GGA functionals. To confirm the results, full geometry optimizations were performed with two codes: the projector-augmented-wave (PAW) approach and the conjugant gradient algorithm as implemented in vasp (Kresse G., Furthmüller J., Phys. Rev. B 1996, 54, 11169, Kresse G., Hafner J., J. Phys.: Condens. Matter 1994, 6 8245). Convergence is considered at differences in total energy less than 10^{-5} eV and maximum Hellmann-Feynmann forces of 10^{-4} eV/Å. Additionally, the all-electron local

orbital approach was applied with the Schlegel algorithm as implemented in the program CRYSTAL14 (Dovesi et al. CRYSTAL14 User's Manual. University of Torino: Torino, 2014. Dovesi, R. et al., Int. J. Quantum Chem., 2014, 114, 1287). Thereby, also the Grimme-d2 correction was used to account for dispersion (VdW) interactions.

For bulk-SnIP a band gap of 1.22 eV was observed while a single, non-coordinated SnIP nano tube is characterized by only a slightly larger band gap of 1.29 eV. Due to the determined values SnIP is exactly located in the band gap range of classical semiconductors like Si (ca. 1.1 eV) or GaAs (1.4 eV).

The direct band gap was determined by diffuse reflectance spectroscopy (see Figure 15) to 1.55 eV. This value is in good accordance with the calculated ones.

Synthesis of GeIP and GeIAs

Microcrystalline GeIP and GeIAs were prepared by reactions of the elements in stoichiometric ratio in evacuated silica ampoules at 773 K. All glassware was dried at 105° in an oven over night. Each ampoule was washed with acetone prior to the usage. GeIP: Amounts are 146.2 mg Ge, 255.8 mg I_2, and 62.4 mg P; GeIAs: 130.9 mg Ge, 228.9 mg I_2 and 135.2 mg As. The temperature program is as follows: in 10 h from room temperature to 773 K, holding the temperature for five days and finally cooling the samples to room temperature within 48 h. Microphotographs of the obtained needle shaped microcrystals are shown in Fig. 10 (GeIP) and 11 (GeIAs).

Elemental analysis

Energy dispersive X-ray spectroscopy (EDX) has been performed for GeIP leading to a composition of Ge 28(4) : P 35(4) : I 37(5) at.-%. Theoretical values: 33:33:33 at.-%.

Synthesis of PbIP and PbBrP

Microcrystalline PbIP and PbBrP were prepared by reactions of PbI_2 or $PbBr_2$ with red phosphorus and lead in stoichiometric ratio in evacuated silica ampoules, in the temperature interval of 643 to 693 K. All glassware has been dried at 105° in an oven over night. Each ampoule was washed with acetone prior to the usage. PbIP: Amounts are 40.0 mg P, 297.8 mg PbI_2, and 133.7 mg Pb; PbBrP: 40.3 mg P, 236.4 mg $PbBr_2$, and 133.6 mg Pb. The temperature program is as follows: in 8 h from room temperature to the target temperature,

holding the temperature for 10 h and finally cooling the samples to room temperature within 75 h. Microphotographs of the obtained needle shaped microcrystals are shown in Fig. 12 (PbIP) and 13 (PbBrP).

Elemental analysis

Energy dispersive X-ray spectroscopy (EDX) has been performed for PbIP and shows Pb 34(1) : P 35(1) : I 31(3) at.-%. Theoretical values: 33:33:33 at.-%.

Synthesis of $Sn_{0.5}Pb_{0.5}IP$

Microcrystalline $Sn_{0.5}Pb_{0.5}IP$ were prepared by reactions of PbI_2, Sn and red phosphorus in stoichiometric ratio in evacuated silica ampoules, in the temperature interval of 643 to 693 K. All glassware has been dried at 105° in an oven over night. Each ampoule was washed with acetone prior to the usage. 39.9 mg P, 76.9 mg Sn, 297.3 mg PbI_2 were reacted to result in $Sn_{0.5}Pb_{0.5}IP$. The temperature program is as following in 10 h from room temperature to the target temperature, holding the temperature for 10 h and finally cooling the samples to room temperature within 75 h. Microphotographs of the obtained needle shaped microcrystals are shown in Fig. 14.

Calculated isotypic structures

The effects of substitution of the elements in isotypic compounds MXQ were estimated from DFT calculations. Assuming structures that are isotypic to experimentally found SnIP all structural parameters were relaxed. Predicted structures are summarized in Table 2. According to the results (1) the structure of SnIP is preserved for all substitutions, (2) the elements M and X have a systematic effect on lattice parameters a, b, c, and ß, (3) the substitutions have a systematic effect on the electronic band gap. Conclusion (1) is underlined by the fact that the P substructure is maintained and all P-P distances are found in the range between 2.17 and 2.20 Å upon substitution – similar to SnIP (all further atomic distances are summarized in Table 3 according to the description of Fig. 9). Estimating Vegard´s law for partial substitution $Sn_{1-x}M_xI_{1-x}X_xP$ expected lattice parameters are obtained from SnIP by linear interpolation to the respective compound for full substitution MXP. (Hint on the applied method – DFT-LDA slightly underestimates bond lengths and lattice parameters by 1-3%). From the lattice parameter effects (2) upon substitution we expect tunable mechanical properties. The same is predicted for electronic and optic properties from changes of the electronic band structure.

Table 2: Predicted lattice parameters from DFT calculations for completely substituted compounds *MXQ* for *M* = Pb, Sn, Ge, Si, *X* = F, Cl, Br, I, *Q* = P. An error of +/- 5 % for each value must be taken into account.

M	*X*	*Q*	*a*/Å	*b*/Å	*c*/Å	*ß*/°	*V*/Å³	ρ/gcm⁻³	*ΔEg*/eV
Pb	I	P	8.11	9.63	18.82	109.73	1310.3	6.48	1.32
Sn	I	P	7.84	9.57	17.96	110.31	1257.8	5.11	1.22
Ge	I	P	7.50	9.26	17.30	110.31	1126.8	4.76	1.50
Si	I	P	7.26	9.19	17.30	110.36	1081.0	4.00	1.16
Pb	Br	P	8.17	8.97	17.08	112.22	1158.4	6.38	1.19
Sn	Br	P	7.92	8.83	17.15	112.60	1107.1	4.82	1.21
Ge	Br	P	7.54	8.63	16.49	112.55	991.0	4.30	1.65
Si	Br	P	7.26	8.53	16.59	113.48	942.4	3.43	1.35
Pb	Cl	P	8.29	8.51	16.58	114.77	1061.8	5.99	1.12
Sn	Cl	P	8.02	8.31	16.70	115.23	1006.2	4.28	1.15
Ge	Cl	P	7.62	8.13	15.97	113.95	904.1	3.58	1.51
Si	Cl	P	7.34	7.92	15.93	111.63	861.5	2.55	1.09
Pb	F	P	8.72	7.91	14.41	121.23	849.9	7.03	1.45
Sn	F	P	8.40	7.31	14.70	122.76	758.6	5.17	0.01
Ge	F	P	7.82	7.41	14.64	118.01	749.4	3.80	1.32
Si	F	P	7.61	7.25	14.57	118.63	705.7	2.57	0.25

Table 3: Predicted lattice parameters from DFT-LDA calculations for completely substituted compounds *MXQ* for *M* = Pb, Sn, Ge, Si, *X* = F, Cl, Br, I, *Q* = P. An error of +/- 5 % for each value must be taken into account.

	distances helix *Q* [Å]				distances helix *MX* [Å]						
	*Q*3-*Q*3	*Q*2-*Q*3	*Q*1-*Q*2	*Q*4-*Q*1	*X*3-*M*2	*M*3-*X*3	*M*3-*X*2	*M*4-*X*2	*M*2-*X*1	*M*1-*X*1	*M*1-*X*4
PbIP	2.16	2.18	2.18	2.20	3.21	3.15	3.21	3.11	3.20	3.22	3.21
SnIP	2.20	2.19	2.20	2.21	3.29	3.06	3.21	3.06	3.12	3.18	3.17
GeIP	2.18	2.20	2.20	2.21	3.06	2.89	3.03	2.89	2.95	2.99	3.01
SiIP	2.19	2.21	2.21	2.21	3.07	2.78	3.00	2.82	2.82	2.97	2.91
PbBrP	2.16	2.17	2.18	2.19	3.09	2.98	3.03	2.96	3.01	3.04	3.03
SnBrP	2.17	2.18	2.19	2.19	2.98	2.88	2.97	2.89	2.93	2.94	2.98
GeBrP	2.18	2.18	2.19	2.19	2.92	2.69	2.89	2.73	2.74	2.85	2.82
SiBrP	2.20	2.20	2.20	2.20	3.18	2.49	2.94	2.65	2.47	3.04	2.61
PbClP	2.17	2.17	2.17	2.18	2.99	2.85	2.92	2.86	2.87	2.95	2.90
SnClP	2.17	2.17	2.18	2.18	2.88	2.75	2.85	2.79	2.79	2.83	2.86
GeClP	2.17	2.17	2.19	2.19	2.54	2.66	2.70	2.64	2.95	2.49	2.95
SiClP	2.16	2.18	2.20	2.21	2.27	2.75	2.44	2.58	3.35	2.24	3.03
PbFP	2.18	2.18	2.17	2.15	2.92	2.55	2.87	2.38	2.29	3.50	2.35
SnFP	2.19	2.18	2.17	2.16	2.51	2.49	2.90	2.39	2.15	3.24	2.39
GeFP	2.19	2.16	2.17	2.18	1.88	3.40	2.01	2.33	3.55	1.86	3.06
SiFP	2.18	2.17	2.18	2.18	1.67	3.47	1.82	2.28	3.62	1.66	3.23

Description of Figures

Figure 1 shows the crystal structure of SnIP with a view along the *a* axis (Fig. 1a) and *b* axis (Fig. 1b).

Figure 2 shows an SEM picture of (bulk) SnIP.

Figure 3 shows a comparison of a measured X-ray powder diffractogram of SnIP and a X-ray powder diffractogram calculated from single crystal structure data. Measurement was performed at room temperature.

Figure 4 show the results of Raman spectroscopy of SnIP at room temperature.

Figure 5 shows Mössbauer spectra of SnIP at 298 (top) and 77 K (bottom).

Figure 6 shows the susceptibility of SnIP.

Figure 7 shows the ^{31}P solid state NMR spectrum of SnIP.

Figure 8 shows high resolution SEM pictures of exfoliated SnIP crystals. 8a: Mechanically (tape method) delaminated crystals of 30 nm diameter of SnIP. 8b: Chemically delaminated SnIP crystal of the same size prepared on a copper grid. 8c: SnIP delaminated and suspended in chloroforme. Coils of SnIP nano tubes with diameters between 5 to 10 nm are provided after evaporation of the solvent.

Figure 9 shows the structure and bond lengths in *MQX* compounds, as predicted by DFT calculations for *M* = Pb, Sn, Ge, Si, *X* = F, Cl, Br, I, *Q* = P (see Table 2, Table 3, and Text).

Figure 10 shows microphotographs of GeIP.

Figure 11 shows microphotographs of GeIAs.

Figure 12 shows microphotographs of PbIP.

Figure 13 shows microphotographs of PbBrP.

Figure 14 shows microphotographs of $Sn_{0.5}Pb_{0.5}IP$

Figure 15 shows the results from diffuse reflectance measurements of SnIP, drawn according the Kubelka-Munk theory. The direct band gap was calculated to ~1.55 eV.

New EP patent application
Technische Universität München
Our ref.: Y1784 EP
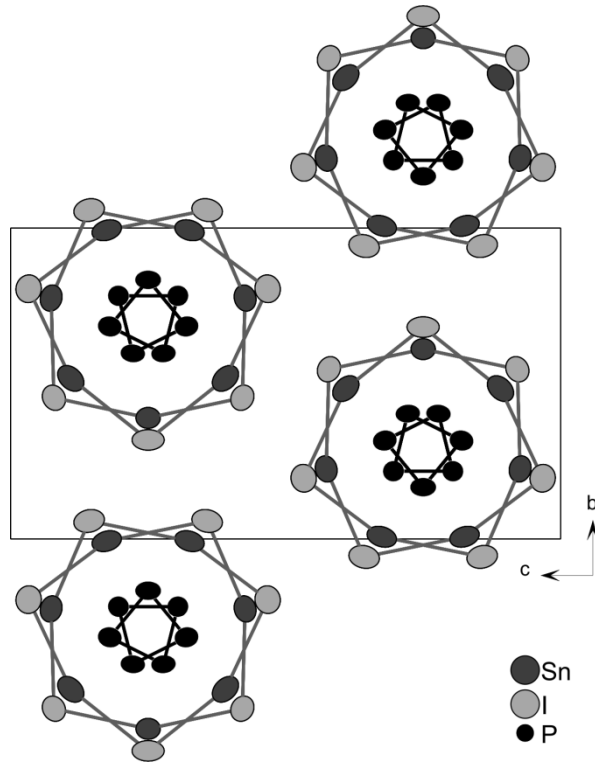
Fig 1a
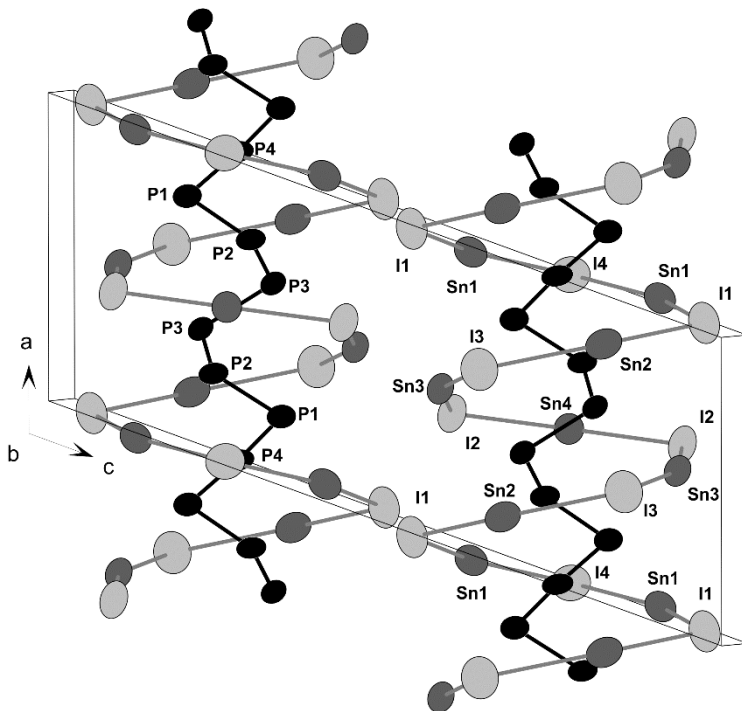
Fig. 1b
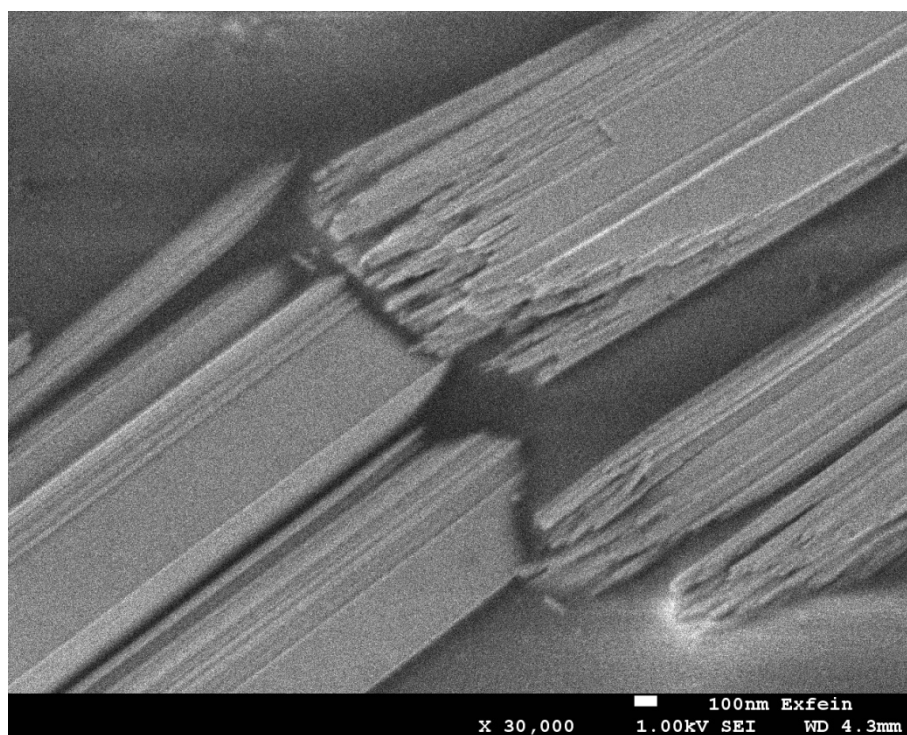
Fig. 2
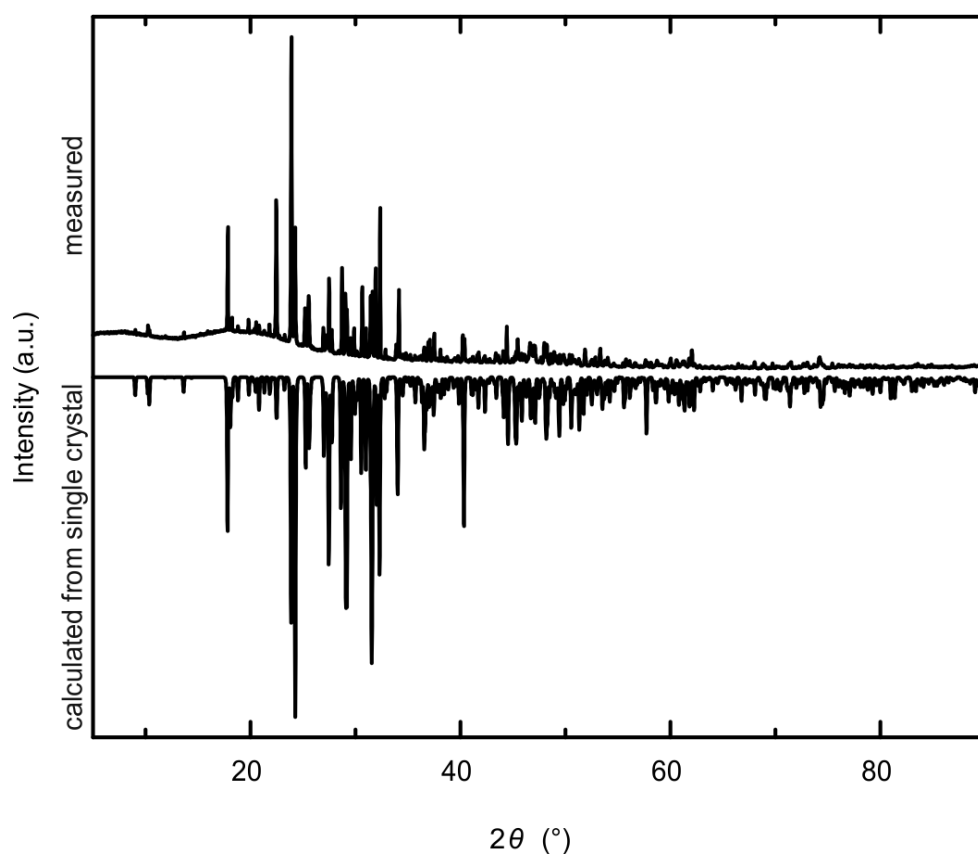
Fig. 3
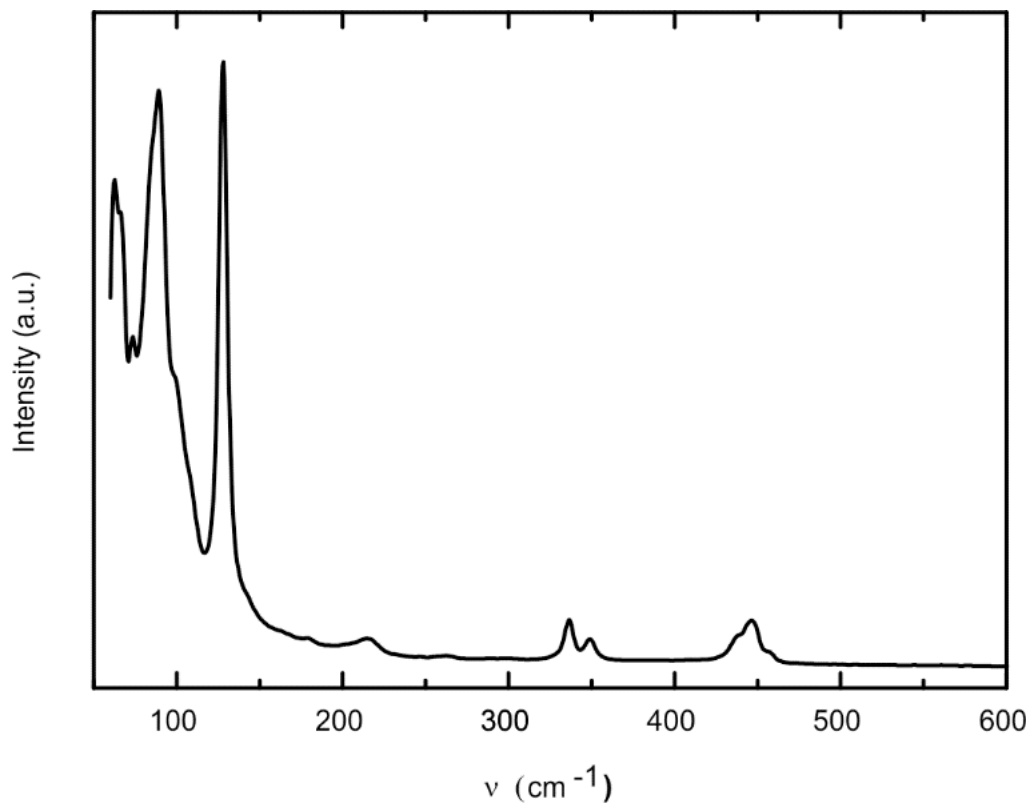
Fig. 4.
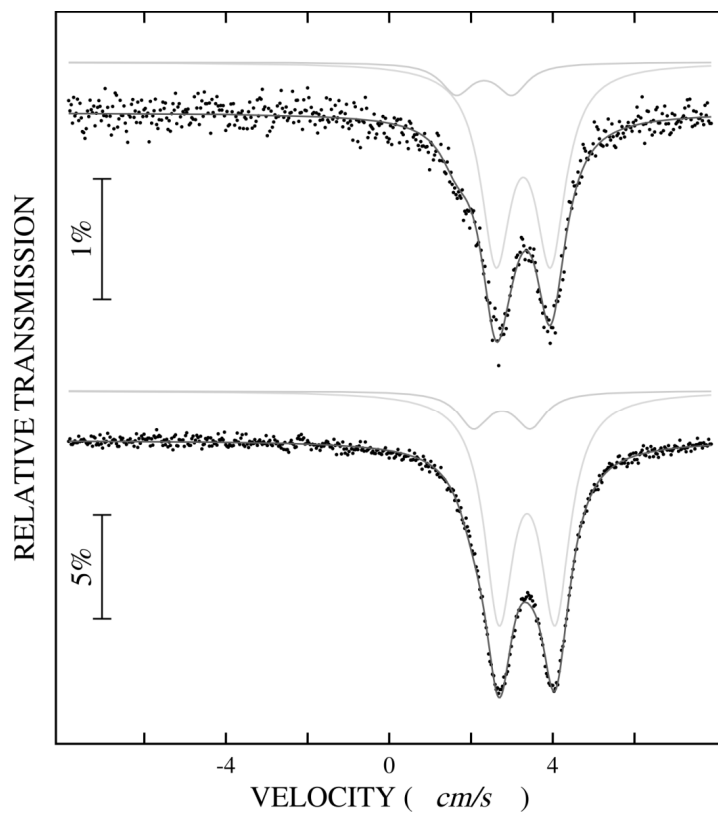
Fig. 5.
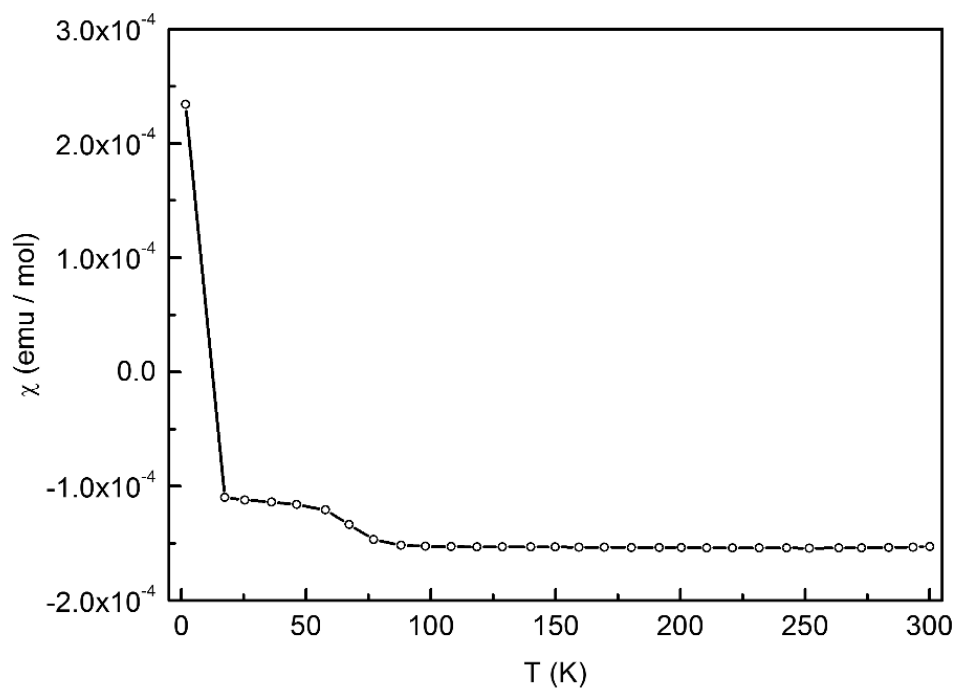
Fig. 6
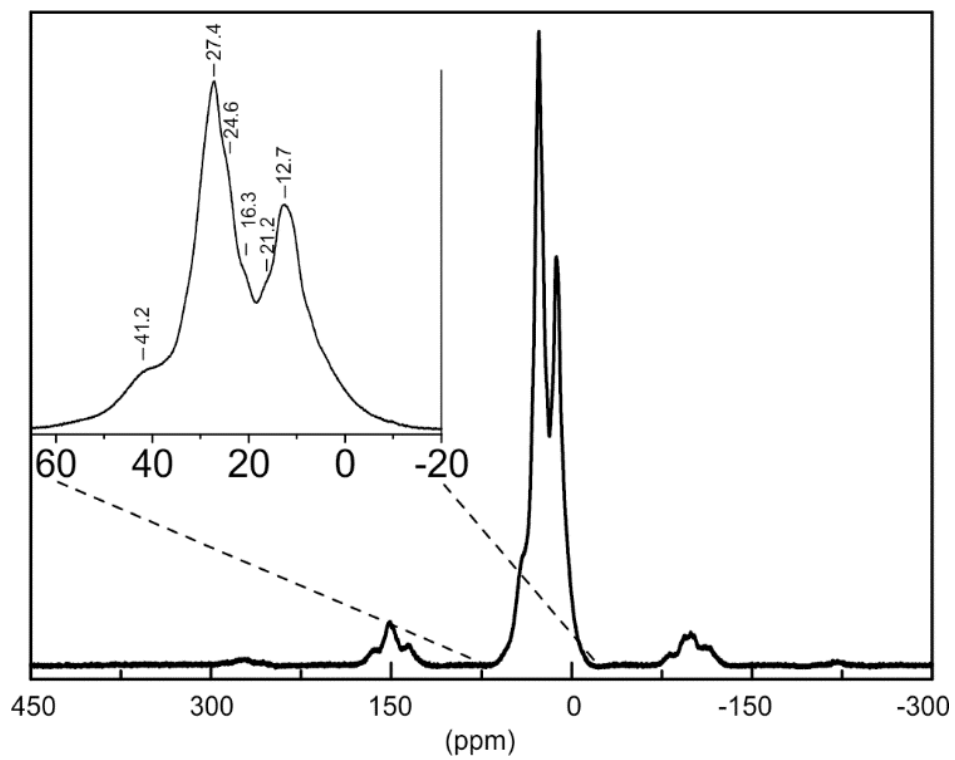
Fig. 7
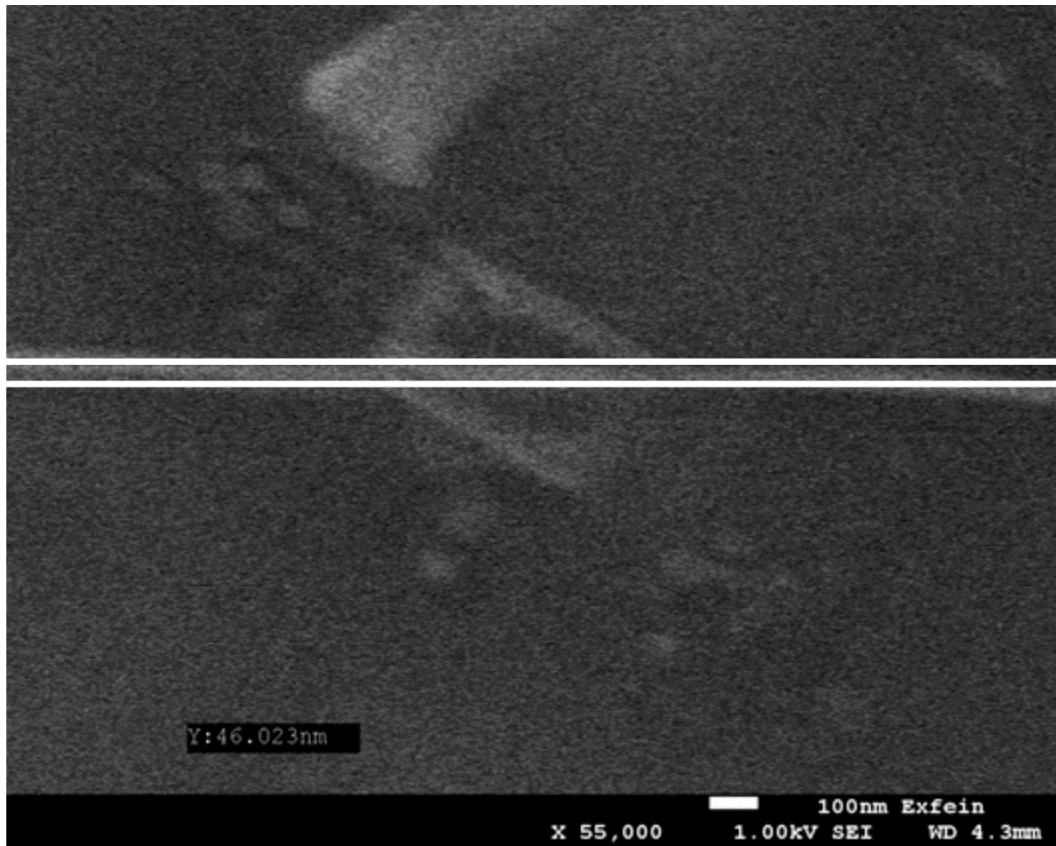
Fig.8a
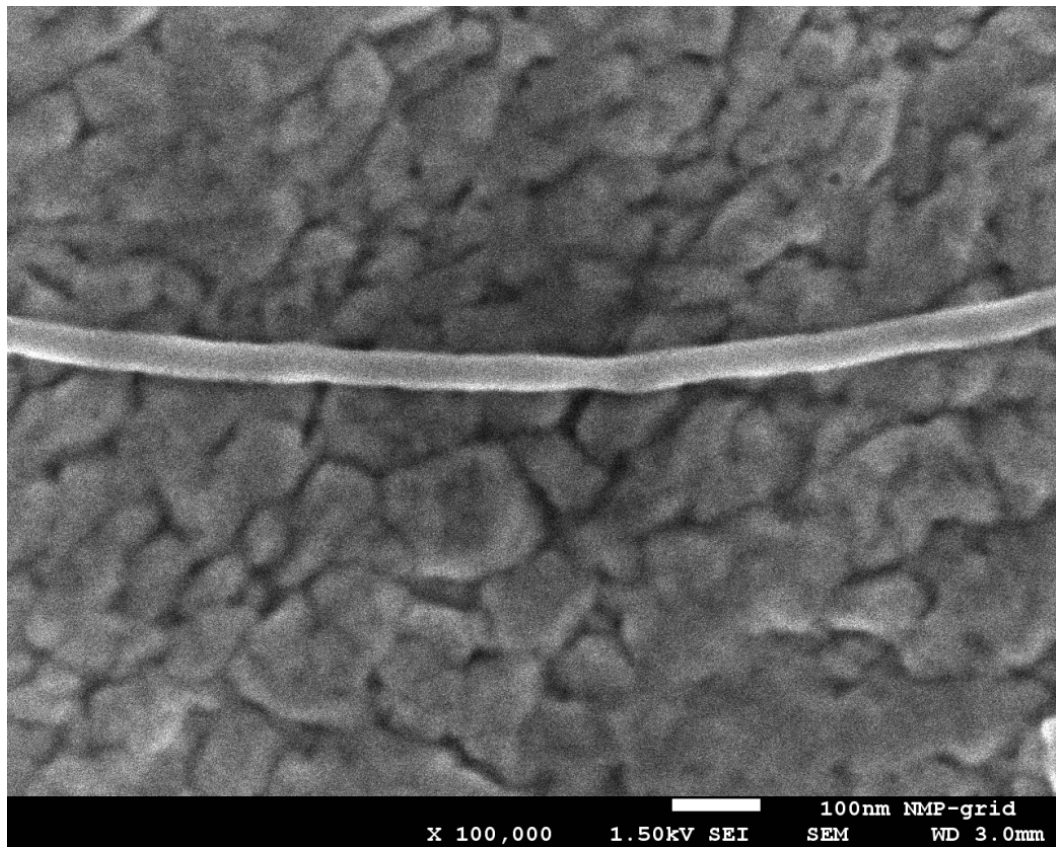
Fig. 8b
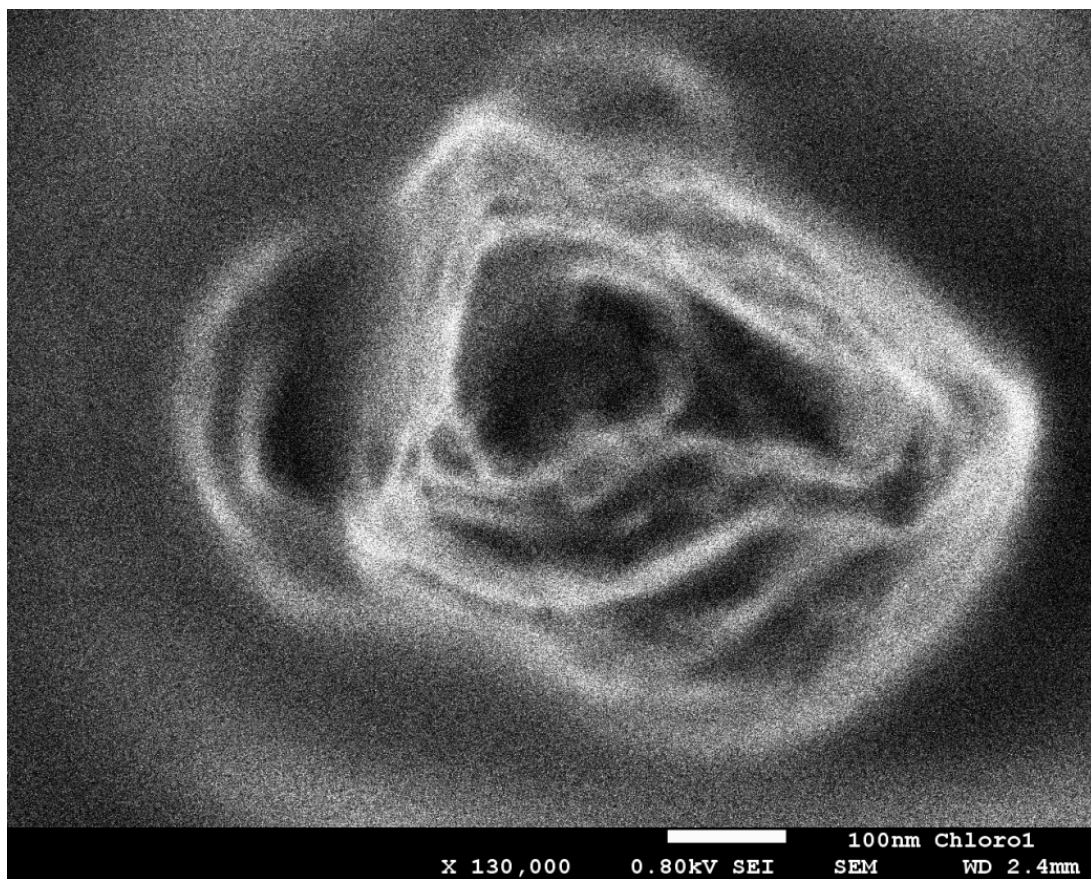
Fig. 8c
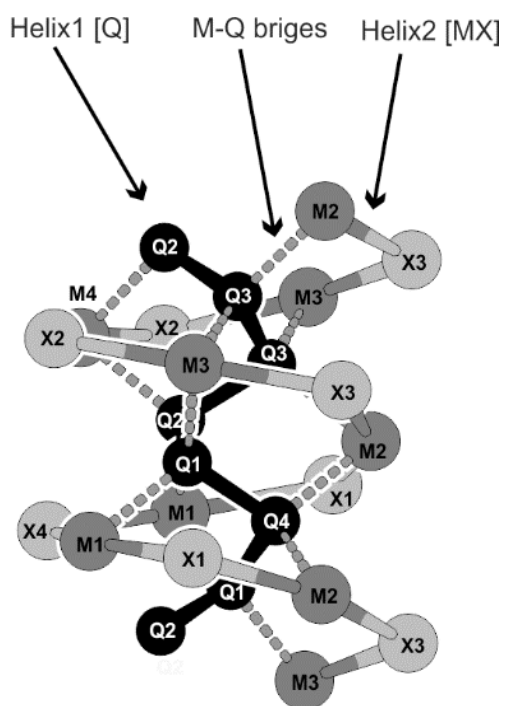
Fig. 9
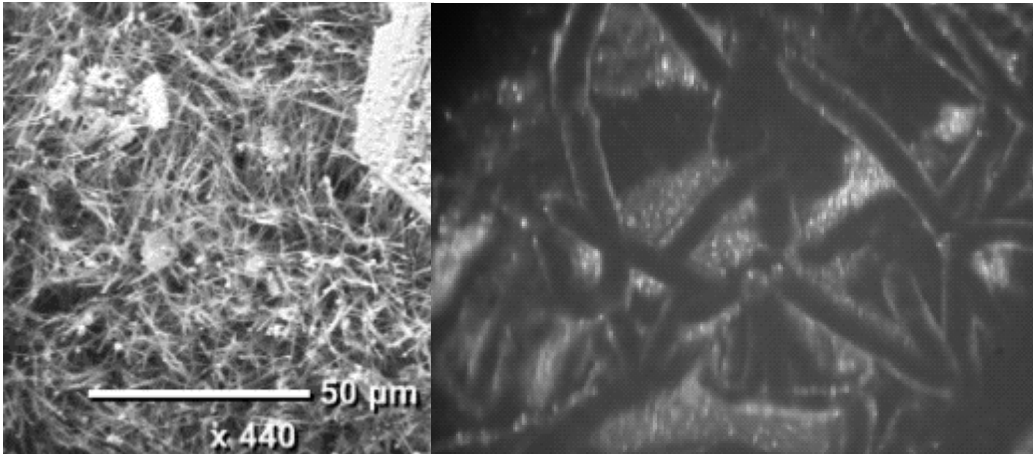
Fig. 10
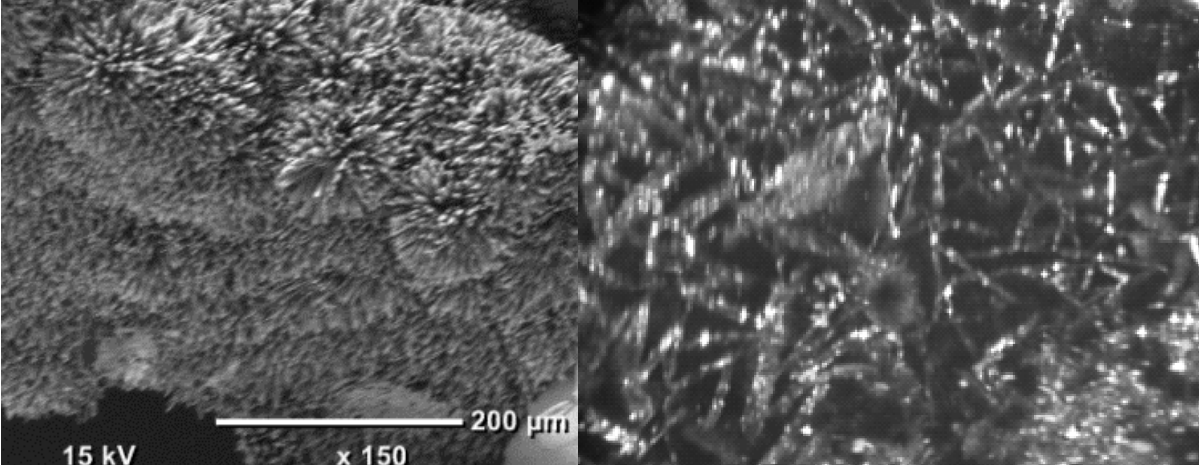
Fig.11
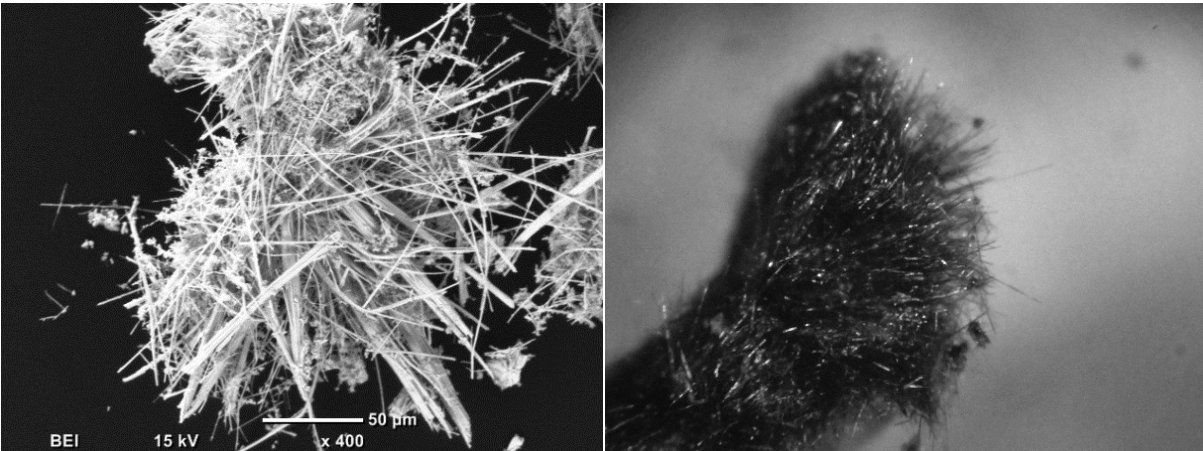
Fig. 12

Fig. 13
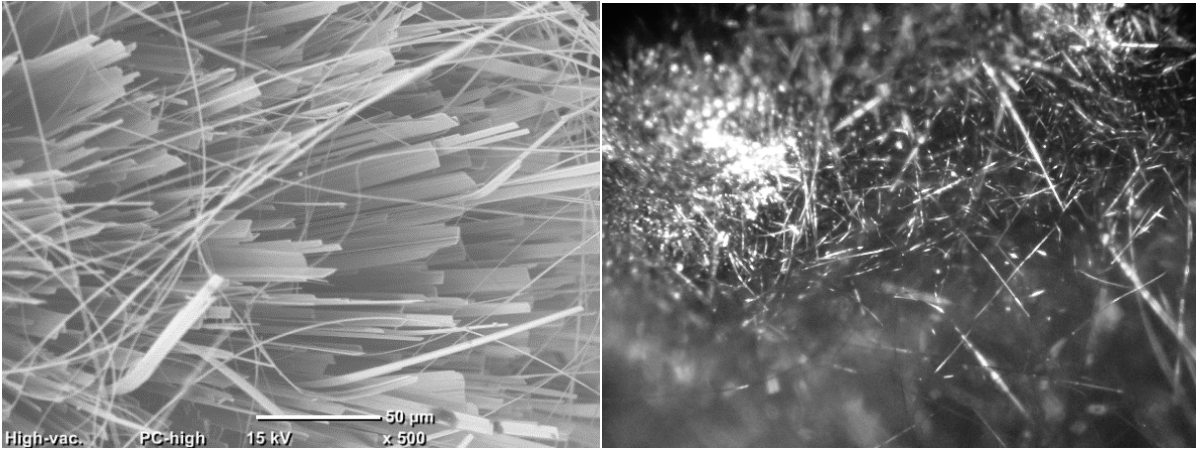
Fig. 14
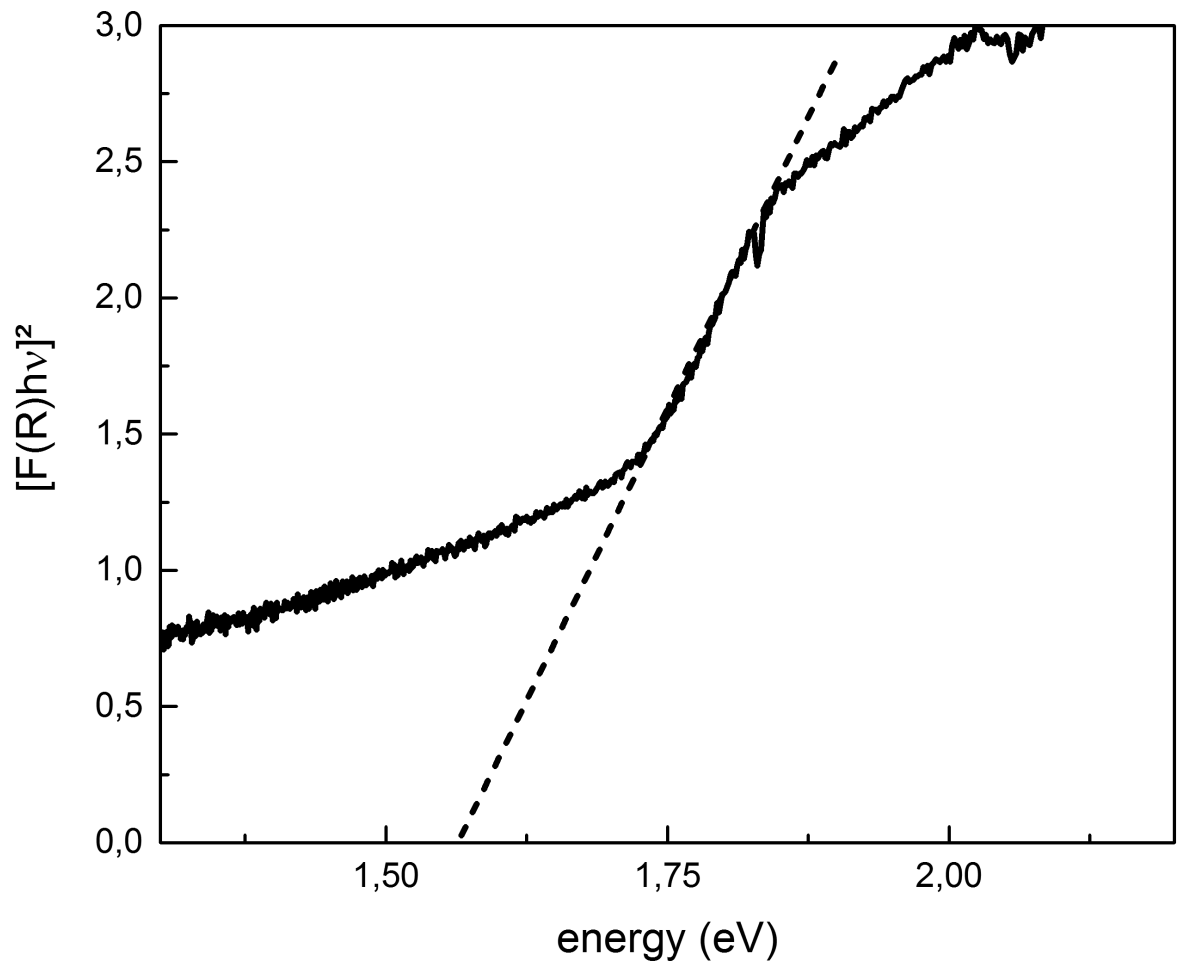
Fig. 15

3.5 Flexible and Ultra-Soft Inorganic 1D Semiconductor and Heterostructure Systems Based on SnIP

Claudia Ott[1,≠], Felix Reiter[1,≠], Maximilian Baumgartner[1], Markus Pielmeier[1], Anna Vogel[1], Stefan Burger[2], Michael Ehrenreich[2], Gregor Kieslich[2, *], Dominik Daisenberger[3], Jeff Armstrong[4], Thakur Ujwal Kumar[5], Pawan Kumar[5], Shunda Chen[6], Davide Donadio[6], Lisa S. Walter[7], R. Thomas Weitzg[8], Karthik Shankar[5, *] and Tom Nilges[1, *]

[1] Prof. Dr. Tom Nilges, Synthesis and Characterization of Innovative Materials group

[2] Dr. Gregor Kieslich, Crystal Chemistry of Functional Materials group both Technical University Munich, Department of Chemistry, Lichtenbergstrasse 4, 85748 Garching, Germany

[3] Dr. Dominik Daisenberger, Diamond Light Source Ltd. Harwell Science & Innovation Campus, Didcot, OX11 0DE, Great Britain

[4] Dr. Jeff Armstrong, ISIS Facility, STFC Rutherford Appleton Laboratory, Didcot, Oxon OX11 0QX, UK

[5] Prof. Karthik Shankar, Thakur Ujwal Kumar, Dr. Pawan Kumar, Deaprtment of Electrical and Computer Engineering, University of Alberta, 11-384 Donadeo Innovation Centre For Engineering, Edmonton, Canada T6G 1H9

[6] Prof. Davide Donadio, Shunda Chen, Department of Chemistry. University of California Davis, One Shields Ave. Davis, 95616, CA. United States

[7] Lisa S. Walter, Prof. Thomas Weitz, Physics of Nanosystems, Department of Physics, Ludwig-Maximilians-University Munich, Amalienstrasse 54, 80799 Munich, Germany

[8] Center for NanoScience (CeNS) and Nanosystems Initiative Munich (NIM), Schellingstrasse 4, 80799 Munich, Germany

≠ Authors contributed equally to this work

The article "Flexible and ultra-soft inorganic 1D semiconductor and heterostructure systems based on SnIP" was published in Advanced Functional Materials, March 2019, 1900233. The main results were presented by Claudia Ott at the Wöhler Tagung 2018 in Regensburg, Germany and the Annual ATUMS meeting 2018 in Munich, Germany.

Reduction in size and shape of materials leads to major changes in the physical properties. Transformations of 3D materials to 2 dimensional particles like graphene or phophorene were already published. They obsevered enhanced electron-electron interactions and anisotropy effects. A reduction to atomic scaled 1 dimensional materials was reached with nanomaterials as free standing, oriented, or randomly arranged structures.

As described in chapter 3.3 on page 71 an atomic scale double helix was found in 2016. The single strands are conjoined via weak van der Waals interactions and therefore pose an ideal system for delamination and the fabrication of hybrid systems on an atomic level.

The pressure dependent lattice parameter properties were investigated in a diamond anvil cell via high pressure powder X-ray diffraction (HPPXRD) between ambient and ~4 GPa pressure. From those results the bulk modulus can be extrapolated. The Young's modulus was measured via atomic force microscopy (AFM) along the double helix axis. These values were found to be 3 to 7 times lower than observed for any other semiconducting material and can be attributed to the spring like behaviour of the SnIP double helices. A second reason for the softness of the material is that the single double helices may slip along the [100] direction due to the weak van der Waals interactions between the strands. Raman measurements confirm the structural stability during bending. We found three distinct regions in the Raman spectrum representing three different vibrational interactions:

120 - 150 cm^{-1}: Sn-I breathing mode, (strong covalent Sn-I, weak van der Waals interactions).

350 - 380 cm^{-1}: P-P stretching mode, (strong covalent P-P interactions).

> 400 cm^{-1}: P-P breathing mode, (dative ionic interactions between P and Sn-I helices).

With high pressure Raman measurements we identified van der Waals interactions as the main binding factor. A hint for structural decomposition could not be found.

The combination of soft inorganic semiconducting fibers like SnIP with organic polymers opens a way to hybrid systems with the combined properties of an inorganic semiconductor and polymer-like systems. Different organic polymers were investigated to adress various applications.

The hybrid system of SnIP and halide-doped (fluorine and chlorine co-doped) C_3N_4 (CNFCl) was investigated considering the potential as a water splitting catalyst. Band gaps of the composite material were investigated with the help of Tauc plots and resulted in two band edges. The resistivity of the CNFCl is not changed while forming the hybrid with SnIP. Steady state photoluminescence (PL) spectroscopy of the starting material CNFCl shows a broad and intense signal at 481 nm while the analysis of the hybrid material exhibits a significant decrease of the PL intensity. That could be attributed to an effective charge separation in the hybrid material. This process was verified with time resolved PL (TRPL) measurements. Both materials by themselves show poor results due to leaching and charge carrier transfer problems. The hybrids on the other hand and especially the one with 30 wt.-% SnIP show promising photoelectrochemical performances and extended durability of the photoresponse. Mott Schottky measurements defined the hybrids as n-type materials. XPS measurements determined the position of the valence bands of SnIP, CNFCl and 30 wt.-% SnIP/CNFCl to 1.19, 1.83 and 2.27 eV respectively. HR-TEM revealed a 1D core-shell nanorod morphology. High magnification showed Moire-fingers with higher d-spacing (0.65 nm) which proves a lattice mismatch and hence the folding of the CNFCl sheets around the SnIP needles preventing the ideal π-π stacking. This wrapping of CNFCl around the SnIP needles was furthermore proven with elemental mapping. All those measurements supported the formation of a core-shell particle consisting of a dense SnIP core surrounded by a CNFCl shell. High resolution X-ray photoelectron spectroscopy (HR-XPS) endorsed the absence of a chemical bond between the core and the shell of those hybrid particles. The interaction is entirely based on weak van der Waals forces.

Author contributions: C.O. and F.R. synthesized and characterized the samples and conducted physical property measurements, M.P. and M.B. executed quantum chemical calculations, A.V. conducted the Raman experiments, Da.Do. determined the phonon spectra, G.K., Do.Da., S.B., M.E. and F.R. performed the pressure-dependent synchrotron experiments, evaluated the obtained data and analysed the results, T.U.K, P.K. and K.S. planned and performed the water

splitting experiments as well as the electrochemical property measurements and evaluated the generated data, L.S.W. and R.T.W. measured the Young's modulus, T.N., K.S. and G.K wrote the paper. All authors discussed the results and reviewed the manuskript.

Flexible and ultra-soft inorganic 1D semiconductor and heterostructure systems based on SnIP

Claudia Ott[a),‡], Felix Reiter[a), ‡], Maximilian Baumgartner, Markus Pielmeier [a)], Anna Vogel [a)], Patrick Walke [a)], Stefan Burger[b)], Michael Ehrenreich[b)], Gregor Kieslich[b,*)], Dominik Daisenberger[c)], Jeff Armstrong[d)], Thakur Ujwal Kumar[e) ‡], Pawan Kumar [e)], Shunda Chen[f)], Davide Donadio[f)], Lisa S. Walter [g)], R. Thomas Weitz[g,h)], Karthik Shankar[e,*)] and Tom Nilges[a,*)]

a) Claudia Ott, Felix Reiter, Dr. Maximilian Baumgartner, Markus Pielmeier, Anna Vogel, Patrick Wallke, Prof. Dr. Tom Nilges, Synthesis and Characterization of Innovative Materials group

b) Stefan Burger, Michael Ehrenreich, Dr. Gregor Kieslich, Crystal Chemistry of Functional Materials group

both Technical University Munich, Department of Chemistry, Lichtenbergstrasse 4, 85748 Garching, Germany

c) Dr. Dominik Daisenberger, Diamond Light Source Ltd. Harwell Science & Innovation Campus, Didcot, OX11 0DE, United Kingdom

d) Dr. Jeff Armstrong, ISIS Facility, STFC Rutherford Appleton Laboratory, Didcot, Oxon OX110QX, United Kingdom

e) Prof. Karthik Shankar, Thakur Ujwal Kumar, Dr. Pawan Kumar, Deaprtment of Electrical and Computer Engineering, University of Alberta, 11-384 Donadeo Innovation Centre For Engineering, Edmonton, Canada T6G 1H9

f) Shunda Chen, Prof. Davide Donadio, Department of Chemistry. University of California Davis, One Shields Ave. Davis, 95616, CA. United States

g) Lisa S. Walter, Prof. R. Thomas Weitz, Physics of Nanosystems, Department of Physics, Ludwig-Maximilians-University Munich, Amalienstrasse 54, 80799 Munich, Germany

h) Center for NanoScience (CeNS) and Nanosystems Initiative Munich (NIM), Schellingstrasse 4, 80799 Munich, Germany

‡ Authors contributed equally to this work

Low dimensionality and high flexibility are key demands for flexible electronic semiconductor devices. Recently, with the discovery of SnIP, the first atomic-scale double helical semiconductor, an ideal one-dimensional system emerged, which combines structural anisotropy and robustness with exceptional electronic properties. The benefit of the most optimized structure in nature, the double helix, combined with a diverse structure on the nano scale, ranging from strong covalent bonding to weak van der Waals interactions, and the large structure and property anisotropy offers a substantial potential for applications in energy conversion and water splitting. It represents the next logical step in down-scaling the inorganic semiconductors from classical 3D systems, via 2D semiconductors like MXenes or transition metal dichalcogenides, to the first down-sizeable, polymer-like atomic-scale 1D semiconductor SnIP.

SnIP shows intriguing mechanical properties featuring a bulk modulus 3 times lower than any IV, III-V or II-VI semiconductor. In situ bending tests substantiates that pure SnIP fibers can be bent without an effect on their bonding properties. Quantum chemical calculations predict a low and anisotropic heat transport expected for a 1D system. Organic and inorganic hybrids were prepared illustrating that SnIP is a potent candidate to fabricate flexible 1D composites for energy conversion and water splitting applications. SnIP@C_3N_4 hybrid form an unusual soft material core-shell topology with graphenic carbon nitride wrapping around SnIP. A 1D van der Waals heterostructure was formed capable to perform effective water splitting.

The development of semiconductors for electronic devices is driven by the need of miniaturization, increasing efficiency, flexibility and stability. Therefore, classical IV, III-V or II-VI three-dimensional semiconductors are fabricated in nano-particular form and applied for instance as quantum dots in numerous electronic devices [Alivisatos 1996, Reithmaier 2004]. The reduction of size leads to fundamental changes in the optical and electronic properties.

Electronic excitations shift to higher energy, and the oscillator strength is concentrated into a few transitions. As a consequence of quantum confinement properties like band gaps, melting points, or phase transition temperatures are tuned. If one focusses on the density of states in semiconductor nanostructures with different dimensionality going from 3D towards 1D and 0D, an increasing texturing of the DOS leading to discrete energy levels in low-dimensional systems can be observed [Alivisatos 1996]. Therefore, a consequent way of development in semiconductor science was to decrease the dimensionality and 2D systems like MXenes (graphene, phosphorene, silicene and others) or transition metal dichalcogenides (TMD) emerged [Geim 2007, Liu 2014, Vogt 2012, Jose 2014]. Here, the layered structure introduced a feature that was not easy to achieve with bulk phase 3D semiconductors namely, morphological (graphene, TMDs) and in some cases structural (phosphorene, silicene) anisotropy. Such systems also offer enhanced flexibility alongside with electronic properties emerging from quantum confinement, and they can be easily prepared and used as monolayer materials.

The reduction in dimensionality resulted in enhanced electron-electron interactions, which for instance results in giant band gap renormalization excitonic effects, Dirac cones, topolocical states and charge density waves as shown for TMDs [Ugeda 2014, Manzeli 2017]. Beside graphene, lacking of a band gap, many other 2D materials like phosphorene or TMDs are semiconductors and can be applied in high-performance electronic devices. Field effect transistors have been made in 2014 with phosphorene [Li 2014] and in 2015 with silicene [Tao 2015]. Another interesting but non-classical 2D semiconductor with intriguing mechanical properties is α-Ag_2S [Shi 2018]. This material offers a metal-like ductility due to weak van der Waals interactions within structure subunits and a fluent and highly dynamic change in bonding between Ag and S atoms.

A further exciting evolution step towards an optimized performance and oxidation stability (or less-pronounced air sensitivity) was the combination of semiconductors like 2D materials to so called van der Waals heterostructures [Geim 2013]. Different 2D materials are connected by weak van der Waals interactions to generate heterostructures with unusual

properties and exciting phenomena. As shown recently, new preparation methods like autoperforation emerged which allows an effective production of 2D heterostructures with remarkable chemical and mechanical stability also making a large scale production possible [Liu 2018].

The consequent next evolution step was to further reduce dimensionality to 1D semiconductor systems. Element and compound nanowire materials have been developed in the past years which offer an increased surface area and flexibility compared with 2D systems. If fabricated in almost atomic diameters [Wang 2013, Ross 2014, Yue 2016], either as free standing oriented or randomly arranged systems, they offer enhanced flexibility and larger specific surface than the 2D counterparts. Here we report on selected physical properties of pure and SnIP heterostructure systems. Various organic polymers frequently used in batteries, solar cells, and thermoelectric applications, or C_3N_4 were successfully used to form heterostructures with SnIP. In the case of SnIP@C_3N_4 heterostructures, a remarkable photoelectrochemical stability and spontaneous core-shell segregation were observed which illustrates the potential of double helical SnIP as a defined 1D material for semiconductor applications. In the SnIP@C_3N_4 composites or heterostructures, the self-organization of C_3N_4 wrapped around SnIP due to van der Waals interactions is an example of polymer-like behavior while the photoelectrochemical performance is contingent to the semiconducting behavior of SnIP.

SnIP, an inorganic double-helical semiconductor

Recently, SnIP, representing the first inorganic, atomic-scale, double helix compound, attracted reasonable interest due to its intriguing structural, electronic, and optical properties [Pfister 2016]. Two helices, a small $^1_\infty[P^-]$ and a larger $^1_\infty[SnI^+]$ helix nested the former into the latter in such a way that a double helix is formed. One left and right-handed double helix are stacked along the crystallographic a-axis in a hexagonal array of rods. In Hermann-Mauguin notation the two double helices present in SnIP with opposite chirality, a left handed

M-helix or a right handed P-helix, fulfill the rod groups $p\,7_32$ and $p\,7_42$, respectively [Müller 2017]. Due to the anisotropic structural features with covalently-bonded helices and weak van der Waals-like interactions between the double-helix rods, this material can be the ideal candidate to combine the beneficial properties of two classes of materials, the electric properties of an inorganic semiconductor and the mechanical properties of polymer-like systems. The structural anisotropy of SnIP is manifest in the pronounced needle-like morphology and gives therefore rise to interesting direction-dependent phenomena. Well-defined anisotropic physical properties are expected.

Mechanical properties of SnIP

Compressibility and bulk modulus of SnIP

The response to (hydrostatic) pressures and in turn the mechanical properties of SnIP were investigated by employing high pressure powder X-ray diffraction (HPPXRD, Table S2-1). In a first step, HPPXRD experiments were performed using a diamond anvil cell (DAC) setup to overview the behaviour of SnIP in the pressure range p = ambient – 4 GPa (see Figure 1a). During this experiment SnIP was constantly illuminated by X-rays (energy of 25.5 keV) for more than 20 hours substantiating the stability against hard X-rays. Subsequent profile fits of the PXRD data allow for extracting the cell parameters as a function of pressure. Lattice parameters are given in Table S2-1. We observe anisotropic contraction upon the application of pressure, SnIP being more compressive within the *bc*-plane. This is in good agreement with the crystal chemistry of SnIP, in which the *bc*-plane is mainly governed by weak Van-der-Waals interactions. Furthermore, the *V*(*p*) relation indicates that SnIP is a very soft material with relatively large changes of the unit cell as function of pressure. In a second experiment we performed HPPXRD using a low-pressure cell (LPC) to access the V(p) relation at very low pressures, ensuring hydrostatic conditions during the experiment. The LPC setup is suitable for HPXRD in the pressure range p = ambient to 0.4 GPa (Figure 1a, purple crosses), being ideal for the investigation of very soft materials [Dissegna 2018].

Figure 1. a) Evolution of lattice parameters and cell volumes (black from DAC; purple crosses from LPC) of SnIP up to pressures of 4 GPa. b) The bulk modulus of 15.57 GPa was derived from a 3rd order Birch Murnaghan equation of state fit given in orange. Two independent sets of cell volume measurements were performed in a diamond anvil cell (DAC) and a low pressure cell (LPC, non DAC). c) Crystal structure sections of SnIP (insets, blue P, grey Sn, purple I) and bulk modulus of SnIP in relation to selected inorganic semiconductors, elements and liquids. d) Normalized cumulative thermal conductivity of SnIP as a function of phonon mean free path.

The bulk modulus of SnIP was extracted by fitting a 3rd order Birch-Murnaghan equation of state to the V(p) values in the compiled dataset between p = ambient to 0.5 GPa. We find a bulk modulus of K = 15.57 GPa (with K' = 8.2 GPa) and an estimated error of 5 % (see Figure 1b and supplement for details). Comparing this value with related materials with semiconducting properties like IV, III-V or II-VI semiconductors, we find SnIP being the softest inorganic main group semiconductor currently known, see Figure 1c. The bulk modulus is 3 to 7 times lower than such state-of-the-art semiconductors. This certainly originates from the unique bond situation, with weak Van-der-Waals interaction within the *bc-*plane which facilitate a high compressibility, together with strong covalent interactions along

the helices which allow a spring-like behaviour and for the formation of semiconducting properties.

Bending properties of SnIP needles

In order to evaluate the bending properties of SnIP in more detail we investigated the Young's modulus by the aid of Atomic Force Microscopy (AFM) in nanoindentation mode along the double helix axis [100] for wires with different diameters. We found an averaged Young's modulus in the order of 190 GPa for SnIP wires consisting of several helix strands, which is in the same order of magnitude as silicon with 175 GPa [111], 130 GPa [100] and Ga*Pn* [100] with *Pn* = N, P, As with 191, 103 and 85 GPa, respectively [Adachi 2005]. A selected measurement is given in Figure 2a. Bending SnIP along the double helix axis is obviously as hard as bending IV or III-V semiconductors in selected directions which leads to the conclusion that the covalently-bonded substructures in SnIP, the different helices and the dative ionic interaction between them (see [Pfister 2016]) define the bending force. SnIP shows a Young's modulus along the double helix axis which is comparable to steel reported to be 180 to 200 GPa [Chen 2016]. The flexibility in [010] and [001] is caused by the intrinsic nature of the SnIP structure, the double helical arrangement itself and the stacking of the double helices along the *a*-axis, which allows reversible bending in those directions without serious degradation. The interplay of both structural features account for the Young's modulus in those wires which seem to consist of several helix strands. Of course, due to the strong anisotropy and direction dependency of the Young's modulus on the one hand and the different structures of Si and Ga*Pn* compared with SnIP on the other hand, a direct comparison of the Young's moduli can only be regarded as a first estimate for the softness of the title compound. Further details concerning the determination of the Young's modulus are given in the supplement (Figures S1 and S2, Table S1-1).
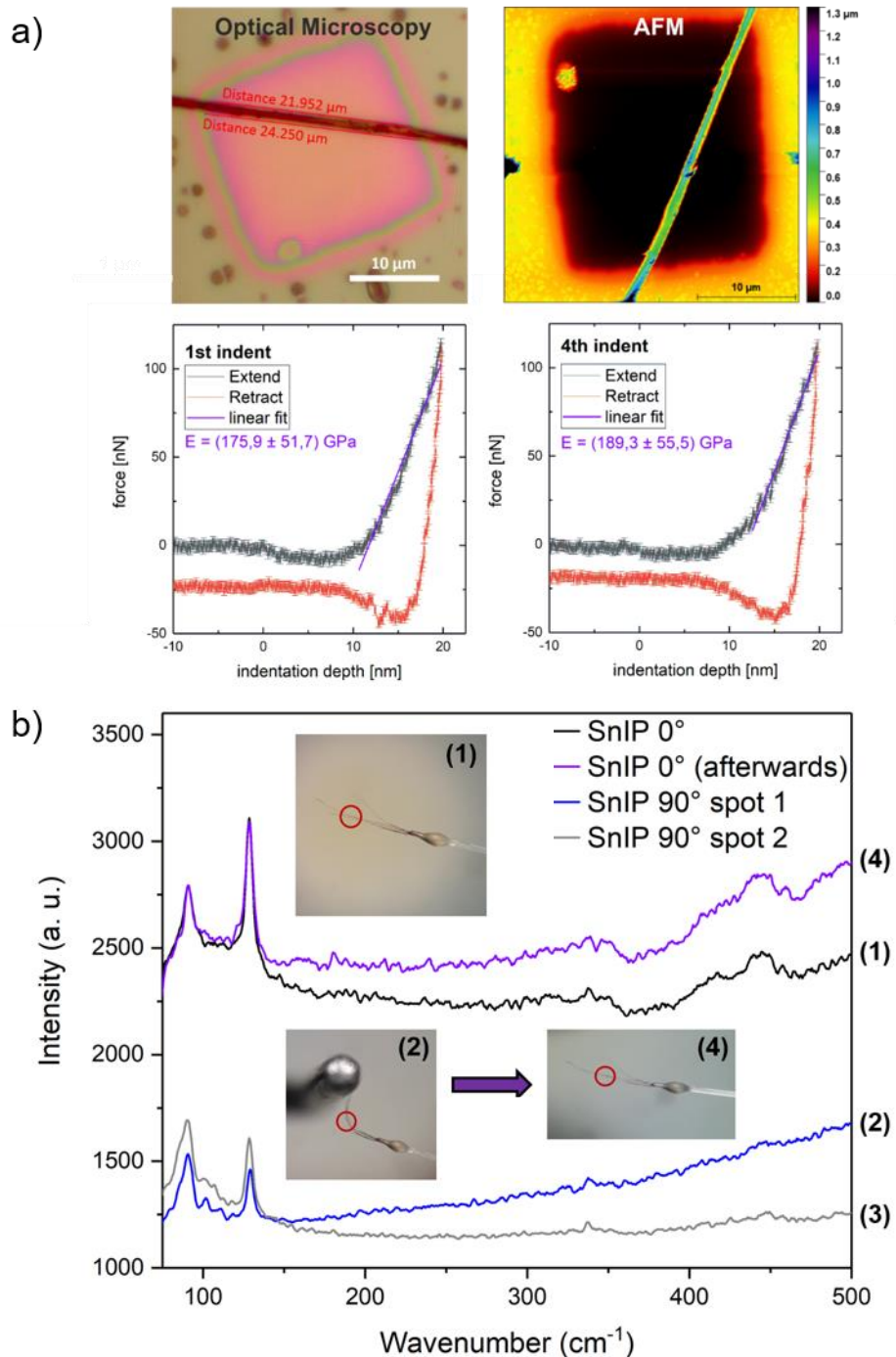
Figure 2. a) Young's Modulus determination by Atomic Force Microscopy (AFM) measurements. Optical- and AFM measurements of a suspended wire (wire 2) are shown. Two force-distance curves (Young's modulus extracted as discussed in the supplement) taken in the middle of the wire. b) In situ Raman spectroscopy on SnIP upon bending. (1) to (4) Raman microscope measurements on red circle, without bending (1), after 90° bending, first bending (2), after second 90° bending (3) and after full relaxation (4).

The question arose whether mechanical deformation (bending) of SnIP crystals will

cause degradation or will have an impact on the bonding within the double helices. For Van-

der-Waals layered α-Ag$_2$S where it was shown that this material prevents cleavage upon bending by sliding along the (100) Ag-S slip planes (slip direction is [001]) [Shi 2018]. In the case of 1D-SnIP a slipping might occur in [100] parallel to the double helix strands.

Quantum chemical calculations were used to assign the main Raman modes and the Phonons of for SnIP (see supplement, Videos and Figure S3 to S5). For both cases, spectra were recorded at room temperature and ambient pressure followed by a full assignment of the modes. In the following, the experiments are briefly discussed in detail.

According to our calculations we defined three distinct regions in the Raman spectrum, representing the interactions of the outer [SnI] helix at 120 to 150 cm^{-1} (Sn-I breathing region), the inner [P] helix at 350 to 380 cm^{-1} (P-P stretching region), and the interaction between the inner [P] and the outer [SnI] helix (P-P breathing region; further details see supplement, Figure S3). Correlating these regions with the crystal structure and bonding situation in SnIP, the Sn-I breathing region is determined by the strong Sn-I and the weak van der Waals interactions between the double helices. Upon a so called breathing of the outer helix the forces are determined by the intra Sn-I interactions realizing the bonding within the helix and the inter Sn-I interactions between adjacent double helix strands. According to previously reported DFT calculations [Pfister 2016] the energy of this inter double helix interaction of van der Waals type is about 25 kJ mole^{-1}. The P-P stretching region is defined by the covalent P-P bonding of the inner [P]-helix. Finally, the P-P breathing region represents the dative-ionic interaction between the outer positively charged [SnI] and the inner negatively-charged [P] helix. In situ Raman spectra were performed using SnIP crystals upon bending. As shown in Figure 2b, SnIP can be bent at least up to 90° without a shift in Raman modes. Especially the strong Sn-I breathing mode at approx. 129 cm^{-1} (observed) 125 cm^{-1} (calculated) is not affected by this mechanical deformation. This result is promising for an application of SnIP in flexible devices. We performed quantum chemical calculations to determine the influence of high-pressure on highly flexible SnIP and to evaluate the pressure-dependent structure changes. Hence, we used the cell parameters determined up to 11 GPa in a DAC cell from our pressure-dependent experiments as fixed

values and optimized the internal coordinates within the framework of DFT theory and using HSE06 functionals with Grimme D2 corrections (citations see materials section). Inter double helix distances between Sn and I of neighboring double helices, representing the origin of the weak van der Waals interactions, are the most affected ones as expected from the chemical bonding situation in SnIP. Upon pressure increase, the bond distances of Sn-I within the outer helix shrink from 3.2 Å (0.1 GPa) to 3.0 Å (11.5 GPa) while the inter double helix Sn-I distance goes down from 3.8 Å (0.1 GPa) to 3.3 Å (11.5 GPa). Nevertheless, we did not find a hint for a structural phase transition up to this pressure. All bond lengths determined for the different atom pairs are in sense full regions (see supplement, Figures S6 to S8).

Phonons and anisotropic thermal properties of SnIP

We calculated the phonon spectra (Figure S4) of SnIP with the aid of DFT and computed phonon-resolved contribution to heat transport. The thermal conductivity is in general very low, and anisotropic, with different values along (κ_a=1.8 W m^{-1} K^{-1} at room temperature) and across the helices (κ_{bc}<1 W m^{-1} K^{-1}). Given the stark difference between the type of bonding along and across the helices, such small anisotropy is surprising. Across the double helices in the *bc* plane we see a significantly lower value for the mean free paths of phonons than along the helices (See Figure 1a and the supplement), indicating that there is still room for suppressing the axial component of the thermal conductivity, either by introducing defects or in composites. While van der Waals interactions account for the low value of κ_{bc}, relatively soft acoustic modes dictate the low thermal conductivity along the helices. Low values of κ may turn out interesting for both thermal insulation and thermoelectric applications.

Phonons were measured by Inelastic Neutron Scattering (INS) and peaks were assigned relying by DFT calculations (Figure S5). In good accordance with the Raman investigations we were able to distinguish between phosphorus and [SnI] phonons in the spectrum (see supplement). The phosphorus motions can be broadly broken down into

concentric helical breathing and twisting modes (442, 330/265 cm^{-1}). Stretching modes along the axis of the helices occur at 339.6 cm^{-1}. The fact that these two sets of modes are comparable in frequency, yet involve spatial dimensions with varying mechanical properties indicates that the P motions are largely localized, and independent of the lateral inter-helical interactions. A phonon mode of the outer Sn-I helix is localized at 99 cm^{-1}.

SnIP heterostructure formation

SnIP@polymer heterostructures

Encouraged by these promising results we started to evaluate if SnIP hybrids with organic polymers can be synthesized. Different polymers were chosen as the polymer part in the hybrids due to their frequent usage in various applications as devices and membranes. We examined polyethylene glycol (PEO, solid electrolyte, batteries) and polyvinyl pyrrolidone (PVP), poly(3,4-ethylenedioxythiophene)-poly(styrenesulfonate) (PEDOT/PSS, solar cells) or Poly(3-hexylthiophen-2,5-diyl) (P3HT; solar cells), and fluorine/chloride doped C_3N_4 (water splitting) due to their importance for energy conversion and storage applications. In all cases, SnIP@polymer hybrids were synthesized by spin-coating for thin films, and electrospinning to achieve fiber membranes. SnIP can be incorporated in all such polymers without the loss of its structural properties (see supplement chapter 3.1, Figures S9 to S12) which qualifies it for a plethora of possible applications.

SnIP@carbon nanotube heterostructures

Another approach is to generate hybrid 1D heterostructures of SnIP with carbon nanotubes. This was, for instance, successfully performed for elements like phosphorus [Zhang 2017, Hart 2017] and selenium [Fujimori 2013] in multi-walled carbon nanotubes. We conducted first principle DFT calculations including empirical dispersion corrections for SnIP@Carbon nanotube(CNT) heterostructures. Three different types of CNT, a metallic, semimetallic and semiconducting one, were selected based on their inner diameter to

accommodate a single P-double helix (rod group $p 7_42$) of SnIP. According to our calculations, a (10,10), (18,0), and (19,0) CNT are the most suitable candidates for the stabilization of single SnIP strands concerning simple space filling aspects of SnIP and the diameter of a given CNT (see supplement Chapter 3.2, Figure S13). Once realized, such heterostructures provide access to chiral right or left-handed SnIP strands which may give rise to interesting topological quantum properties (e.g. Kramers-Weyl fermions [Chang 2018]). Single SnIP strands are highly helicoidal, if not perfectly helicoidal, and could therefore exhibit quantized electronic effects.

SnIP@C_3N_4(F,Cl) heterostructures and water splitting

We investigated one promising 1D heterostructure in more detail, that is the combination of SnIP with halide-doped C_3N_4 (Figure S14). Fluorine and chlorine co-doped C_3N_4 (CNFCl) were used to fabricate SnIP@C_3N_4(F,Cl) thin-film devices for water splitting experiments (Figure 3a). A series of devices with compositions starting from 10 wt% SnIP in C_3N_4(F,Cl) up to 90 wt% were fabricated. They will be called SnIP/CNFCl_X with X = 10, 20, …, 90 in the following. Three representative devices are shown in Figure 3a (further details in Figure S15). UV-Vis spectra in Figure 3b clearly show the two distinct absorption band edges, corresponding to CNFCl at ~ 420 nm and to SnIP at ~ 650 nm for the different samples. The CNFCl displayed a peak at *ca.* 300 nm due to π-π* transition and another peak at *ca.* 380 nm with an extended band tail up to 500 nm originated due to n-π* transition. For the SnIP/CNFCl the UV-Vis absorbance was strongly increased in the visible spectral region with a sharp band edge at 690 nm clearly indicating improvement of visible light absorption by SnIP/CNFCl composite. Further, the band gap of materials was determined with the help of Tauc plots. The band gap of CNFCl was found to be 2.41 eV, slightly lower than previously reported method for F doped g-C_3N_4 which might be due to formation of sheets and intercalation of some chlorine. The SnIP/CNFCl composites show two band edge positions corresponded to CNFCl and SnIP at 2.39 and 1.70 eV respectively. For higher SnIP content,

the band edge is red-shifted to 1.50 eV due to the dominant contribution of SnIP in photon absorption pattern.

All devices were subject to extensive characterization. Adding SnIP to CNFCl does not significantly change the resistivity (Figure 3c) of the thin film device and SnIP remained crystalline after the fabrication process (cf. Figure 3e). The XRD diffractogram of CNFCl display a broad reflection at 2θ values ~27.1º corresponded to (002) planes with a 0.33 nm interlayer d than that reported for pristine g-C_3N_4 (0.32 nm) which was assumed to be due to increased repulsion owing to out-of-plane F atoms. SnIP exhibits various XRD reflections at 2θ values of 24.1º, 27.4º, 29.1º, 30.4º, 31.6º, 32.3º, 34.1º, 40.1º and 44.5º in excellent agreement with the previous literature. On mixing and wrapping CNFCl around the SnIP nanorod structure, as the wt% of SnIP in the blend is increased, the peak at ~27.1º for CNFCl weakens and the peaks of SnIP begin to strengthen in intensity. Steady state PL spectra (Figure S16) of CNFCl show an intense and broad PL peak at centered at 481 nm, which is indicative of radiative recombination process of photogenerated charge carriers. For SnIP the PL peak intensity was extremely small. After coating of CNFCl on SnIP nanorod structure, the PL intensity of CNFCl was decreased significantly which was assumed due to efficient charge separation process. Further to investigate nature of charge carrier recombination processes and their lifetime, we have performed time resolved photoluminescence lifetime (TRPL) measurement by using 405 nm excitation laser. The PL decay curve of the CNFCl and SnIP can be fitted tri-exponentially using following equation:

$$I(t) = A_1 e^{-t/\tau_1} + A_2 e^{-t/\tau_2} + A_3 e^{-t/\tau_3} \qquad (1)$$

where, A_1, A_2 and A_3 represent normalized percentage of each decay components and τ_1, τ_2 and τ_3 are e lifetime of each decay components respectively. The presence of three PL lifetime decay components in PL lifetime decay curve of CNFCl was in good agreement with previously reported literature and originated due to inter-band π*-π, π*-LP and trap assisted recombination within sheets respectively [Yang 2017, Kang 2016]. The effective lifetime (τ_{eff})

which is more accurate and rational measure of charge carrier separability was calculated using following expression.

$$\tau_{\text{eff}} = (A_1\tau_1^2 + A_2\tau_2^2 + A_3\tau_3^2) / (A_1\tau_1 + A_2\tau_2 + A_3\tau_3) \tag{2}$$

The average lifetimes of CNFCl, 10% SnIP/CNFCl, 20% SnIP/CNFCl, 30% SnIP/CNFCl and 70% SnIP/CNFCl were found to be 4.57, 4.85, 4.67, 4.77 and 4.54 ns respectively, which revealed efficient charge separation process, which was assumed to occur due to efficient coating and breaking of π-π stacking symmetry of wrapped CNFCl sheets [Kang 2015].
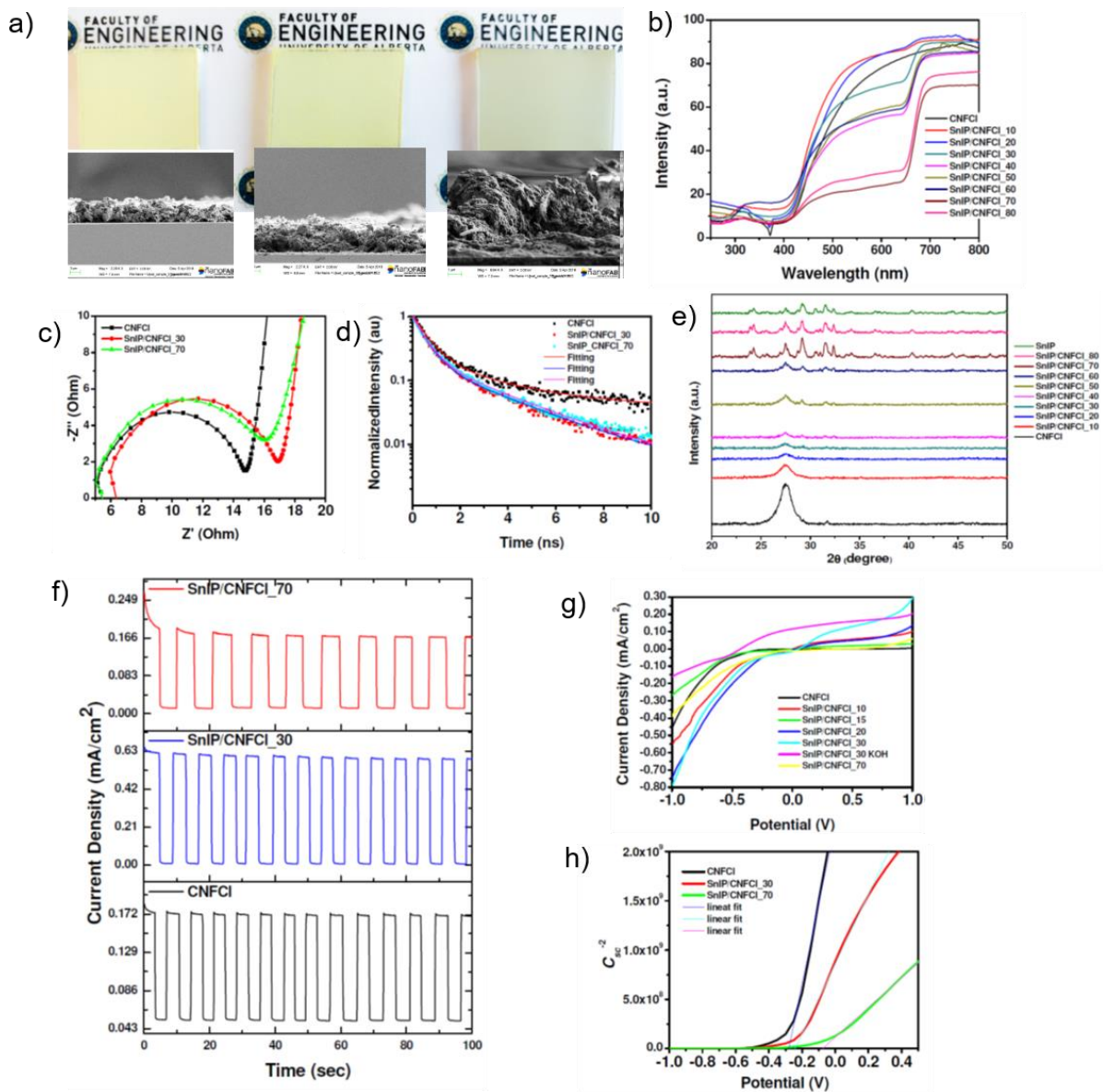
Figure 3. SnIP@C$_3$N$_4$(F,Cl) devices of different compositions were tested for water splitting properties. a) SnIP@C$_3$N$_4$(F,Cl) thin-film devices and SEM pictures of bare CNFCl, SnIP/CNFCl_30 and SnIP/CNFCl_70 samples. b) UV-Vis spectra of a series of SnIP@C$_3$N$_4$(F,Cl) devices. c) Impedance measurements of bare CNFCl, SnIP/CNFCl_30 and SnIP/CNFCl_70 devices. d) Photoluminescence lifetime measurements bare CNFCl, SnIP/CNFCl_30 and SnIP/CNFCl_70 devices. e) Powder-XRD measurements of SnIP@C$_3$N$_4$(F,Cl) devices. f) Light response and current densities of bare CNFCl, bare SnIP and SnIP/CNFCl_30 devices. g) Current density vs. potential curves for SnIP@C$_3$N$_4$(F,Cl) devices. h) Mott-Schottky measurements performed in 0.5M NaSO$_4$ solution featuring flat band positions for CNFCl, 30% SnIP/CNFCl and 70% CNFCl at −0.28, −0.24 and −0.07 V vs. Ag/AgCl, respectively.
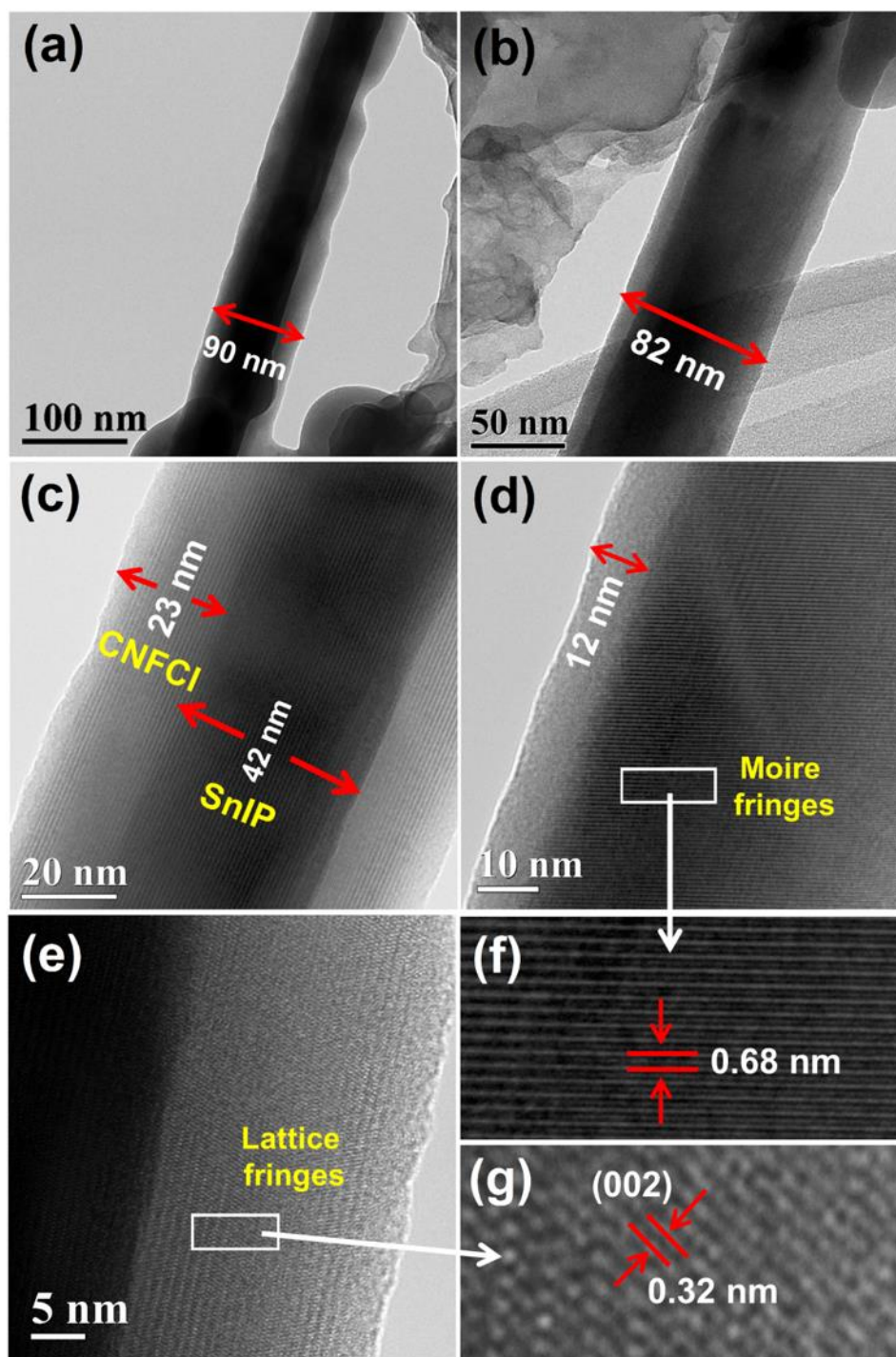
Figure 4. HRTEM images of 30% SnIP/CNFCl showing CNFCl wrapped SnIP nanorods at (a-b) 100 nm scale bar showing average thickness of CNFCl enwrapped nanostructures, (c) image at 20 nm scale showing inner SnIP core and CNFCl wrapped shell, (d) enlarged image at 10 nm depicting Moire fringes and shell of CNFCl, (e) image at 5 nm scale showing lattice fringes of CNFCl shell, (f) showing zoomed view of Moire fringes and (g) zoomed view of shell showing 2 spacing of CNFCl sheets.

The beneficial properties explained above encouraged us to measure the activity of the SnIP@CNFCl hybrids in photoelectrochemical water splitting. By themselves, SnIP and CNFCl are subject to severe leaching in aqueous electrolytes and the photoelectrochemical

performance of each is very poor due to leaching and charge transfer problems. However, the SnIP@CNFCl hybrids displayed very promising photoelectrochemical performance (Figures 3f and 3g) and extended durability of the photoresponse (Figure 3f). The light response was checked for bare $C_3N_4(F,Cl)$ as well as selected $SnIP@C_3N_4(F,Cl)$ hybrid devices, as shown in Figure 3f. While $C_3N_4(F,Cl)$ and the $SnIP/C_3N_4(F,Cl)\_70$ sample show almost the same current density of 160 to 170 $\mu A/cm^2$ in on/off measurements, an optimized ratio of the two components in $SnIP/C_3N_4(F,Cl)\_30$ led to a significant almost four-fold improvement resulting in a current density of 0.6 mA/cm^2. Such a remarkable improvement in both the photoelectrochemical stability and photoelectrochemical performance of the SnIP@CNFCl hybrids over the stand-alone SnIP and CNFCl photoanodes stimulated further characterization to understand the structure of the heterojunction.

To elucidate the energy level alignment in the hybrids, Mott Schottky measurements were performed in 0.5 M Na_2SO_4 solution (Figure 3h). The flat band positions from Mott Schottky plot for CNFCl, 30% SnIP/CNFCl and 70% CNFCl were found to be at −0.28, −0.24 and −0.07 V vs. Ag/AgCl, respectively. The wrapping of CNFCl on SnIP nanorod structures leads to n-type behavior of the hybrids. Further to determine the position of valence band (VB) XPS spectra were collected and extrapolation of linear region on X and Y scale and point of intersection gave the position of the valence band with respect to the Fermi level. From the VB XPS spectra, the position of the valence band of SnIP, CNFCl and 30% SnIP/CNFCl were determined to be 1.19, 1.83 and 2.27 eV. The value of VB for 30% SnIP/CNFCl was found to be intermediate between pristine CNFCl and SnIP.

The HR-TEM image of 30% SnIP/CNFCl composite shows a clear 1D core-shell nanorod morphology with a diameter of ~80-90 nm, consisting of a dense SnIP core (~ 40-50 nm) and sparse CNFCl shell wrapping the SnIP (Figure 4a-c). However, the thickness of CNFCl shell was not constant and varied from 12-25 nm. High magnification HR-TEM images show higher *d* spacing (0.65 nm) Moire fringes (Figure 4d-f). The Moire fringes are usually observed in layered materials and originate from mismatched superimposition (dislocation or rotational) of two lattices with identical or very small difference in *d* spacing.

The presence of Moire fringes implicates that process of few layered CNFCl sheets folding on SnIP cores leads to lattice mismatch (probably rotational) and prevents perfect π-π stacking. Additionally, the HR-TEM image at 5 nm scale bar also shows lattice fringes with smaller *d* spacing of 0.32 nm corroborated to (002) planes of multilayered sheets with graphitic structure. The presence of CNFCl sheets wrapped around SnIP nanorods was validated by quantitative elemental mapping which displays the relative concentration of various elements in a single core-shell nanorod measured in STEM mode (Figure 5). Figure 5a displays the bright field electron images of 30% SnIP/CNFCl and the area of scanning. The elemental mapping of SnIP/CNFCl shows equally intense and evenly distributed concentration of Sn, I and P in the center of scanned area confirms presence of SnIP core (Figure 5b-d) while the higher concentration of C, N, F and O at the outer shell confirms the presence of CNFCl wrapped shell (Figure 5e-h). Further, integration of images on RGB (red, green and blue) scale to determine comparative distribution C, N and F to Sn, I and P clearly demonstrates dense SnIP core surrounded by CNFCl shell and confirms the SnIP/CNFCl core shell structure (Figure 5i-l). Additionally, EDX spectra of mapped area show presence of Sn, I, P, C, N and F elements with approximately 3:4 C:N at% ratio, and further confirms the SnIP/CNFCl core shell morphology (Figure S17a). Elemental line scan to verify an even distribution of CNFCl over SnIP nanorod structure indeed shows an even distribution of C, N and F with high signal intensities for Sn, I and P at the center confirming that SnIP nanorods were efficiently covered with CNFCl sheets (Figure S17b).
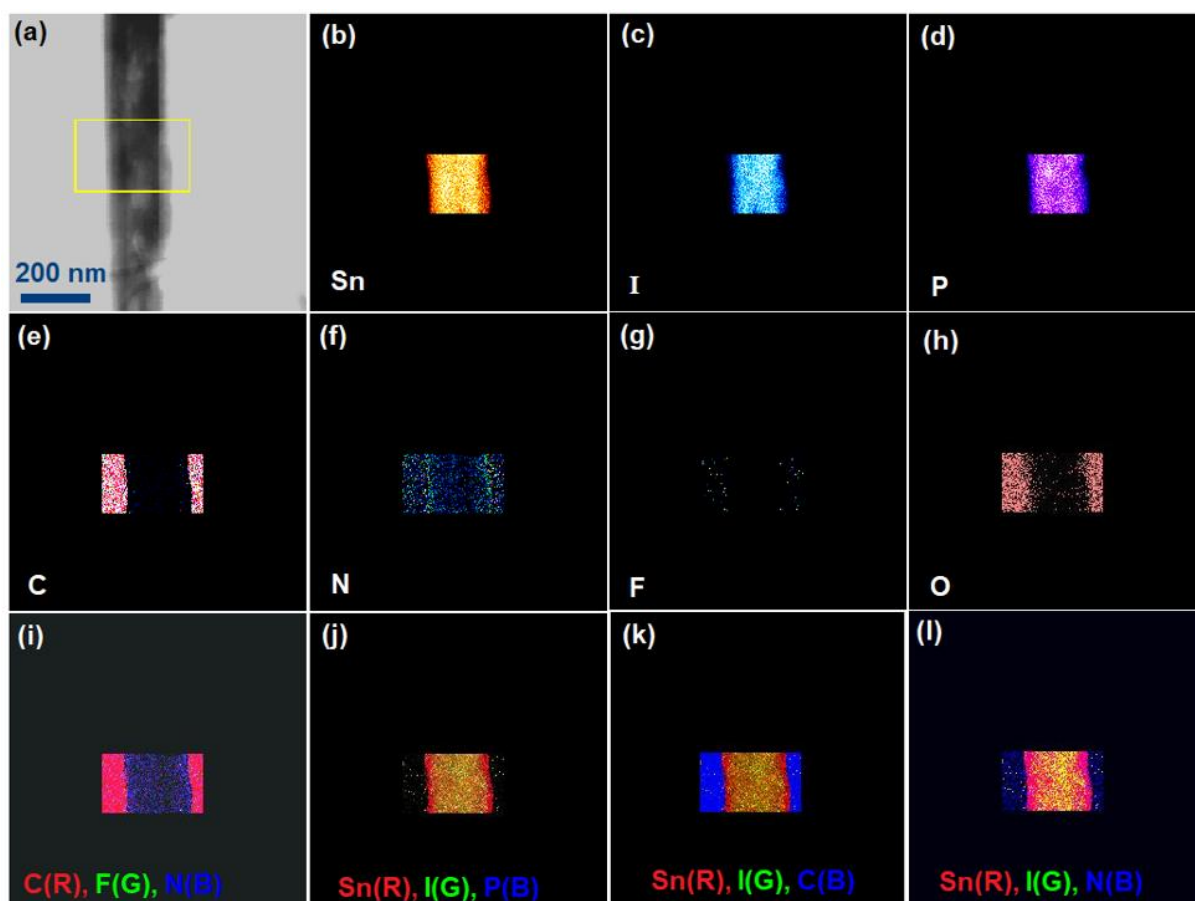
Figure 5. STEM elemental mapping of 30% SnIP/CNFCl (a) HAADF image, and mapping for (b) Sn, (c) I, (d) P, (e) C, (f) N, (g) F, (h) O, and RGB images (i) C (red), F (green), N (blue), (j) Sn (red), I (green), P (blue), (k) Sn (red), I (green), C (blue), (l) Sn (red), I (green), N (blue).

High resolution X-ray photoelectron spectroscopy (HR-XPS) was employed to unveil the surface chemical composition (Figure 6). There was no indication of chemical bonding between SnIP and CNFCl, thus lending support to the strong interaction between the two materials being governed entirely by weaker van der Waals forces. Various peaks in the XPS survey scan of SnIP (Sn3d, I3d, P2p), CNFCl (C1s, N1s, F1s) and 30% SnIP/CNFCl (Sn3d, I3d, P2p, C1s, N1s, F1s) confirm the presence of all the relevant elements in the materials (Figure S18a). The deconvoluted HR-XPS spectra of pristine SnIP in Sn 3d region gave two peaks centered at binding energy (BE) 487.05 and 495.50 eV corroborated to $Sn3d_{5/2}$ and $Sn3d_{3/2}$ components which reveals the presence of chemically equivalent Sn^{2+} (Figure S18b). The HR-XPS in I3d region depicted two peak components at binding energies 619.32 and 630.91 eV. While the peak in P2p region can be split into two peak components located at 133.57 and 139.44 eV assigned to crystallographically different P species in SnIP (Figure

S18d). The HR-XPS spectrum of CNFCl in C1s region after deconvolution gave peak components located at BE values of 284.5, 286.12 and 288.12 eV assigned to adventitious and sp^3 hybridized C, C-N and $N=C-N_2$ carbons in $g-C_3N_4$ [Yu 2017]. Further, deconvoluted N1s spectra show four peak components at binding energies of 398.58, 399.90, 401.17 and 404.40 eV, which were assigned to C-N=C, $N-(C)_3$, $H-N-C_2$ and π-π* confirming a well ordered $g-C_3N_4$ structure [Fang 2015]. Further, F1s XPS shows one intense peak at a binding energy of 686.13 eV confirming successful doping of F atoms in the carbon nitride scaffold. Additionally, the presence of a single peak component in the O1s region at a BE value of 532.04 eV originates from surface adsorbed water and -OH moiety. The XPS spectra of 30% SnIP/CNFCl display all the peaks corresponding to SnIP and CNFCl.
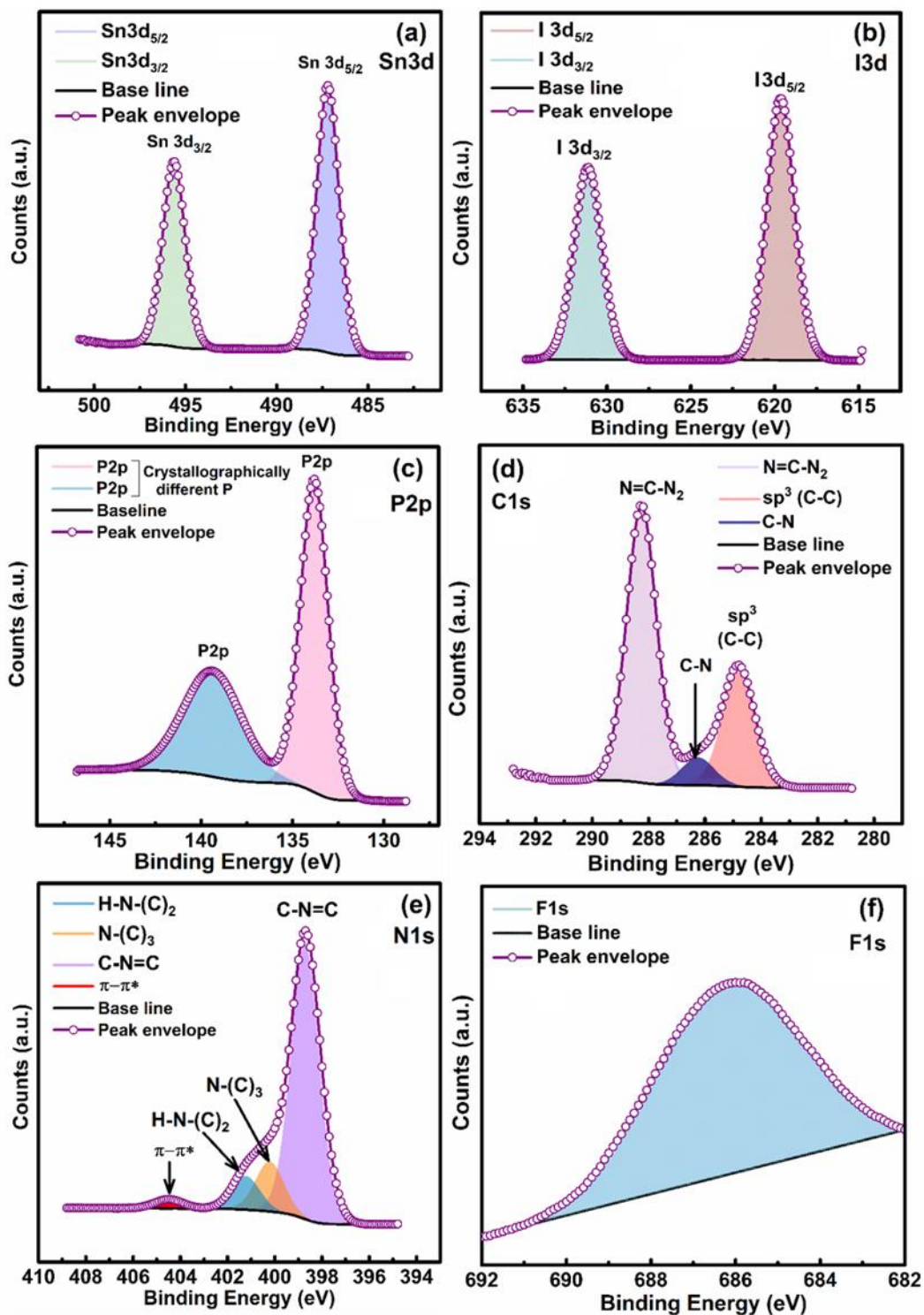
Figure 6. HR-XPS core level spectra of 30% SnIP/CNFCl in (a) Sn3d, (b) I3d, (c) P2p, (d) C1s, (e) N1s, (f) F1s regions.

Conclusion and outlook

SnIP has proven to be a highly flexible and stable 1D semiconductor for 1D semiconductor devices. In situ Raman spectroscopy substantiated the robustness and flexibility of SnIP upon bending, featuring an unaffected bonding within the single helices. SnIP show a comparable Young's modulus like steel along the double helix axis while the bulk modulus of bare SnIP is remarkably low, being approximately four times smaller than any state-of-the-art inorganic group IV, III-V or II-VI semiconductors. Due to its structure, SnIP shows polymer-like behavior which is unusual for a pure inorganic material. Its structural anisotropy is also reflected in the thermal transport properties. According to DFT calculations, SnIP shows a very low and anisotropic, thermal conductivity with significantly shorter mean free pathways for phonons perpendicular than along the double helices. Heading towards the first atomic-scale chiral inorganic semiconductor, first principle calculations regarding the existence and possible formation of single SnIP double helix@CNT heterostructures were successful and reasonable metallic, semimetallic and semiconducting CNTs were identified as possible hosts.

Based on the anisotropy of SnIP, its ability to be delaminated into small nanofibers, and the weak van der Waals bonding among SnIP double helices and to neighbored species, this material offers remarkable mechanic properties. Different important non-conductive/conductive polymers and halide-doped C_3N_4 were selected for the successful fabrication of thin-film and electrospun hybrid materials as well as 1D heterostructures. SnIP is stable in such environments and therefore defines a solid basis for future application in energy conversion and storage processes. Especially the ability of SnIP to coordinate to extended π systems offers great opportunities for functionalization and heterostructure formation with organic and inorganic compounds. 1D van der Waals type SnIP@C_3N_4(F,Cl) heterostructures were tested for water splitting purposes. An almost fourfold increase of the water splitting tendency was observed for a C_3N_4(F,Cl) 30:70 heterostructure device. Beside 3D quantum dots, the large family of layered or so called 2D semiconductors, strongly anisotropic 1D SnIP and its hetero structure representatives are promising candidates of a

new class of flexible semiconductors with a great potential in materials science and energy

related developments.

References

[Adachi 2005] S. Adachi in Properties of Group IV, III-V and II-VI Semiconductors, John Wiley & Sons, Chinchester, GB, P. 55.

[Alivisatos 1996] A. P. Alivisatos, Semiconductor Clusters, Nanocrystals, and Quantum Dots. A. P. Science (1996), 271, 933–937.

[Chang 2018] Guoqing Chang, Benjamin J. Wieder, Frank Schindler, Daniel S. Sanchez, Ilya Belopolski, Shin-Ming Huang, Bahadur Singh, Di Wu, Tay-Rong Chang, Titus Neupert, Su-Yang Xu, Hsin Lin, M. Zahid Hasan, Topological quantum properties of chiral crystals. Nature Mater., 2018, 17, 978–985.

[Chen 2016] Z. Chen, U. Ghandi, J. Lee, R. H. Wagoner, Variation and consistency of Young's modulus in steel, J. Mater. Pro. Tec., 2016, 227, 227-243.

[Fang 2015] J. Fang, H. Fan, M. Li, C. Long, Nitrogen self-doped graphitic carbon nitride as efficient visible light photocatalyst for hydrogen evolution. J. Mater. Chem. A (2015) 3, 13819–13826.

[Fujimori 2013] T. Fujimori, R. Batista dos Santos, T. Hayashi, M. Endo, K. Kaneko, D. Tománek, Formation and properties of Selenium Double Helices inside Double-wall Carbon Nanotubes: Experiment and Theory. ACS Nano (2013), 7, 5607–5613.

[Geim 2007] A. K. Geim, K. S. Novoselov, The rise of graphene. Nature Mater. (2007), 6, 183–191.

[Geim 2013] A. K. Geim, I. V. Grigorieva, Van der Waals heterostructures. Nature (2013), 499, 419–425.

[Hart 2017] M. Hart, E. R. White, J. Chen, C. M. McGilvery, C. J. Pickard, A. Michaelides, A. Sella, M. S. P. Shaffer, C. G. Salzmann, Encapsulation and Polymerization of White Phosphorus Inside Carbon Nanotubes. Angew. Chem. Int. Ed. (2017), 56, 8144–8148.

[Jose 2014] D. Jose, A. Datta, Structures and Chemical Properties of Silicene: Unlike Graphene. Acc. Chem. Res. (2014), 47, 593–602.

[Kang 2015] Y. Kang, Y. Yang, L.-C. Yin, X. Kang, G. Liu, H.-M. Cheng, An Amorphous Carbon Nitride Photocatalyst with Greatly Extended Visible-Light-Responsive Range for Photocatalytic Hydrogen Generation. Adv. Mater. (2015) 27, 4572–457.

[Kang 2016] Y. Kang, Y. Yang, L.-C. Yin, X. Kang, L. Wang, G. Liu, H.-M. Cheng, Selective breaking of hydrogen bonds of layered carbon nitride for visible light photocatalysis. Adv. Mater. (2016) 28, 6471–6477.

[Li 2014] L. Li, Y. Yu, G. J. Ye, Q. Ge, X. Ou, H. Wu, D. Feng, X. H. Chen, Y. Zhang, Black phosphorus field-effect transistors. Nature Nanotechnol. (2014), 9, 372–377.

[Liu 2014] H. Liu, A. T. Neal, Z. Zhu, Z. Luo, X. Xu, D. Tománek, P. D. Ye, Phosphorene: An Unexplored 2D Semiconductor with a High Hole Mobility. ACS Nano (2014), 8, 4033–4041.

[Liu 2018] P. Liu, A. T. Liu, D. Kozawa, J. Dong, J. F. Yang, V. B. Koman, M. Saccone, S. Wang, Y. Son, M. H. Wong, M. S. Strano, Autoperforation of 2D materials for generating two-terminal memristive Janus particles. Nature Mater, 2018, 17, 1005–1012.

[Manzeli 2017] S. Manzeli, D. Ovchinnikov, D. Pasquier, O. V. Yazyev, A. Kis, 2D Transition Metal Dichalcogenides. Nat. Rev. Mater. 2017, 2, 17033.

[Mao 2017] J. Mao, T. Peng, X. Zhang, K. Li, L. Ye, L. Zan, Effect of graphitic carbon nitride microstructures on the activity and selectivity of photocatalytic CO_2 reduction under visible light. Catal. Sci. Technol. (2013) 3, 1253–1260.

[Pfister 2016] D. Pfister, K. Schäfer, C. Ott, B. Gerke, R. Pöttgen, O. Janka, M. Baumgartner, A. Efimova, A. Hohmann, P.Schmidt, S. Venkatachalam, L. van Wüllen, U. Schürmann, L. Kienle, V. Duppel, E. Parzinger, B. Miller, J. Becker, A. Holleitner, R. Weihrich, T. Nilges, Inorganic Double Helices in Semiconducting SnIP. Adv. Mater. (2016), 28, 9783–9791.

[Reithmaier 2004] J. P. Reithmaier, G. Sek, A. Löffler, C. Hofmann, S. Kuhn, S. Reitzenstein, L. V. Keldysh, V. D. Kulakovskii, T. L. Reinecke, A. Forchel, Strong coupling in a single quantum dot-semiconductor microcavity system. Nature (2004), 432, 197–200.

[Ross 2014] Y.-C. Chou, K. Hillerich, J. Tersoff, M. C. Reuter, K. A. Dick, F. M. Ross, Atomic-scale variability and control of III-V nanowire growth kinetics. Science (2014), 343, 281–284.

[Vogt 2012] P. Vogt, P. De Padova, C. Quaresima, J. Avila, E. Frantzeskakis, M. C. Asensio, A. Resta, B. Ealet, G. Le Lay, Silicene: Compelling Experimental Evidence for Graphenelike Two-Dimensional Silicon. Phys. Rev. Lett. (2012), 108, 155501.

[Shi 2018] X. Shi, H. Chen, F. Hao, R. Liu, T. Wang, P. Qiu, U. Burkhardt, Y. Grin, L. Chen, Room-temperature ductile inorganic semiconductor. Nature Mater. (2018), 17, 421–426.

[Tao 2015] L. Tao, E. Cinquanta, D. Chiappe, C. Grazianetti, M. Fanciulli, M. Dubey, A. Molle, D. Akinwande, Silicene field-effect transistors operating at room temperature. Nature Nanotechnol. (2015), 10, 227–231.

[Manzeli 2017] S. Manzeli, D. Ovchinnikov, D. Pasquier, O. V. Yazyev, A. Kis, 2D Transition Metal Dichalcogenides. Nat. Rev. Mater. 2017, 2 (8), 17033.

[Müller 2017] U. Müller, Die Symmetrie von Spiralketten. Acta Cryst. B (2017), 73, 443–452.

[Ugeda 2014] M. M. Ugeda, A. J. Bradley, S.-F. Shi, F. H. da Jornada, Y. Zhang, D. Y. Qiu, W. Ruan, S.-K. Mo, Z. Hussain, Z.-X. Shen, F. Wang, S. G. Louie, M. F. Crommie, Giant bandgap renormalization and excitonic effects in a monolayer transition. Nature Mater. (2014), 13, 1091–1095.

[Wang 2013] H. Wang, L. A. Zepeda-Ruiz, G. H. Gilmer, M. Upmanyu, Atomistics of vapour–liquid–solid nanowire growth. Nat. Commun. 2013, 4, 1956 doi: 10.1038/ncomms2956.

[Yang 2017] P. Yang, H. Ou, Y. Fang, X. Wang, A facile steam reforming strategy to delaminate layered carbon nitride semiconductors for photoredox catalysis. Angew. Chem. Int. Ed. (2017) 129, 4050–4054.

[Yu 2017] H. Yu, R. Shi, Y. Zhao, T. Bian, Y. Zhao, C. Zhou, G. I. N. Waterhouse, L.-Z. Wu, C.-H. Tung, T. Zhang, Alkali-Assisted Synthesis of Nitrogen Deficient Graphitic Carbon Nitride with Tunable Band Structures for Efficient Visible-Light-Driven Hydrogen Evolution. Adv. Mater. 2017, 29, 1605148.

[Yue 2016] Y. Yue, Q. Zhang, Z. Yang, Q. Gong, L. Guo, Study of the Mechanical Behavior of Radially Grown Fivefold Twinned Nanowires on the Atomic Scale. Small, 2016, 12, 3503–3509.

[Zhang 2017] J. Zhang, D. Zhao, D. Xiao, C. Ma, H. Du, X. Li, L. Zhang, J. Huang, H. Huang, C.-L. Jia, D. Tománek, C. Niu, Assembly of Ring-Shaped Phosphorus within Carbon Nanotube Nanoreactors. Angew. Chem. Int. Ed., 2017, 56, 1850–1854.

Acknowledgement

Author contributions

T.N. and K.S. initiated the study. C.O. and F.R. prepared the samples and measured physical properties. M.P. and M.B. conducted the quantum chemical calculations and A.V. measured Raman spectra. S.C. and Da.Do. calculated the phonon spectra and thermal conductivity. G.K., Do.Da., S.B., M.E. and F.R. collected and analyzed the pressure-dependent synchrotron data. T.U.K., P.K. and K.S. planned and conducted the water splitting experiments and measured the electrochemical properties. L.S.W. and R.T.W. performed the Young's modulus experiments. T.N., K.S., and G.K. wrote the paper with contributions from all other authors.

Competing interests

The authors declare no competing interests.

Methods.

Synthesis of SnIP. SnIP was prepared from the elements in a solid state short-way transport reaction according to the procedure described in the literature (Pfister 2016). 48.3 mg Tin (99.99%, VWR CHEMICALS), 16.8 mg red phosphorous (> 99.999%, CHEMPUR) and 84.9 mg SnI_4 were mixed and sealed in a silica glass ampule under vacuum ($\rho < 10^{-3}$ mbar). Phase pure SnI_4 was prepared according to literature [Köpf 2014].

The ampoule (length 6 cm) was placed in a NABERTHERM Muffle Furnace (L3/11/330) with the educts located close to the heating plates and the empty part of the ampoule towards in the cooler middle part of the oven. The mixture was then heated up to 673 K within 4 h, kept at this temperature for 48 h within the natural temperature gradient of the muffle furnace, and cooled down to room temperature in 120 h afterwards.

Phase purity was checked prior to all following experiments by powder X-ray phase analysis and semi-quantitative EDX analyses. SnIP was phase pure within the detection limit of X-ray diffraction and EDX analyses showed the expected atomic ratio of 1:1:1 for Sn:P:I. No other impurities were found.

Chemical exfoliation of SnIP. SnIP needles were mechanically ground in an agate mortar and suspended in toluene or water. The mixture treated with an IKA T18 digital ULTRA TURRAX at 13000 rpm for 10 min. To achieve even smaller particles the suspension was treated with a SONOPLUS ultrasonic-homogenizer from BANDELIN for 10 h. This approach yields in nanorods with diameters smaller than 25 nm. The suspension was dried under vacuum to obtain a homogeneous powder. The product was analyzed via an optical light microscope from LEICA DM 1750 M (10 × 100 magnification), powder diffraction and scanning electron microscopy.

Film Formation, coating methods and electrospinning. The different polymers were dissolved in a suitable solvent and stirred for an hour. SnIP was added to the polymer solution and stirred until a homogeneous 10:1, 1:1 or 1:10 suspension was achieved. The suspension was drop coated, spin coated or solution casted onto a glass microscope slide and dried at room temperature. If the polymer was unstable under ambient conditions, the procedure was conducted under inert conditions, in the dark or at a reduced temperature. The homogeneity of the formed films was verified via optical light microscopy (LEICA DM 1750 M, 10 × 100 magnification) and scanning electron microscopy.

The electrospinning solution was prepared by dissolving PEO (7.95 mmol, 0.35 g) in 5 mL acetonitrile (VWR, >99.8, H2O <30 ppm). After 1 h SnIP was added in a PEO:SnIP weight ratio of 10:1 or 1:1. The obtained suspension was stirred 24 h for homogenization. The whole process was performed in a flask under Argon atmosphere. Subsequently, the solution was used for electrospinning in a self-made electrospinning apparatus described elsewhere [Freitag 2017]. During electrospinning a 0.9 mm (inner diameter) injector was used at a flow rate of 3.5 mL min^{-1} and an acceleration voltage of 10.9 kV. To aim for membranes with aligned fibers, a collector consisting of two parallel, separately grounded, aluminum plates was used. The obtained membranes were dried under vacuum for 24 h prior to analysis.

Formation of SnIP-CNFCl hybrids.
For the synthesis of SnIP/CNFCl composites, 30 mg mL^{-1} suspension of CNFCl was prepared in chlorobenzene by sonicating 4 h followed by addition of calculated wt% amount (10−90 wt%) of SnIP. The obtained mixture was sonicated for 30 min and later stirred for 24 h to get CNFCl enwrapped SnIP nanocomposite (SnIP/CNFCl). The afforded SnIP/CNFCl nanocomposite was dried by evaporating chlorobenzene. For comparison, control samples of SnIP and CNFCl was also prepared under identical conditions.

Quantum-chemical calculations. Pressure dependent calculations were performed in the framework of DFT using the Crystal14 code [Dovesi 2014]. For the contemplated elements effective core pseudopotential (ECP) and all electron valence basis sets [Pascale 2005] were used. A shrinking factor of 8 8, creating a Pack-Monkhorst net of 170 k-points in the irreducible part of the reciprocal unit cell, delivered reliable results. The pressure was simulated by reducing the respective unit cell axis lengths in steps of 2% of the axis lengths. For a better description of the weak dispersion interactions between the double helical strands the Grimme D2 dispersion [Grimme 2006] was applied.

Phonon dispersion relations and thermal transport are computed by first-principles density functional theory (DFT) calculations within local density approximation (LDA) of the exchange and correlation functional [Perdew 1981], using the Quantum-Espresso package [Giannozzi 2009]. Core electrons are approximated using Projector-Augmented Wave (PAW) pseudopotentials [Blöchl 1994, Kresse 1999], and the Kohn-Sham wavefunctions are expanded on a plane wave basis set with a cutoff of 60 Ry (816 eV). The charge density is integrated on 4x4x2 Monkhorst-Pack meshes of k-points [Monkhorst 1976]. The convergence thresholds for electronic self-consistent calculation and for ionic relaxation are 10^{-12} Ry and 10^{-4} Ry/au, respectively.

Harmonic second order interatomic force constants (IFCs) and phonon spectra are computed using density-functional perturbation theory (DFPT) [Baroni 2001] with 4x4x2 q-mesh. Anharmonic third order IFCs are computed by finite differences ($\Delta x=0.01$ Å), in a 2x2x1 a supercell containing 168 atoms, with a cutoff interaction distance up to the 6th shell of neighbours. Translational invariance of the anharmonic force constants is enforced using the Lagrangian approach [Li 2014] . With the second and third order IFCs, the thermal conductivity of SnIP is computed by solving the phonon Boltzmann transport equation (BTE) with an iterative self-consistent algorithm, using the ShengBTE code [Li 2014] with q-point grids up to 12x12x6, considering phonon-phonon and isotopic scattering [Tamura 1983].

Ab-initio calculations on SnIP@CNT heterostructures were performed using the Crystal17 code [Dovesi 2017]. Due to the size of the systems the GGA-level functional from Perdew, Burke and Enzerhof (PBE) [Perdew 1996, Paier 2005] was used to optimize the geometry as a 1D-material. The converged structures were restarted with the HSE06 functional [Krukau 2008, Heyd 2006] for better comparability. For contemplated elements, LCAO - basis sets with an effective core pseudopotential (ECP) and an all electron valence were chosen. With the shrinking factor of 10 10, a Pack-Monkhorst net [Monkhorst 1976] was converged in the reciprocal space. The structures were optimized with (and without) assumed strong dispersion forces following the Grimme scheme [Grimme 2006]. For the visualization of the structures the graphical surface of the JMOL package was used. The electronic properties (band structure, DOS and frequency) were calculated with the Crystal17 properties setup [Dovesi 2017] and visualized by the CRYSPLOT online tool from the university of Torino [Crysplot 2016].

Morphology, structure, composition and optical properties. Semi-quantitative elemental analyses were performed using a JOEL JCM-6000 NeoScop™ scanning electron microscope with an integrated JOEL JED-2200 EDS unit. The acceleration voltage was 15 kV. The measured composition is in good agreement with the nominal composition. No impurities were detected. The FE-SEM elemental mapping and energy dispersive spectrometry (EDS) was acquired on Zeiss Sigma FESEM w/EDX&EBSD integrated with Oxford AZtecSynergy system working at 15 kV acceleration voltage. The acquisition time for collecting elemental scan was 300 s. High resolution transmission microscopy (HR-TEM) for determining ultrafine morphological features, EDX elemental mapping and bright field images of materials were recorded on a JEOL JEM-ARM200CF S/TEM equipped with STEM EDX detector, operating at an acceleration voltage of 200 keV. The samples for HR-TEM were prepared by deposition of very dilute suspension of sample in methanol on a lacy carbon coated copper TEM grid

followed by drying under table lamp. The system generated .dm3 HR-TEM files were processed with Gatan micrograph to determine size and interplanar 2d spacing while elemental mapping files were processed with INCA Energy to extract 16-bit depth files and later processed in Gatan micrograph to derive RGB images. The surface chemical nature and binding energy of various elements in samples were determined with X-ray photoelectron spectroscopy (XPS) employing XPS (Axis-Ultra, Kratos Analytical) instrument endowed with monochromatic Al-Kα source (15 kV, 50 W) and photon energy of 1486.7 eV under ultrahigh vacuum (~10^{-8} Torr). To assign the binding energy of various elements the C1s XPS peak of adventitious carbons at binding energy BE ≈ 284.8 eV was used as standard for carbon correction. Acquired raw data were deconvoluted in to various peak component by using CasaXPS software and exported .csv files and plotted in origin 8.5. The crystalline features and phase structure of materials were executed with powder X-ray diffraction (XRD) recorded on Bruker D8 Discover instrument using Cu-Kα radiation (40 kV, λ = 0.15418 nm) equipped with a LynxEYE 1-dimensional detector. The spectra were recorded in a range of 2θ value 20–70° with a scan size 0.02°. The absorption properties of materials in UV-Vis region were determined by diffuse reflectance UV-Vis (DR UV-Vis) using a Perkin Elmer Lambda-1050 UV–Vis-NIR spectrophotometer equipped with an integrating sphere accessory. The steady state photoluminescence (PL) spectra to investigate photoluminescence behavior of materials were executed by using Varian Cary Eclipse fluorimeter armed with xenon lamp excitation source with a slit width of 5 nm. The PL lifetime decay curve of materials were determined with Time-resolved photoluminescence (TRPL) using a homemade single photon counting. A 405-nm picosecond diode laser (Alphalas GmbH) operated at a frequency of 13 MHz was used to excite the samples, and a Becker-Hickl HPM-100-50 PMT interfaced to an SPC-130 pulse counter system to collect signals. The response time of setup was ~100 ps.

Raman spectroscopy on SnIP. Raman spectra of pure SnIP and hybrids were obtained by a SENTERRA Spectrometer (BRUKEROPTICS GmbH) equipped with a 532 nm laser, between 0.1 and 1% power (1 mW) and an integration time between 30 and 250 s. The magnification was of 50× (slide 50 × 1000 μm, zoom lens 50 long distance).

Inelastic neutron scattering on SnIP. High-resolution INS measurements on a 3 g powder sample in a flat aluminium cell of cross-sectional area 4×4.8 cm² were performed at the inverted-geometry neutron spectrometer TOSCA [Pinna 2018], spanning energy transfers up to 4000 cm^{-1}, at the ISIS Pulsed Neutron & Muon Source, Rutherford Appleton Laboratory, United Kingdom. The spectral resolution of TOSCA is similar to that of infrared and Raman techniques, being approximately 2% of the energy in question. The sample was studied at low temperature (~10 K) using a dedicated closed-cycle helium refrigerator, so as to minimize the effect of the Debye Waller factor, thus allowing us to fully distinguish the individual peaks. Data were reduced with the Mantid software [Arnold 2014]. DFT phonon calculations were compared directly to the data from TOSCA via data processing in the software package AbINS [Krzysztof 2018].

High pressure synchrotron experiments. All high-pressure powder X-ray experiments were performed at the beamline I15 at the Diamond Lightsource, UK with an X-ray wavelength of 25.5 keV (Ag K edge). For Diamond Anvil Cell experiments, DACs with Diamonds with 750 μ in diameter were used with Daphne oil 50 as pressure transmitting medium and ruby fluorescence as pressure calibrant. Daphne oil is known to behave hydrostatic until a pressure of approximately p = 0.9 GPa. However, HPXRD DAC experiments were performed in the pressure range p = ambient – 4 GPa. For the DAC measurements a 2D Mythen area detector was used, of which the sample-to-detector distance was calibrated prior to the experiment with a CeO$_2$ standard. High pressure experiments in the low-pressure regime between p = ambient – 0.4 GPa in 250 bar steps were performed by using a self-built high-pressure cell (https://www.imperial.ac.uk/pressurecell/). Similar to the DAC experiments, Daphne oil 50 was

used as pressure transmitting medium. In the case of these experiments, a 2D PerkinElmer detector was used and the sample-to-detector distance calibrated with using CeO2 as standard. It should be noted that during sample loading, the sample-to-detector distance might be slightly changed, which was taken care of in the profile fit analysis. The 2D detector files of both experiments were compiled to 1D HPPXRD data by using DAWN.

Powder diffraction (PXRD). Phase analysis of the nanostructured SnIP powder and the obtained hybrid films was conducted using X-ray powder diffraction. The unit cell parameters were determined with the software suit STOE WINXPOW [Stoe 2011]. The crystal parameters of SnIP were taken from the literature [Pfister 2016]. All analyzed samples were ground in an agate mortar, placed between two stripes of SCOTCH® MagicTM 810, 3M tape and fixed onto a flat sample holder. The measurements were conducted using Cu-Kα1 radiation (λ = 1.54051 Å, Ge(111) monochromator) on a STOE Stadi-P powder diffraction diffractometer, equipped with a DECTRIS MYTHEN 1K detector. The measurements were conducted in a range between 5 and 90° 2θ within 15 min.

High pressure PXRD analysis. Profile fits of the obtained HPPXRD data were performed with TOPAS academic v5. As mentioned above, the sample-to-detector distance of the LPC possibly changes due to sample mounting. Therefore, HPPXRD data of the LPC setup was initially calibrated against the V(p=ambient) volume of the DAC experiments. The obtained values, and particularly the slopes of both datasets are in very good agreement (see Figure 1b in the manuscript). Additionally, attention was paid to the evolution of the full-width of half maximum (FWHM) as a function of pressure. Whilst there is no significant change of the FWHM of the LPC experiment, we find an onset of increasing FWHM for the DAC experiments at around ~ 1.1 GPa which is in good agreement with the reported hydrostatic limit of Daphne oil of approximately 0.9 GPa. Furthermore, a Ff-plot (strain vs. normalized pressure), points at the presence of a pressure induced phase transition in SnIP at around 0.6 GPa which is not visible by normal inspection of the PXRD pattern. Since the bulk modulus is not defined over a phase transition, only 5 data points from DAC experiments can be used for the analysis of the bulk modulus in the range p < 0.6 GPa. To obtain the bulk modulus to the highest possible accuracy, LPC experiments were performed and the bulk modulus obtained from both fitting a Birch-Murnaghan equation of state to the compiled dataset, obtaining a bulk modulus of K = 15.45 (with K' = 8.21 GPa). In order to test the accuracy of the bulk modulus against measurement errors due to different cell setups, the bulk moduli of the single measurement were also calculated to K(LPC) = 15.1 GPa and K(DAC) = 16.1 GPa. Hence, we estimate the error of the bulk modulus of approximately 5%.

Thermal Analysis. The thermal analysis of the starting polymers and hybrid films were conducted with a NETZSCH DSC 200 F3 Maia up to a maximum of 623 K. The samples were sealed under inert conditions in an aluminum crucible. Both, the heating and cooling rate were set to 10 K min^{-1}.

Electrochemical characterization. Mott-Schottky plot was accumulated from impedance-potential values in 0.5 M Na_2SO_4 in the −1.0 to +1.0 V voltage range at 1K frequency. Nyquist plot was prepared by Electrochemical impedance spectroscopy (EIS), measured using a three electrodes configuration at applied voltage of −0.5 V vs. Ag/AgCl in 0.1 M Na_2SO_4, with AC amplitude of 0.005 V at frequency value 100 kHz.

Photoelectrochemical experiments. Prior to photoelectrochemical measurements, a 60 nm thick TiO_2 blocking layer was deposited on cleaned FTO glass slides by spin casting using titanium isopropoxide solution as precursor, and then used as the substrate for subsequent experiments. The CNFCl and various wt% SnIP/CNFCl samples were mixed with α-terpineol (film forming agent) to obtain a concentration of 30 mg mL^{-1} and stirred for 2 h. The obtained solution was drop coated onto the substrate followed by heating at 250 ℃ for 1 h. The

fabricated thin film was sealed with a Surlyn sheet keeping a 1-inch diameter circular surface exposed. The thin film on substrate was assigned as the photoanode (working electrode) in a three electrode system water-splitting setup while Pt and Ag/AgCl were used as counter electrode (cathode) and reference electrode, respectively. The photoelectrochemical water splitting experiment was performed by immersing the electrodes in 0.1 M Na_2SO_4 solution. The photoanode was irradiated under simulated sunlight (AM 1.5 G) with an intensity of 100 mW cm^{-2} at the surface of the sample. Wavelengths lower than 420 nm were filtered using a UV cut off filter to ascertain the visible light response of samples. Photocurrent density vs. applied voltage graph to check photoresponse of samples were determined by linear sweep voltammetry by sweeping voltage from –0.8V to +0.8 V. Additionally, photoresponse at 425 and 505 nm wavelength was investigated by irradiating sample with 450 and 505 nm LEDs. The LEDs were calibrated with a photodiode and the power density on the surface of samples were calculated to be 47.70 and 40.48 mW cm^{-2} for 425 and 505 nm LEDs respectively. For comparison dark current was also measured.

Young's modulus determination. The Young's modulus was determined using a Nanoscope Dimension 3000 Atomic Force Microscope (AFM) in nanoindenation mode. We have etched 500 nm deep, about 25 x 25 µm² wide trenches into an SiO_2 coated Si wafer via reactive ion etch using a TEM grid as shadow mask. Subsequently, SnIP wires were deposited by immersing the etched substrates into the SnIP suspension for about 10 min until the solvent (toluene) was evaporated. The samples were not rinsed off or blow-dried to prevent displacement of the wires. Suitable wires bridging etched holes were located under an optical microscope (Figures S1a and S2a).

References material section

[Arnold 2014] <u>O. Arnold</u>, <u>J. C. Bilheux</u>, <u>J. M. Borreguero</u>, <u>A. Buts</u>, <u>S. I. Campbell</u>, <u>L. Chapon</u>, <u>M. Doucet</u>, <u>N. Draper</u>, <u>R. Ferraz Leal</u>, <u>M. A. Gigg</u>, <u>V. E. Lynch</u>, <u>A. Markvardsen</u>, <u>D. J. Mikkelson</u>, <u>R. L. Mikkelson</u>, <u>R. Miller</u>, <u>K. Palmen</u>, <u>P. Parker</u>, <u>G. Passos</u>, <u>T. G. Perring</u>, <u>P. F. Peterson</u>, <u>S. Ren</u>, <u>M. A. Reuter</u>, <u>A. T. Savici</u>, <u>J. W. Taylor</u>, <u>R. J. Taylor</u>, <u>R. Tolchenov</u>, <u>W. Zhou</u>, <u>J. Zikovsky</u>, Mantid—Data analysis and visualization package for neutron scattering 15 and SR experiments. Nuclear Instruments and Methods in Physics Research Section A: Accelerators, Spectrometers, Detectors and Associated Equipment 2014, 764, 156-166.

[Baroni 2001] S. Baroni, S. De Gironcoli, A. Dal Corso, P. Giannozzi, Phonons and related crystal properties from density-functional perturbation theory. Rev. Mod. Phys. 2001, 73 (2), 515–562.

[Blöchl 1994] P. E. Blöchl, Projector augmented-wave method. Phys. Rev. B 1994, 50, 17953–17979.

[Crysplot 2016] CRYSPLOT. 2016; Available from:
 http://crysplot.crystalsolutions.eu/index.html.

[Dovesi 2014] R. Dovesi, R. Orlando, A. Erba, C. M. Zicovich-Wilson, B. Civalleri, S. Casassa, L. Maschio, M. Ferrabone, M. De La Pierre, P. D'Arco, Y. Noël, M. Causà, M. Rérat, B. Kirtman, CRYSTAL14: A Program for the Ab Initio Investigation of Crystalline Solids. Int. J. Quant. Chem. 2014, 114, 1287–1317.

[Dovesi 2017] R. Dovesi, C. Roetti, R. Orlando, C. M. Zicovich-Wilson, F. Pascale, B. Civalleri, K. Doll, N. M. Harrison, I. J. Bush, P. D'Arco, M. Llunell, M. Causà, Y. Noël, L. Maschio, A. Erba, M. Rerat, S. Casassa, CRYSTAL 17 User's Manual. 2017: University of Torino.

[Freitag 2017] K. M. Freitag, H. Kirchhain, L. van Wüllen, Tom Nilges, Enhancement of Li Ion Conductivity by Electrospun Polymer Fibers and Direct Fabrication of Solvent-Free Separator Membranes for Li Ion Batteries. Inorg. Chem. 2017, 56, 2100–2107.

[Giannozzi 2009] P.Giannozzi, et al., QUANTUM ESPRESSO: a modular and open-source software project for quantum simulations of materials. J. Phys. Condens. Matter 2009, 21, 395502.

[Grimme 2006] S. Grimme, Semiempirical GGA-type density functional constructed with a long-range dispersion correction. J. Comput. Chem., 2006, 27, 1787-1799.

[Heyd 2006] J. Heyd, G. E. Scuseria, M. Ernzerhof, Hybrid functionals based on a screened Coulomb potential. J. Chem. Phys., 2006, 124, 219906.

[Li 2014] W. Li, J. Carrete, N. A. Katcho, N. Mingo, ShengBTE: A solver of the Boltzmann transport equation for phonons. Comput. Phys. Commun., 2014, 185, 1747–1758.

[Köpf 2014] M. Köpf, N. Eckstein, D. Pfister, C. Grotz, I. Krüger, M. Greiwe, T. Hansen, H. Kohlmann, T. Nilges. Access and in situ growth of phosphorene-precursor black phosphorus. J. Cryst. Growth, 2014, 405, 6.

[Kresse 1999] G. Kresse, D. Joubert, From ultrasoft pseudopotentials to the projector augmented-wave method. Phys. Rev. B 1999, 59, 1758–1775.

[Krukau 2008] A. V. Krukau, et al., Hybrid functionals with local range separation. J. Chem. Phys., 2008, 129, 124103.

[Krzysztof 2018] K. Dymkowski, S. F. Parker, F. Fernandez-Alonso, S. Mukhopadhyay, AbINS: The modern software for INS interpretation, Physica B: Condensed Matter (2018) 1–6

[Monkhorst, 1976] H. J. Monkhorst, J. D. Pack, Special points for Brillouin-zone integrations. Phys. Rev. B 1976, 13 (12), 5188–5192.

[Paier 2005] J. Paier, et al., The Perdew–Burke–Ernzerhof exchange-correlation functional applied to the G2-1 test set using a plane-wave basis set. J. Chem. Phys., 2005, 122, 234102.

[Pascale 2005] F. Pascale, C. M. Zicovich-Wilson, R. Orlando, C. Roetti, P. Ugliengo, R. Dovesi, Vibration Frequencies of $Mg_3Al_2Si_3O_{12}$ Pyrope. An ab Initio Study with the CRYSTAL Code. J. Phys. Chem. B, 2005, 109, 6146−6152.

[Perdew 1981] J. P. Perdew, A. Zunger, Self-interaction correction to density-functional approximations for many-electron systems. Phys. Rev. B 1981, 23 (10), 5048–5079.

[Perdew 1996] J. P. Perdew, K. Burke, M. Ernzerhof, Generalized Gradient Approximation Made Simple. Phys. Rev. Lett., 1996, 77, 3865-3868.

[Pinna 2018] R. S. Pinna, S. Rudić, S. F. Parker, J. Armstrong, M. Zanetti, G. Škoro, S. P. Waller, D. Zacek, C. A. Smith, M. J. Capstick, D. J. McPhail, D. E. Pooley, G. D. Howells, G. Gorini, F. Fernandez-Alonso, The neutron guide upgrade of the TOSCA spectrometer. Nucl. Instrum. Methods Phys Res A, 2018, 896, 68-74.

[Stoe 2011] WinXpow Software, Stoe & Cie GmbH, Darmstadt, Germany, Version 3.0.2.1. (2011).

[Tamura 1983] S.-I. Tamura, Isotope scattering of dispersive phonons in Ge. Phys. Rev. B, 1983, 27, 858–866.

Supplement

1. Mechanical properties of individual, suspended SnIP nanowires

To determine the mechanical properties of individual SnIP nanowires, we have realized suspended nanowires and measured the Young's modulus of such individual wires using an Atomic Force Microscope. The double helix axis runs along the needle axis.

Force-deflection spectroscopy

The Young's modulus has been measured with an Atomic Force Microscope (AFM) in nanoindenation mode following a protocol similar to what has previously been described e.g. by G. Xiong et al. [Xiong 2006]. However, it is noteworthy that usually wires with diameters one order of magnitude below ours are detected using this procedure [Xiong 2006, Nam 2006, Habtoun 2017]. Prior to each measurement, the profile of the respective wire was recorded (see e.g. Figure S1b and S2b), to make sure that a clean region of the wire is indented. The indentation was performed in approximately the middle of the holes. For the indentation measurements, we used a maximal force between approximately 100 and 250 nN. The AFM detects the deflection of the laser beam as a voltage difference on a four-quadrant diode D depending on the position of the piezo z. The raw data are calculated to the force applied to the wire according to Hook's Law $F = k \cdot x = k \cdot S \cdot D$ and the indentation depth $\delta = z - \frac{F}{k}$, where $k = 40 N/m$ is the spring constant of the cantilever (BudgetSensors, BS-Tap300Al) and S is the cantilever sensitivity determined by a calibration measurement on a hard substrate (here pure SiO$_2$).

For determination of the Young's modulus we have used the Euler-Bernoulli beam equation as has also been used in [Xiong 2006], giving the relation of indentation depth to applied force in the middle of the freestanding wire part as

$$\delta = \frac{F \, l^3}{192 \, E \, I} \textbf{(1)}$$

with l the length of the suspended part of the wire, E the Young's modulus. As area-moment of inertia I in the direction parallel to the indentation direction, we have used the formula $I = \frac{\pi}{64} w h^3$ for a beam with an elliptic cross section with w the width and h the height of the beam [Gere 2006]. The wire height is measured as height difference between wire and substrate next to the trench using the AFM (Figure S1b and S2b), while its width is measured after all mechanical measurements using a scanning electron microscope (SEM, Figure S1c and S2c). The wire length across the hole is determined using optical microscopy (Figure S1a and S2a). If we include the moment of inertia into equation (1), we find:

$$\mathbf{F} = \frac{3\pi w h^3}{l^3} E \cdot \delta \quad \textbf{(2)}$$

Fitting the slope of the linear regime in the force-distance curve and dividing by the factor $\frac{3\pi w h^3}{l^3}$ results in the Young's modulus E (Figure S1d, e and S2d, e).

For each wire, we have indented three to four times to test if the applied force has affected the mechanical properties of the wires and found that for four out of the five wires tested the extracted Young's modulus has not changed significantly for the indents. For one of the wires (wire 8), a slight increase of the Young's modulus for each indentation can be observed.

We have indented about 20 – 40 nm for each wire, thus making sure that the bending angle is well below 5° and the previously described theory can be applied [Wang 2018]. Also, our wires were not clamped on the SiO_2 surface at the edges of the holes and thus might in principle slip during indentation resulting in a non-linear behavior in the force-distance curve [Wang 2018]. However, such a deviation can only be supposed for one of the wires (wire 11). Consequently, we assume (as also was previously done [Xiong 2006, Wang 2018]) that in our measurements the substrate-supported parts of the wires do not move due to a sufficient adhesion of the wires on the substrate.

According to the theory described above, the force-distance curve has to be detected in the center of the wire. However, as it was also assured that no dirt on top of the wire was indented, it was not always possible to precisely hit the wire center. Furthermore, the wires are not perfectly uniform (compare e.g. Figure S2b), making the value for the area-moment of inertia only an approximation.

We have measured the Young's modulus E of five suspended wires, the detailed data of two of these wires are shown in Figures S1 and S2. Wire 2, 10 and 11 showed comparable results and were used to characterize SnIP. Figure S1 illustrates such a measurement. In the case of wire 5 (Figure S2) and wire 8 we found strongly deviating values for the Young's modulus which are related to structural degradation or sliding of SnIP double helices of the wire upon indentation. At the point where the indentation took place (Figure S2b, c) one can observe a deformation of the wire. Therefore, such measurements were not used for the characterization of the material.

E was found to be on the order of 190 GPa and consequently higher than in the bulk measurements discussed in the main text. Possibly the reason is that during sample preparation the wires were disassembled mechanically, thereby applying high forces and hardening the wires. Furthermore, we measured smaller Young's Moduli for thicker wires, which in contradiction seem to consist of several helix strands, allowing them to slip along each other upon bending.

Furthermore, the nanoindenation measurements only probe E in the direction along the wire, while the bulk measurements provide an average over all directions, hence giving evidence for the strong anisotropic behavior of SnIP. The respective Young's modulus of all measured wires and a selection of reported Young's modulus of different main group element semiconductors is given in Table S1-1.
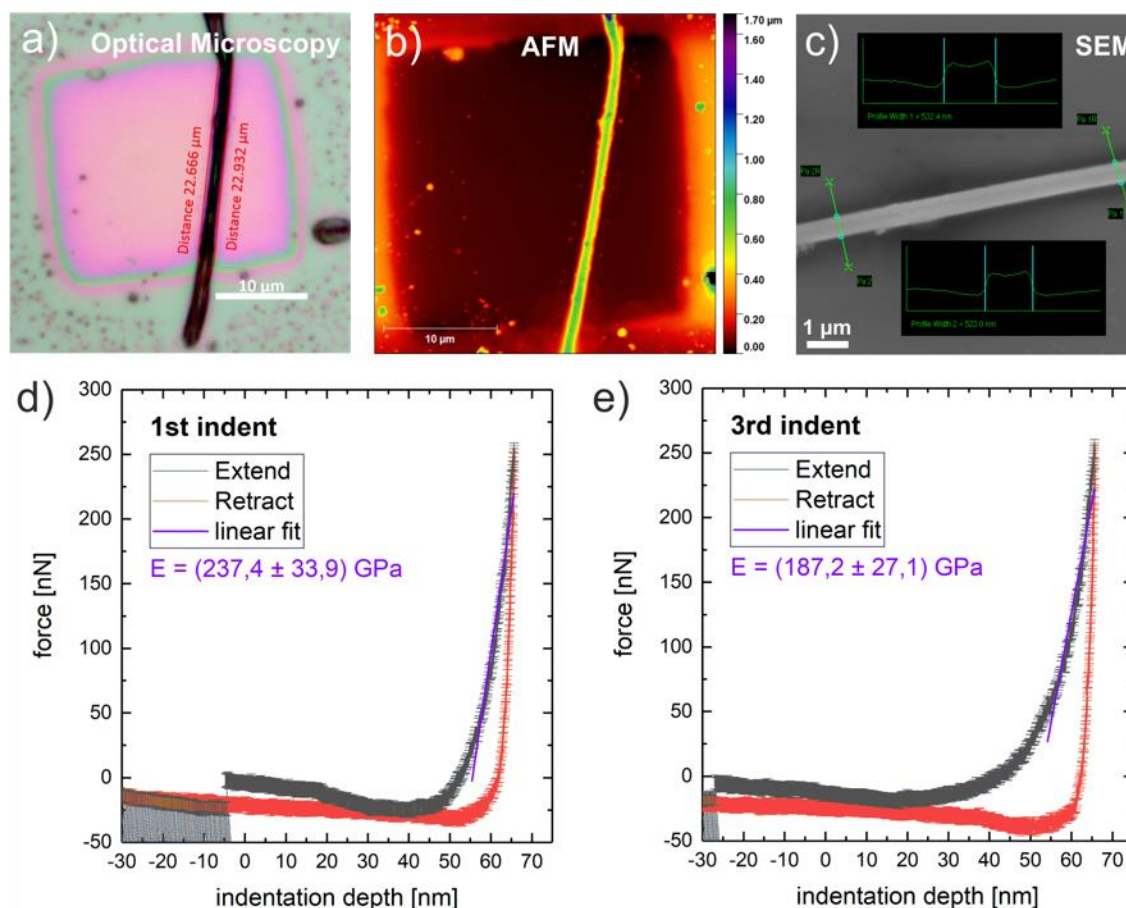
Figure S1. a) and b) Optical- and Atomic Force Microscopy (AFM) measurements of a suspended wire (wire 11). c) Scanning-electron microscopy (SEM) image of part of the wire. The respective measured widths are given. d) and e) Two force-distance curve taken in the middle of the wire.
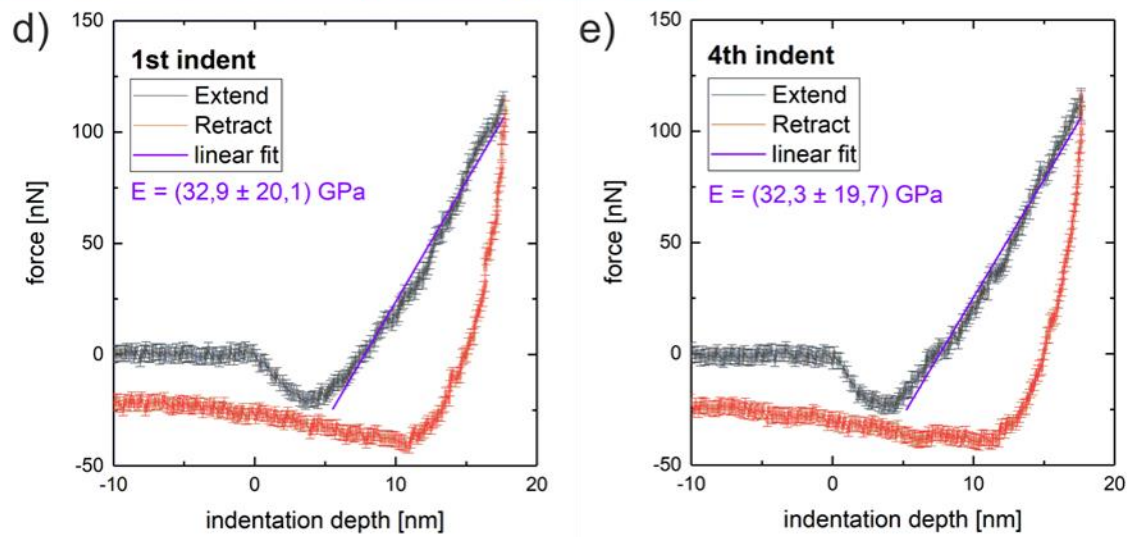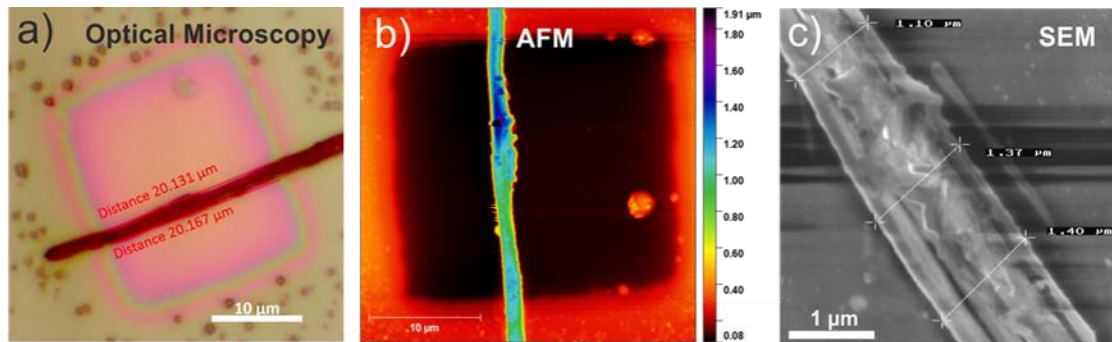
Figure S2. Characterization of a further SnIP wire (wire 5), see legend for Figure S1 for details.

Table S1-1. Width (measured by SEM) and height (measured by AFM) as well as the measured Young's modulus of all wires investigated. The Young's modulus is given as an average of at least three indents with the error being the standard deviation. Young's modulus of IV, III-V and II-VI semiconductors are taken from literature.

Comp., [hkl]	Width w [nm]	Height h [nm]	Young's modulus [GPa]	Literature
SnIP, [100] Wire 2	535 ± 4	562 ± 10	181 ± 7	This work
SnIP, [100] Wire 5	1295 ± 187	604 ± 90	33 ± 1	This work
SnIP, [100] Wire 8	713 ± 34	330 ± 9	810 ± 149	This work
SnIP, [100] Wire 10	1719 ± 61	685 ± 21	189 ± 12	This work
SnIP, [100] Wire 11	524 ± 19	603 ± 12	205 ± 28	This work
GaN, [120]	36 - 48		227 - 305	[Nam 2006]
Si, [001]			130	[Adachi 2005]
Ge, [001]			103	[Adachi 2005]
a-Sn, [001]			52	[Adachi 2005]
b-GaN, [001]			191	[Adachi 2005]
GaP, [001]			103	[Adachi 2005]
GaAs, [001]			85	[Adachi 2005]
GaSb, [001]			63	[Adachi 2005]
InP, [001]			61	[Adachi 2005]
InAs, [001]			51	[Adachi 2005]
InSb, [001]			42	[Adachi 2005]
b-ZnS, [001]			51	[Adachi 2005]
ZnSe, [001]			48	[Adachi 2005]
ZnTe, [001]			42	[Adachi 2005]
c-CdS, [001]			33	[Adachi 2005]
c-CdSe, [001]			29	[Adachi 2005]
CdTe, [001]			23	[Adachi 2005]

2. Quantum chemical DFT calculations

2.1. Calculation of Raman modes for SnIP at normal and high pressure conditions

Raman spectra were calculated within the framework of Density Functional Theory (DFT). HSE06 functionals were applied including Grimme D2 corrections to address the weak van der Waals interactions in SnIP. A band assignment was performed for the modes detectable in Raman experiments. Selected modes defining the three different areas detectable in the experimental Raman spectrum of SnIP are given below.

125 cm^{-1} mode	339 cm^{-1} mode	355 cm^{-1} mode
125SnIP.mp4	339P.mp4	355P.mp4
Sn-I breathing region	P-P stretching region	P-P stretching region

422 cm^{-1} mode	458 cm^{-1} mode
422P.mp4	458P.mp4
P-P breathing region	P-P breathing region

Based on these assignments we defined three general regions in the spectrum as stated below the videos and denoted in Figure S3.
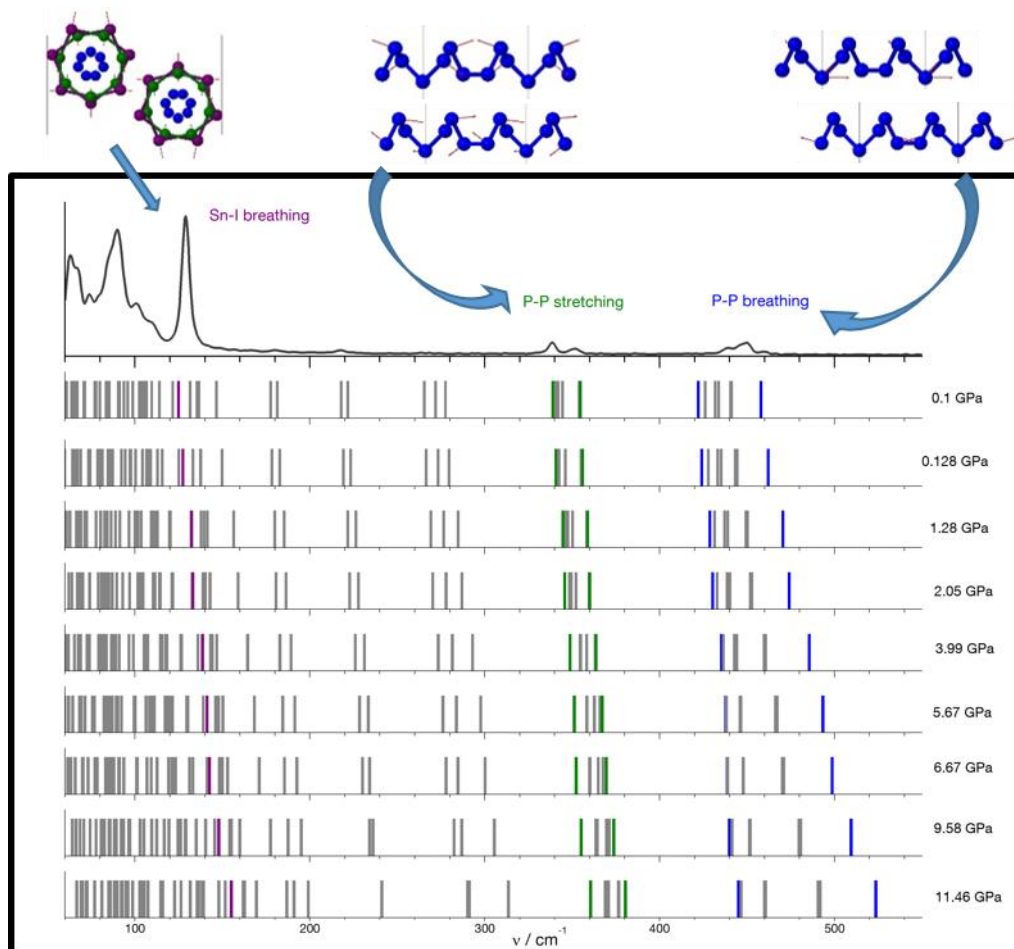
Figure S3. Illustrations of Raman modes (top), experimental Raman spectrum and Raman mode positions derived from Quantum-chemical (DFT) calculations for different pressures (lines). Calculations are based on experimental cell parameters measured in a DAC cell including a geometry optimization of the structure for SnIP with restrained lattice parameters. Band assignments are given for highlighted modes in the Sn-I breathing, P-P stretching and P-P breathing regions. Videos of the modes are given above.

2.2. Calculation of phonon spectra and thermal conductivity of SnIP

Quantum chemical calculations within the framework of DFT within the local density approximation were performed to evaluate the electronic band structure (S5.a) and the phonon dispersion relations of SnIP (S5.b). The electronic band structure calculations are in good accordance with data reported earlier on [Pfister 2016]. The phonon dispersion relations account for the low thermal conductivity of the system and for its anisotropy. They feature a very narrow frequency range for the acoustic modes and flat optical bands in the Γ-Z direction, whereas modes are more dispersive in the Γ-Y direction that corresponds to propagation along the helices.
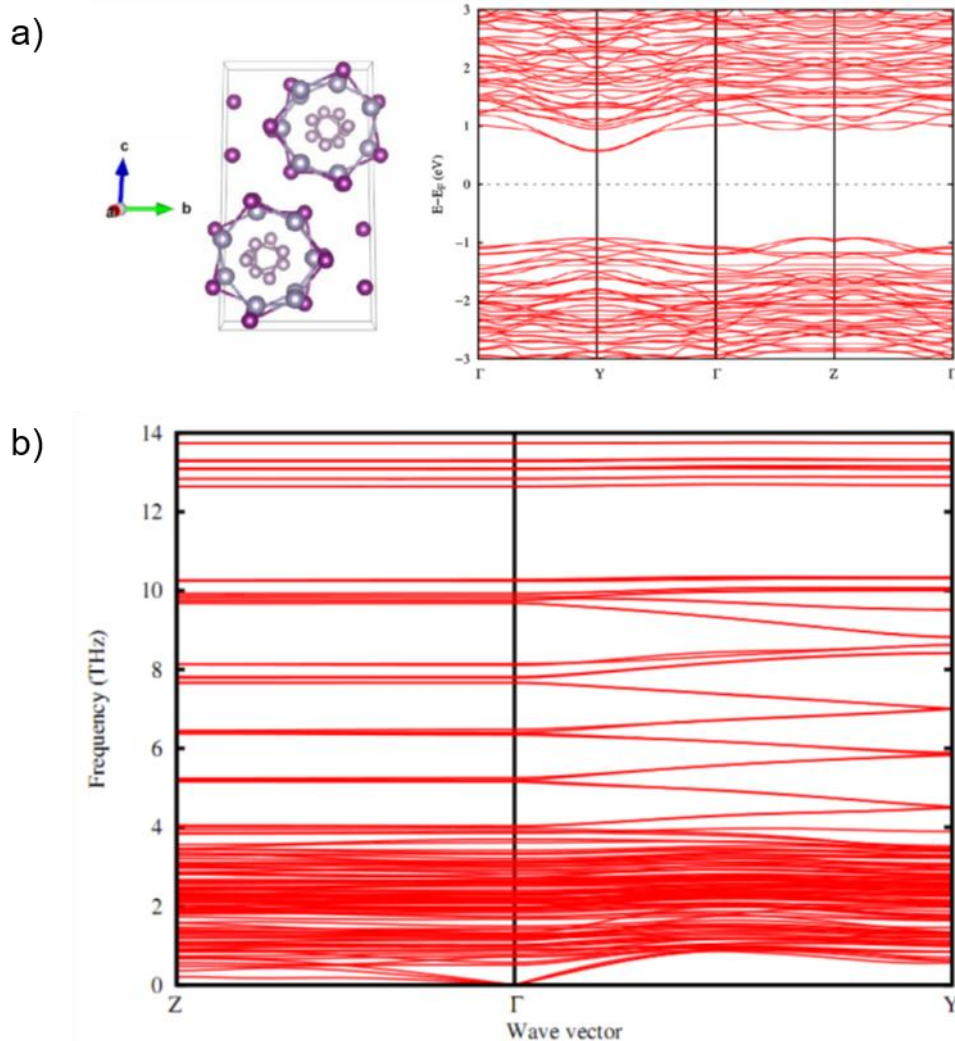
Figure S4. a) Calculated band structure and b) phonon dispersion curves of SnIP.

Although this was a remarkably challenging experiment for inelastic neutron scattering (INS) due to the extremely low non-hydrogenous scattering cross sections, we were nonetheless able to obtain clearly distinguishable signals in the high frequency region (> 250 cm^{-1}) through a careful background/cell subtraction (Figure S5).
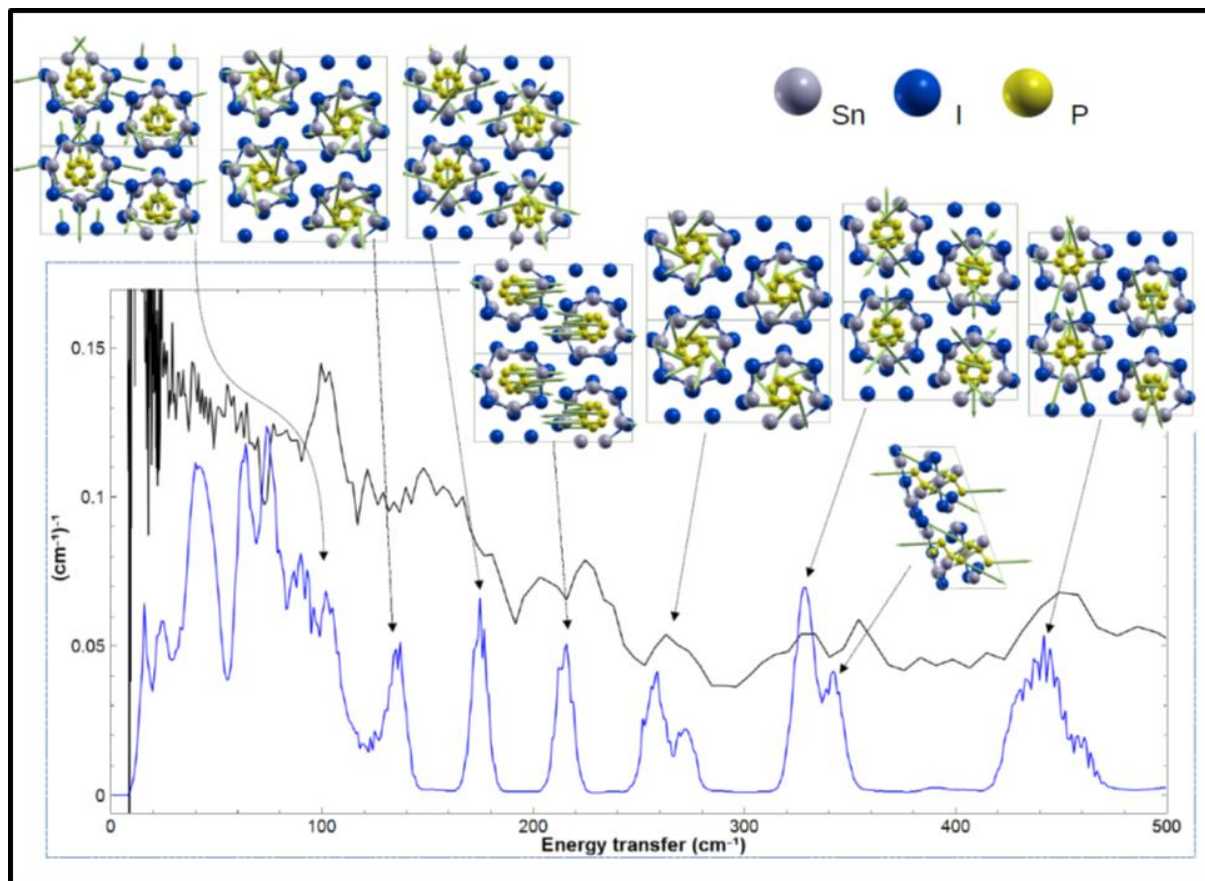
Figure S5. Calculated and measured phonon spectra for SnIP.

These signals were corroborated with comparison to DFT phonon and high-frequency peaks can be clearly assigned to result from different motions of the lighter P atoms. These P motions can be broadly broken down into concentric helical breathing/twisting modes (442, 330/265 cm^{-1}), and stretching modes along the axis of the helices (339.6 cm^{-1}). The fact that these two sets of modes are comparable in frequency, yet involve spatial dimensions with largely varying mechanical properties indicates that the P motions are largely localized, and independent of the lateral inter-helical interactions. Our measurements do in fact quite clearly show the presence of low frequency modes in the region where DFT predicts lateral inter-helical motions (< 100 cm^{-1}), however the low sensitivity and resolution in this region makes it difficult to unambiguously assign modes to quantitative agreement. Nonetheless we attempt a coarse guide to the eye assignment in Figure S5 and give a tentative assignment of a "complete helical breathing" at 99 cm^{-1}. This result indicates that P-P interactions both in

the axis of the helix and laterally are similar in strength, yet seem to have a larger effect on the mechanical properties along the axis on the helix due to the observed decoupling of frequencies between the internal P-P breathing modes, and the "complete helical breathing" as a whole.

2.3. Pressure dependent crystal structure evolution of SnIP

Results from quantum chemical DFT calculations after geometry optimization on SnIP. Cell parameters were taken from Rietveld calculations of high-pressure synchrotron data between 0.1 and 11.5 GPa (DAC) and kept as fixed parameters during the structure optimization.

Table S2-1. Lattice parameters derived from Rietveld refinements on SnIP up to a pressure of 11 GPa. Standard deviations are equal or less than 0.0001 Å for the lattice parameters, 0.01° for the angle, 0.01 Å^3 for the cell volume and 0.02 GPa for the pressure.

Pressure [GPa]	a [Å]	b [Å]	c [Å]	β [°]	Cell volume [Å^3]
0	7.9388	9.8098	18.4376	110.4400	1345.48
0.28	7.9151	9.7363	18.3192	110.5427	1321.98
1.28	7.8532	9.6031	18.1031	110.7214	1276.94
2.05	7.8236	9.5512	18.0271	110.8018	1259.25
3.99	7.7272	9.4141	17.83204	111.0325	1210.75
5.67	7.6571	9.2982	17.67464	111.3293	1172.18
6.67	7.6260	9.2224	17.58983	111.552	1150.61
9.59	7.5485	9.0625	17.39729	112.1655	1102.16
11.46	7.4208	8.8867	17.17087	112.1716	1048.63
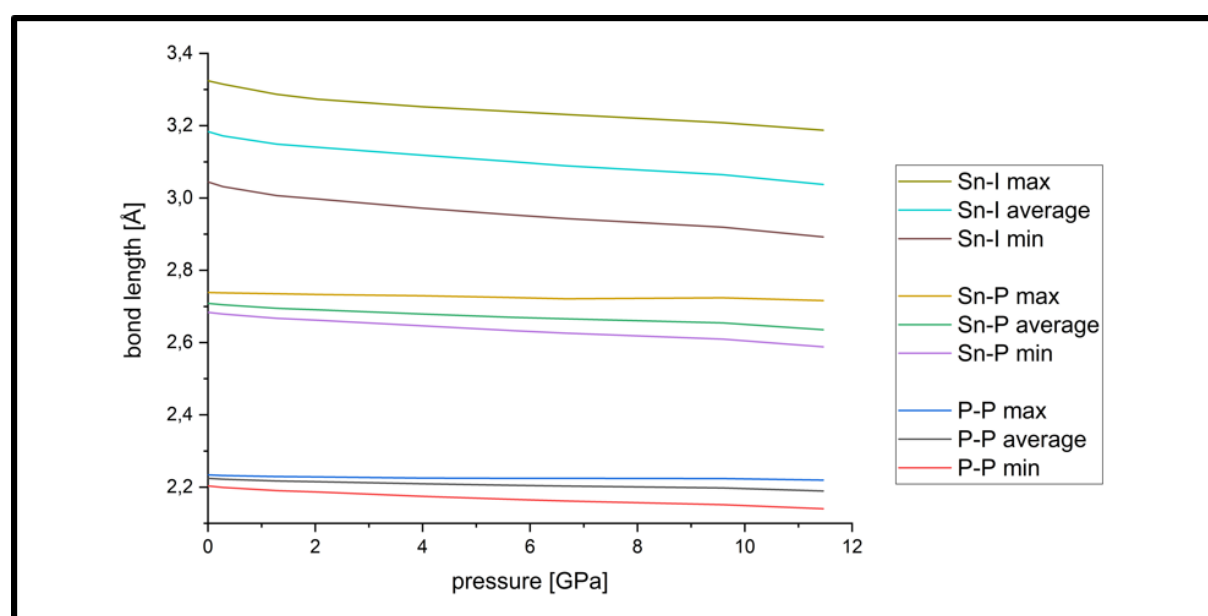
Figure S6. Summary of selected bond lengths with minimal, maximal and average values for SnIP in a pressure range of 0.1 to 11.5 GPa.
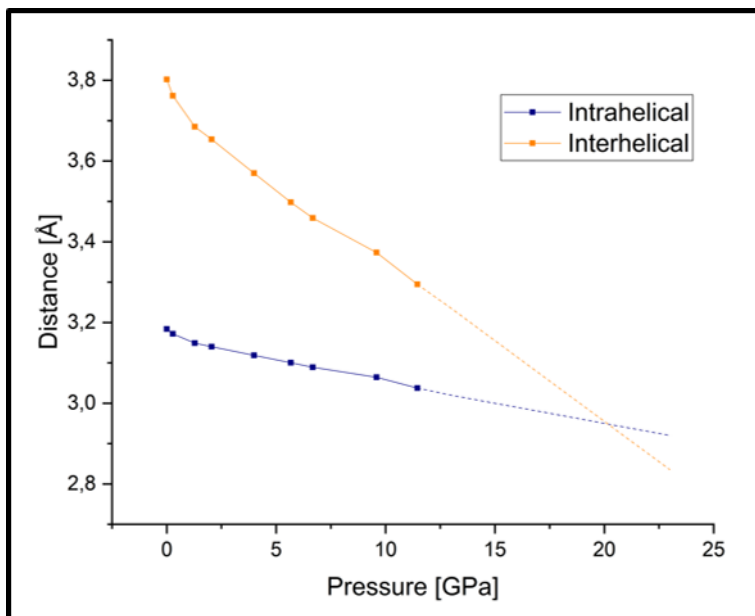
Figure S7. Inter-helical and intra-helical Sn-I distances for SnIP in a pressure range or 0.1 to 11.5 GPa. Dotted lines are extrapolated bond distances which cross each other at 20 GPa. At this pressure the intra and interhelical distances are not distinguishable any more.
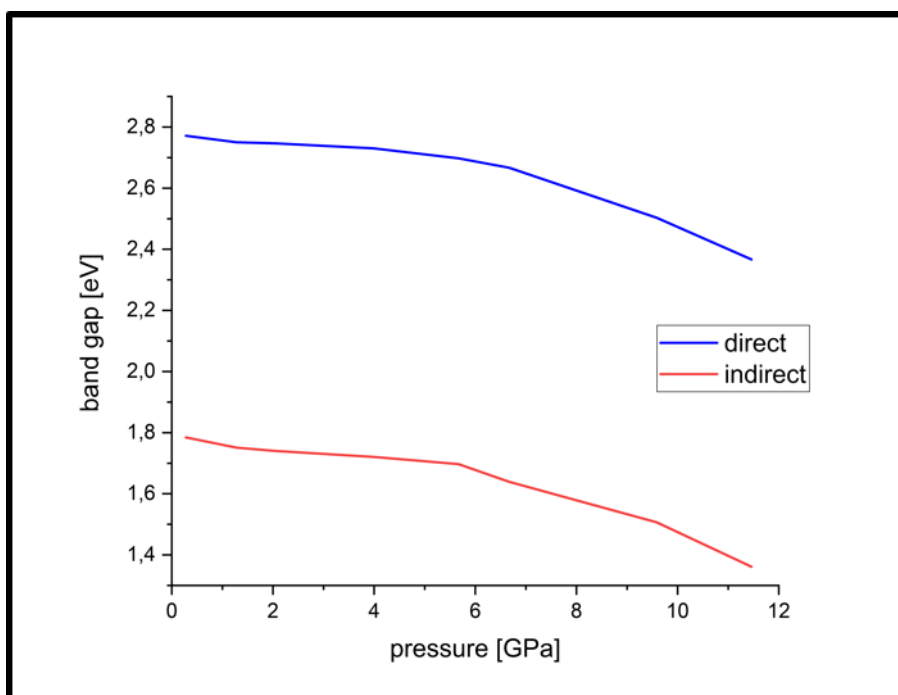
Figure S8. Evolution of the calculated band gaps (DFT, HSE06 functionals, Grimme D2 correction for SnIP in a pressure range of 0.1 to 11.5 GPa.

3. Hybrid materials

3.1. Raman spectroscopy on SnIP and SnIP@polymer hybrids

The Raman measurement of the delaminated SnIP needles (25 to 100 nm diameter) shows the same bands as the bulk sample (several micrometer-sized crystals in diameter). Figure S9 shows the Raman spectrum of delaminated (red) and bulk (black) SnIP. The inserted image illustrates a magnified view on the Sn-I breathing mode region of the compound. It is obvious, that the intensity of the main and most intensive visible mode in this region chances while delamination and the outer Sn-I-helix at 128 cm^{-1} is no longer the dominating one. The mode at 142 cm^{-1} becomes dominant after exfoliation. Such a behavior of varying the intensity of modes upon delamination was also observed for layered materials like black phosphorus if it is transferred to phosphorene [Phaneuf 2016]. An important finding is that all modes of SnIP are invariant in terms of their position which illustrates a comparable and non-influenced chemical bonding for all helices in the bulk and delaminated material.
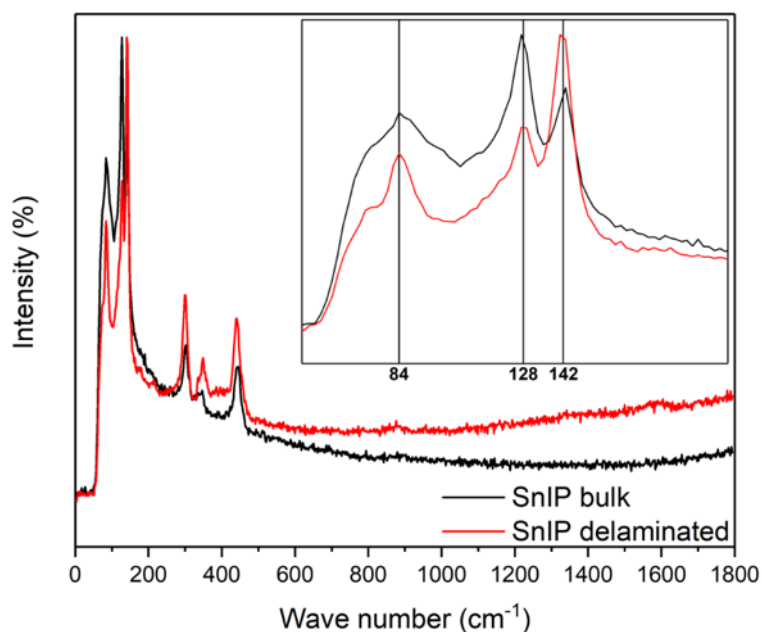
Figure S9. Raman spectra of as prepared SnIP (black, diameter >10 μm) and chemically delaminated SnIP crystals (red, diameter ~ 25 nm). The inserted image shows a detail graph ranging from 50 to 200 cm^{-1}. Modes are changing their intensity upon delamination.

After delamination of SnIP we prepared different SnIP@polymer hybrid materials in order to evaluate the possibility to incorporate SnIP into different matrices. SnIP reference spectra (25 to 100 nm diameters of needle-shaped crystals) shown in the oncoming figures are measured for delaminated SnIP which was used to fabricate the hybrid materials afterwards. Our intention was to verify if commonly used polymers are possible matrices to host nano-

sized SnIP without any degradation effects. We examined polyethylene glycol (PEO, solid electrolyte, batteries), polyvinyl pyrrolidone (PVP), polyethylene (PE), poly(3,4-ethylenedioxythiophene)-poly(styrenesulfonate) (PEDOT/PSS, solar cells) or Poly(3-hexylthiophen-2,5-diyl) (P3HT; solar cells), and fluorine/chloride doped C_3N_4 (water splitting) due to their importance for energy conversion and storage applications. In the following we illustrate the effect on the Raman modes of SnIP in such non-conductive and conductive polymer matrices.

In some cases, a small shift in the main Raman modes of SnIP is observed which points towards a certain influence on the bonding in the respective hybrids. For the SnIP@PEO we found a 28 cm^{-1} red shift for the Sn-I breathing mode which illustrates a weakening of bonding in the outer [SnI] helix (Figure S10). In accordance with this we found a slight shift in the direct (0.05 eV) and indirect band gaps (0.025 eV) towards lower energies.

A comparable shift of the Sn-I breathing modes is observed for SnIP@PVP but we see different not assigned modes in the SnI breathing region which needs to be addressed in the future. For SnIP@PE this shift of the Sn-I breathing mode is significantly reduced to only 14 cm^{-1} (see Figure S11). Interestingly, the P-P breathing and stretching modes are shifted to slightly higher wavenumbers for the same two polymers indicating larger force constants and stronger interactions in that case.

Interestingly, a blue shift of the Sn-I breathing mode towards higher wavenumbers is found for the conductive PEDOT/PSS polymer. It seems to be the case that the breathing mode is strengthened which points towards a certain electron transfer from the conductive polymer to SnIP. Further experiments including P3HT are underway to substantiate this assumption. In the case of SnIP@P3HT hybrids we were not able to measure reliable Raman spectra at the present stage but it seems to be the case that hybrids can also be formed without showing degradation effects.

In sum, each polymer used for the preparation of SnIP@polymer hybrid materials is capable to host SnIP without a visible degradation or dissolution process. Slight red and blue shifts in the modes is an indicator for a certain influence of the matrix to different substructures within SnIP. At least for the conductive polymers a charge transfer from the polymer to SnIP seems to occur. Therefore, SnIP might be a suitable candidate for thermoelectric or solar hybrid devices in the near future but the influence of the matrix material must be taken into account.
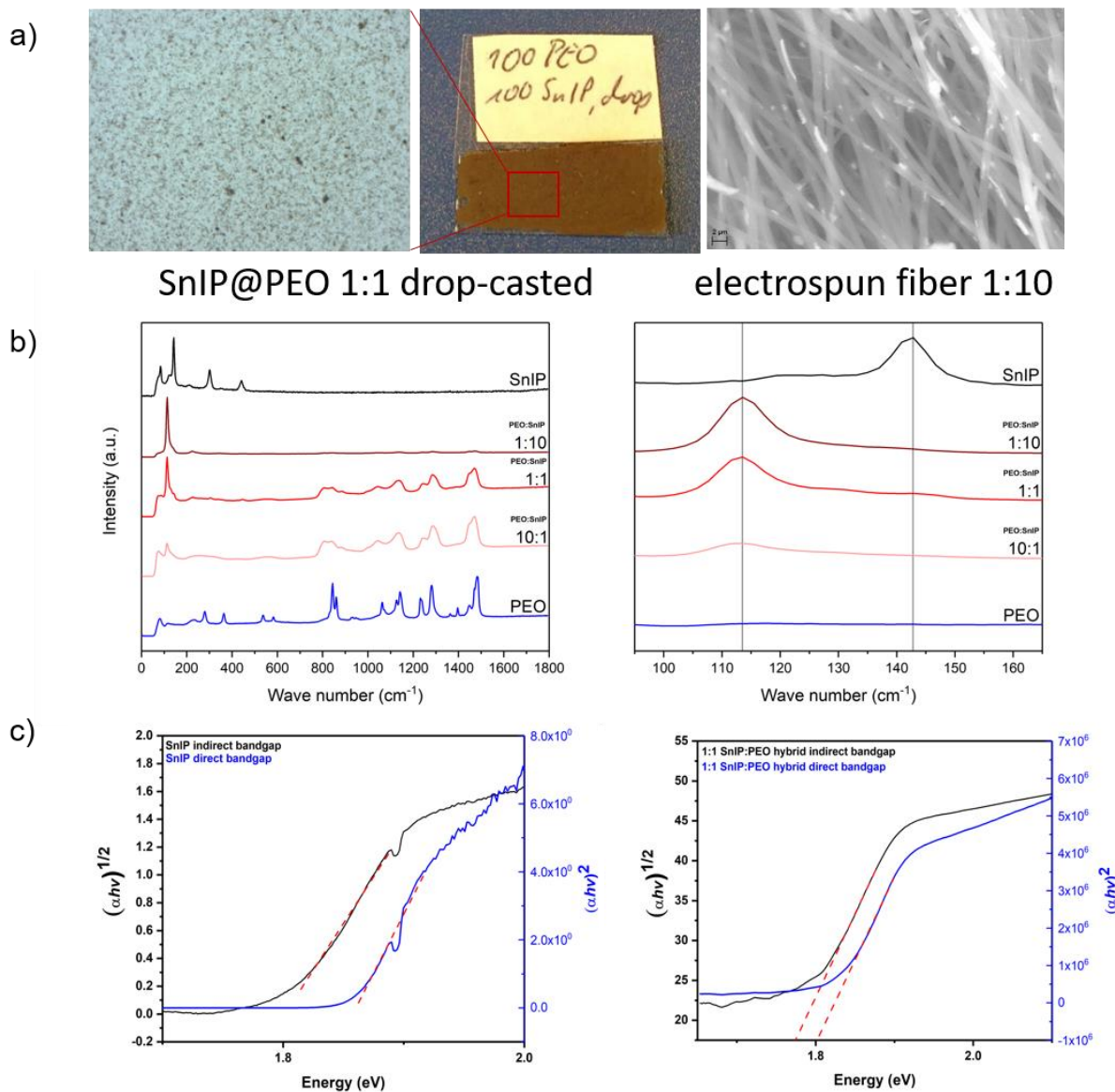
Figure S10. a) Pictures of selected drop and electrospun SnIP@polymer hybrids. Left and middle: Delaminated SnIP@PEO 1:1 (mass ratio) drop-casted; Right: Electrospun SnIP@PEO 1:10 (mass ratio) membrane. b) Raman spectra of drop-casted SnIP@PEO thin-film hybrids representing pure, delaminated SnIP, a 1:10, 1:1 and 10:1 (mass ratio) hybrid and pure PEO. A significant shift of 28 cm^{-1} was observed for the 142 cm^{-1} mode in SnIP which points towards a weakening of the Sn-I bonding interactions in the hybrid. Laser wavelength 532 nm. c) Diffuse reflectance measurements of pure, delaminated SnIP (diameters > 25 nm) and the 1:1 SnIP@PEO hybrid fabricated from such sample. The direct and indirect band gap shifts slightly to lower energies.
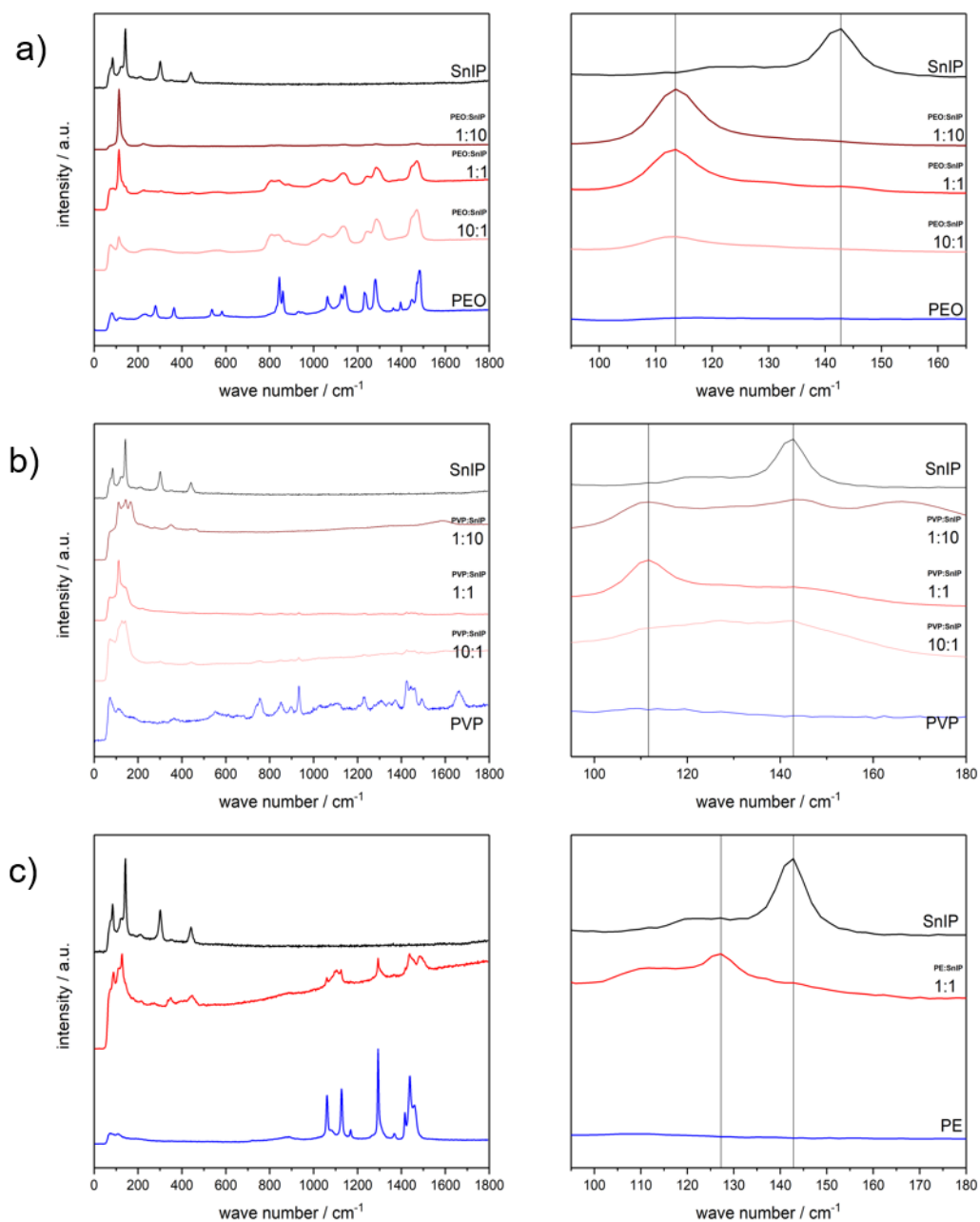
Figure S11. Raman spectra of SnIP@polymer hybrids using non-conductive polymers PEO, PVP and PE. Left: Full Raman spectrum. Right: Enlarged view on the Sn-I breathing region with the most dominant Raman modes. The mass ratio for each blend is stated.
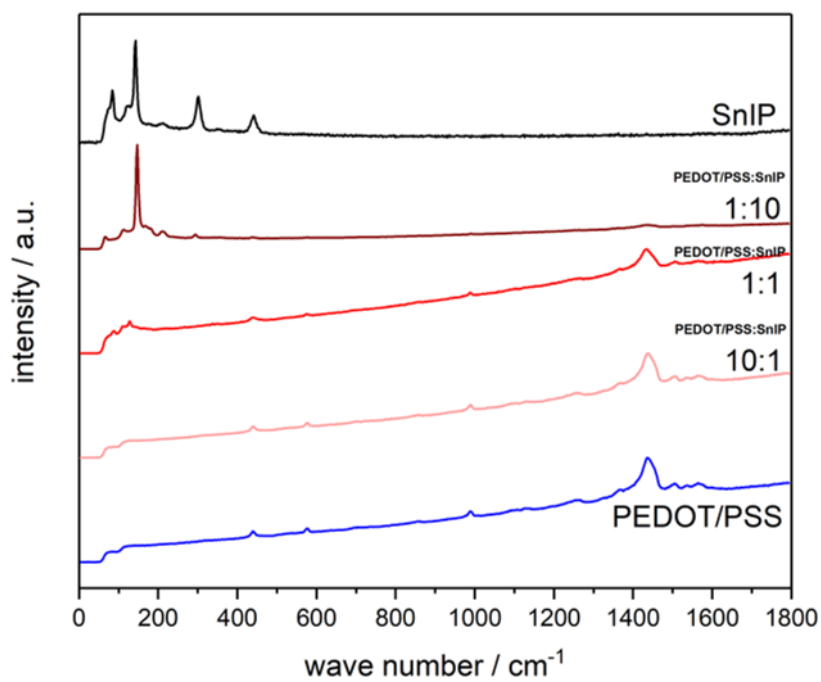
Figure S12. Raman spectra of SnIP@polymer hybrids using conductive polymers. Left: Full Raman spectrum. Right: Enlarged view on the Sn-I breathing region with the most dominant Raman modes. The mass ratio for each blend is stated.

3.2. SnIP@carbon nanotube heterostructures

Carbon nanotubes might be helpful in getting bulk SnIP transferred to the one of the smallest and chiral semiconductor fiber made so far. SnIP crystallizes in a racemic mixture on right and left handed double helices. Each double helix itself represents an atomic-scale, chiral, inorganic semiconductor fiber and once we are able to delaminate bulk SnIP to single one-nanometer sized chiral fibers this will generate new perspectives for optic and electronic applications, including the possibility to introduce chirality for inorganic semiconductors. In general, there are two ways to achieve such chiral double helices. Either one might be able to prepare them directly in a top-down approach by delaminating bulk SnIP into single fiber nanotubes or one introduces a bottom-up approach atom by atom in a step by step process. The top-down approach has been successfully used to prepare 2D materials from bulk phases like for instance in the case of graphite/graphene [Novoselov 2004] and black phosphorus/phosphorene [Li 2014, Liu 2014].

In these cases, crystalline monolayers were achieved which still resembled the properties of the bulk material. For 1D SnIP the top down approach, either by mechanical or chemical delamination led to 10 to 20 nm diameter fibers or five to ten shells of hexagonally stacked, right and left handed double helices [Pfister 2016]. If one intends to get smaller fibers one might think about a direct synthesis following a template approach in suitable matrices. This has for instance successfully performed for phosphorus [Zhang 2017, Hart 2017] and selenium [Fujimori 2013] in multi-walled carbon nanotubes. We conducted first principle DFT calculations including empirical dispersion corrections for SnIP@Carbon nanotube(CNT) heterostructures. Three different types of CNT, a metallic, semimetallic and semiconducting one, were selected based on their inner diameter to accommodate a single P-double helix (rod group p $7_4$2) of SnIP. According to our calculations, a (10,10), (18,0), and (19,0) CNT are the most suitable candidates for the stabilization of single SnIP strands concerning simple space filling aspects of SnIP and the diameter of a given CNT (see Figure S13a and b). Band structures of such heterostructures taking simple and empirical dispersion corrections into account are given in Figure S13c. In those cases, where the CNT is achiral, also the expected heterostructure will show a racemic mixture of right and left-handed double helices. In order to separate the SnIP enantiomers one has to use chiral CNTs like (15,5) or (16,10), to realize a separation of the two enantiomeric form. If a synthesis of SnIP directly into such CNT will be possible will be subject to further investigations. At the moment it mostly suffers from the availability of phase pure CNT of a given type to verify our predictions. The synthesis of such CNTs might be realized in the future.
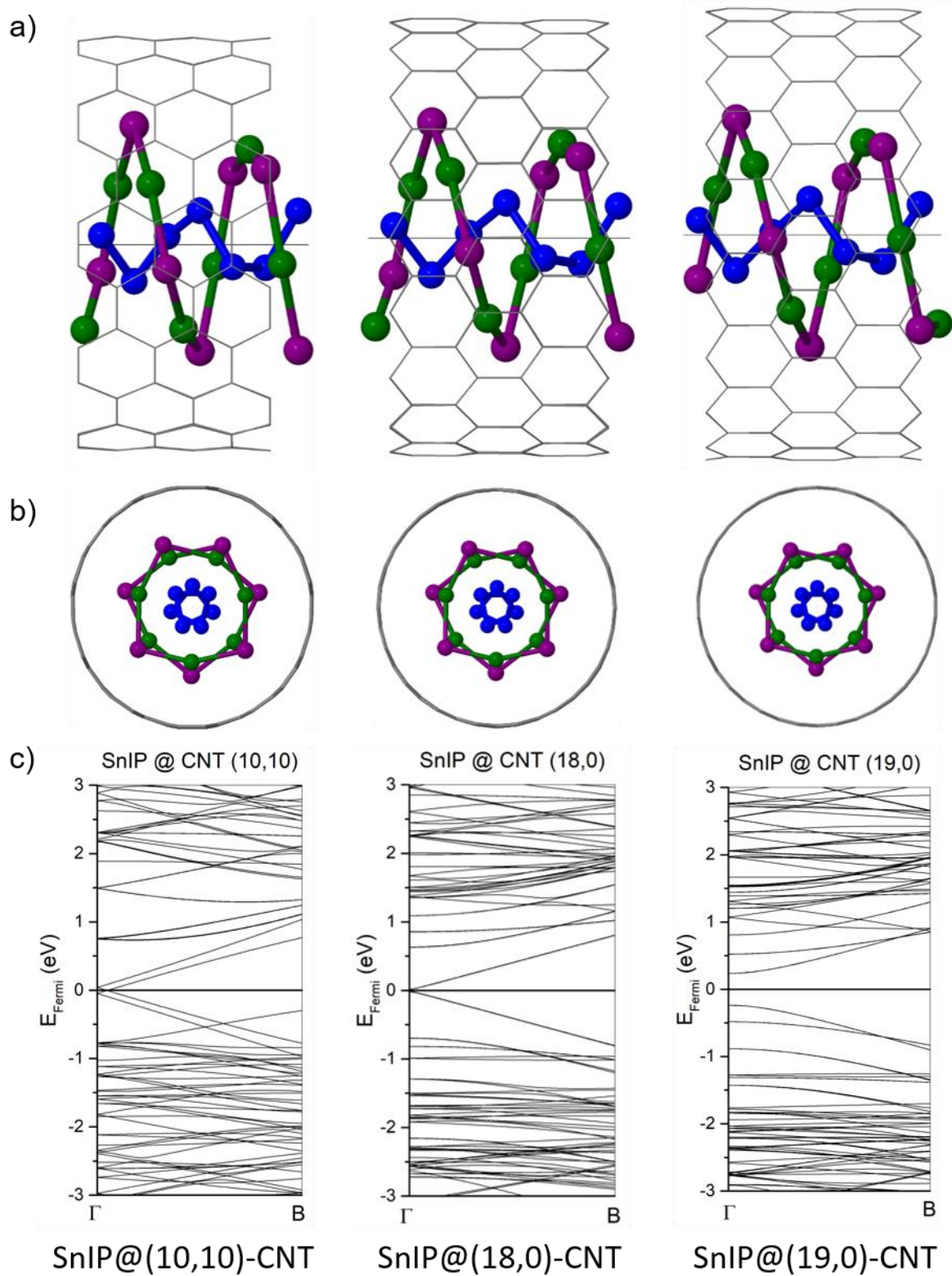
Figure S13. SnIP@CNT heterostructure representations. a) View onto the SnIP a-axis. b) View along the double helix and CNT axis. c) Band structures of SnIP@CNT heterostructures.

3.3. Hybrid materials and water splitting
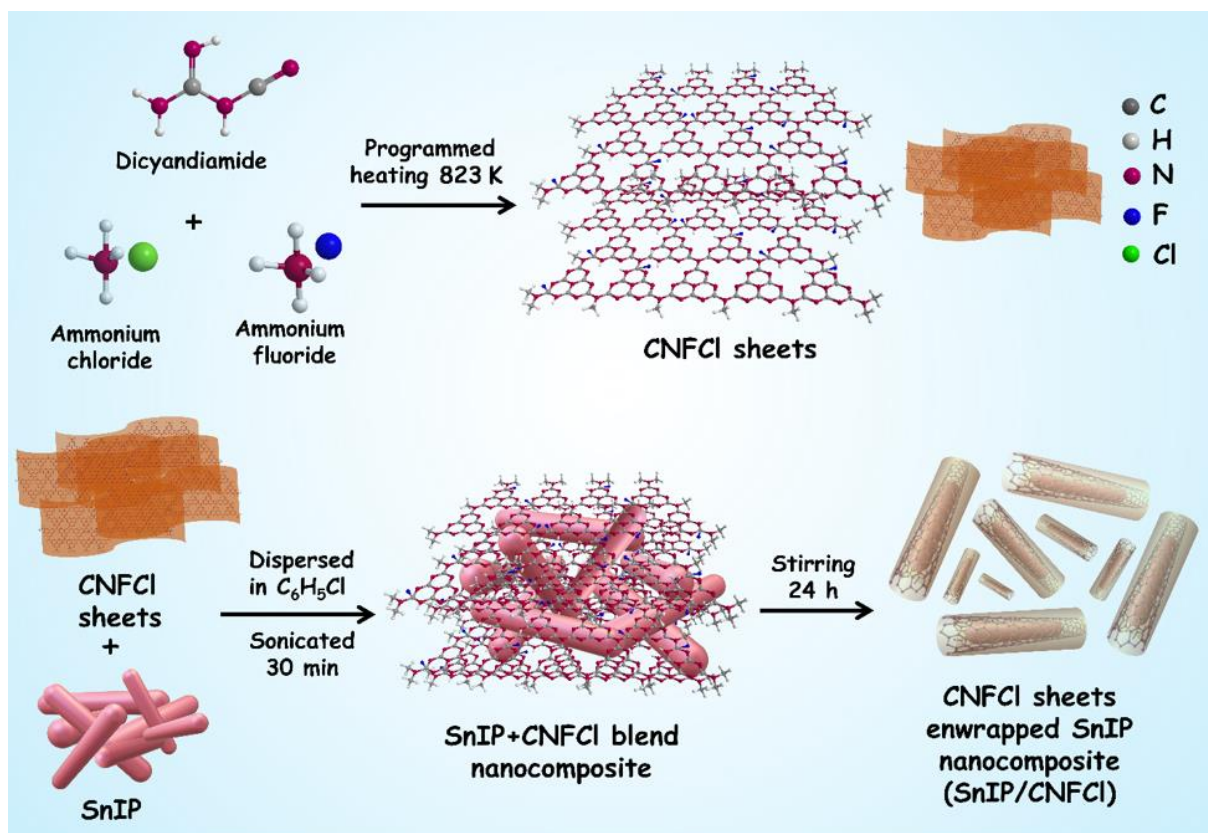
Figure S14. Synthetic scheme for CNFCl sheets wrapped SnIP/CNFCl nanocomposite.

CNFCl
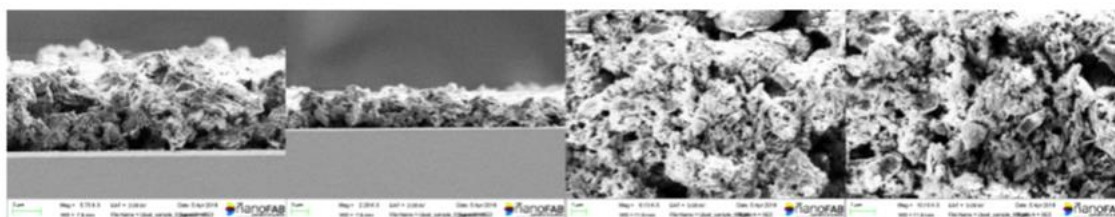
SnIP/CNFCl_30
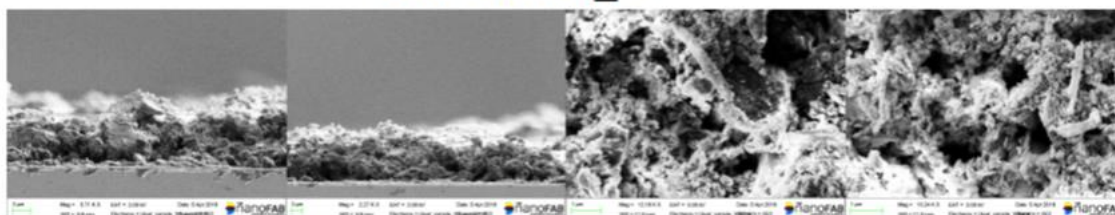
SnIP/CNFCl_70
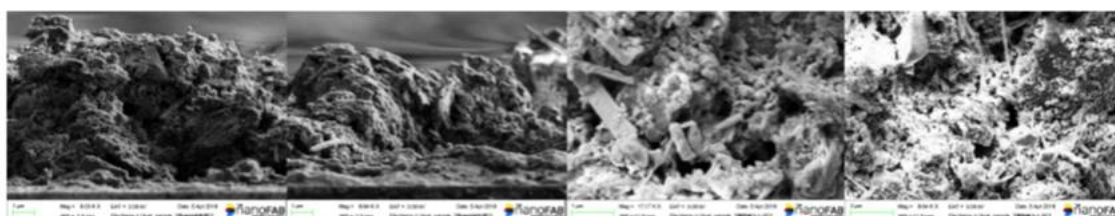
Figure S15. SEM pictures of of SnIP@C_3N_4(F,Cl) thin film devices.
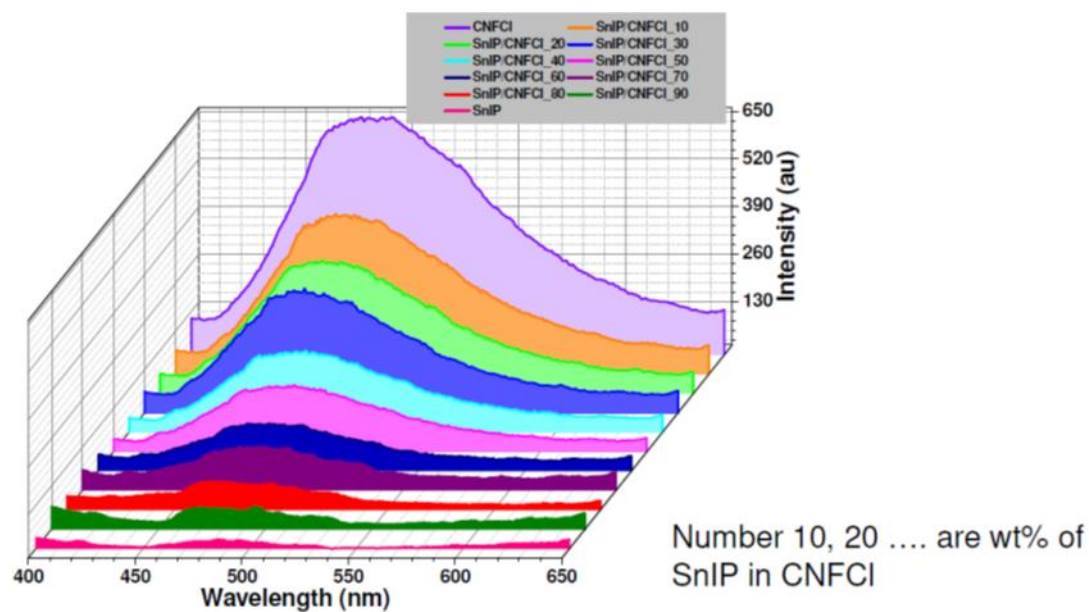
Figure S16. Photoluminescence measurements of SnIP@CNFCl thin film devices.
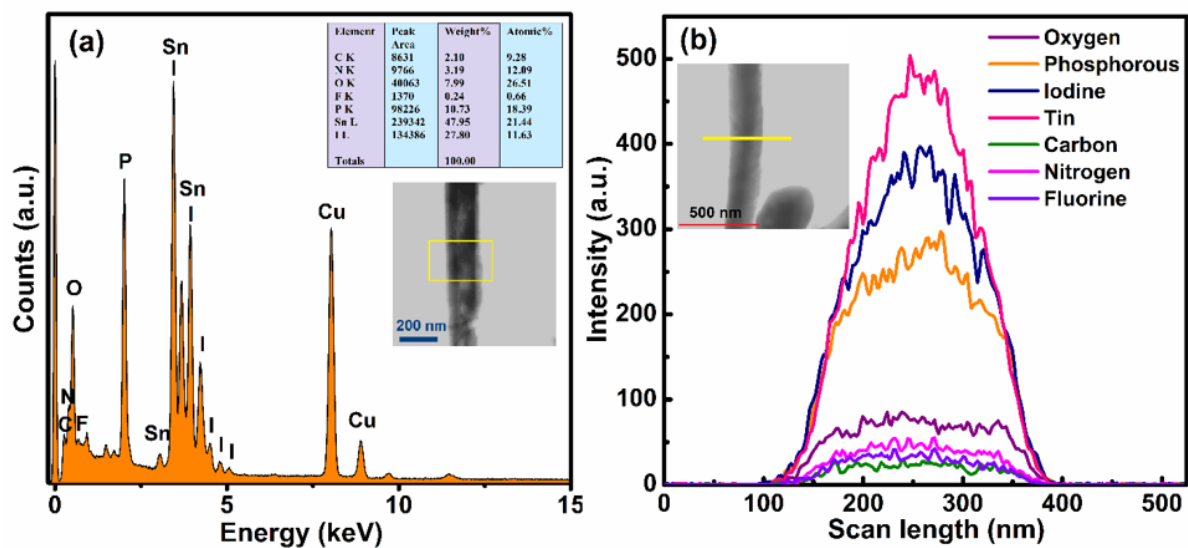
Figure S17. (a) EDX elemental mapping of 30% SnIP/CNFCl; inset showing area of interest, (b) line scale for different elements inset showing area of interest scan.
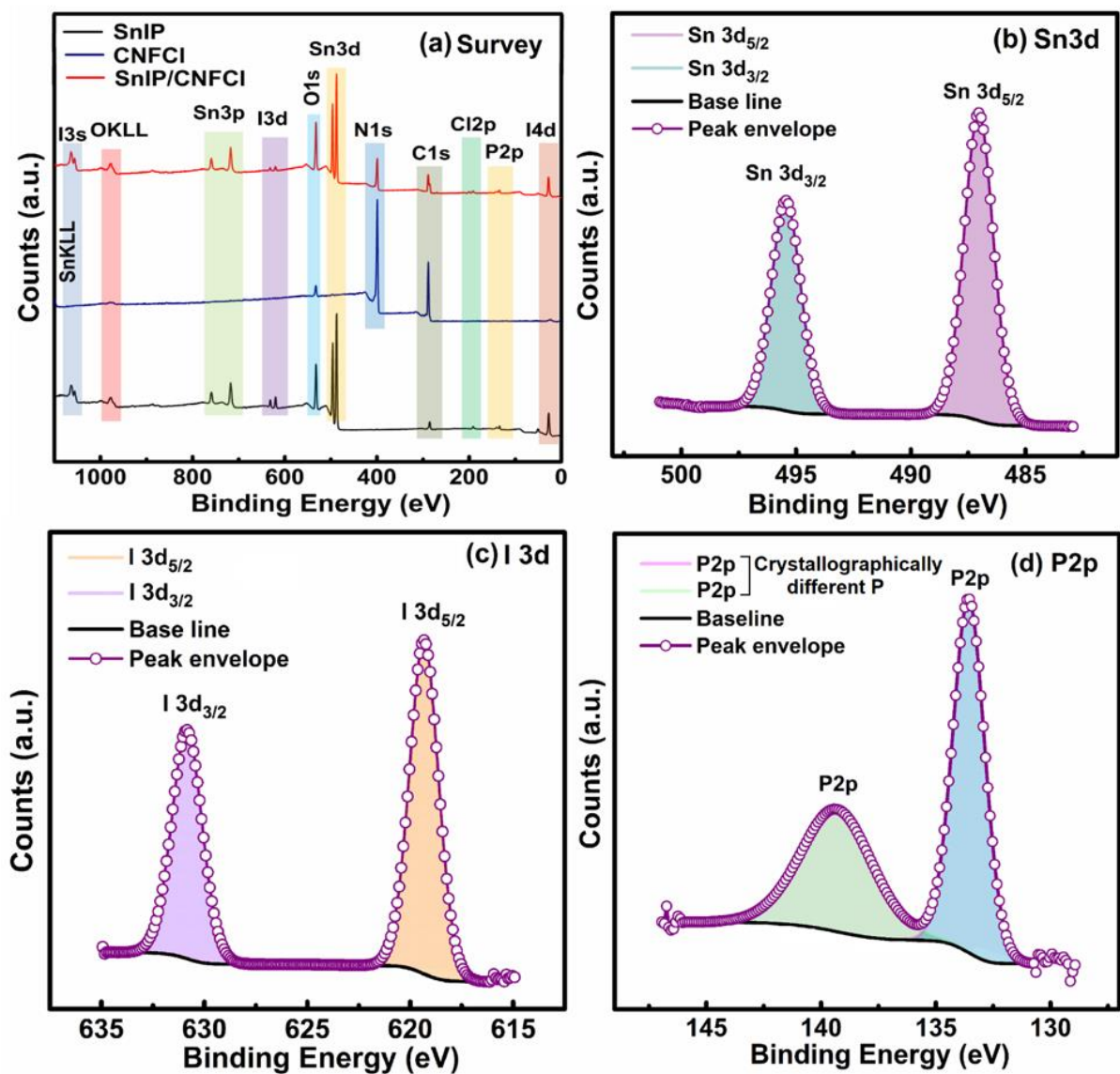
Figure S18. (a) Elemental survey scan for SnIP (black), CNFCl (navy blue), 30% SnIP/CNFCl (red), and HR-XPS of SnIP in (b) Sn3d, (c) I3d, (d) P2p regions.
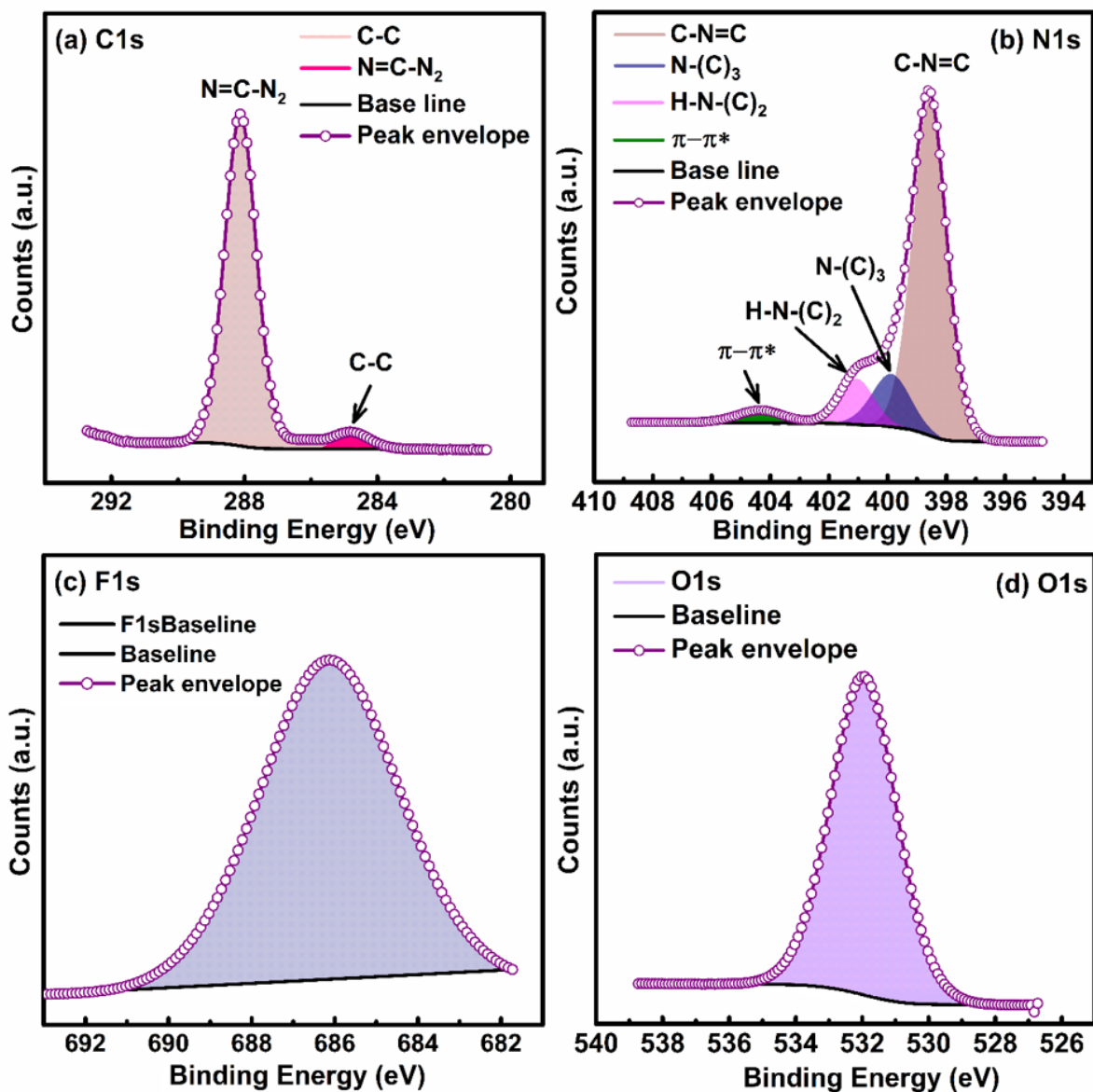
Figure S19. HR-XPS of CNFCl in (a) C1s, (b) N1s, (c) F1s, (d) O1s region.
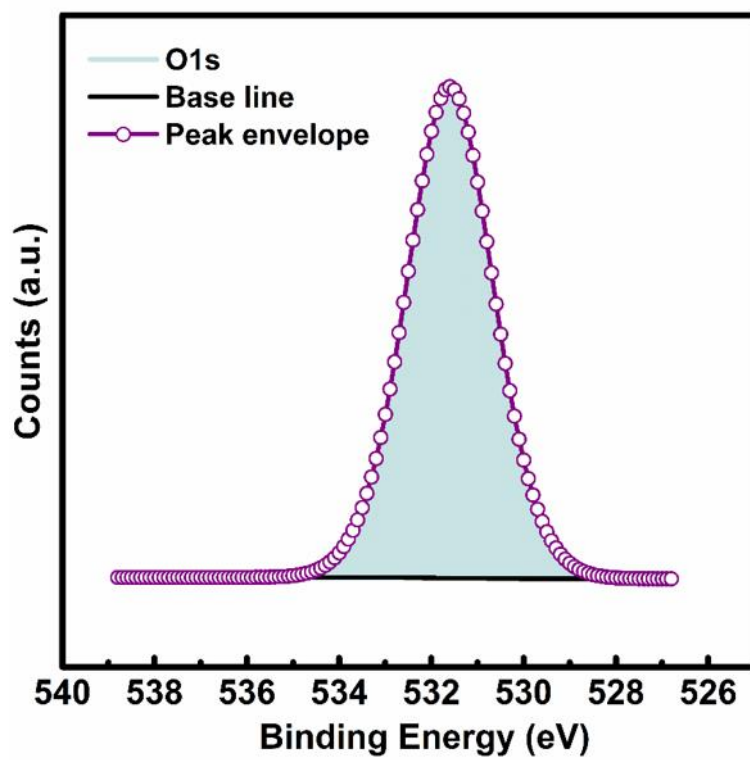
Figure S20. HR-XPS of 30% SnIP/CNFCl in O1s region.

References Supplement

[Gere 2006] J. M. Gere, Mechanics of materials. 6th ed., Brooks/Cole, 2004.

[Habtoun 2017] S. Habtoun, S. Houmadi, B. Reig, E. Pouget, D. Dedovets, M.-H. Delville, R. Oda, F. Cristiano, C. Bergaud, Structural and mechanical characterization of hybrid metallic-inorganic nanosprings. Mater. Res. Express, 2017, 4, 105023.

[Nam 2006] C.-Y. Nam, P. Jaroenapibal, D. Tham, D. E. Luzzi, S. Evoy, J. E. Fischer, Diameter-Dependent Electromechanical Properties of GaN Nanowires, Nano Lett. 2006, 6, 153–158.

[Novoselov 2004] K. S. Novoselov, Electric Field Effect in Atomically Thin Carbon Films. Science 2004, 306, 666-669.

[Phaneuf 2016] A.-L. Phaneuf-L'Heureux, A. Favron, J.-F. Germain, P. Lavoie, P. Desjardins, R. Leonelli, R. Martel, S. Francoeur, Bi-Axial Growth Mode of Au–TTF Nanowires Induced by Tilted Molecular Column Stacking. Nano Lett. 2016, 16, 7761–7767.

[Wang 2018] W. Wang, P. Ciselli, E. Kuznetsov, T. Peijs, A. H. Barber, Effective reinforcement in carbon nanotube-polymer composites. Phil. Trans. R. Soc. A, 2018, 366, 1613.

[Xiong 2006] Q. Xiong, N. Duarte, S. Tadigadapa, and P.C. Eklund, Force-Deflection Spectroscopy: A New Method to Determine the Young's Modulus of Nanofilaments. Nano Letters 2006, 6, 1904.

3.6 Room Temperature High-Detectivity Mid-Infrared Photodetectors Based on Black Arsenic Phosphorous

Mingsheng Long[1], Anyuan Gao[1], Peng Wang[2], Hui Xia[2], **Claudia Ott**[3], Chen Pan[1], Yajun Fu[1], Erfu Liu[1], Xiaoshuang Chen[2], Wei Lu[2], Tom Nilges[3], Jianbin Xu[4], Xiaomu Wang[1, 5], Weida Hu[2] and Feng Miao[1]

[1] National Laboratory of Solid State Microstructures, School of Physics, Collaborative Innovation Center of Advanced Microstructures, Nanjing University, Nanjing 210093, China.

[2] National Laboratory for Infrared Physics, Shanghai Institute of Technical Physics, Chinese Academy of Sciences, Shanghai 200083, China.

[3] Synthesis and Characterization of Innovative Materials, Department of Chemistry, Technical University of Munich, Garching bei München 85748, Germany.

[4] Department of Electronic Engineering and Materials Science and Technology Research Center, Chinese University of Hong Kong, Hong Kong SAR, China. [5] School of Electronic Science and Technology, Nanjing University, Nanjing 210093, China.

The article "Room Temperature High-Detectivity Mid-Infrared Photodetectors Based on Black Arsenic Phosphorous" was submitted in February 2017 to the Journal "Science Advances" and published online in June 2017.

$As_{0.83}P_{0.17}$ (b-AsP) can be easily delaminated to thin flakes. After device fabrication the absorption peak of this material was determined to be located at a wave number of 2760 cm^{-1}. This correlates with a wavelength of 3.62 μm and therefore represents the mid-wavelength infrared spectrum. The photocurrent is defined as the difference between measurable current under MIR irradiation and in the dark. To determine the mechanisms of the generated photoresponse of this device different source-drain (V_{ds}) and gate voltages (V_g) are analyzed.

An increase in gate voltage leads to a switch in polarity of the photocurrent. At gate voltages between -15 and 15 V (low-doped, intrinsic) the photovoltaic effect (PVE) dominates. This can be seen at the positive photoresponse and the zero-bias response. [126–130] The junction between b-AsP and the metal contacts plays a crucial role in the photocurrent generation. At this point the electron-hole pairs are separated. If the device is p-type doped the photocurrent is mainly generated at the reverse biased b-AsP/drain junction, if n-type doped at the reverse-biased b-AsP/source junction. These junctions were further mapped with spatial photocurrent mapping measurements. If the gate voltage is increased over 15 V (high-doped) thermal effects (the photothermoelectric (PTE) and bolometric effect) dominate as the photocurrent is negative relative to V_{ds} and shows weak gate dependence. For b-AsP devices (low source-drain bias) the photocurrent is mainly attributed to thermal effects due to it's high electrical and low thermal conductivity. [5,123,126,131–134] The thermally driven processes have a slower response time. Therefore, the device was primarily used in conditions where the photocurrent could be ascribed to the photovoltaic effect.

In this work the device was operated under zero bias since high photoresponse generates photocurrent under zero source-drain bias through the unapparent assymmetry of the device. This also allows a suppression of dark current and thus lowers the power consumption of the device. A MIR range between 2.4 and 8.05 μm was investigated which resulted in high responsivity. An efficiency of about 6.1% was calculated, which is promising for devices working in this MIR range at ambient temperatures. The speed of response is slower than expected, nevertheless it is more than enough for IR imaging applications.

Furthermore, the laser-power dependence of the photocurrent near the absorption peak of the b-AsP device was investigated. It suggests a weaker influence of the photogating effect in this range due to saturation of the trapping centers under intense light. [135] The generated photoresponse periodically varies with polarization of the incident light and current collection direction due to the anisotropy of the b-AsP crystal structure. The anisotropic factor caused by conductivity deviations is slightly larger than in black phosphorous. [5,134–136] The photocurrent anisotropy ratio for b-AsP is higher than the reported values for black phosphorous. [5]

The main issue of modern narrow-bandgap semiconductor based MIR photodetectors is the high dark current noise. This can be suppressed by using stacked 2D van der Waals (vdW) het-

erojunctions. In this work b-AsP/MoS$_2$ p-n-junction heterostructures were investigated. b-AsP represents a p-type, MoS$_2$ a n-type semiconductor. The current noise density increases significantly with using b-AsP/MoS$_2$ heterojunctions. The energy barrier between the materials suppresses the random transport of photogenerated carriers and therefore inhibits the $1/f$ noise.

The specific detectivity (D*) for our junction can be calculated to 9.2×10^9 Jones which is over ten times larger than all previously known room temperature MIR detectors. Even D* for the b-AsP FET is beyond the commercially available thermistor bolometer and by using the b-AsP/MoS$_2$ junction it is enhanced significantly.

Author contributions: C.O. synthesized and characterized the b-AsP crystals, M.L., A.G., P.W., H.X., C.P., Y.F., and E.L. performed device fabrication and characterization, M.L., A.G., X.W., F.M., and W.H. analyzed and interpretet the data, X.W., M.L., F.M., T.N. and W.H. wrote the paper, All authors discussed the results and reviewed the manuskript.

MATERIALS SCIENCE

Room temperature high-detectivity mid-infrared photodetectors based on black arsenic phosphorus

Mingsheng Long,[1] Anyuan Gao,[1] Peng Wang,[2] Hui Xia,[2] Claudia Ott,[3] Chen Pan,[1] Yajun Fu,[1] Erfu Liu,[1] Xiaoshuang Chen,[2] Wei Lu,[2] Tom Nilges,[3] Jianbin Xu,[4] Xiaomu Wang,[1,5]* Weida Hu,[2]* Feng Miao[1]*

The mid-infrared (MIR) spectral range, pertaining to important applications, such as molecular "fingerprint" imaging, remote sensing, free space telecommunication, and optical radar, is of particular scientific interest and technological importance. However, state-of-the-art materials for MIR detection are limited by intrinsic noise and inconvenient fabrication processes, resulting in high-cost photodetectors requiring cryogenic operation. We report black arsenic phosphorus–based long-wavelength IR photodetectors, with room temperature operation up to 8.2 μm, entering the second MIR atmospheric transmission window. Combined with a van der Waals heterojunction, room temperature–specific detectivity higher than 4.9×10^9 Jones was obtained in the 3- to 5-μm range. The photodetector works in a zero-bias photovoltaic mode, enabling fast photoresponse and low dark noise. Our van der Waals heterojunction photodetectors not only exemplify black arsenic phosphorus as a promising candidate for MIR optoelectronic applications but also pave the way for a general strategy to suppress 1/f noise in photonic devices.

INTRODUCTION

State-of-the-art mid-infrared (MIR) detectors are generally made of certain narrow–band gap semiconductors, such as HgCdTe alloys (1, 2) or quantum-well and quantum-dot structures based on group III to V materials (3, 4). Unfortunately, these materials suffer from several major challenges that limit their wide application. First, the growth of these materials is usually sophisticated and environmentally hazardous, making it challenging to flexibly form a heterojunction with other semiconductors. Second, operation of these detectors generally requires a cryogenic environment with complex cooling facilities, which prohibit their usage in portable contexts, such as distributed environmental monitoring or compact telecommunication networks. The discovery of graphene has provided a promising alternative solution for MIR photodetectors (5–8) that can be easily fabricated and operated at room temperature. However, the practical application of graphene has been limited by very low light absorption and an inherent vanishing band gap, which results in an extremely high dark current and noise level. High-performance MIR photodetectors working at room temperature and in the second atmosphere window of long-wavelength IR (~8 to 14 μm) has yet to be demonstrated.

Very recently, a new two-dimensional (2D) layered material, black phosphorus, has arisen as an attractive candidate for optoelectronic applications (9–15) because it possesses a tunable narrow band gap that is always direct regardless of layer number (16–18) and exhibits excellent strong in-plane anisotropic physical properties (11, 19–21). Here, we demonstrate high-performance room temperature MIR photodetectors based on black arsenic phosphorus (b-AsP), which is an alloy of black phosphorus with arsenic atoms in the forms of As_xP_{1-x}. By varying the composition of phosphorus, x, the band gap correspondingly changes from 0.3 to 0.15 eV. This energy range suggests that b-AsP may interact with light, whose wavelength is as long as 8.5 μm. The extended detection range not only fully covers the first atmospheric window of mid-wavelength IR (~3 to 5 μm) but also is broadened to the second atmospheric window of long-wavelength IR (~8 to 14 μm), making b-AsP a highly attractive material for ultra-broadband photodetection and energy conversion.

RESULTS

Fabrication of b-AsP phototransistor

We first examined the photoresponse of b-AsP by a phototransistor (as schematically shown in the inset of Fig. 1A). To prevent degradation of b-AsP flakes during the fabrication processes, we prepared b-AsP thin films by mechanically exfoliating bulk b-AsP samples ($As_{0.83}P_{0.17}$) onto a highly doped silicon substrate covered by 300-nm SiO_2 in a glove box. We chose flakes of b-AsP ranging from 5 to 20 nm thick for device fabrication due to the desired compromise between high light absorption and low dark current. The devices were then fabricated by standard electron-beam lithography, metallization, and a lift-off process. After the fabrication processes, we spin-coated a thin layer of polymethyl methacrylate (PMMA) to protect the samples from oxidation in the air. Figure 1A shows a typical optical absorption spectrum of the b-AsP samples we used. The absorption peak is located at approximately 2760 cm^{-1}, which corresponds to 3.62 μm. The relatively large thickness plays a beneficial role in boosting the optical absorption and thus the responsivity of the b-AsP–based photodetectors. As the wave number decreases from the peak, the absorption decreases linearly to approximately 1250 cm^{-1} (corresponding to 8.27 μm), marked by the cross of two red lines (as guides to the eye). These results suggest that the absorption edge is at approximately 1250 cm^{-1}, corresponding to a ~0.15-eV band gap. By combining energy-dispersive spectroscopy with Raman spectra studies, the compositions of the samples were confirmed to be $As_{0.83}P_{0.17}$ (see fig. S1) (21). We also measured the electrical transport of b-AsP field-effect transistors (FETs), the field-effect mobility of which was calculated to be ~307 cm^2 V^{-1} s^{-1} at 0.01-V bias (see fig. S2).

[1]National Laboratory of Solid State Microstructures, School of Physics, Collaborative Innovation Center of Advanced Microstructures, Nanjing University, Nanjing 210093, China. [2]National Laboratory for Infrared Physics, Shanghai Institute of Technical Physics, Chinese Academy of Sciences, Shanghai 200083, China. [3]Synthesis and Characterization of Innovative Materials, Department of Chemistry, Technical University of Munich, Garching bei München 85748, Germany. [4]Department of Electronic Engineering and Materials Science and Technology Research Center, Chinese University of Hong Kong, Hong Kong SAR, China. [5]School of Electronic Science and Technology, Nanjing University, Nanjing 210093, China.
*Corresponding author. Email: miao@nju.edu.cn (F.M.); wdhu@mail.sitp.ac.cn (W.H.); xiaomu.wang@nju.edu.cn (X.W.)
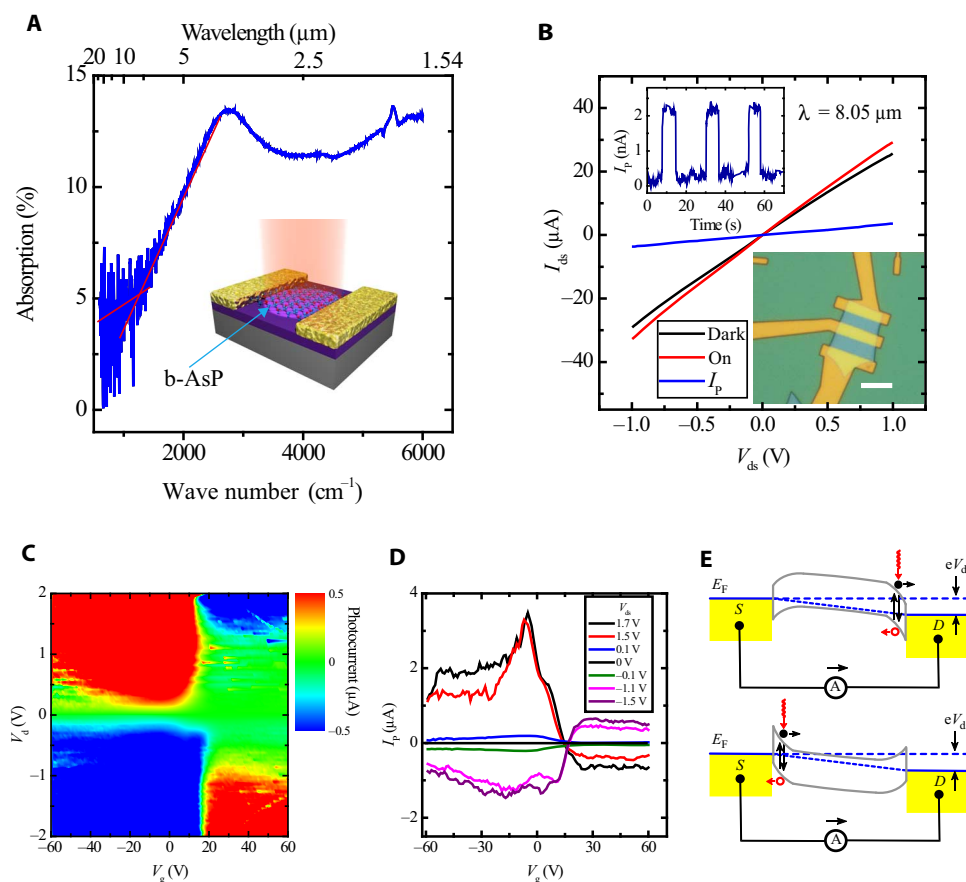
Fig. 1. MIR photovoltaic detector based on b-AsP. (**A**) IR absorption spectra of the b-As$_{0.83}$P$_{0.17}$ sample. Inset: Schematic drawing of the b-As$_{0.83}$P$_{0.17}$ phototransistor for photodetection. (**B**) I_{ds}-V_{ds} characteristic curves with and without illumination, and photocurrent I_P as a function of bias voltage at $V_g = 0$ V. The wavelength of the laser was 8.05 µm, and the power density was 0.17 W cm^{-2}. Inset: Optical image of the device. Scale bar, 5 µm. (**C**) 2D counter plot of the MIR (4.034 µm) photocurrent as a function of V_{ds} and V_g. The photocurrent generation mechanism is dominated by the PVE and PTE at zero-bias voltage. The incident laser power density was fixed at ~0.1 W cm^{-2}. (**D**) Photocurrent versus gate voltage at various bias voltages. The sign of the photocurrent changes as the gate voltage increases at ~15 V from negative (p-doped) to positive (highly n-doped). (**E**) Schematic diagrams of energy structure diagrams at different doping types under a bias voltage V_{ds}. Top panel: The sample of b-AsP working at the p-type region. Bottom panel: The device working at the n-type region. The black horizontal arrows indicate the direction of the photocurrent, which was caused by the PVE.

Photocurrent mechanisms of b-AsP

We now turn to study the origin of photocurrent generation in b-AsP. For simplicity and to extract the intrinsic photoresponse, we still use the phototransistor structure. As shown in Fig. 1B, a typical phototransistor (shown in the down inset) exhibits nearly linear I-V curves under dark conditions and under the illumination of an 8.05-µm MIR laser. The photocurrent ($I_P = I_{light} - I_{dark}$) increased linearly with increasing bias voltage together with the observed zero-biased photoresponse (Fig. 1B, upper inset), suggesting a significant MIR photoresponse. To reveal the detailed photoresponse mechanisms of the devices at the MIR range, we systematically measured the generated photocurrent at various source-drain voltage V_{ds} and gate voltage V_g values, with typical results presented in Fig. 1 (C and D). The photocurrent switched its polarity with increasing gate voltage at all source-drain biases. The opposite photocurrents in different regions are attributed to the photovoltaic (PVE) and photothermoelectric effect (PTE).

At low-doped or intrinsic regimes (−15 V < V_g < 15 V), the photocurrent is positive relative to V_{ds} and reaches a maximum near the charge neutrality point. The positive polarity together with the zero-bias response suggests that the PVE dominates (9, 14, 22–24). In this scenario, the b-AsP/metal Schottky junction plays a key role in the photocurrent generation. Figure 1E schematically shows the photovoltaic response of b-AsP devices in which photogenerated electron-hole pairs are separated at the b-AsP/metal junctions. If the channel is p-type–doped, then the photocurrent is mainly generated at the reverse-biased b-AsP/drain junction (top panel). In the case of slightly n-type–doped b-AsP, the photocurrent is mainly generated at the reverse-biased b-AsP/source junction (bottom panel). Here, V_{ds} is assumed to be positive regardless of the channel type for simplicity. In both cases, the photocurrent is positive relative to the conduction current. We further characterized these junctions through spatial photocurrent mapping measurements (at near-IR range). Figure S3 presents the optical image of the device and corresponding photocurrent mapping results at $V_{ds} = 50$ and 0 mV. The spatial mappings verify that the photocurrent is mainly generated at Schottky junctions. The photocurrent has opposite polarity at the two contacts due to the opposite junction bias direction. The mapping also excludes the photogating effect as the major working mechanism; if photogating dominates the response, then the photocurrent would be mainly generated in the channel center. The PVE is mostly pronounced in the intrinsic

regime due to the lower-channel carrier density and longer photo-carrier lifetime.

By contrast, the photocurrent is negative relative to V_{ds} and shows very weak gate dependence in the highly doped regime ($V_g > 15$ V), as shown in the line traces plotted in Fig. 1D. In this case, thermally driven processes (the PTE and bolometric effect) dominate the photoresponse. Unlike in the case of graphene, for which the photocurrent is generated by the bolometric effect only, in b-AsP devices under low source-drain bias, the photocurrent is mainly attributed to the thermally driven processes due to the high electrical conductivity (25–29) and low thermal conductivity (9, 30) of b-AsP. This result can be understood from the expression of the PTE-generated photocurrent: $I_{PTE} = (S_1 - S_2) \Delta T / R_d$, where ΔT is the temperature gradient, R_d is the resistance of the device, and S_1 (S_2) is the Seebeck coefficient of b-AsP (metal electrodes). Under higher source-drain biases, the bolometric effect may be pronounced, manifested by a linearly increased photocurrent with V_{ds}. Compared with the PVE, the thermally driven processes present a lower responsivity. Therefore, we mainly operated our device in the PVE condition below.

MIR photoresponse of b-AsP

Next, we fully characterized the photoresponse of b-AsP in MIR. It is worth mentioning that the large photovoltaic response eventually generates photocurrent under zero source-drain bias through the unapparent asymmetry of metal electrodes or device shape. Higher photoreponses are expected in large built-in filed systems (for example, devices with asymmetric electrodes or p-n junctions). Here, for simplicity, we generally operated devices under zero bias, which also effectively suppresses dark current and therefore power consumption of photodetectors. We measured the zero-biased photoresponse of the b-AsP detectors at the MIR range from 2.4 to 8.05 µm, with typical responsivity data (defined as the ratio of photocurrent to incidence laser power) shown in Fig. 2A [see fig. S4 for results from the visible (0.45 µm) to the near-IR (1.55 µm) range]. Although the responsivity decreases slightly with increasing wavelength of the illumination laser due to decreased optical absorption around the band edges, the device presented a high responsivity (15 to 30 mA W^{-1}) across the entire MIR range tested. To quantify the efficiency of light conversion to current, we extracted the external quantum efficiency (EQE), that is, the ratio of the number of photoexcited charge carriers to the number of incident photons. EQE can be derived by EQE $= (hcI_P/e\lambda P_I)$, where h is the Planck constant, c is the speed of light, and λ is the wavelength of the incident laser. The calculated EQE is as high as ~6.1% under the illumination of a 3.662-µm laser, which indicates a promising performance at the MIR range. The speed of response is another important figure of merit of photodetectors; thus, we further measured photoresponse time using a 4.034-µm IR laser, with the results shown in Fig. 2B. The rise/fall time is defined as from 10/90% to 90/10% of the stable photocurrent after turning the laser on/off. The rise time ($\tau_{rise} = 0.54$ ms) and the fall time ($\tau_{fall} = 0.52$ ms) were obtained, as shown in Fig. 2B. Faster photoresponses at typical b-AsP FET devices were observed under the illumination of a 1.55-µm laser with higher power (see fig. S5). In principle, a much faster photoresponse is expected for the PVE. We attribute the relatively slower photoresponse to the percolation transport mode resulting from the imperfect material interface. Namely, the electronic transport turns from a hopping regime at low carrier densities to a band-like regime at high carrier densities. As a result, the photoresponse is slower at low carrier densities (and thus for low incident light power) due to the low mobility and high disorder, which is consistent with the

study of Guo *et al.* (12). Nevertheless, the speed demonstrated here is more than sufficient for IR imaging applications. We further measured the laser power–dependent photocurrent near the absorption peak, with the calculated photoresponsivity and EQE plotted as a function of laser power, as shown in Fig. 2C. The measurements were performed under 3.662-µm MIR laser excitation at $V_{ds} = 0$ V at room temperature. The photoresponsivity decreased from 180.0 to 20.3 mA W^{-1} as the power increased from 70.1 nW to 44.3 µW (the corresponding EQE decreased from 6.1 to 0.69%), which indicates that the photogating effect plays weaker roles in our illuminating power range due to the trapping centers being saturated under intense light (12).

The puckered crystal structure of b-AsP could naturally yield unique anisotropic photoresponses with many important applications; that is, the photocurrent periodically varies with the polarization of incident light or the current collection direction. Figure 2D shows the measured photocurrent along the x- (armchair edge) and y-directions (zigzag edge) of the same device (inset of Fig. 2D) at room temperature. The conductivity along the x-direction (without light illumination) is approximately 1.73 times higher than that along the y-direction at $V_g = 0$ V. This anisotropic factor, $\sigma_{xx}/\sigma_{yy} = 1.73$, is slightly larger than that in black phosphorus (~1.6) (12) and is consistent with previously reported results (20, 25, 31). Under the illumination of a 4.034-µm laser, I_{Px}/I_{Py} is approximately 3.51 at $V_{ds} = 1$ V. We also measured the polarization-resolved photoresponse, whereby the polarization of a linearly polarized incident laser was controlled by a half-wave plate. The polarization-dependent photocurrent mappings are presented in fig. S6. The photocurrent was observed to be maximum when the light polarization was along the x-direction and minimum when the light was along the y-direction, similar to the observation in black phosphorus (10, 24). The photocurrent anisotropy ratio, $\gamma = (I_{Pmax} - I_{Pmin})/(I_{Pmax} + I_{Pmin})$, was approximately 0.59, which is larger than that of black phosphorus (~0.3) (24).

b-AsP based van der Waals photodetector

High dark current noise is the major challenge of modern narrow–band gap semiconductor–based MIR photodetectors. Next, we demonstrate a general strategy to suppress dark current noise by using 2D van der Waals (vdW) heterojunctions. Integrability is an inherent merit of 2D materials by which different 2D flakes can be sequentially stacked into vdW heterojunctions. High energy barriers naturally formed at the interfaces of vdW junctions can effectively reduce dark noise. Note that this highly desired yet facile strategy simply does not work in traditional materials due to the difficulty of obtaining high-quality heterojunctions.

Following this idea, we fabricated photodetectors based on a b-AsP/MoS$_2$ heterostructure. The photoresponse of a typical heterostructure device together with its optical image is shown in Fig. 3A. The b-AsP is a p-type semiconductor, whereas MoS$_2$ is an n-type semiconductor. The typical rectification curves are presented in Fig. 3A, indicating that the vdW p-n junction was formed. This result is further confirmed by the photocurrent mapping at $V_{ds} = 0$ V (fig. S7). The current at the forward bias is more than two orders of magnitude larger than that of under a reverse bias. Because of the energy barrier in the b-AsP/MoS$_2$ heterostructure, the dark current is markedly depressed. The photoresponsivity and EQE as a function of wavelength are plotted in fig. S8. The photoresponsivity ranges from 216.1 to 115.4 mA W^{-1} as the wavelength increased from 2.36 to 4.29 µm. The corresponding EQE decreased from 11.36 to 3.33%.

Finally, the current noise density was measured. As shown in Fig. 3B, the noise figure (and thus the detectivity, as discussed below) at the
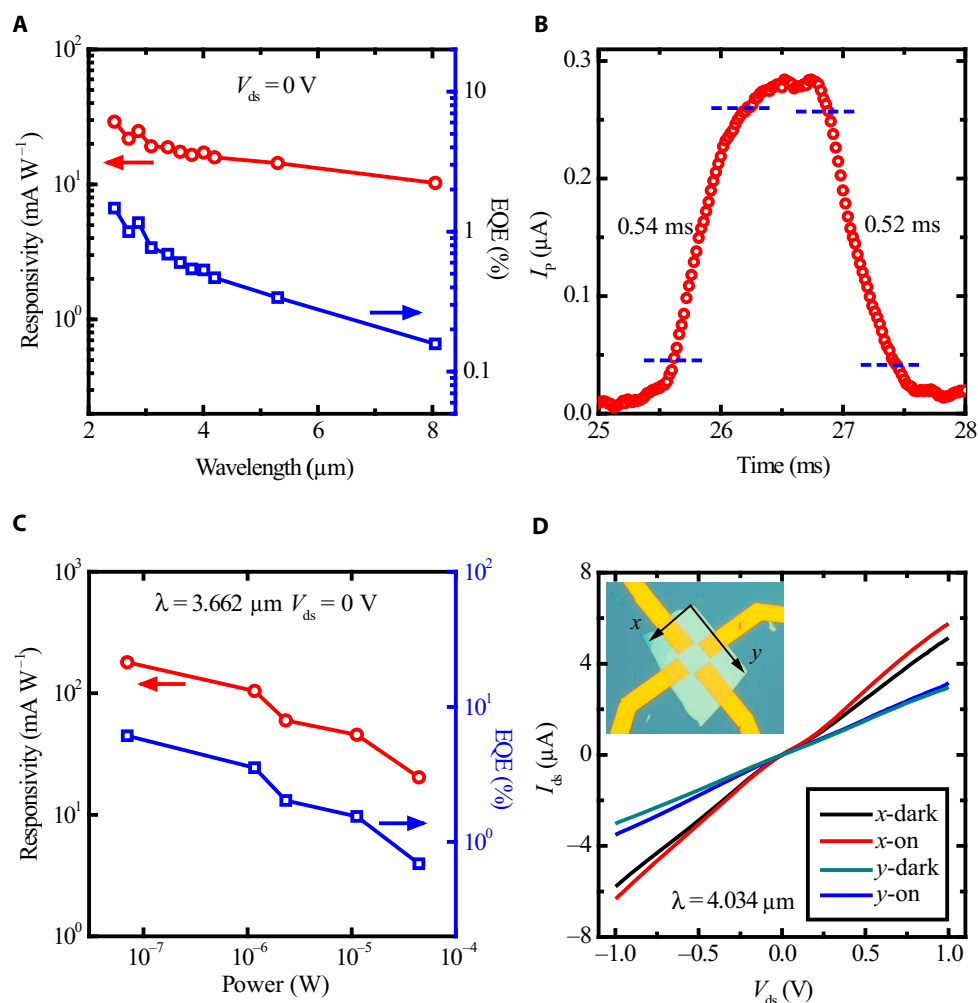
Fig. 2. Performance of the b-AsP photodetectors at MIR range at room temperature. (**A**) Photoresponsivity R (left) and EQE (right) of a typical device for wavelengths ranging from 2.4 to 8.05 µm. The measurements were performed at $V_{ds} = 0$ V and $V_g = 0$ V. (**B**) Fast photoresponse of a typical device measured under a 4.034-µm laser (21.5 W cm^{-2}) at $V_{ds} = 0$ V and $V_g = 0$ V. Here, the rise/fall time was defined as the photocurrent increased/decreased from 10/90% to 90/10% of the stable photocurrent. (**C**) Measured photoresponsivity R (left axis) and EQE (right axis) of a typical device versus power of the incident laser (4.034 µm). The measurements were performed with $V_{ds} = 0$ V and $V_g = 0$ V. (**D**) The I_{ds}-V_{ds} curves with and without illumination of the device. The x- and y-directions are labeled in the optical image in the inset. Scale bar, 5 µm. The wavelength of the incident laser was 4.034 µm, and the laser power was fixed at 21.5 Wcm^{-2}.

b-AsP/MoS$_2$ heterostructure was improved significantly compared with that of at the b-AsP FET. The frequency dependence results are also different, reflecting their different dominant noise sources. For the b-AsP FET devices, the 1/f noise prevails at low frequencies (1 to 100 Hz) and is considerably above the Johnson noise level. 1/f noise originates from fluctuations of local electronic states induced by the disorder or defects (*32*) that generally exist in 2D systems (*33*, *34*). Conversely, for the b-AsP/MoS$_2$ heterostructure devices, generation-recombination (g-r) noise dominates. g-r noise is caused by the fluctuation of carrier density due to the existence of trapping-detrapping centers. Its noise current spectrum is flat at low frequency and quickly decreases up to a frequency f_0. As shown in Fig. 3B, the spectrum fits a Lorentzian spectral model well (*35*, *36*) as

$$\frac{\langle i_n^2 \rangle}{\Delta f} = \frac{A}{1 + (f/f_0)^2}$$

where $f_0 = 1/2\pi\tau$ is the 3-dB corner frequency, and τ is the lifetime of the trap centers. These results indicate that the energy barrier at the junction efficiently depresses the random transport of the photogenerated carriers and therefore inhibits the undesired 1/f noise. Consequently, using the b-AsP/MoS$_2$ junction successfully decreased the total noise. Figure 3C shows the favorable NEP (defined by i_n/R, where R is the responsivity, and i_n is the measured noise current) obtained from our devices. The room temperature NEP of a junction at the MIR range is below 0.24 pW Hz$^{-1/2}$, and that of FET is lower than 4.35 pW Hz$^{-1/2}$, even for 8.05-µm MIR light. With the knowledge of noise density and NEP, another important figure of merit is the specific detectivity, D^*, which determines the minimum illumination light power that a detector can distinguish from the noise. This value can be calculated by $D^* = (AB)^{1/2}/\text{NEP}$, where A is the active area of the device, and B is the measuring bandwidth. The active area is used to normalize the dark noise. Figure 3D shows D^* as a function of wavelength. For comparison, data from the best available room temperature–operated MIR semiconductor (PbSe-based) detector, bolometer, and thermopile
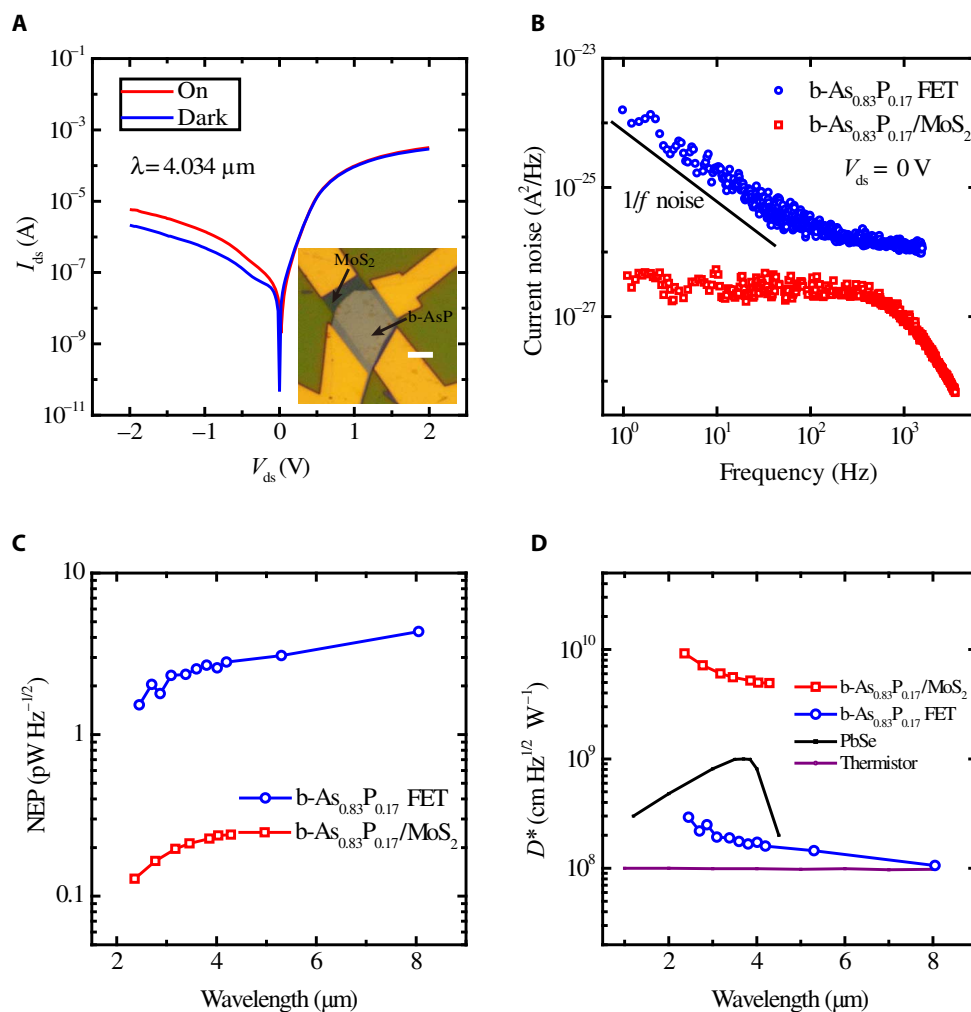
Fig. 3. Rectifying curves and photoresponse of the b-AsP/MoS$_2$ heterostructure detectors. (**A**) I_{ds}-V_{ds} characteristic curves (in logarithmic scale) with and without illumination ($V_g = 0$ V). The wavelength of the laser was 4.034 μm, and the power density was 1.09 W cm^{-2}. Inset: Optical image of a typical b-AsP/MoS$_2$ heterostructure device. Scale bar, 5 μm. (**B**) The current noise power spectra at $V_{ds} = 0$ V of a b-AsP FET device (blue open circles) and a b-AsP/MoS$_2$ heterostructure (red open squares). The black solid line (plotted as $A/[1 + (f/f_0)^2]$) is a reference for the $1/f$ noise trend. (**C**) Wavelength dependence of the noise equivalent power (NEP). (**D**) Wavelength dependence of the specific detectivity, D^* (right axis), at $V_{ds} = 0$ V. The purple and dark lines are commercial specific detectivity for a thermistor bolometer and PbSe MIR detectors, respectively, at room temperature.

are also given in the figure (*37, 38*). The peak D^* of our junction approaches 9.2×10^9 Jones, and it is consistently larger than 4.9×10^9 Jones in the 3- to 5-μm range; these values are well beyond all room temperature MIR photodetectors to date (for example, the black line in Fig. 3D). Actually, the room temperature D^* of b-AsP FET is considerably larger than 1.06×10^8 Jones (cm Hz$^{1/2}$ W^{-1}), even for 8.05-μm MIR light, which is already higher than that of the commercial thermistor bolometer (the purple line in Fig. 3D). The performance of photodetection shows a significant enhancement for these b-AsP/MoS$_2$ heterostructure devices.

DISCUSSION

In summary, we demonstrated room temperature–operated MIR (entering the second atmospheric transmission window) photodetectors based on b-AsP. Compared with other MIR detectors, such as graphene (*5, 39, 40*), the b-AsP detectors exhibit significant advantages of promising broadband MIR responsivity, fast speed, and excel-

lent anisotropic photoresponse. In addition, the 2D nature of b-AsP renders it inherently easy to integrate with other materials. The specific detectivity is one of the most important figures of merit for photodetectors. Long-wavelength detection generally requires small-gap semiconductors to absorb light. For junctionless photoconductors, especially for the narrow–band gap 2D materials, poor dark noise causes low signal-to-noise ratio and small specific detectivity. Junctions thus propose an effective approach to enhance specific detectivity considerably. Taking advantage of the promising optical properties of b-AsP and facile fabrication of vdW heterojunctions, we demonstrated that the overall performances, especially the dark current noise and specific detectivity, can be further improved. The main working mechanisms of the devices were also revealed. Further work may include a large-area synthesis of b-AsP thin films and scalable fabrication of MIR devices. Our findings not only exemplify an ideal photodetector for challenging MIR imaging tasks but also pave the way for novel MIR technologies, such as polarization-sensitive detection and free space telecommunication.

MATERIALS AND METHODS

Materials synthesis

Bulk b-AsP (As$_x$P$_{1-x}$) crystals were synthesized using the mineralizer-assisted short-way transport reaction method (41). Briefly, a mixture of gray arsenic and red phosphorus with molar ratios ranging from 5:5 to 2:8 was used as the precursor. Presynthesized lead iodide (PbI$_2$, weighing 10 mg per 500 mg) was added as the mineralization agent. The mixture was then evacuated in a 10-cm silica glass ampoule and placed horizontally in a furnace. The mixture was heated up to 550°C for 8 hours, held at this temperature for 20 to 80 hours, and slowly cooled to room temperature within 20 hours. In this process, the heating elements of the furnace were configured within the walls. The mixture of reactive materials was located at the hot end, with the empty part of the ampoule toward the cooler center. The arsenic composition, x, obtained by this method is distributed from 0.36 to 0.83. The b-AsP samples with different arsenic compositions were tested in this project, and a typical set of results from the sample with $x \sim 0.83$ is described in the main text.

Device fabrication

We used a standard mechanical exfoliation method to isolate few-layer black phosphorus flakes, typically ranging from 5 to 20 nm, on a highly doped Si wafer covered by a 300-nm-thick SiO$_2$ layer. The thickness of the flakes was first measured using a Bruker MultiMode 8 atomic force microscope. The b-AsP/MoS$_2$ heterostructure was fabricated using a polymer-free vdW assembly technique in a glove box filled with an inert atmosphere. The devices were fabricated using a conventional electron-beam lithography process followed by standard electron-beam evaporation of metal electrodes (typically 5-nm Ti/50-nm Au).

After the fabrication processes, we spin-coated a thin layer of PMMA to protect the samples from oxidation in air. The stability improvement was verified by checking the optical image, dark current, and photovoltaic response (fig. S9). We did not find any obvious degradation in the protected samples fabricated 2 months ago.

Electrical and photoresponse measurements

Electrical transport and photoresponse measurements were performed using a Keithley 2636A dual-channel digital source meter. The wavelength-dependent photoresponse in Fig. 2A was measured using a custom-built wavelength-tunable multichannel MIR laser source. The spectrum spanned from 2 to 4.3 μm with ~0.43-mm^2 spot size. The 5.3- and 8.05-μm light sources were custom-built quantum cascade lasers with ~9-mm^2 spot size and ~50-mW power. In the visible- to near-IR range from 450 to 1550 nm, the laser was focused on the device using a 20× objective lens. Noise measurements were performed at room temperature. The devices were set in a thoroughly screened metal box to ensure that the device was working in the dark and to reduce the noise originating from the environment. Noise spectra were acquired by a spectrum analyzer (Stanford Research System SR770, with a measuring bandwidth of 100 kHz) at different biases. All the measurements were performed under ambient conditions.

SUPPLEMENTARY MATERIALS

Supplementary material for this article is available at http://advances.sciencemag.org/cgi/content/full/3/6/e1700589/DC1

fig. S1. Raman spectra of b-AsP with different thicknesses.
fig. S2. The transfer curves of two typical b-AsP FET devices.
fig. S3. The photocurrent mappings of a typical device at near-IR range.
fig. S4. The performance of a typical b-AsP device at visible- and near-IR range.
fig. S5. Fast photoresponse at near-IR.
fig. S6. Laser polarization direction–sensitive photocurrent mapping.
fig. S7. Photocurrent mapping of the b-As$_{0.83}$P$_{0.17}$/MoS$_2$ heterostructure.
fig. S8. Photoresponsivity and EQE of a typical b-As$_{0.83}$P$_{0.17}$/MoS$_2$ heterostructure device.
fig. S9. The stability of b-AsP samples spin-coated by a PMMA layer.

REFERENCES AND NOTES

1. P. Norton, HgCdTe infrared detectors. *Opto-Electron. Rev.* **10**, 159–174 (2002).
2. A. Rogalski, Toward third generation HgCdTe infrared detectors. *J. Alloys. Compd.* **371**, 53–57 (2004).
3. B. F. Levine, K. K. Choi, C. G. Bethea, J. Walker, R. J. Malik, New 10 μm infrared detector using intersubband absorption in resonant tunneling GaAlAs superlattices. *Appl. Phys. Lett.* **50**, 1092 (1987).
4. A. Rogalski, P. Martyniuk, InAs/GaInSb superlattices as a promising material system for third generation infrared detectors. *Infrared Phys. Technol.* **48**, 39–52 (2006).
5. Y. Zhang, T. Liu, B. Meng, X. Li, G. Liang, X. Hu, Q. J. Wang, Broadband high photoresponse from pure monolayer graphene photodetector. *Nat. Commun.* **4**, 1811 (2013).
6. M. Long, E. Liu, P. Wang, A. Gao, H. Xia, W. Luo, B. Wang, J. Zeng, Y. Fu, K. Xu, W. Zhou, Y. Lv, S. Yao, M. Lu, Y. Chen, Z. Ni, Y. You, X. Zhang, S. Qin, Y. Shi, W. Hu, D. Xing, F. Miao, Broadband photovoltaic detectors based on an atomically thin heterostructure. *Nano Lett.* **16**, 2254–2259 (2016).
7. G. Konstantatos, M. Badioli, L. Gaudreau, J. Osmond, M. Bernechea, F. P. Garcia de Arquer, F. Gatti, F. H. L. Koppens, Hybrid graphene–quantum dot phototransistors with ultrahigh gain. *Nat. Nanotechnol.* **7**, 363–368 (2012).
8. C.-H. Liu, Y.-C. Chang, T. B. Norris, Z. Zhong, Graphene photodetectors with ultra-broadband and high responsivity at room temperature. *Nat. Nanotechnol.* **9**, 273–278 (2014).
9. N. Youngblood, C. Chen, S. J. Koester, M. Li, Waveguide-integrated black phosphorus photodetector with high responsivity and low dark current. *Nat. Photonics* **9**, 247–252 (2015).
10. H. Yuan, X. Liu, F. Afshinmanesh, W. Li, G. Xu, J. Sun, B. Lian, A. G. Curto, G. Ye, Y. Hikita, Z. Shen, S.-C. Zhang, X. Chen, M. Brongersma, H. Y. Hwang, Y. Cui, Polarization-sensitive broadband photodetector using a black phosphorus vertical p–n junction. *Nat. Nanotechnol.* **10**, 707–713 (2015).
11. J. Qiao, X. Kong, Z.-X. Hu, F. Yang, W. Ji, High-mobility transport anisotropy and linear dichroism in few-layer black phosphorus. *Nat. Commun.* **5**, 4475 (2014).
12. Q. Guo, A. Pospischil, M. Bhuiyan, H. Jiang, H. Tian, D. Farmer, B. Deng, C. Li, S.-J. Han, H. Wang, Q. Xia, T.-P. Ma, T. Mueller, F. Xia, Black phosphorus mid-infrared photodetectors with high gain. *Nano Lett.* **16**, 4648–4655 (2016).
13. S. Zhang, J. Yang, R. Xu, F. Wang, W. Li, M. Ghufran, Y.-W. Zhang, Z. Yu, G. Zhang, Q. Qin, Y. Lu, Extraordinary photoluminescence and strong temperature/angle-dependent Raman responses in few-layer phosphorene. *ACS Nano* **8**, 9590–9596 (2014).
14. T. Low, A. S. Rodin, A. Carvalho, Y. Jiang, H. Wang, F. Xia, A. H. Castro Neto, Tunable optical properties of multilayer black phosphorus thin films. *Phys. Rev. B* **90**, 075434 (2014).
15. M. Buscema, D. J. Groenendijk, G. A. Steele, H. S. J. van der Zant, A. Castellanos-Gomez, Photovoltaic effect in few-layer black phosphorus PN junctions defined by local electrostatic gating. *Nat. Commun.* **5**, 4651 (2014).
16. A. S. Rodin, A. Carvalho, A. H. Castro Neto, Strain-induced gap modification in black phosphorus. *Phys. Rev. Lett.* **112**, 176801 (2014).
17. J. Guan, Z. Zhu, D. Tománek, Phase coexistence and metal-insulator transition in few-layer phosphorene: A computational study. *Phys. Rev. Lett.* **113**, 046804 (2014).
18. S. Das, W. Zhang, M. Demarteau, A. Hoffmann, M. Dubey, A. Roelofs, Tunable transport gap in phosphorene. *Nano Lett.* **14**, 5733–5739 (2014).
19. X. Wang, A. M. Jones, K. L. Seyler, V. Tran, Y. Jia, H. Zhao, H. Wang, L. Yang, X. Xu, F. Xia, Highly anisotropic and robust excitons in monolayer black phosphorus. *Nat. Nanotechnol.* **10**, 517–521 (2015).
20. F. Xia, H. Wang, Y. Jia, Rediscovering black phosphorus as an anisotropic layered material for optoelectronics and electronics. *Nat. Commun.* **5**, 4458 (2014).
21. B. Liu, M. Köpf, A. N. Abbas, X. Wang, Q. Guo, Y. Jia, F. Xia, R. Weihrich, F. Bachhuber, F. Pielnhofer, H. Wang, R. Dhall, S. B. Cronin, M. Ge, X. Fang, T. Nilges, C. Zhou, Black arsenic-phosphorus: Layered anisotropic infrared semiconductors with highly tunable compositions and properties. *Adv. Mater.* **27**, 4423–4429 (2015).
22. M. Freitag, T. Low, F. Xia, P. Avouris, Photoconductivity of biased graphene. *Nat. Photonics* **7**, 53–59 (2013).
23. M. Buscema, J. O. Island, D. J. Groenendijk, S. I. Blanter, G. A. Steele, H. S. J. van der Zant, A. Castellanos-Gomez, Photocurrent generation with two-dimensional van der Waals semiconductors. *Chem. Soc. Rev.* **44**, 3691–3718 (2015).
24. T. Hong, B. Chamlagain, W. Lin, H.-J. Chuang, M. Pan, Z. Zhou, Y.-Q. Xu, Polarized photocurrent response in black phosphorus field-effect transistors. *Nanoscale* **6**, 8978–8983 (2014).

25. H. Liu, A. T. Neal, Z. Zhu, Z. Luo, X. Xu, D. Tománek, P. D. Ye, Phosphorene: An unexplored 2D semiconductor with a high hole mobility. *ACS Nano* **8**, 4033–4041 (2014).

26. L. Li, Y. Yu, G. J. Ye, Q. Ge, X. Ou, H. Wu, D. Feng, X. H. Chen, Y. Zhang, Black phosphorus field-effect transistors. *Nat. Nanotechnol.* **9**, 372–377 (2014).

27. L. Li, G. J. Ye, V. Tran, R. Fei, G. Chen, H. Wang, J. Wang, K. Watanabe, T. Taniguchi, L. Yang, X. H. Chen, Y. Zhang, Quantum oscillations in a two-dimensional electron gas in black phosphorus thin films. *Nat. Nanotechnol.* **10**, 608–613 (2015).

28. X. Chen, Y. Wu, Z. Wu, Y. Han, S. Xu, L. Wang, W. Ye, T. Han, Y. He, Y. Cai, N. Wang, High-quality sandwiched black phosphorus heterostructure and its quantum oscillations. *Nat. Commun.* **6**, 7315 (2015).

29. N. Gillgren, D. Wickramaratne, Y. Shi, T. Espiritu, J. Yang, J. Hu, J. Wei, X. Liu, Z. Mao, K. Watanabe, T. Taniguchi, M. Bockrath, Y. Barlas, R. K. Lake, C. N. Lau, Gate tunable quantum oscillations in air-stable and high mobility few-layer phosphorene heterostructures. *2D Mater.* **2**, 011001 (2015).

30. Z. Luo, J. Maassen, Y. Deng, Y. Du, R. P. Garrelts, M. S. Lundstrom, P. D. Ye, X. Xu, Anisotropic in-plane thermal conductivity observed in few-layer black phosphorus. *Nat. Commun.* **6**, 8572 (2015).

31. A. Mishchenko, Y. Cao, G. L. Yu, C. R. Woods, R. V. Gorbachev, K. S. Novoselov, A. K. Geim, L. S. Levitov, Nonlocal response and anamorphosis: The case of few-layer black phosphorus. *Nano Lett.* **15**, 6991–6995 (2015).

32. N. Clément, K. Nishiguchi, A. Fujiwara, D. Vuillaume, One-by-one trap activation in silicon nanowire transistors. *Nat. Commun.* **1**, 92 (2010).

33. J. Na, Y. T. Lee, J. A. Lim, D. K. Hwang, G.-T. Kim, W. K. Choi, Y.-W. Song, Few-layer black phosphorus field-effect transistors with reduced current fluctuation. *ACS Nano* **8**, 11753–11762 (2014).

34. A. A. Balandin, Low-frequency 1/f noise in graphene devices. *Nat. Nanotechnol.* **8**, 549–555 (2013).

35. L. D. Yau, C.-T. Sah, Theory and experiments of low-frequency generation-recombination noise in MOS transistors. *IEEE T. Electron. Devices* **16**, 170–177 (1969).

36. J. A. Copeland, Semiconductor impurity analysis from low-frequency noise spectra. *IEEE T. Electron. Devices* **18**, 50–53 (1971).

37. www.vision-systems.com/articles/print/volume-16/issue-4/features/the-infrared-choice.html.

38. A. L. Hsu, P. K. Herring, N. M. Gabor, S. Ha, Y. C. Shin, Y. Song, M. Chin, M. Dubey, A. P. Chandrakasan, J. Kong, P. Jarillo-Herrero, T. Palacios, Graphene-based thermopile for thermal imaging applications. *Nano Lett.* **15**, 7211–7216 (2015).

39. X. Wang, Z. Cheng, K. Xu, H. K. Tsang, J.-B. Xu, High-responsivity graphene/silicon-heterostructure waveguide photodetectors. *Nat. Photonics* **7**, 888–891 (2013).

40. Y. Yao, R. Shankar, P. Rauter, Y. Song, J. Kong, M. Loncar, F. Capasso, High-responsivity mid-infrared graphene detectors with antenna-enhanced photocarrier generation and collection. *Nano Lett.* **14**, 3749–3754 (2014).

41. O. Osters, T. Nilges, F. Bachhuber, F. Pielnhofer, R. Weihrich, M. Schöneich, P. Schmidt, Synthesis and identification of metastable compounds: Black arsenic—Science or fiction? *Angew. Chem. Int. Ed.* **51**, 2994–2997 (2012).

Citation: M. Long, A. Gao, P. Wang, H. Xia, C. Ott, C. Pan, Y. Fu, E. Liu, X. Chen, W. Lu, T. Nilges, J. Xu, X. Wang, W. Hu, F. Miao, Room temperature high-detectivity mid-infrared photodetectors based on black arsenic phosphorus. *Sci. Adv.* **3**, e1700589 (2017).

Science Advances

Room temperature high-detectivity mid-infrared photodetectors based on black arsenic phosphorus

Mingsheng Long, Anyuan Gao, Peng Wang, Hui Xia, Claudia Ott, Chen Pan, Yajun Fu, Erfu Liu, Xiaoshuang Chen, Wei Lu, Tom Nilges, Jianbin Xu, Xiaomu Wang, Weida Hu and Feng Miao

ARTICLE TOOLS	http://advances.sciencemag.org/content/3/6/e1700589
SUPPLEMENTARY MATERIALS	http://advances.sciencemag.org/content/suppl/2017/06/26/3.6.e1700589.DC1
REFERENCES	This article cites 40 articles, 0 of which you can access for free http://advances.sciencemag.org/content/3/6/e1700589#BIBL
PERMISSIONS	http://www.sciencemag.org/help/reprints-and-permissions

Use of this article is subject to the Terms of Service

Science Advances

Supplementary Materials for

Room temperature high-detectivity mid-infrared photodetectors based on black arsenic phosphorus

Mingsheng Long, Anyuan Gao, Peng Wang, Hui Xia, Claudia Ott, Chen Pan, Yajun Fu, Erfu Liu, Xiaoshuang Chen, Wei Lu, Tom Nilges, Jianbin Xu, Xiaomu Wang, Weida Hu, Feng Miao

This PDF file includes:

fig. S1. Raman spectra of b-AsP with different thicknesses. (**A**) Three characteristic vibrational modes: A_g^1, B_{2g} and A_g^2, located at 224 cm^{-1}, 233cm^{-1} and 256 cm^{-1}, respectively. Numbers 1 and 2 correspond to different flakes with optical images shown in (B). The silicon peak at 520 cm^{-1} was used as calibration of the measurements. (**B**) Optical image of the sample for Raman measurement with the scale bar of 5 μm. A 50× objective lens was used to focus the 514 nm laser, with beam size ~1 μm.
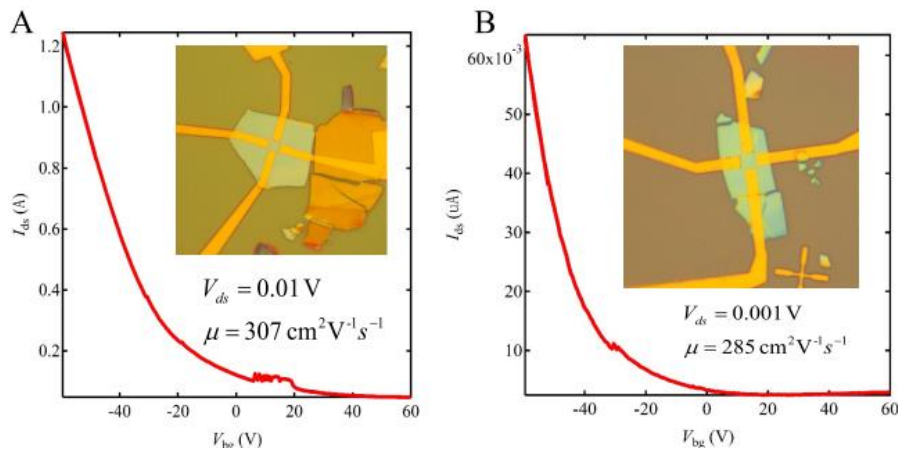
fig. S2. The transfer curves of two typical b-AsP FET devices. The length-to-width ratio of the channels is ~1. The mobility of device#1 (**A**) and device #2 (**B**) was estimated to be ~307 cm^{2}V^{-1}s^{-1} and ~285 cm^{2}V^{-1}s^{-1}, respectively.
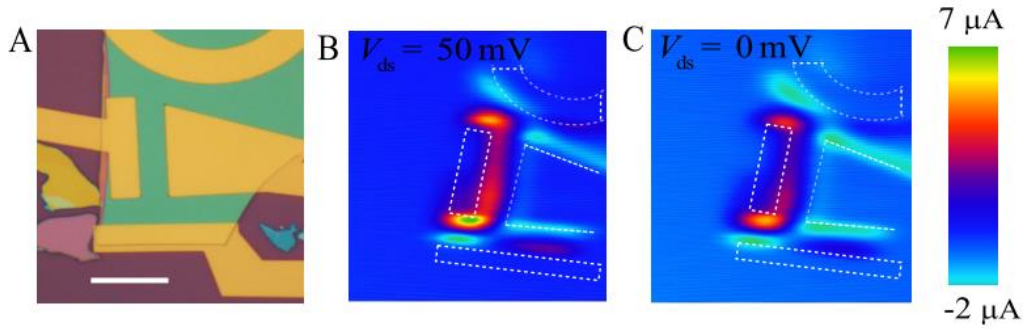
fig. S3. The photocurrent mappings of a typical device at near-IR range. (**A**) The optical image of a b-As$_{0.83}$P$_{0.17}$ FET device for photocurrent mapping study. The scale bar is 5 μm. (**B**) and (**C**) The photocurrent mappings measured with source-drain bias of 50 mV and 0 mV respectively. The wavelength of the laser was 1060 nm and the power was fixed at 64.5 μW.
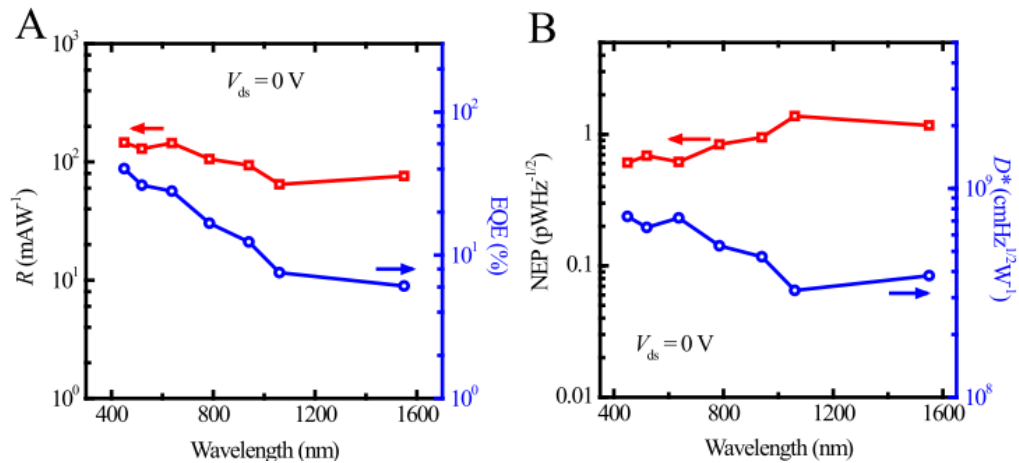
fig. S4. The performance of a typical b-AsP device at visible- and near-IR range.
(**A**) Photoresponsivity R (left axis) and EQE (right) of a typical device for wavelength ranging from 450 nm to 1550 nm. The photoresponsivity and EQE were measured to be up to 146.0 mAW^{-1} and 40.2% respectively under a 450 nm laser illumination at V_g = 0 V. (**B**) Wavelength dependence of the noise equivalent power (NEP, left axis) and specific detectivity D^* (right) at V_{ds} = 0 V for wavelength ranging from 450 nm to 1550 nm. The NEP is lower than 1.3 pWHz$^{-1/2}$, indicating the detector is capable of detecting weak light signal below 1.3 pW at visible and near infrared range. The specific detectivity D^* is up to 7.33 $\times 10^8$ Jones for 450 nm and 3.8$\times 10^8$ Jones for 1550 nm laser. The measurements were performed at ambient conditions.
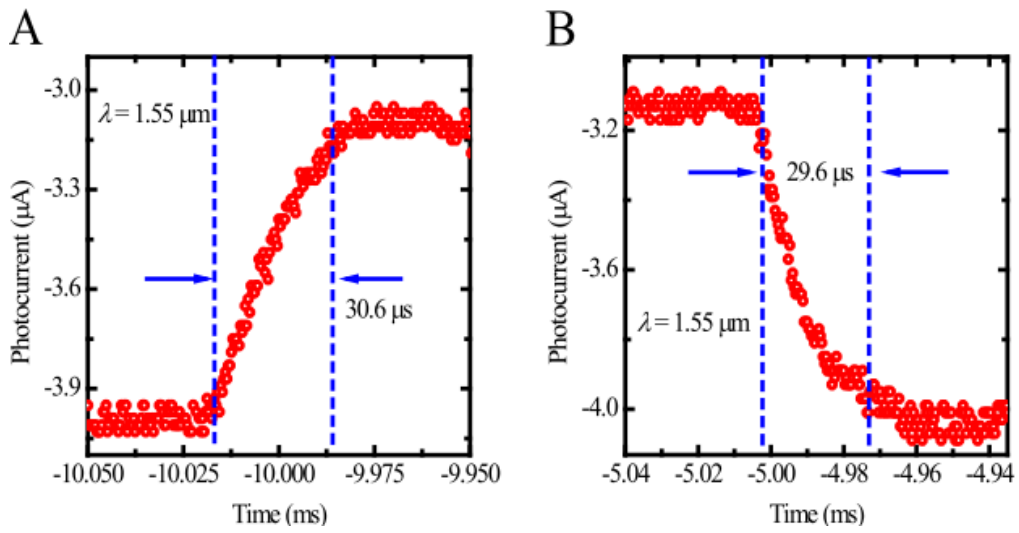
fig. S5. Fast photoresponse at near-IR. (**A**) The rise time ~30.6 μs and (**B**) decay time ~29.6 μs of a typical b-As$_{0.83}$P$_{0.17}$ FET measured under a 1550 nm laser at $V_{ds} = 0$ V and $V_g = 0$ V in ambient air. The data was collected by an oscilloscope.
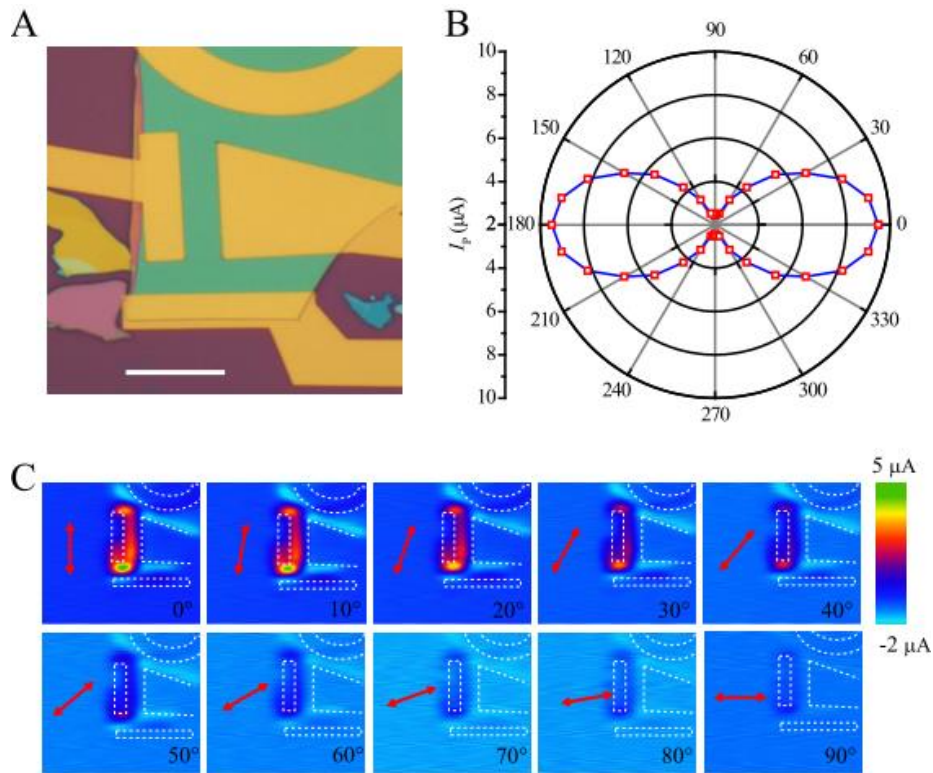
fig. S6. Laser polarization direction–sensitive photocurrent mapping. (**A**) optical image of a typical b-As$_{0.83}$P$_{0.17}$ FET device. The scale bar is 5 μm. (**B**) The light polarization direction dependent photocurrent at V_{ds}=0 V in ambient air. The light polarization direction of the incident laser was adjusted by a half wavelength plate at a step of 10°. The 0° denotes the polarization direction parallel to the contact edge of the metal. The red double arrows present the polarization directions. (**C**) Photocurrent mapping of the b-AsP detector at various laser polarization directions at V_{ds} = 0 V. The wavelength was 1550 nm and the power was fixed at 177.2 μW. The photocurrent is at a maxima with light polarization at 0° and at a minima with light polarization at 90°. The results are in good consistency with the recent studies on black phosphorus.
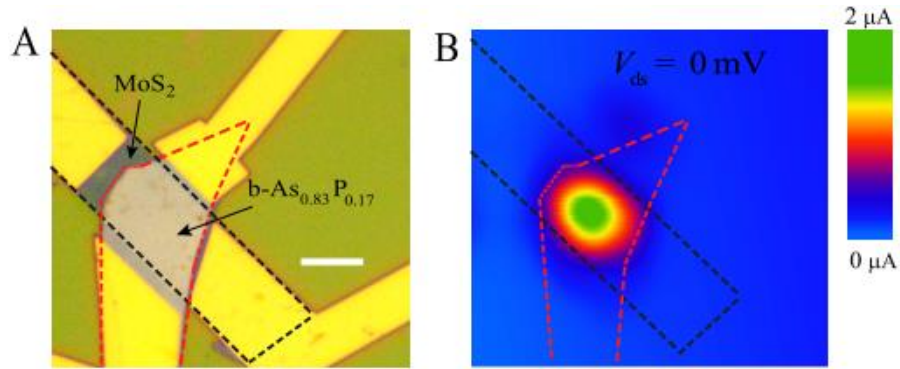
fig. S7. Photocurrent mapping of the b-As$_{0.83}$P$_{0.17}$/MoS$_2$ heterostructure. (**A**) The optical image of a typical b-As$_{0.83}$P$_{0.17}$/MoS$_2$ heterostructure device. The scale bar is 5 μm. (**B**) The photocurrent mapping of the b-As$_{0.83}$P$_{0.17}$/MoS$_2$ heterostructure photodetector at V_{ds} = 0 V.
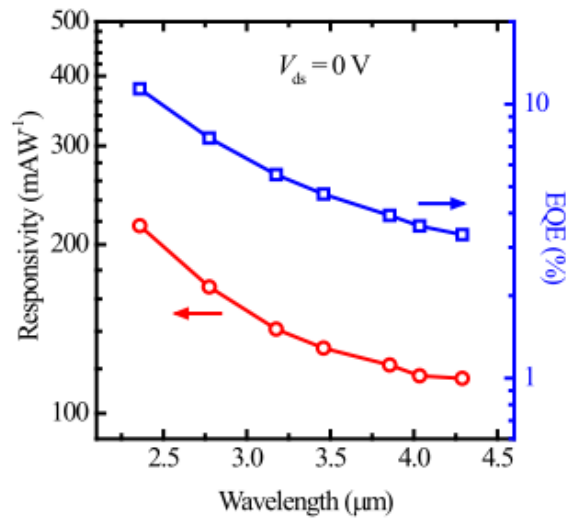
fig. S8. Photoresponsivity and EQE of a typical b-As$_{0.83}$P$_{0.17}$/MoS$_2$ heterostructure device. The photoresponsivity decreased from 216.1 mAW^{-1} to 115.4 mAW^{-1} as the wavelength increased from 2.36 μm to 4.29 μm (corresponding EQE decreased from 11.36% to 3.33%). The measurements were carried out at V_{ds} = 0 V and V_{g} = 0 V.
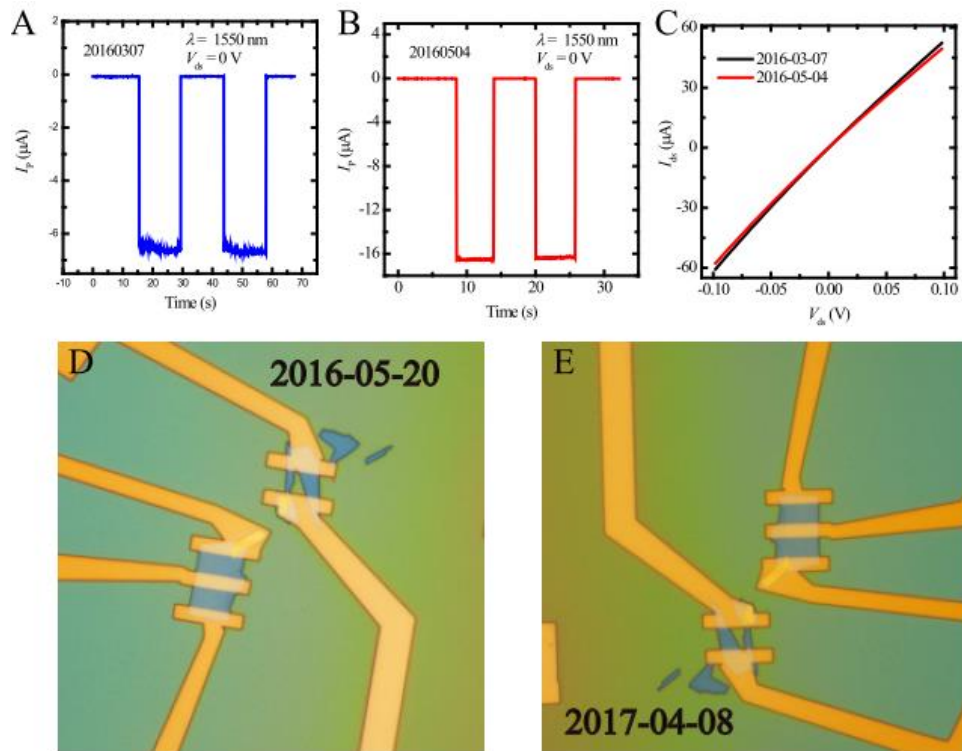
fig. S9. The stability of b-AsP samples spin-coated by a PMMA layer. (**A**) and (**B**) The photovoltaic responses of a typical b-AsP FET device at 1.55 μm for the as-fabricated device and after stored in air for two months. (**C**) The *I-V* curves of a typical b-AsP FET device. The black and red lines present data from the as-fabricated device and the one after stored in air for two months. (**D**) and (**E**) optical images of two as-fabricated devices and the ones after being stored for over ten months.

3.7 Air-Stable Room-Temperature Mid-Infrared Photodetectors Based on hBN/Black Arsenic Phosphorus/hBN Heterostructures

Shaofan Yuan[1], Chenfei Shen[2], Bingchen Deng[1], Xiaolong Chen[1], Qiushi Guo[1], Yuqiang Ma[3], Ahmad Abbas[3], Bilu Liu[3], Ralf Haiges[4], **Claudia Ott**[5], Tom Nilges[5], Kenji Watanabe[6], Takashi Taniguchi[6], Ofer Sinai[7], Doron Naveh[7], Chongwu Zhou[2, 3] and Fengnian Xia[1]

[1] Department of Electrical Engineering, Yale University, New Haven, Connecticut 06511, United States.

[2] Mork Family Department of Chemical Engineering and Materials Science, University of Southern California, Los Angeles, California 90089, United States.

[3] Ming Hsieh Department of Electrical Engineering, University of Southern California, Los Angeles, California 90089, United States.

[4] Loker Hydrocarbon Research Institute and Department of Chemistry, University of Southern California, Los Angeles, California 90089, United States.

[5] Department of Chemistry, Technical University Munich, Lichtenbergstr 4, Garching bei München 85748, Germany.

[6] National Institute for Materials Science, 1-1 Namiki, Tsukuba, 305-0044, Japan.

[7] Faculty of Engineering and Bar-Ilan Institute for Nanotechnology and Advanced Materials, Bar-Ilan University, Ramat Gan 52900, Israel.

The article "Air-Stable Room-Temperature Mid-Infrared Photodetectors Based on hBN/Black Arsenic Phosphorus/hBN Heterostructures" was submitted in February 2018 to the Journal "Nano Letters" and published online in March 2018.

As$_{0.83}$P$_{0.17}$ was analyzed via EDX, powder and single crystal XRD, electron backscatter diffraction (EBSD) and SEM. To derive the absorption constant $\alpha(\omega)$ of bulk b-AsP the Lambert-

Beer's law was applied. Since b-AsP is sensitive towards oxidation it was engulfed in a hBN protective layer. The device shows symmetrical ambipolar transfer characteristics. This is in contrast with previous reported results.[78,135] The electron and hole mobility was calculated to 79 and 75 cm$^2 \cdot$ (V·s)$^{-1}$ respectively. Considering different back gate voltages a linear relation between I_{ds} and V_{ds} could be observed. This verifies that an Ohmic contact is achieved between the metal electrodes and b-AsP.

The photoresponse of the device was measured at MWIR wavelengths of 3.4, 5.0 and 7.7 μm. Due to the intrinsic anisotropic properties of b-AsP, the photocurrent depends on the polarization of the incident light. Polarization dependent photocurrent was investigated at the charge neutral point and V_{ds} = 300 mV. The measured anisotropy is higher than observed in the infrared extinction curve due to the small b-AsP grain size (about 9 μm) compared to the infrared light spot size (about 30 $\times$ 30 μm). The measured value is an average over the irradiated area and therefore over multiple crystalline domains which explains the higher number.

The photocurrent dependency on V_{bg} is measured along the armchair direction.[137] The photocurrent shows a maximum at the charge neutral point for every laser. I_{ds} is enhanced by the illumination of a 3.4 μm laser compared to dark conditions due to the presence of photocarriers. I_{ph} shows the same effect. These are typical signs of the photoconductive effect. Higher doping away from the charge-neutral point leads to a reduced photocurrent.[138] At the charge neutral point the photocurrent scales linearly with V_{ds} (with $|V_{ds}| < 0.4$ V). At large V_{ds} a saturation can be observed. This is caused by the Joule heating effect.[128]

For the here described photodetector, the photocurrent scales linearly with the input power. The photoconduction is increased by the encapsulation of b-AsP in hBN and thus more electron-hole pairs can be proportionally excited. Compared to the device discussed in chapter 3.6 on page 210 it shows that the encapsulation of the b-AsP flake further improves the performance in mid-infrared photodetection.

The estimated absorption of the used 37 nm flake was calculated to be 12% using the Lambert-Beer's law and the absorption coefficient $\alpha(\omega)$ from the extinction spectra. The internal quantum efficiency (IQE) at the charge neutral point (assuming V_{ds} = 1 V) can be calculated to an IQE of 97.7%. Another improvement achieved in this work, is the higher photocarrier lifetime compared to the device using bare b-AsP discussed in chapter 3.6 (here: 11 GHz, former: 3 kHz).

Due to the high operating frequencies of this devices the frequency-independent shot noise ($S_I = 2eI_{ds}$ with e: elemental charge) and thermal noise ($S_I = \frac{4kT}{R}$ with k: Boltzmann constant, T: working temperature of device, R: device resistance) are the most prominent issues in detection. The $1/f$ noise can be neglected at high frequencies. Another source for noise is the generation and recombiantion of photocarriers.[139] The noise equivalent power (NEP) is in the order of tens of pW/Hz$^{1/2}$ for this device at a wavelength of 3.4 μm.

Author contributions: C.O. synthesized and characterized the starting materials, all authors contributed in the writing of the manuscript.

Air-Stable Room-Temperature Mid-Infrared Photodetectors Based on hBN/Black Arsenic Phosphorus/hBN Heterostructures

Shaofan Yuan,[†] Chenfei Shen,[‡] Bingchen Deng,[†] Xiaolong Chen,[†] Qiushi Guo,[†] Yuqiang Ma,[○] Ahmad Abbas,[○,∇,¶,#] Bilu Liu,[○,◇] Ralf Haiges,[◆] Claudia Ott,[§] Tom Nilges,[§] Kenji Watanabe,[∥] Takashi Taniguchi,[∥] Ofer Sinai,[⊥] Doron Naveh,[⊥] Chongwu Zhou,*,[‡,○] and Fengnian Xia*,[†]

[†]Department of Electrical Engineering, Yale University, New Haven, Connecticut 06511, United States

[‡]Mork Family Department of Chemical Engineering and Materials Science, University of Southern California, Los Angeles, California 90089, United States

[○]Ming Hsieh Department of Electrical Engineering, University of Southern California, Los Angeles, California 90089, United States

[◆]Loker Hydrocarbon Research Institute and Department of Chemistry, University of Southern California, Los Angeles, California 90089, United States

[§]Department of Chemistry, Technical University Munich, Lichtenbergstr 4, Garching bei München 85748, Germany

[∥]National Institute for Materials Science, 1-1 Namiki, Tsukuba, 305-0044, Japan

[⊥]Faculty of Engineering and Bar-Ilan Institute for Nanotechnology and Advanced Materials, Bar-Ilan University, Ramat Gan 52900, Israel

S Supporting Information

ABSTRACT: Layered black phosphorus (BP) has attracted wide attention for mid-infrared photonics and high-speed electronics, due to its moderate band gap and high carrier mobility. However, its intrinsic band gap of around 0.33 electronvolt limits the operational wavelength range of BP photonic devices based on direct interband transitions to around 3.7 μm. In this work, we demonstrate that black arsenic phosphorus alloy (b-As$_x$P$_{1-x}$) formed by introducing arsenic into BP can significantly extend the operational wavelength range of photonic devices. The as-fabricated b-As$_{0.83}$P$_{0.17}$ photodetector sandwiched within hexagonal boron nitride (hBN) shows peak extrinsic responsivity of 190, 16, and 1.2 mA/W at 3.4, 5.0, and 7.7 μm at room temperature, respectively. Moreover, the intrinsic photoconductive effect dominates the photocurrent generation mechanism due to the preservation of pristine properties of b-As$_{0.83}$P$_{0.17}$ by complete hBN encapsulation, and these b-As$_{0.83}$P$_{0.17}$ photodetectors exhibit negligible transport hysteresis. The broad and large photoresponsivity within mid-infrared resulting from the intrinsic photoconduction, together with the excellent long-term air stability, makes b-As$_{0.83}$P$_{0.17}$ alloy a promising alternative material for mid-infrared applications, such as free-space communication, infrared imaging, and biomedical sensing.

KEYWORDS: Two-dimensional materials, black arsenic phosphorus, heterostructures, medium-wavelength infrared photodetector, photoconduction
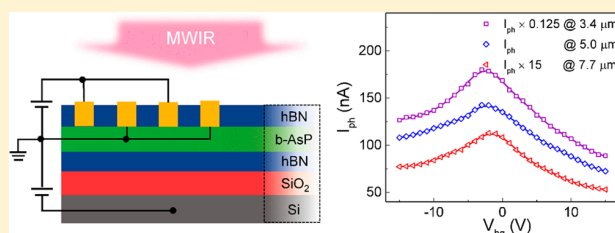
S emiconducting two-dimensional (2D) materials including various transition-metal dichalcogenides (TMDCs) and black phosphorus (BP)[1−4] have been extensively explored for photonic and electronic applications. The band gaps of most semiconducting TMDCs, such as molybdenum disulfide and tungsten diselenide, are close to or larger than 1 eV, which limits their optical applications to ultraviolet (UV), visible, and near-infrared (NIR) regions.[5] Black phosphorus, which has a band gap of 0.33 eV in thin film (>10 layers) or bulk form, can cover the short-wavelength infrared (SWIR) (0.9−2.5 μm) and part of the medium-wavelength infrared (MWIR) (3−5 μm).[6,7] Various studies on BP photodetection in UV,[8] visible,[9−11] NIR,[12] SWIR,[13,14] and MWIR (up to 3.4 μm)[15] were reported in the past few years, demonstrating the potential of BP in

wideband optoelectronic applications. Extending the operational range of BP photodetectors to even longer wavelength will significantly enhance its optical functionalities in various applications, such as thermal imaging and sensing. For example, blackbody radiation of objects with temperatures ranging from 300 to 1000 K has a peak intensity from 9.7 to 2.9 μm, which is crucial for industrial thermal imaging and infrared tracking.[16] Additionally, free-space optical communication at the first atmosphere window (3−5 μm) avoids significant signal attenuation for the wavelength-dependent nature of light scattering and at the same time keeps the unique advantages,

3172

such as a higher data rate and enhanced transmission security.[17−19] Currently, the most commonly used material for photodetector applications in MWIR and long-wavelength infrared (LWIR) is $Hg_{1−x}Cd_xTe$ (MCT).[20] MCT is a popular choice due to its tunable band gap through the control of the composition and its high absorption in MWIR and LWIR.[20] However, besides its toxicity, its bulk nature makes its integration with other optical structures and components challenging.[21]

The black arsenic phosphorus was previously synthesized and its structural phase transition and superconductivity were studied.[22−25] Recently, one of the coauthors' group systematically synthesized and structurally characterized the layered black arsenic phosphorus ($b-As_xP_{1−x}$) alloy ($x \leq 0.83$) and demonstrated it still has a similar crystal structure to that of orthorhombic BP.[26] The synthesized $b-As_xP_{1−x}$ alloy has a tunable band gap down to ∼0.12 eV, with an As concentration of 83%.[27] In a recent study, an IR detector based on the $b-As_xP_{1−x}$ alloy was reported with a decent responsivity for MWIR light.[28] In this device, the interplay among photovoltaic, photothermo-electric, and photogating effects leads to complicated photocurrent generation mechanisms at different incident power levels and operational speed. Moreover, the trap states on the $b-As_xP_{1−x}$/substrate interface can play an important role in such $b-As_xP_{1−x}$ photodetectors, and accordingly, the photoresponse time is long (0.5 ms), making its fast operation challenging. Another very recent work also reports $b-As_xP_{1−x}$ alloy based photodetectors.[29] In that work, the $b-As_{0.91}P_{0.09}$ photodetectors show very impressive responsivity and detectivity under mid-infrared excitation up to the wavelength of around 4.6 μm. The reported long carrier lifetime (above 1 μs) indicates that most likely the carrier trapping can also play a role in those devices.[29] In this study, we fully characterize the structural and optical properties of synthesized $b-As_{0.83}P_{0.17}$ and then utilize the narrow band gap of $b-As_{0.83}P_{0.17}$ to fabricate room temperature MWIR photodetectors operational in the intrinsic photoconduction regime, covering a wavelength range from 3.4 to 7.7 μm. In particular, to demonstrate the long-term stability of $b-As_{0.83}P_{0.17}$, which can be oxidized under exposure to air, we leverage the hexagonal boron nitride (hBN)/$b-As_{0.83}P_{0.17}$/hBN heterostructure for the effective protection. The as-fabricated photodetector shows an extrinsic responsivity of 190, 16, and 1.2 mA/W for 3.4, 5.0, and 7.7 μm incident light, respectively. We further study the photocurrent dependence on the applied gate (V_{bg}) and drain (V_{ds}) biases, from which we conclude that the photocurrent originates from the intrinsic photoconductive effect. Subsequent investigations of power and frequency dependence confirm the photoconduction mechanism. Moreover, due to the in-plane anisotropy in the crystal structure of $b-As_{0.83}P_{0.17}$,[27] a polarization-dependent photocurrent is observed. Our demonstration represents an important step for the future applications of $b-As_xP_{1−x}$ in a broad mid-infrared wavelength range, in particular for potential high-speed operations.

Results and Discussion. The $b-As_{0.83}P_{0.17}$ used for device demonstration in this work was prepared by an ampule synthesis method as demonstrated previously.[27] The stoichiometry of the $b-As_xP_{1−x}$ was controlled by the molar ratio of starting materials (gray arsenic/red phosphorus = 83:17). Details of the synthesis are presented in Methods.[30] The energy dispersive X-ray spectroscopy (EDS) spectrum of the synthesized $b-As_xP_{1−x}$ confirms that the compound is composed of ∼83 atomic percent (at %) As and ∼17 at % P.

(See the Supporting Information.) The powder X-ray diffraction (XRD) pattern of $b-As_{0.83}P_{0.17}$ is shown in Figure 1a. All diffraction peaks are indexed to corresponding planes. In $b-As_xP_{1−x}$, the interlayer distance is larger than that of gray arsenic at an arsenic concentration $\rho_{As} \approx 10\%$ and it increases monotonically as ρ_{As} further rises up to 83%,[26] which shows that the $b-As_xP_{1−x}$ crystal structure is very different from that of
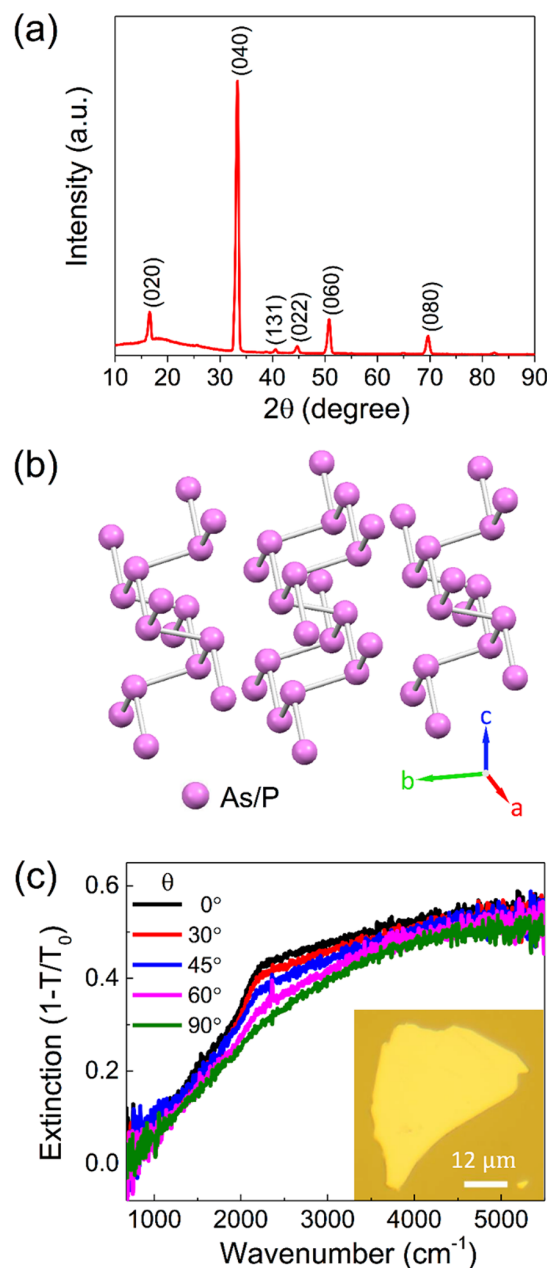
Figure 1. Crystal structure and infrared extinction characterizations. (a) X-ray diffraction pattern of the as-synthesized crystal with Miller indices labeled for peaks. The broad peak at 18° is from the Kapton tape, which is used to encapsulate the $b-As_{0.83}P_{0.17}$. (b) The orthorhombic puckered honeycomb crystal structure of $b-As_{0.83}P_{0.17}$ alloy. The lattice parameters, extracted from the X-ray diffraction profile, are a = 3.561(3) Å, b = 10.803(9) Å, and c = 4.493(4) Å. (c) Polarization-resolved IR extinction spectra of the $b-As_{0.83}P_{0.17}$ alloy. The optical image of the investigated flake is shown in the inset.
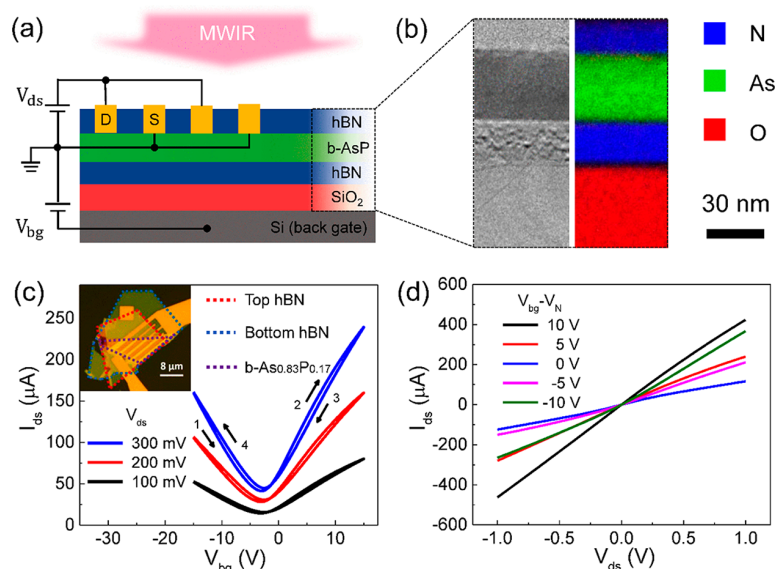
Figure 2. Device structure and electrical characterizations. (a) The cross-sectional schematic of the as-fabricated $hBN/b-As_{0.83}P_{0.17}/hBN$ heterostructure photodetector. (b) Left: the cross-sectional view of the device by transmission electron microscope (TEM). Right: the elemental analysis mapping by electron energy loss spectroscopy (EELS). In the EELS mapping, red, blue, and green colors denote O, N, and As elements, respectively. Only part of the silicon oxide layer is shown. The encapsulated $b-As_{0.83}P_{0.17}$ layer is 37 nm, free from oxidation even several months after its fabrication. (c) Transfer characteristic of the as-fabricated phototransistor. The optical image of the as-fabricated device is shown in the inset. The gate bias was swept in both directions, with numbers denoting the sweeping sequence. The charge neutral point is at $V_{bg} = -3$ V, and the hysteresis of the transfer curve is small. (d) Output characteristics of the $b-As_{0.83}P_{0.17}$ phototransistor. The output curves were measured with different V_{bg}, and V_N represents the gate bias, at which the charge neutral point of the device is achieved ($V_N = -3$ V in this case).

gray arsenic. The diffraction pattern obtained in $b-As_{0.83}P_{0.17}$ here is consistent with the previous work,[26] and the interlayer distance is observably larger than that of gray arsenic. Detailed investigation of the crystal structure of $b-As_{0.83}P_{0.17}$ was done with single-crystal XRD. The single-crystal XRD analysis indicates that the $b-As_{0.83}P_{0.17}$ has an orthorhombic structure with a puckered honeycomb lattice as shown in Figure 1b.[27,30] (The atoms in Figure 1b represent either As or P.) The lattice parameters of the $b-As_{0.83}P_{0.17}$ are $a = 3.561(3)$ Å, $b = 10.803(9)$ Å, and $c = 4.493(4)$ Å, where a, b, and c are the lattice constants along the zigzag, stacking, and armchair direction. The details of the crystallographic data of $b-As_{0.83}P_{0.17}$ are provided in the Supporting Information.

Figure 1c shows the polarization-resolved infrared extinction spectra of a typical exfoliated $b-As_{0.83}P_{0.17}$ flake on the zinc sulfide (ZnS) substrate (shown in the inset), where T and T_0 are the optical transmission of the $b-As_{0.83}P_{0.17}$ flake on the ZnS substrate and the bare ZnS substrate, respectively. The measured extinction of the $b-As_{0.83}P_{0.17}$ flake shows an absorption edge around 1000 cm^{-1}, corresponding to a photon energy of 0.124 eV. The thickness of the investigated flake is measured to be 188 nm using an atomic force microscope (AFM), and the height profile of the flake edge can be found in the Supporting Information. We employ the Lambert−Beer's Law: $A(\omega) = 1 - e^{-\alpha(\omega)Z}$ to estimate the absorption constant $\alpha(\omega)$ of bulk $b-As_{0.83}P_{0.17}$, where $A(\omega)$ is the absorption, ω is the frequency of incident light, and Z is the flake thickness. In the calculation, we assume the absorption constant $\alpha(\omega)$ is the same for the bulk material $Z \gg 5$ nm.[31] The absorption constant can be slightly overestimated in this approach, considering the reflection at the $b-As_{0.83}P_{0.17}$ surface. (See the Supporting Information.) For incident light wavelength $\lambda = 3.4$ μm ($v = 2950$ cm^{-1}), the absorption constant α is calculated to

be 2.7×10^4 cm^{-1}, using the 48% absorption in the 188 nm-thick flake.

After fully characterizing $b-As_{0.83}P_{0.17}$ flakes, we fabricated photodetectors based on $hBN/b-As_{0.83}P_{0.17}/hBN$ heterostructures. The bottom hBN flakes were first exfoliated on a silicon substrate (Si) covered by a 90 nm-thick silicon oxide layer (SiO_2), and then the substrate was annealed in an argon/hydrogen (Ar/H_2) atmosphere at 600 °C for 6 h to remove possible polymer residues in the exfoliation. The $b-As_{0.83}P_{0.17}$ flake and the top hBN were transferred onto the bottom hBN flakes subsequently using a polymer-free dry transfer method.[32] All transfer processes were performed in an argon-filled glovebox to minimize oxidation. After 6 h of annealing in Ar/H_2 atmosphere at 300 °C, the defined metal contact region was etched to expose $b-As_{0.83}P_{0.17}$ and then electrodes (3/47 nm Chromium/Gold) were deposited.[33] Details of fabrication can be found in Methods.

Similar to BP,[34,35] $b-As_xP_{1-x}$ can also be oxidized in air, which makes the naked devices unstable in the long run. The encapsulation provides reliable protection for the $b-As_{0.83}P_{0.17}$ alloy against the oxidation and degradation. Figure 2a shows the cross-sectional schematic of the $hBN/b-As_{0.83}P_{0.17}/hBN$ heterostructure photodetector on a SiO_2/Si substrate. It is based on a field-effect transistor scheme with an interdigitated source and drain electrodes to maximize the photocurrent collection efficiency. The cross-sectional view of the device and the elemental analysis by transmission electron microscope (TEM) are shown in Figure 2b. The 37 nm-thick $b-As_{0.83}P_{0.17}$ is well preserved in hBN and free from oxidation several months after its fabrication as shown in the elemental analysis in Figure 2b. The relatively thick $b-As_{0.83}P_{0.17}$ flake is chosen to enhance the absorption of IR light. The thicknesses of the top and bottom

hBN layers are 20 and 22 nm, respectively, determined from the cross-sectional TEM image.

The transfer characteristics of the as-fabricated device are plotted in Figure 2c. The inset shows its optical image. The device exhibits a rather symmetrical ambipolar property compared to previous studies,[15,28] probably due to the hBN encapsulation, which leads to the preservation of the intrinsic properties of b-As$_{0.83}$P$_{0.17}$. When V_{bg} is swept in both directions, the encapsulated b-As$_{0.83}$P$_{0.17}$ transistors exhibit negligible hysteresis, due to the clean hBN/b-As$_{0.83}$P$_{0.17}$ interfaces. The electron and hole mobilities can be extracted using $\mu = \left(\frac{dI_{ds}}{dV_{bg}}\right)(L/W)(1/V_{ds}C_g)$, where I_{ds} is the drain current, C_g is the gate capacitance, and $L = 1.5\ \mu m$ and $W = 30\ \mu m$ are the length and the total width of the transistor channel. Here both the hBN and SiO$_2$ are taken into account for the gate capacitance calculation, with a relative dielectric constant of 3.1 and 3.9, respectively.[36] Based on this approach, the extracted effective electron and hole mobilities are about 83 and 79 cm^2/(V s), respectively. We note that the intrinsic carrier mobilities could be higher than the extracted effective mobilities above, which do not exclude the contribution of the contact resistance. Figure 2d shows the output curves of the as-fabricated device at various back gate biases. The near-linear relation between I_{ds} and V_{ds} indicates that the Ohmic contact is achieved between metal electrodes and b-As$_{0.83}$P$_{0.17}$. The slight asymmetry in the magnitude of drain currents at opposite V_{ds} biases is most likely caused by the doping difference ($V_{bg} - V_{ds}$) around the drain electrode, which has previously been observed in conventional metal oxide semiconductor (MOS) transistors.[37]

Then we characterized the photoresponse of b-As$_{0.83}$P$_{0.17}$ devices for MWIR light at 3.4, 5.0, and 7.7 μm. The incident IR light was mechanically chopped at a certain frequency (3 kHz, if not specified), and the alternating photocurrent (I_{ph}) at a corresponding frequency was acquired using a lock-in amplifier. Since b-As$_x$P$_{1-x}$ has intrinsic anisotropic optical properties, the photocurrent naturally depends on the incident light polarization. The polarization-dependent photocurrent was measured when the device was biased at the charge neutral point and V_{ds} = 300 mV. In Figure 3a, the photocurrent is plotted in a polar coordinate as a function of the polarization for 3.4, 5.0, and 7.7 μm incident light. The photocurrent anisotropy, defined as the photocurrent ratio along the armchair and zigzag directions, is ~12, 14, and 1.3 for 3.4, 5.0, and 7.7 μm lasers, respectively. We notice that the anisotropy of photocurrent is stronger than that observed in the infrared extinction curves as shown in Figure 1c. In infrared extinction spectra, a large area (~30 μm × 30 μm × 0.188 μm) flake was used to accommodate the incident light from Fourier transform infrared spectrometer (FTIR), while the device was fabricated on a much smaller flake (~8 μm × 8 μm × 0.037 μm). Accordingly, the measured anisotropy in extinction spectra is the average over a larger area, which can contain multiple crystalline domains. As a result, the infrared extinction spectra show much less anisotropy. The weak photocurrent and infrared extinction at the band edge may be due to the emergence of a new less anisotropic valence band at a high arsenic concentration, as suggested by the recent calculations based on the density function theory.[38]

The photocurrent dependence on V_{bg} was measured at a light polarization along the armchair direction.[27] For an incident laser with different photon energies, the photocurrent always
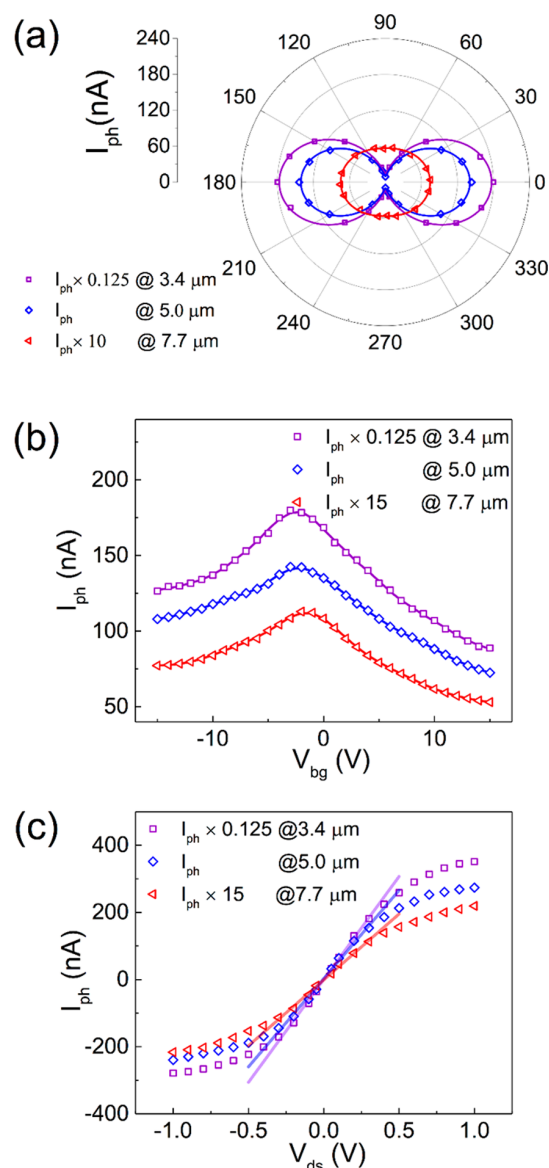
Figure 3. Photoresponse of hBN-encapsulated b-As$_{0.83}$P$_{0.17}$ phototransistor. (a) Polarization-resolved photocurrents of the b-As$_{0.83}$P$_{0.17}$ phototransistor for 3.4, 5.0, and 7.7 μm light excitation at V_{ds} = 0.3 V when the device is biased at a charge neutral point. (b) V_{bg} dependence of the photocurrent in the b-As$_{0.83}$P$_{0.17}$ phototransistor at V_{ds} = 0.3 V. (c) The photoresponse as a function of source-drain bias V_{ds}. In this measurement, the device works at a charge neutral point. Transparent colored lines are the linear fitting in the range of |V_{ds}| < 0.4 V. The photocurrent in panels b and c was measured when the polarization of incident light was aligned with the armchair direction.

peaks at the charge neutral point, as shown in Figure 3b. This is the typical feature of the photoconductive effect, since the higher doping away from the charge neutral point reduces the photocarrier lifetime, leading to the reduction in photocurrent.[39] At the charge neutral point, the photocurrent scales almost linearly with V_{ds} when |V_{ds}| < 0.4 V, as shown in Figure 3c. The saturation of the photocurrent at a large V_{ds} can be attributed to the Joule heating effect, which sets the limit of the internal amplification for the decreasing photocarrier lifetime at

a higher temperature.[40] The extrinsic responsivity is estimated using $R_{ex} = I_{ph}/(P_{in}\xi)$, where P_{in} is the power of incident light and ξ is the ratio of the incidence power on the device to the total incidence power, considering the Gaussian distribution of light intensity. (See the Methods for the calculation of ξ.) When the device is biased at $V_{ds} = 1$ V and $V_{bg} = -3$ V (corresponding to the charge neutrality point), the corresponding extrinsic responsivity for 3.4, 5.0, and 7.7 μm laser is calculated to be $\sim$190, 16, and 1.2 mA/W, respectively.

To further elucidate the photocurrent generation mechanism, the power and frequency dependence of the photocurrent were also measured. As shown in Figure 4a, in our hBN/b-$As_{0.83}P_{0.17}$/hBN photodetectors, the photocurrent scales approximately linearly with input power. This is distinctively different from the previously demonstrated b-$As_{0.83}P_{0.17}$ photodetector,[28] which shows a sublinear power-dependent photocurrent. The decreasing responsivity at a higher intensity light in the previous work can be attributed to trap states on the b-As_xP_{1-x}/SiO_2 interface. At a higher illumination condition, surface trap states are densely occupied, leading to the saturation of the photogating effect and decreasing responsivity. In our device, the intrinsic photoconduction leads to a photocurrent linearly scaled with the input power, since more electron–hole pairs can be excited proportionally by a higher intensity light. Besides the distinguished power dependency, our hBN-encapsulated b-$As_{0.83}P_{0.17}$ MWIR photodetector also shows an excellent response speed. The photocurrent remains constant when the chopped frequency of incident light ranges from 1 to 10 kHz, which indicates that the 3 dB cutoff frequency of the device is well beyond 10 kHz (Figure 4b). Here we use the photocarrier lifetime to estimate the intrinsic 3 dB cutoff frequency of the device.[41] With the absorption constant $\alpha(\omega)$ calculated from the extinction spectra, we estimate the absorption (η) of the 37 nm-thick flake to be 12% at 3.4 μm using Lambert–Beer's Law. Then the product of internal quantum efficiency (IQE) and photoelectric current gain G at the charge neutral point and $V_{ds} = 1$ V is calculated, with IQE·$G = (R_{ex}/\eta)(E_{ph}/e)$, to be around 60%, where E_{ph} is the photon energy and e is the elementary charge. On the other hand, the transition time $\tau_{tr} = L^2/(\mu V_{ds})$ for electrons and holes is calculated to be 27 and 29 ps, respectively. Considering both carrier transition time and IQE·G, the photocarrier lifetime at the charge neutral point ($\tau_{life} = \tau_{tre}\tau_{trh}/(\tau_{trh} + \tau_{tre})$·IQE·$G$) is estimated to be around 8 ps, where $\tau_{tre/h}$ is the transition time for electrons or holes.[41] Here the estimated photocarrier lifetime in b-$As_{0.83}P_{0.17}$ is about an order of magnitude smaller than the previously measured value of $\sim$100 ps in hBN covered BP using the time-resolved reflection measurements.[42] This is probably due to the lower quality of compound b-$As_{0.83}P_{0.17}$ and its smaller band gap. The compound nature of b-$As_{0.83}P_{0.17}$ can lead to a lower sample quality, which can result in an enhanced nonradiative recombination rate and reduced photocarrier lifetime. Moreover, its smaller band gap results in a higher intrinsic carrier density, which can lead to an enhanced recombination rate and hence reduced carrier lifetime.[43] However, it is much shorter than previously reported device response times (longer than 1 μs in refs 28 and 29) because the intrinsic photocarrier lifetime and device response time are two different physical quantities. The device response time in refs 28 and 29 is likely dominated by the lifetime of the trapped photocarriers at the band edge, which sometimes can be extremely long.[44] The calculated photocarrier lifetime in this work suggests a potential 3 dB cutoff frequency ($f_{3dB} = 1/$
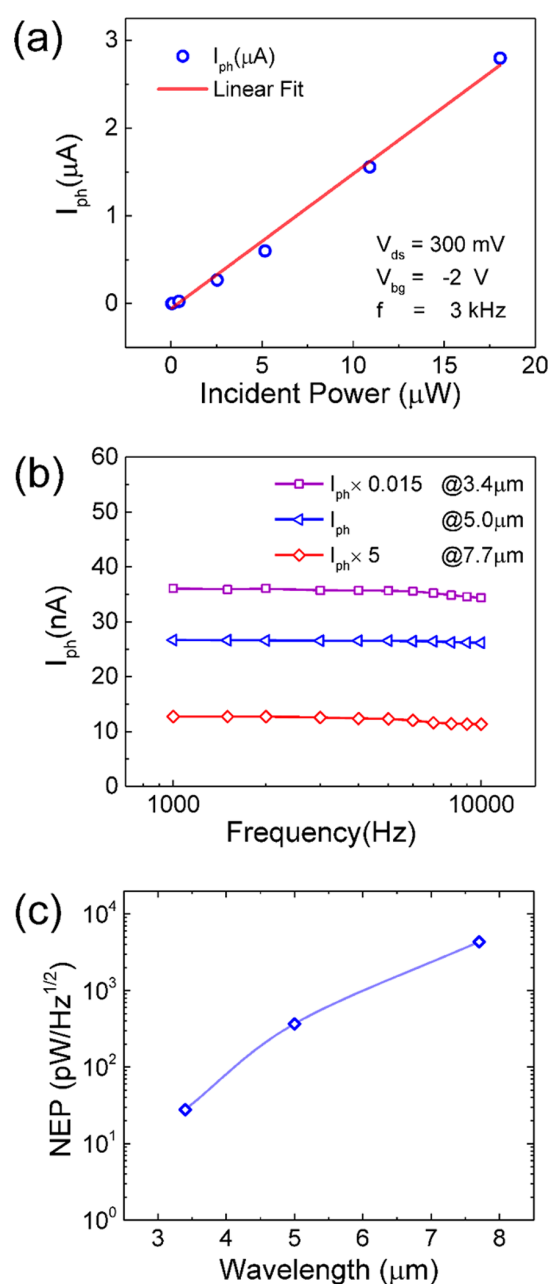
Figure 4. Power and frequency dependence of the photocurrent and noise characteristics. (a) Photocurrent as a function of incident power at 3.4 μm when the device works at a charge neutral point and $V_{ds} = 0.3$ V. The laser polarization is aligned with the armchair direction. (b) Photoresponse as a function of the incident light intensity modulation frequency from 1 to 10 kHz, showing no sign of response roll-off. (c) Noise equivalent power at $V_{ds} = 1$ V for 3.4, 5.0, and 7.7 μm incident light when the device works at a charge neutral point and the light polarization is aligned with the armchair direction.

$(2\pi\tau_{life})$) of the photoconductor at around 19 GHz. In terms of the photocurrent generation mechanism, the observed fast photoresponse also eliminates the probability of photogating effects in our hBN-encapsulated b-$As_{0.83}P_{0.17}$ photodetectors.[15]

Since the as-fabricated b-$As_{0.83}P_{0.17}$ photodetectors intrinsically operate at high frequencies, the frequency-independent shot noise and thermal noise play the major role in the

detection. The contribution from $1/f$ flicker noise is significant only at low operating frequencies (<10 kHz)[45] and, hence, is out of scope in this work. We estimated the detection noise and corresponding noise equivalent power (NEP) at high frequencies considering the shot noise, thermal noise, and generation-recombination noise in the device.[41] The current noise power spectral density function S_S of the shot noise, generated from the discrete nature of electrons, is given by $S_S = 2eI_{ds}$. For thermal noise, it originates from a random thermal motion of electrons and is expressed as $S_T = \frac{4kT}{R}$, where k is Boltzmann constant, T is the device working temperature, and R is the device resistance. The generation and recombination of photocarriers is another generation source of noise, but we estimate the generation-recombination noise, $S_{GR} = 4eI_{ph}(\tau_{life}/\tau_{tr})/(1 + (2\pi f \tau_{life})^2$,[41] to be smaller than the shot noise by more than one order and contributes little to the NEP in our case (Supporting Information). The noise measurement at a charge neutral point indicates that the $1/f$ noise is not significant at frequencies above 2 kHz, as shown in the Supporting Information. With considerations above, we estimate the noise current density ($\delta i = \sqrt{S_S + S_T}$) and the noise equivalent power (NEP $= \delta i/R_{ex}$) at $V_{ds} = 1$ V at charge neutral points for 3.4, 5.0, and 7.7 μm incident light when the light polarization is aligned along the armchair direction. The operating dark current is 117 μA. and the associated noise current density is 6.3 pA/Hz$^{1/2}$. Then we calculate the NEP of our photodetector to be 28, 370, and 4300 pW/Hz$^{1/2}$ for 3.4, 5.0, and 7.7 μm incident light as shown in Figure 4c. Compared with previous works on black arsenic phosphorus MWIR photodetectors (refs 28 and 29), our sandwiched b-As$_{0.83}$P$_{0.17}$ device is different in terms of the operational mechanism, dynamical range, and potential speed. The b-As$_x$P$_{1-x}$ FET photodetector reported in ref 28 has an impressive NEP ~ 3 pW/Hz$^{1/2}$ at 3.4 μm, and the molybdenum disulfide/b-AsP heterostructure results in an even smaller NEP ~ 0.2 pW/Hz$^{1/2}$ at 3.4 μm. In ref 29, the authors characterized the comprehensive spectral response of black arsenic phosphorus FET using the blackbody flood illumination. They reported an impressive peak detectivity of 2.4×10^{10} cm Hz$^{1/2}$W^{-1} at around 4.2 μm instead of the NEP. In this work, we calibrate the device responsivity at three typical mid-infrared wavelengths using the quantum cascade lasers and provide accurate measurement results especially at longer wavelengths. In both refs 28 and 29, the photogating induced gain is likely to play an important role for improved NEP and detectivity values.[15] Here our device operates in the intrinsic photoconduction regime due to the hBN encapsulation. As a result, although the NEP and detectivity of our devices are not as impressive as previously demonstrated values, our devices have a larger operational dynamical range and potentially much improved operational speed. The layered nature of b-As$_{0.83}$P$_{0.17}$ allows further integration with resonant microcavities or mid-infrared waveguide,[14,46] which is expected to further improve its responsivity and may ultimately be used in on-chip spectroscopy and free-space optical communications.

Conclusions. In conclusion, we investigate the structural and optical properties of the synthesized b-As$_{0.83}$P$_{0.17}$ and further demonstrate the MWIR photodetectors, which cover a broad mid-IR wavelength range from 3.4 to 7.7 μm. Most importantly, the hBN encapsulation provides long-term air stability for the device and eliminates trap states at the

interfaces. In terms of the photocurrent generation mechanism, on the contrary to previously demonstrated BP and b-As$_x$P$_{1-x}$ photodetectors,[15,28,29] the b-As$_{0.83}$P$_{0.17}$ photodetectors demonstrated in this work operate in intrinsic photoconduction mode and exhibit extrinsic photoresponsivity of 190, 16, and 1.2 mA/W for 3.4, 5.0, and 7.7 μm incident light, respectively. The 3 dB cutoff frequency for MWIR detection can potentially be as high as 19 GHz.

Methods. *Crystal Synthesis.* The b-As$_{0.83}$P$_{0.17}$ samples were prepared from a mixture of gray arsenic (Chempur, 99.9999%) and red phosphorus (Chempur, 99.999$^+$%) with a molar ratio of 83:17. Lead(II) iodide (PbI$_2$, 12 mg per 625 mg batch) was added as the mineralizing agent. The chemicals were enclosed in evacuated silica glass ampules during reaction (length 100 mm, inner diameter 10 mm). Synthesis was performed in a Nabertherm furnace (L3/11/P330). The samples were heated up to 550 °C within 8 h, held at this temperature for 24 h, and then cooled to room temperature within 20 h.

Crystal Characterization. Powder X-ray diffraction (XRD) was carried out on a Rigaku Ultima IV powder/thin-film diffractometer with a Cu Kα radiation source. The diffractometer consists of an APEX II CCD detector and an Oxford Cryosystems Cryostream 700 apparatus for the collection of data at low temperatures. The crystals were mounted in Cryo-Loops using Paratone oil. A complete hemisphere of data was scanned on Ω (0.5°) at a detector distance of 50 mm and a resolution of 512 × 512 pixels. A total of 2520 frames were collected. The frames were integrated using the SAINT algorithm[47] to produce the (hkl) data file. Data were corrected for absorption effects using the multiscan method (SADABS).[48] The structures were solved and refined on F^2 using the Bruker SHELXTL Software Package.[49,50] CCDC nos. 1582392 and 1582393 contain the supplementary crystallographic data for this paper. These data can be obtained free of charge from The Cambridge Crystallographic Data Centre (www.ccdc.cam.ac.uk). Energy dispersive X-ray spectroscopy (EDS) was conducted on the JEOL JSM-7001 system.

Device Fabrication. The bottom hBN thin film was exfoliated on a 90 nm SiO$_2$/Si substrate and was then annealed at 600 °C in argon/hydrogen (Ar/H$_2$) to eliminate the possible polymer contamination in the exfoliation. The b-As$_{0.83}$P$_{0.17}$ and top hBN thin film were exfoliated mechanically from bulk crystals on polydimethylsiloxane (PDMS), which is attached to a glass slide. Then the b-As$_{0.83}$P$_{0.17}$ and hBN thin film were transferred on the bottom hBN subsequently to form the heterostructures. All of the steps above except annealing were finished in the glovebox, in which the oxygen and water concentration is well below 1 ppm. The sandwich structure was annealed at 300 °C in an Ar/H$_2$ atmosphere to decrease possible polymer residues in the structure. Poly methyl methacrylate (PMMA) e-beam resist was spin coated on the chip, and electron-beam lithography was used to define metal electrodes. The top hBN in the defined region was etched with fluoroform/oxygen (CHF$_3$/O$_2$) in the Oxford Plasmalab 100 system to open the source-drain window and to make contact with the b-As$_{0.83}$P$_{0.17}$ below. Finally, chromium/gold (3/47 nm) was deposited to make electrodes using a Kurt J. Lesker thermal evaporator.

Transmission Electron Microscope Imaging. High-resolution TEM (HR-TEM) images were acquired using an FEI Tecnai F-30 instrument at a working voltage of 300 kV. The device cross-sectional lamella was prepared using a focused Ga-ion beam (FIB) in a FEI Helios DualBeam machine after the

thermal evaporation of 6−10 nm amorphous carbon on the sample for conductivity. During the transfer to HR-TEM, the lamella was exposed to air for less than 5 min. Elemental mapping of the cross section was acquired using electron energy loss spectroscopy (EELS) combined with a Gatan imaging filter (GIF), yielding energy-filtered TEM (EFTEM) images.

Transport Measurements. The transport characteristics were measured with an Agilent B1500A semiconductor parameter analyzer in a Lakeshore cryogenic probe station. All electrical measurements above were performed in a vacuum (10^{-5} Torr) at room temperature.

Photocurrent Measurements. MWIR photocurrent measurements were performed in an ambient condition. The output light from MIR lasers was coupled into a Fourier transform infrared spectrometer (FTIR) and then was focused onto the device using an integrated Hyperion 2000 microscope. A 15× zinc selenide (ZnSe) objective in the Hyperion microscope was used to focus the light. The total incident power was around 30, 50, and 100 μW for 3.4, 5.0, and 7.7 μm lasers, respectively. In the calculation of extrinsic responsivity, the active device area A_{device} is 45 μm^2, and the standard deviations in the Gaussian distributions are measured to be around 5.1, 7.2, and 14 μm for 3.4, 5.0, and 7.7 μm lasers, respectively. The ratio ξ (power on the device directly to the total incident power) is estimated to be 0.83, 0.60, and 0.20 for 3.4, 5.0, and 7.7 μm light.

Polarized Infrared Extinction Measurements. The infrared absorption measurements were also performed using the FTIR and Hyperion 2000 microscope discussed above. An infrared polarizer was used to control the polarization of the infrared light.

■ ASSOCIATED CONTENT

⑤ Supporting Information

The Supporting Information is available free of charge on the ACS Publications website at DOI: 10.1021/acs.nanolett.8b00835.

> Elemental composition analysis of b-$As_{0.83}P_{0.17}$, crystallographic information on b-$As_{0.83}P$, thickness profile of the exfoliated b-$As_{0.83}P_{0.17}$ used for extinction measurements, reflection measurements of the b-$As_{0.83}P_{0.17}$ flake on a ZnS substrate, calculation of noise equivalent power (NEP), and noise current density measurements at a charge neutral point (PDF)

■ AUTHOR INFORMATION

Corresponding Authors

*E-mail: chongwuz@usc.edu.
*E-mail: fengnian.xia@yale.edu.

ORCID ⓘ

Chenfei Shen: 0000-0001-8635-3429
Bilu Liu: 0000-0002-7274-5752
Kenji Watanabe: 0000-0003-3701-8119
Doron Naveh: 0000-0003-1091-5661
Chongwu Zhou: 0000-0001-8448-8450
Fengnian Xia: 0000-0001-5176-368X

Present Addresses

∇Center of Excellence for Green Nanotechnologies, Joint Centers of Excellence Program, King Abdulaziz City for Science and Technology, P.O Box 6086, Riyadh 11442, Saudi Arabia

¶Department of Electrical and Computer Engineering, University of Jeddah, Dhahban 23881, Saudi Arabia
#Department of Electrical and Computer Engineering, King Abdulaziz University, Abdullah Sulayman Street, Jeddah 22254, Saudi Arabia
◇Tsinghua-Berkeley Shenzhen Institute (TBSI), Tsinghua University, Shenzhen, 518055, P.R. China

Author Contributions

The manuscript was written through contributions of all authors. S.Y. and C.S. contributed equally to this work.

Notes

The authors declare no competing financial interest.

■ REFERENCES

(1) Li, L. K.; Yu, Y. J.; Ye, G. J.; Ge, Q. Q.; Ou, X. D.; Wu, H.; Feng, D. L.; Chen, X. H.; Zhang, Y. B. *Nat. Nanotechnol.* **2014**, *9*, 372−377.
(2) Xia, F. N.; Wang, H.; Jia, Y. C. *Nat. Commun.* **2014**, *5*, 4458.
(3) Liu, H.; Neal, A. T.; Zhu, Z.; Luo, Z.; Xu, X. F.; Tomanek, D.; Ye, P. D. D. *ACS Nano* **2014**, *8*, 4033−4041.
(4) Koenig, S. P.; Doganov, R. A.; Schmidt, H.; Neto, A. H. C.; Ozyilmaz, B. *Appl. Phys. Lett.* **2014**, *104*, 104.
(5) Wang, Q. H.; Kalantar-Zadeh, K.; Kis, A.; Coleman, J. N.; Strano, M. S. *Nat. Nanotechnol.* **2012**, *7*, 699−712.
(6) Li, L. K.; Kim, J.; Jin, C. H.; Ye, G. J.; Qiu, D. Y.; da Jornada, F. H.; Shi, Z. W.; Chen, L.; Zhang, Z. C.; Yang, F. Y.; et al. *Nat. Nanotechnol.* **2016**, *12*, 21−25.
(7) Rodin, A. S.; Carvalho, A.; Castro Neto, A. H. *Phys. Rev. Lett.* **2014**, *112*, 112.
(8) Wu, J.; Koon, G. K. W.; Xiang, D.; Han, C.; Toh, C. T.; Kulkarni, E. S.; Verzhbitskiy, I.; Carvalho, A.; Rodin, A. S.; Koenig, S. P.; et al. *ACS Nano* **2015**, *9*, 8070−8077.
(9) Huang, M. Q.; Wang, M. L.; Chen, C.; Ma, Z. W.; Li, X. F.; Han, J. B.; Wu, Y. Q. *Adv. Mater.* **2016**, *28*, 3481−3485.
(10) Buscema, M.; Groenendijk, D. J.; Steele, G. A.; van der Zant, H. S. J.; Castellanos-Gomez, A. *Nat. Commun.* **2014**, *5*, 4651.
(11) Miao, J. S.; Zhang, S. M.; Cai, L.; Wang, C. *Adv. Electron. Mater.* **2016**, *2*, 1500346.
(12) Buscema, M.; Groenendijk, D. J.; Blanter, S. I.; Steele, G. A.; van der Zant, H. S. J.; Castellanos-Gomez, A. *Nano Lett.* **2014**, *14*, 3347−3352.
(13) Engel, M.; Steiner, M.; Avouris, P. *Nano Lett.* **2014**, *14*, 6414−6417.
(14) Youngblood, N.; Chen, C.; Koester, S. J.; Li, M. *Nat. Photonics* **2015**, *9*, 247−252.
(15) Guo, Q. S.; Pospischil, A.; Bhuiyan, M.; Jiang, H.; Tian, H.; Farmer, D.; Deng, B. C.; Li, C.; Han, S. J.; Wang, H.; et al. *Nano Lett.* **2016**, *16*, 4648−4655.
(16) Luong, M. P. *Nucl. Eng. Des.* **1995**, *158*, 363−376.
(17) Majumdar, A. K. *Free-Space Laser Communications: Principles and Advances*; Springer: New York, 2008.
(18) Hranilovic, S. *Wireless Optical Communication Systems*; Springer: New York, 2005.

(19) Capasso, F.; Paiella, R.; Martini, R.; Colombelli, R.; Gmachl, C.; Myers, T. L.; Taubman, M. S.; Williams, R. M.; Bethea, C. G.; Unterrainer, K.; et al. *IEEE J. Quantum Electron.* **2002**, *38*, 511−532.

(20) Dhar, N. K.; Dat, R.; Sood, A. K. Advances in Infrared Detector Array Technology. In *Optoelectronics - Advanced Materials and Devices*; Pyshkin, S. L., Ballato, J. M., Eds.; InTech: Rijeka, 2013.

(21) Rogalski, A.; Adamiec, K.; Rutkowski, J. *Narrow-Gap Semiconductor Photodiodes*; SPIE Press: Bellingham, WA, 2000.

(22) Krebs, H.; Holz, W.; Worms, K. H. *Chem. Ber.* **1957**, *90*, 1031−1037.

(23) Smith, P. M.; Leadbetter, A. J.; Apling, A. J. *Philos. Mag.* **1975**, *31*, 57−64.

(24) Shirotani, I.; Kawamura, H.; Tsuburaya, K.; Tachikawa, K. *Jpn. J. Appl. Phys.* **1987**, *26*, 921.

(25) Shirotani, I; Mikami, J.; Adachi, T.; Katayama, Y.; Tsuji, K.; Kawamura, H.; Shimomura, O.; Nakajima, T. *Phys. Rev. B: Condens. Matter Mater. Phys.* **1994**, *50*, 16274−16278.

(26) Osters, O.; Nilges, T.; Bachhuber, F.; Pielnhofer, F.; Weihrich, R.; Schoneich, M.; Schmidt, P. *Angew. Chem., Int. Ed.* **2012**, *51*, 2994−2997.

(27) Liu, B. L.; Kopf, M.; Abbas, A. N.; Wang, X. M.; Guo, Q. S.; Jia, Y. C.; Xia, F. N.; Weihrich, R.; Bachhuber, F.; Pielnhofer, F.; et al. *Adv. Mater.* **2015**, *27*, 4423−4429.

(28) Long, M.; Gao, A.; Wang, P.; Xia, H.; Ott, C.; Pan, C.; Fu, Y.; Liu, E.; Chen, X.; Lu, W.; et al. *Sci. Adv.* **2017**, *3*, e1700589.

(29) Amani, M.; Regan, E.; Bullock, J.; Ahn, G. H.; Javey, A. *ACS Nano* **2017**, *11*, 11724.

(30) Kopf, M.; Eckstein, N.; Pfister, D.; Grotz, C.; Kruger, I.; Greiwe, M.; Hansen, T.; Kohlmann, H.; Nilges, T. *J. Cryst. Growth* **2014**, *405*, 6−10.

(31) Fox, M. *Optical Properties of Solids*; Oxford University Press: New York, 2010.

(32) Castellanos-Gomez, A.; Buscema, M.; Molenaar, R.; Singh, V.; Janssen, L.; van der Zant, H. S. J.; Steele, G. A. *2D Mater.* **2014**, *1*, 011002.

(33) Chen, X. L.; Wu, Y. Y.; Wu, Z. F.; Han, Y.; Xu, S. G.; Wang, L.; Ye, W. G.; Han, T. Y.; He, Y. H.; Cai, Y.; et al. *Nat. Commun.* **2015**, *6*, 7315.

(34) Favron, A.; Gaufres, E.; Fossard, F.; Phaneuf-L'Heureux, A. L.; Tang, N. Y. W.; Levesque, P. L.; Loiseau, A.; Leonelli, R.; Francoeur, S.; Martel, R. *Nat. Mater.* **2015**, *14*, 826−832.

(35) Wood, J. D.; Wells, S. A.; Jariwala, D.; Chen, K. S.; Cho, E.; Sangwan, V. K.; Liu, X. L.; Lauhon, L. J.; Marks, T. J.; Hersam, M. C. *Nano Lett.* **2014**, *14*, 6964−6970.

(36) Kim, K. K.; Hsu, A.; Jia, X. T.; Kim, S. M.; Shi, Y. M.; Dresselhaus, M.; Palacios, T.; Kong, J. *ACS Nano* **2012**, *6*, 8583−8590.

(37) Muller, R. S.; Kamins, T. I. *Device Electronics for Integrated Circuits*; John Wiley & Sons: Hoboken, NJ, 2002.

(38) Zhu, Z.; Guan, J.; Tomanek, D. *Nano Lett.* **2015**, *15*, 6042−6046.

(39) Nelson, J. *The Physics of Solar Cells*; Imperial College Press: London, 2003.

(40) Freitag, M.; Low, T.; Xia, F. N.; Avouris, P. *Nat. Photonics* **2013**, *7*, 53−59.

(41) Chuang, S. L. *Physics of Photonic Devices*; John Wiley & Sons: Hoboken, NJ, 2009.

(42) He, J. Q.; He, D. W.; Wang, Y. S.; Cui, Q. N.; Bellus, M. Z.; Chiu, H. Y.; Zhao, H. *ACS Nano* **2015**, *9*, 6436−6442.

(43) Rockett, A. *The Materials Science of Semiconductors*; Springer: Boston, MA, 2008.

(44) Furchi, M. M.; Polyushkin, D. K.; Pospischil, A.; Mueller, T. *Nano Lett.* **2014**, *14*, 6165−6170.

(45) Haartman, M. V.; Östling, M. *Low-Frequency Noise in Advanced MOS Devices*; Springer: Dordrecht, The Netherlands, 2007.

(46) Unlu, M. S.; Strite, S. *J. Appl. Phys.* **1995**, *78*, 607−639.

(47) *SAINT*, V7.68A; Bruker AXS: Madison, WI, 2009.

(48) *SADABS*, V2008/1; Bruker AXS: Madison, WI, 2008.

(49) Sheldrick, G. *Acta Crystallogr., Sect. A: Found. Crystallogr.* **2008**, *64*, 112−122.

(50) *Bruker SHELXTL*, V2011.4−0; Bruker AXS: Madison, WI, 2008.

Supporting Information

Air-Stable Room-Temperature Mid-Infrared Photodetectors Based on hBN/Black Arsenic Phosphorus/hBN Heterostructures

Shaofan Yuan[†,Δ], Chenfei Shen[‡, Δ], Bingchen Deng[†], Xiaolong Chen[†], Qiushi Guo[†], Yuqiang Ma[¤],

Ahmad Abbass[¤,1,2,3], Bilu Liu[¤,4], Ralf Haiges[w], Claudia Ott[§], Tom Nilges[§], Kenji Watanabe[||],

Takashi Taniguchi[||], Ofer Sinai[⊥], Doron Naveh[⊥], Chongwu Zhou[‡,¤] and Fengnian Xia*[†]*

[†]Department of Electrical Engineering, Yale University, New Haven, Connecticut 06511, United

States

[‡] Mork Family Department of Chemical Engineering and Materials Science, University of

Southern California, Los Angeles, California 90089, United States

[¤] Ming Hsieh Department of Electrical Engineering, University of Southern California, Los

Angeles, California 90089, United States

[w] Loker Hydrocarbon Research Institute and Department of Chemistry, University of Southern

California, Los Angeles, California 90089, United States

[§] Department of Chemistry, Technical University Munich, Lichtenbergstr.4, 85748 Garching b.

München, Germany

[||] National Institute for Materials Science, 1-1 Namiki, Tsukuba, 305-0044, Japan

1

[1]Faculty of Engineering and Bar-Ilan Institute for Nanotechnology and Advanced Materials,

Bar-Ilan University, Ramat-Gan 52900, Israel

Corresponding Author

[*] E-mail: fengnian.xia@yale.edu and chongwuz@usc.edu

I. The elemental composition analysis of b-As$_{0.83}$P$_{0.17}$.
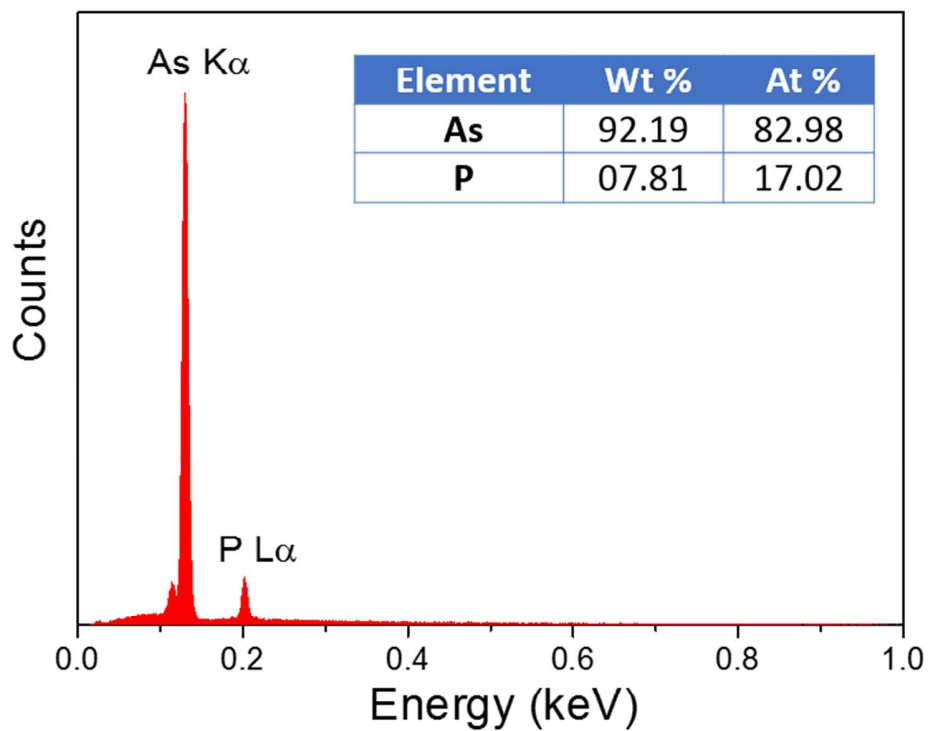
Figure S1. EDS spectrum of As$_{0.83}$P$_{0.17}$. The elemental composition is summarized in the inset table. The relative abundance is calculated considering the X-ray emission peaks of As Kα and P Lα transitions.[1]

II. The crystallographic information of b-As$_{0.83}$P$_{0.17}$.

Empirical formula	As$_{0.83}$P$_{0.17}$
Space group	Cmca
Crystal system	orthorhombic
Unit cell dimensions	a=3.561(3) Å α=90°
	b=10.803(9) Å β=90°
	c=4.493(4) Å γ=90°
Volume	172.8(3) Å^3
Z	8
Calculated density	5.759 g/cm^3
Transmission ratio (max/min)	0.3950/0.1310
Absorption coefficient	38.049 mm^{-1}
F(000)	264
θ range	3.77°-30.30°
Total number of reflections	763
Independent reflections	147 (R$_{int}$ = 0.0467)
Data/restraints/parameters	147/0/7
Goodness-of-fit on F^2	1.101
Final R indices [I > 2σ(I)]	R$_1$ = 0.0334
	wR$_2$ = 0.0760
R indices (all data)	R$_1$ = 0.0364
	wR$_2$ = 0.0775
Largest diff. peak and hole	1.239 and -2.215 eÅ^{-3}

Table S1. Summary of crystallographic data of the b-As$_{0.83}$P$_{0.17}$ measured at 100 K.

In the refinement, standard parameters are used in the SHELXTL software as explained below.[2,3] $F_o(hkl)$ and $F_c(hkl)$ are the observed and calculated structure factor corresponding to certain Miller index (hkl). The diffraction intensity I_{hkl} is related to $F(hkl)$ by $I_{hkl} \propto |F(hkl)|^2$, and σ is the standard uncertainty. The merging residuals from merging equivalent reflections, such as Friedel opposites, are defined as $R_{int} = \frac{\sum |F_o^2 - \langle F_o^2 \rangle|}{\sum F_o^2}$ and $R_{sig} = \frac{\sum \sigma(F_o^2)}{\sum F_o^2}$. The residual factors of the structure refinement are defined as $R_1 = \frac{\sum ||F_o| - |F_c||}{\sum |F_o|}$ and $wR_2 = \sqrt{\frac{\sum w(F_o^2 - F_c^2)^2}{\sum w F_o^2}}$, where w is the weight parameter and F_o and F_c are the observed and calculated structure factors. The Goodness-of-fit S is

4

defined by $S = \sqrt{\frac{\sum w\left(F_o^2 - F_c^2\right)^2}{(N_R - N_P)}}$, where N_R is the number of independent reflections and N_P is the

number of refined parameters.
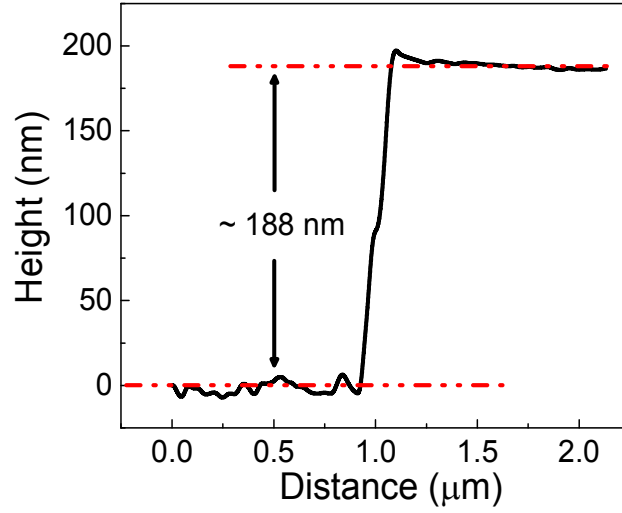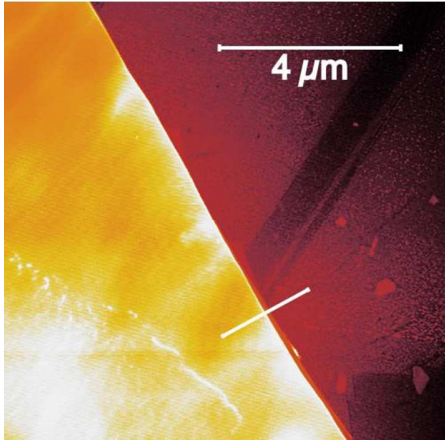
III. The thickness profile of the exfoliated b-As$_{0.83}$P$_{0.17}$ shown in Figure 1c.

Figure S2. The thickness profile of the exfoliated b-As$_{0.83}$P$_{0.17}$ flake used for extinction spectra characterization acquired using atomic force microscope.

IV. The reflection measurements of b-As$_{0.83}$P$_{0.17}$ flake on ZnS substrate

The reflection measurements were performed on the same flake as shown in Figure 1c. The optical configuration for extinction and reflection measurements are drawn in Figure S4 a and b. In the reflection spectra below, R is the reflection of b-As$_{0.83}$P$_{0.17}$ flake on ZnS substrate, and R$_0$ corresponds to the reflection of bare ZnS substrate, which is estimated to be around 15% (R$_0$ = $|\frac{n-1}{n+1}|^2$, n $\approx$ 2.25, and the imaginary part is neglected). So, the extra reflection (ΔR = (γ-1)·R$_0$) due to AsP is actually a minor term (~5%) in the extinction.
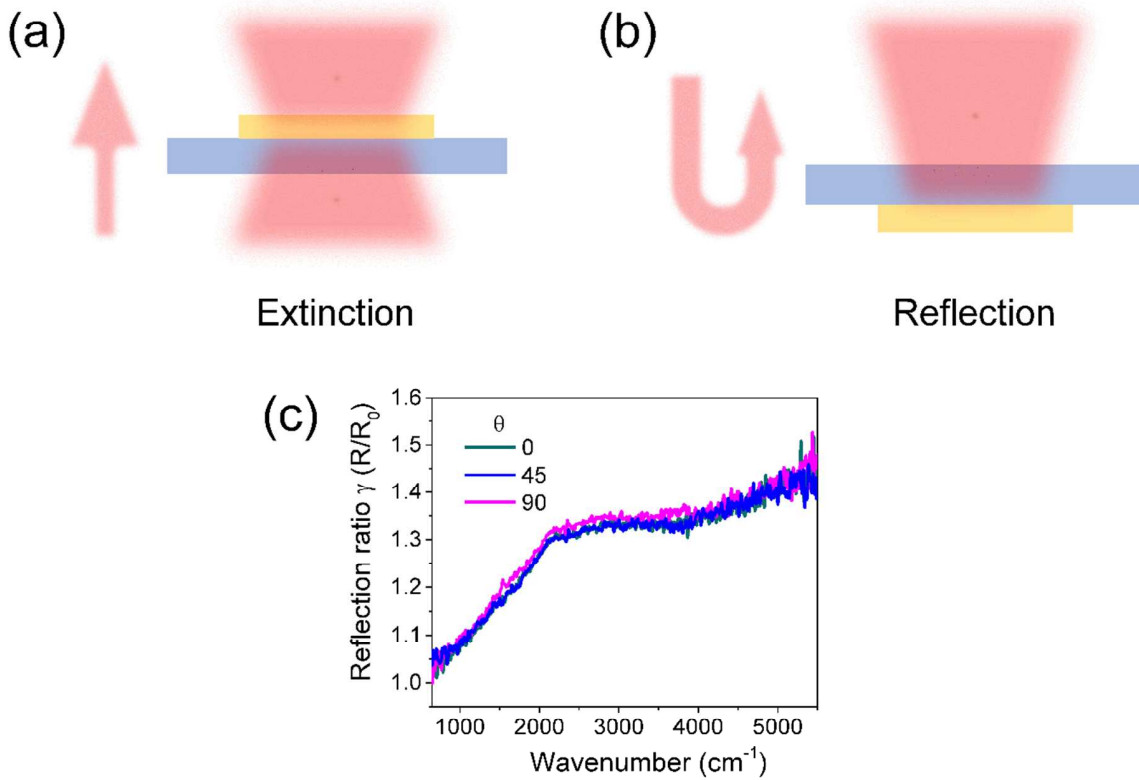
Figure S3. (a), (b) The optical configuration of infrared extinction (a) and reflection (b) measurements. **(c)** The measured infrared reflection ratio between b-As$_{0.83}$P$_{0.17}$ flake on ZnS and the bare ZnS substrate.

V. Calculation of noise equivalent power (NEP)

NEP is defined as the incident power, at which the signal-to-noise ratio is one in a bandwidth (Δf) of 1 Hz, $I_{ph}^2/(S_n \Delta f) = 1$, where S_n is the spectral density function of total noise.[4] NEP can be calculated as NEP $= \sqrt{S_n}/R_{ex}$. As discussed in ref. 4 in this Supporting Information, the total noise in the photoconductive devices consists of thermal noise (S_T), shot noise (S_S), and generation-recombination noise (S_{GR}), $S_n = S_T + S_S + S_{GR}$. With above consideration, we have

$$R_{ex}^2 \cdot NEP^2 = 2eI_{ds} + {4k_B T}/{R} + {4eR_{ex} \cdot NEP \cdot (\tau_{life}/\tau_{tr})}\Big/{\left(1 + \left(2\pi f \tau_{life}\right)^2\right.}^2,$$ here we set

$\Delta f = 1$ Hz. We get NEP $= {\left(2e + \sqrt{4e^2 \left(\frac{\tau_{life}}{\tau_{tr}}\right)^2 / ((1 + \left(2\pi f \tau_{life}\right)^2)^2 + 2eI_{ds} + \frac{4k_B T}{R}}\right)}\Big/{R_{ex}}$ by

solving the equation. We notice $4e^2 \left(\frac{\tau_{life}}{\tau_{tr}}\right)^2 \ll 2eI_{ds}$ in our case, so the generation-recombination noise contributes little to the NEP in our device. For simplicity, we calculate NEP with NEP $= {\sqrt{2eI_{ds} + \frac{4k_B T}{R}}}\Big/{R_{ex}}$ in the main text.

VI. Noise current density measurements at charge neutral point

Noise current density was measured with lock-in amplifier (Stanford Research SR830) and preamplifier (Femto DLPCA-200) in a Lakeshore probe station at room temperature. The tested device was biased at charge neutral point at $V_{ds} = 1$ V. The noise voltage (S_V) was acquired from lock-in amplifier and converted to noise current density by $S_I = S_V/(G \times ENBW)$, where G is the gain of the preamplifier and ENBW is the equivalent noise band-width of the lock-in amplifier. The noise measurements at each frequency were repeated twenty times consistently, and the averaged values were given in Figure S3 with error bars. Certain frequencies (f = $60 \times n$ Hz, where n =1, 2, 3…) were intentionally avoided in the measurements to minimize the effect of 60 Hz environmental noise and its harmonics.

The measured noise current density shows clear 1/f decreasing trend from 1 to 100 Hz, while the noise current levels off above ~2 kHz. This observation indicates that the 1/f noise only dominates at very low frequencies. The measured value at high frequencies (2 to 10 kHz) is about three times as large as the calculated value, probably due to the additional noise introduced by our measurement setup.

As a result, for the intended operational speed of our detector (well above 10 kHz), it is not necessary to consider the 1/f noise.
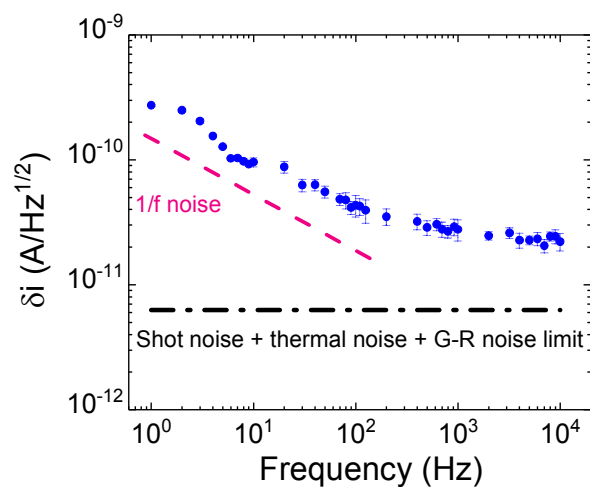
Figure S4. The measured noise current density (blue dots) at room temperature, compared with the calculated value (black dashed line). The red dashed line shows a reference 1/f noise current density.

REFERENCES

1.   Shindo, D.; Oikawa, T., *Energy Dispersive X-ray Spectroscopy*. Springer Japan: Tokyo, 2002.
2.   *Bruker SHELXTL*, V2011.4-0; Bruker AXS: Madison, WI, 2008.
3.   Muller, P.; Herbst-Irmer, R.; Spek, A.; Schneider, T.; Sawaya, M., *Crystal Structure Refinement: A Crystallographer's Guide to SHELXEL* Oxford University Press: New York, 2006.
4.   Chuang, S. L., *Physics of Photonic Devices*. John Wiley & Sons: Hoboken, 2009.

4   Conclusion

In this work different compounds containing main group elements were synthesized, analyzed and possible applications were investigated. Two compounds SnIP and La$_2$NiBi were found and tested for possible utilizations. Two compounds already known to literature (black P and black AsP) could be studied in terms of behaviour in battery and photodetector systems.

La$_2$NiBi is a new ternary version of the Bi$_3$Ni structure type. It can be synthesized via a ceramic solid state reaction of the elements. The compound shows a Ni-Ni distance of 256 pm which is extraordinarily short. DFT band structure calculations suggest metallic behaviour. Physical property measurements substantiated this fact. La$_2$NiBi is a metallic compound with a thermal stability up tp 873 K under inert conditions and a weak Pauli paramagnet. Further works should concern the growth of larger single crystals with the intention to analyse the conductivity along the crystallographic *b*-axis and therefor the conductivity along the Ni-Ni zig-zag chains. This could show interesting properties like anisotropic behaviour of the investigated compound.

SnIP represents the first inorganic double helix compound with two enantiomeric double helices per unit cell attached by weak van der Waals forces. It can be synthesized in an easy gasphase transport reaction from the elements and delaminated with mechanical and chemical procedures to one-dimensional nano-rods. Different physical property measurements and quantum chemical calculations have been conducted. It is a very flexible semiconductor exhibiting strong anisotropy. A SnIP/CNFCl hybrid system was investigated in the light of photocatalytical water splitting. The compound also shows great potential as candidate of a new class of flexible semiconductors for various applications. Further works should concentrate on the practical implementation of this intriguing compound in flexible devices and energy related developments.

The work about the behaviour of black phosphorous in sodium ion batteries and the influence of copper on this system concentrated on the preparation route of black phosphorous active material and an easy coating approach with copper for SIBs. Three different preparation ways for the active material were investigated and yielded different crystallinities and particle sizes. The resulting capacities of the coin cells are found to be in the order BM < ST < US which leads to the assumption that the crystallinity of the black phosphorous active material, besides its particle size, playes a crucial role in it's battery performance. Furthermore, the influence of

copper (used as current collector material for anodes) was investigated. An easy route to apply a copper coating to the surface of the active material was developed and resulted in a capacity improvement but loss in initial coloumbic efficiency of each active material sample. This simple and effective coating might open a way to industrial application but also rises the question of corrosion effects as a negative factor for the battery stability. For future works the reaction mechanism of black phosphorous with sodium under the influence of copper should be identified and investigated in more detail.

Black AsP could be applied in MIR photodetectors on its own and embodied in hBN as a vdW heterojunction-device operating at room temperature. Another aspect was to realize long-term air stability of such a device. MIR detection is a very important aspect in various fields like free space telecommunication, molecular "fingerprint" imaging or even optical radar applications. In this work it was managed to fabricate devices showing a broadband MIR responsivity, fast photoresponse and low dark noise.

New and already known inorganic compounds were studied in various important fields like battery applications and water splitting. It might open a new way to improve commercially available technology for further downscaling of devices and even new applications like flexible gadgets. All compounds with an emphasis on SnIP showed extraordinary behaviour and interesting new possibilities. Future works should concentrate on the practical and large scale realization of devices based on the here gathered intel.

5 Scientific Contributions

Articles:

- **C. Ott**, F. Reiter, M. Baumgartner, M. Pielmeier, A. Vogel, S. Burger, M. Ehrenreich, G. Kieslich, D. Daisenberger, J. Armstrong, T.U. Kumar, P. Kumar, S. Chen, D. Donadio, L.S. Walter, R.T. Weitzg, K. Shankar and T. Nilges, "Flexible and Ultra-Soft Inorganic 1D Semiconductor and Heterostructure Systems Based on SnIP", Adv. Funct. Mater., 1900233 (2019).

- **C. Ott**, A. Degg, P. Walke, F. Reiter and T. Nilges, "Influence of Copper on the Capacity of Phosphorus-Anodes in Sodium-Ion-Batteries", J. Solid State Chem., 270, 636 (2019).

- S. Yuan, C. Shen, B. Deng, X. Chen, Q. Guo, Y. Ma, A. Abbas, B. Liu, R. Haiges, **C. Ott**, T. Nilges, K. Watanabe, T. Taniguchi, O. Sinai, D. Naveh, C. Zhou and F. Xia, "Air-Stable Room-Temperature Mid-Infrared Photodetectors Based on hBN/Black Arsenic Phosphorus/hBN Heterostructures", *Nano Lett.*, 18, 3172 (2018).

- **C. Ott**, M. Baumgartner, K. Schäfer, F. Baumer, K. Freitag, L. Scherf, L. Heletta, R. Weihrich, R. Pöttgen and T. Nilges, "Structure and Bonding of La$_2$NiBi", *ZAAC*, 645, 340 (2018).

- M. Long, A. Gao, P. Wang, H. Xia, **C. Ott**, C. Pan, Y. Fu, E. Liu, X. Chen, W. Lu, T. Nilges, J. Xu, X. Wang, W. Hu and F. Miao, "Room Temperature High-Detectivity Mid-Infrared Photodetectors Based on Black Arsenic Phosphorous", *Sci. Adv.*, 3(6), e1700589 (2017).

- D. Pfister, K. Schäfer, **C. Ott**, B. Gerke, R. Pöttgen, O. Janka, M. Baumgartner, A. Efimova, A. Hohmann, P. Schmidt, S. Venkatachalam, L. vanWüllen, U. Schürmann, L. Kienle, V. Duppel, E. Parzinger, B. Miller, J. Becker, A. Holleitner, R. Weihrich and T. Nilges, "Inorganic Double Helices in Semiconcucting SnIP", *Adv. Mater.*, 28(44), 9783 (2016).

- T. Nilges, D. Pfister, **C. Ott**, K. Schäfer, M. Baumgartner and R. Weihrich, "Inorganic Semiconducting Compounds" *EP patent*, EP 15176311.7 (2015).

Oral Presentations:

- "Flexible and ultra-soft inorganic 1D semiconductor and heterostructure systems based on SnIP", Annual ATUMS meeting, Garching near Munich, Germany, November 2018.

- "SnIP-Polymer Hybrid Materials", Annual ATUMS meeting, Jasper, Alberta, Canada, November 2017.

- "Carbon@Metal-Pnictogen Hybrids for Li- and Na-Ion Battery Applications and the new compound SnIP", Annual ATUMS meeting, Raitenhaslach, Germany, November 2016.

Poster Presentations:

- "One-dimensional semiconducting SnIP for flexible heterostructure devices", Annual ATUMS meeting, Garching near Munich, Germany, November 2018. 2nd Poster Price.

- "One-dimensional semiconducting SnIP for flexible heterostructure devices", Wöhler Tagung (Poster #P-202), Regensburg, Germany, September 2018.

- "La_2NiBi – A new ternary ordered version of the Bi_3Ni structure type", 11th IGGSE Forum, Raitenhaslach, Germany, May 2017.

- "La_2NiBi – A new ternary ordered version of the Bi_3Ni structure type", Annual ATUMS meeting, Raitenhaslach, Germany, November 2016.

- "La_2NiBi – A new ternary ordered version of the Bi_3Ni structure type", 6th Energy Colloquium, Garching near Munich, Germany, June 2016.

- "Carbon@Metal-Pnictogen Hybrids for Efficient Li- and Na-ion Battery Applications" 10th IGGSE Forum, Raitenhaslach, Germany, May 2016.

- "Carbon@Metal-PnictogenHybrids for Efficient Li-and Na-ion Battery Applications" Kick-Off Seminar, Frauenchiemsee, Germany, January 2016.

- "Carbon@Metal-Pnictogen Hybrids for Efficient Li- and Na-ion Battery Applications", Annual ATUMS meeting, Edmonton, Alberta, Canada, November 2015.

References

[1] D.T. Larose and C. D. Larose. *Discovering Knowledge in Data, An Introduction to Data Mining.* John Wiley & Sons, New Jersey, 2 edition, 2014.

[2] A.K. Geim and K.S. Novoselov. *The rise of graphene*, pages 11–19.

[3] E.V. Castro, K.S. Novoselov, S.V. Morozov, N.M.R. Peres, J.M.B. Lopes dos Santos, J. Nilsson, F. Guinea, A.K. Geim, and A.H. Castro Neto. Biased bilayer graphene: Semiconductor with a gap tunable by the electric field effect. *Phys. Rev. Lett.*, 99:216802, 2007.

[4] P. Vogt, P. De Padova, C. Quaresima, J. Avila, E. Frantzeskakis, M.C. Asensio, A. Resta, B. Ealet, and G. Le Lay. Silicene: Compelling experimental evidence for graphenelike two-dimensional silicon. *Phys. Rev. Lett.*, 108:155501, 2012.

[5] H. Liu, A.T. Neal, Z. Zhu, Z. Luo, X. Xu, D. Tománek, and P.D. Ye. Phosphorene: An unexplored 2d semiconductor with a high hole mobility. *ACS Nano*, 8(4):4033–4041, 2014.

[6] D. Jose and A. Datta. Structures and chemical properties of silicene: Unlike graphene. *Accounts of Chemical Research*, 47(2):593, 2014.

[7] M.P. McDonald, R. Chatterjee, J. Si, B. Jankó, and M. Kuno. Dimensional crossover in semiconductor nanostructures. *Nat. Com.*, 7:12726, 2016.

[8] D. Pfister, K. Schäfer, C. Ott, B. Gerke, R. Pöttgen, O. Janka, M. Baumgartner, A. Efimova, A. Hohmann, P. Schmidt, S. Venkatachalam, L. van Wüllen, U. Schürmann, L. Kienle, V. Duppel, E. Parzinger, B. Miller, J. Becker, A. Holleitner, R. Weihrich, and T. Nilges. *Adv. Mater.*, 28(44):9783, 2016.

[9] M. Baumgartner, R. Weihrich, and T. Nilges. Inorganic snip-type double helices in main-group chemistry. *Chemistry ? A European Journal*, 23(26):6452–6457, 2017.

[10] L.Q. Sun, M.J. Li, K. Sun, S-H. Yu, R.S. Wang, and H.M. Xie. Electrochemical activity of black phosphorus as an anode material for lithium-ion batteries. *The Journal of Physical Chemistry C*, 116(28):14772, 2012.

[11] R. Yazami. Surface chemistry and lithium storage capability of the graphite?lithium electrode. *Electrochimica Acta*, 45(1):87, 1999.

[12] M. Faraday. Experimental researches in electricity. seventh series. *Philosophical Transactions of the Royal Society of London*, 124:77, 1834.

[13] R.G. Ehl and A.J. Ihde. Faraday's electrochemical laws and the determination of equivalent weights. *Journal of Chemical Education*, 31(5):226, 1954.

[14] F.C. Strong. Faraday's laws in one equation. *Journal of Chemical Education*, 38(2):98, 1961.

[15] R.A. Sharma and R.N. Seefurth. Thermodynamic properties of the lithium?silicon system. *J. Electrochem. Soc.*, 123:1763, 1976.

[16] B.A. Boukamp, G.C. Lesh, and R.A. Huggins. All-solid lithium electrodes with mixed-conductor matrix. *J. Electrochem. Soc.*, 128(4):725, 1981.

[17] C.V.D. Marel, G.J.B. Vinke, and W.V.D. Lugt. The phase diagram of the system lithium-silicon. *Solid State Commun.*, 54:917, 1985.

[18] P.W. Bridgman. Two new modifications of phosphorous. *JACS*, 36(7):1344, 1914.

[19] A. Brown and S. Rundqvist. Refinement of the crystal structure of black phosphorus. *Acta Crystallogr., Sect. A: Found. Crystallogr.*, 19(4):684–685, 1965.

[20] C.M. Park and H.J. Sohn. Black phosphorus and its composite for lithium rechargeable batteries. *Adv. Mater.*, 19(18):2465, 2007.

[21] C. Marino, A. Debenedetti, B. Fraisse, F. Favier, and L. Monconduit. Activated-phosphorus as new electrode material for li-ion batteries. *Electrochem. Commun.*, 13(4):346, 2011.

[22] M.C. Stan, J. von Zamory, S. Passerini, T. Nilges, and M. Winter. Puzzling out the origin of the electrochemical activity of black p as a negative electrode material for lithium-ion batteries. *J. Mater. Chem. A*, 1:5293, 2013.

[23] N. Nitta and G. Yushin. High-capacity anode materials for lithium-ion batteries: Choice of elements and structures for active particles. *Particle & Particle Systems Characterization*, 31(3):317, 2014.

[24] M. Nagao, A. Hayashi, and M. Tatsumisago. All-solid-state lithium secondary batteries with high capacity using black phosphorus negative electrode. *J. Power Sources*, 196(16): 6902, 2011.

[25] J. Qian, D. Qiao, X. Ai, Y. Cao, and H. Yang. Reversible 3-li storage reactions of amorphous phosphorus as high capacity and cycling-stable anodes for li-ion batteries. *Chem. Commun.*, 48:8931, 2012.

[26] *http://www.lithiummine.com*, 23.10.2018.

[27] J. Qian, X. Wu, Y. Cao, X. Ai, and H. Yang. High capacity and rate capability of amorphous phosphorus for sodium ion batteries. *Angew. Chem.*, 125(17):4731, 2013.

[28] Y. Kim, Y. Park, A. Choi, N.S. Choi, J. Kim, J. Lee, J.H. Ryu, S.M. Oh, and K.T. Lee. An amorphous red phosphorus/carbon composite as a promising anode material for sodium ion batteries. *Adv. Mater.*, 25(22):3045, 2013.

[29] N. Yabuuchi, Y. Matsuura, T. Ishikawa, S. Kuze, J.Y. Son, Y.T. Cui, H. Oji, and S. Komaba. Phosphorus electrodes in sodium cells: Small volume expansion by sodiation and the surface-stabilization mechanism in aprotic solvent. *ChemElectroChem*, 1(3): 580, 2014.

[30] N. Yabuuchi, K. Kubota, M. Dahbi, and S. Komaba. Research development on sodium-ion batteries. *Chem. Rev.*, 114(23):11636, 2014.

[31] G.E.R. Schulze. *Metallphysik: Ein Lehrbuch.* Akademie-Verlag, Berlin, 1967.

[32] A.F. Hollemann and N. Wiberg. *Lehrbuch der Anorganischen Chemie.* Walter de Gruyter und Co., Berlin, 102. Auflage, 2007.

[33] A. von Keitz, G. Sauthoff, and P. Neumann. Laves phases for high temperatures - structure, stability and constitution. *Zeitschrift fuer Metallkunde/Materials Research and Advanced Techniques*, 89:803, 1998.

[34] A. von Keitz and G. Sauthoff. Laves phases for high temperatures?part ii: Stability and mechanical properties. *Intermetallics*, 10(5):497, 2002.

[35] O.A. Neumüller. *Römpps Chemie-Lexikon.* Franckh'sche Verlagshandlung, Stuttgart, 1988.

[36] E. Riedel and C. Janiak. *Anorganische Chemie.* De Gruyter, Berlin, 2015.

[37] W.W. Scanlon. Intermetallic compounds. 142(3597):1265, 1963.

[38] G. Natta, M. Peraldo, and G. Allegra. Crystalline modification of syndiotactic polypropylene having a zig?zag chain conformation. *Die Makromolekulare Chemie*, 75(1):215, 1964.

[39] N.D.R. Barnett and R.E. Muhey. Butyllithium cubane tetramers linked by li-tmeda-li bridges in an infinite, zig-zag chain arrangement: First crystallographic study of a simple butyl compound of an early main group element. *J. Am. Chem. Soc.*, 115:1573, 1993.

[40] M.L. Godino-Salido, M.D. Gutiérrez-Valero, R. López-Garzón, and J.M. Moreno-Sánchez. Zn(ii) complexes with thiopyrimidine derivatives: solution study, synthesis and crystal structure of a zig-zag chain zinc(ii) complex with the ligand 4,6-dimethyl-2-thiopyrimidine. *Inorg. Chim. Acta*, 221(1):177, 1994.

[41] E. Colacio, J.M. Domínguez-Vera, M. Ghazi, R. Kivekäs, M. Klinga, and J.M. Moreno. Singly anti-anti carboxylate-bridged zig-zag chain complexes froma carboxylate-containing tridentate schiff base ligand and m(hfac)$_2$[m = mn^{II},ni^{II}, and cu^{II}]: Synthesis, crystal structure,and magnetic properties. *Eur. J. Inorg. Chem.*, page 441, 1999.

[42] D. Sun, R. Cao, Y. Liang, Q. Shi, W. Su, and M. Hong. Hydrothermal syntheses, structures and properties of terephthalate-bridged polymeric complexes with zig-zag chain and channel structures. *J. Chem. Soc., Dalton Trans.*, 16:2335, 2001.

[43] M. Ade, D. Kotzott, and H. Hillebrecht. Synthesis and crystal structures of the new metal-rich ternary borides ni$_{12}$alb$_8$, ni$_{12}$gab$_8$and ni$_{10.6}$ga$_{0.4}$b$_6$?examples for the first b$_5$zig-zag chain fragment. *J. Solid State Chem.*, 183(8):1790, 2010.

[44] A.E. Dwight, R.A. Conner, and J.W. Downey. Equiatomie compounds of the transition and lanthanide elements with rh, ir, ni and pt. *Acta Crystallogr.*, 18:835, 1965.

[45] N.C. Baenziger and J.L. Moriarty. Gadolinium and dysprosium intermetallic phases. i. the crystal structures of dyga and gdpt and their related compounds. *Acta Crystallogr.*, 14: 946, 1961.

[46] M. Ruck and T. Söhnel. Transmissionsoptimierte einkristallstrukturbestimmung und elektronische struktur von bi$_3$ni. *Z. Naturforsch.*, 61b:785, 2006.

[47] K. Schäfer, A. Isaeva, M. Ruck, B. Gerke, C. Schwickert, and R. Pöttgen. La$_2$nisb ? a ternary ordered version of the bi$_3$ni type with highly polar bonding. *Z. Naturforsch.*, 69b: 1097, 2014.

[48] M.C. Robert, R. Saravanan, K. Saravanakumar, and M.P. Ranib. Structural analysis of al, ni, and cu using the maximum entropy method, multipole and pair distribution function. *Z. Naturforsch.*, 64b:361, 2009.

[49] J.D. Watson and F.H. Crick. Molecular structure of nucleic acids: A structure for deoxyribose nucleic acid. *Nature*, 171(1-3):737, 1953.

[50] L. Pauling, R.B. Corey, and H.R. Branson. The structure of proteins: Two hydrogen-bonded helical configurations of the polypeptide chain. *Proceedings of the National Academy of Sciences*, 37(4):205, 1951.

[51] A. Yonath and W. Traub. Polymers of tripeptides as collagen models: Iv. structure analysis of poly(l-prolyl-glycyl-l-proline). *Journal of Molecular Biology*, 43(3):461, 1969.

[52] R. Berisio, L. Vitagliano, L. Mazzarella, and A. Zagari. Crystal structure of the collagen triple helix model [(pro?pro?gly)$_{10}$]$_3$. *Protein Science*, 11(2):262, 2002.

[53] M.Q. Zhao, Q. Zhang, G.L. Tian, and F. Wei. Emerging double helical nanostructures. *Nanoscale*, 6:9339, 2014.

[54] C.W. Bunn and E.R. Howells. Structures of molecules and crystals of fluoro-carbons. *Nature*, 174:549, 1954.

[55] J. Sharma, R. Chhabra, Y. Liu, Y. Ke, and H. Yan. Control of self-assembly of dna tubules through integration of gold nanoparticles. *Angew. Chem. Int. Ed.*, 45(5):730, 2006.

[56] J. Sharma, R. Chhabra, A. Cheng, J. Brownell, Y. Liu, and H. Yan. Control of self-assembly of dna tubules through integration of gold nanoparticles. *Science*, 323(5910):112, 2009.

[57] C.C. Easterday, L.R. Dedon, M. Zeller, and C.M. Oertel. Helical $^1_\infty[pb_2o]$ chains in polymorphs of $pb_2o(c_6h_5coo)_2$. *Crystal Growth & Design*, 14(4):2048, 2014.

[58] H.G. von Schnering. Homonucleare bindungen bei hauptgruppenelementen. *Angewandte Chemie*, 93(1):44, 1981.

[59] E.D. Sone, E.R. Zubarev, and S.I. Stupp. Supramolecular templating of single and double nanohelices of cadmium sulfide. *Small*, 1(7):694, 2005.

[60] J. Goldberger, R. He, Y. Zhang, S. Lee, H. Yan, H.J. Choi, and P. Yang. Single-crystal gallium nitride nanotubes. *Nature*, 422:599, 2003.

[61] Y. Wang, Q. Wang, H. Sun, W. Zhang, G. Chen, Y. Wang, X. Shen, Y. Han, X. Lu, and H. Chen. Chiral transformation: From single nanowire to double helix. *JACS*, 133(50): 20060, 2011.

[62] H. Morito and H. Yamane. Double-helical silicon microtubes. *Angew. Chem. Int. Ed.*, 49 (21):3638, 2010.

[63] A.S. Ivanov, A.J. Morris, K.V. Bozhenko, C.J. Pickard, and A.I. Boldyrev. Inorganic double-helix structures of unusually simple lithium?phosphorus species. *Angew. Chem. Int. Ed.*, 51(33):8330, 2012.

[64] A.S. Ivanov, A.I. Boldyrev, and G. Frenking. Inorganic double-helix nanotoroid of simple lithium?phosphorus species. *Chemistry - A European Journal*, 20(9):2431, 2014.

[65] A.S. Ivanov, T. Kar, and A.I. Boldyrev. Nanoscale stabilization of zintl compounds: 1d ionic li-p double helix confined inside a carbon nanotube. *Nanoscale*, 8:3454, 2016.

[66] A.K. Jissy and A. Datta. What stabilizes the li_np_n inorganic double helices? *J. Phys. Chem. Lett.*, 4(6):1018–1022, 2013.

[67] P. Norton. Hgcdte infrared detectors. *Opto-Electron. Rev.*, 10:159, 2002.

[68] A. Rogalski. Toward third generation hgcdte infrared detectors. *J. Alloys. Compd.*, 371: 53, 2004.

[69] R. Thorn. High density infrared detector arrays, patent, 08 1977.

[70] D. Reago, S. Horn, J. Campbell, and R. Vollmerhausen. Third-generation imaging sensor system concepts. *Proc.SPIE*, 3701:108, 1999.

[71] P. Norton, J. Campbell, S. Horn, and D. Reago. Third-generation infrared imagers. *Proc.SPIE*, 4130:226, 2000.

[72] B.F. Levine, K.K. Choi, C.G. Bethea, J. Walker, and R.J. Malik. New 10 μm infrared detector using intersubband absorption in resonant tunneling gaalas superlattices. *Applied Physics Letters*, 50(16):1092–1094, 1987.

[73] W.D. Lawson, S. Nielson, E.H. Putley, and A. S. Young. Preparation and properties of hgte and mixed crystals of hgte-cdte. *J. Phys. Chem. Solids*, 9:325, 1959.

[74] A. Rogalski, K. Adamiec, and J. Rutkowski. *Narrow-Gap Semiconductor Photodiodes.* SPIE Press, Bellingham, WA, 2000.

[75] Y. Zhang, T. Liu, B. Meng, X. Li, G. Liang, X. Hu, and Q. J. Wang. Broadband high photoresponse from pure monolayer graphene photodetector. *Nat. Commun.*, 4:1811, 2013.

[76] M. Long, E. Liu, P. Wang, A. Gao, H. Xia, W. Luo, B. Wang, J. Zeng, Y. Fu, K. Xu, W. Zhou, Y. Lv, S. Yao, M. Lu, Y. Chen, Z. Ni, Y. You, X. Zhang, S. Qin, Y. Shi, W. Hu, D. Xing, and F. Miao. Broadband photovoltaic detectors based on an atomically thin heterostructure. *Nano Letters*, 16(4):2254, 2016.

[77] G. Konstantatos, M. Badioli, L. Gaudreau, J. Osmond, M. Bernechea, F.P. Garcia de Arquer, F. Gatti, and F.H.L. Koppens. Hybrid graphene?quantum dot phototransistors with ultrahigh gain. *Nat. Nanotechnol.*, 7:363, 2012.

[78] M. Long, A. Gao, P. Wang, H. Xia, C. Ott, C. Pan, Y. Fu, E. Liu, X. Chen, and W. Lu. Room temperature high-detectivity mid-infrared photodetectors based on black arsenic phosphorus. *Science Advances*, 3(6), 2017.

[79] M. Köpf, N. Eckstein, D. Pfister, C. Grotz, I. Krüger, M. Greiwe, T. Hansen, H. Kohlmann, and T. Nilges. Access and in situ growth of phosphorene-precursor black phosphorus. *J. Cryst. Growth*, 405:6–10, 2014.

[80] B. Tian, B. Tian, B. Smith, M.C. Scott, Q. Lei, R. Hua, Y. Tian, and Y. Liu. Facile bottom-up synthesis of partially oxidized black phosphorus nanosheets as metal-free photocatalyst for hydrogen evolution. *Proceedings of the National Academy of Sciences*, 115(17):4345, 2018.

[81] S. Lange, P. Schmidt, and T. Nilges. Au$_3$snp$_7$@black phosphorus: An easy access to black phosphorus. *Inorg. Chem.*, 46(10):4028–4035, 2007.

[82] *https://www.berghof-instruments.com/en/products*, 06.11.2018.

[83] K. S. Novoselov, A. K. Geim, S. V. Morozov, D. Jiang, Y. Zhang, S. V. Dubonos, I. V. Grigorieva, and A. A. Firsov. Electric field effect in atomically thin carbon filmss. *Science*, 306(5696):666–669, 2004.

[84] A. Castellanos-Gomez, M. Buscema, R. Molenaar, V. Singh, L. Janssen, H.S.J. van der Zant, and G.A. Steele. Deterministic transfer of two-dimensional materials by all-dry viscoelastic stamping. *2D Mater.*, 1:011002, 2014.

[85] K.M. Freitag, H. Kirchhain, L. van Wüllen, and T. Nilges. Enhancement of li ion conductivity by electrospun polymer fibers and direct fabrication of solvent-free separator membranes for li ion batteries. *Inorganic Chemistry*, 56(4):2100, 2017.

[86] *https://www.dectris.com/mythen_overview.html*, 08.04.2013.

[87] *WinXPOW*, volume Version 3.05. Stoe & Cie GmbH, Materials Park, Ohio, USA, 2003. ASM International.

[88] P. Villars and K. Cenzual. *Pearson's Crystal Data: Crystal Structure Database for Inorganic Compounds(on CD-ROM)*. Release, 2013/2014.

[89] Stoe & Cie GmbH. X-area, version 1.56. 2011.

[90] V. Petricek, M. Dusek, and L. Palatinus. *JANA2006, Crystallographic computing system.* Institute of Physic, Czech Academy of Sciences, Prague, Czech Republic, 2006.

[91] L. Palatinus and G. Chapuis. Superflip - a computer program for the solution of crystal structures by charge flipping in arbitrary dimensions. *J. Appl. Crystallogr.*, 40:786, 2007.

[92] R.S. Pinna, S. Rudić, S.F. Parker, J. Armstrong, M. Zanetti, G. Škoro, S.P. Waller, D. Zacek, C.A. Smith, M.J. Capstick, D.J. McPhail, D.E. Pooley, G.D. Howells, G. Gorini, and F. Fernandez-Alonso. The neutron guide upgrade of the tosca spectrometer. *Nuclear Instruments and Methods in Physics Research Section A: Accelerators, Spectrometers, Detectors and Associated Equipment*, 896:68, 2018.

[93] *https://www.imperial.ac.uk/pressurecell/*, 06.11.2018.

[94] U. Schürmann, V. Duppel, S. Buller, W. Bensch, and L. Kienle. Precession electron diffraction - a versatile tool for the characterization of phase change materials. *Cryst. Res. Technol.*, 46:561, 2011.

[95] R. Vincent and P.A. Midgley. *Ultramicroscopy*, 53:27, 1994.

[96] P.A. Stadelmann. Ems - a software package for electron diffraction analysis and hrem image simulation in materials science. *Ultramicroscopy*, 21:131, 1987.

[97] *Netzsch Proteus Thermal Analysis V4.8.2.* Netzsch-Gerätebau GmbH, Selb, Germany, 2006.

[98] P. Schmidt, M. Schöneich, M. Bawohl, T. Nilges, and R. Weihrich. The use of the high-temperature gas-balance (htgb) for thermogravimetric measurements. *J. Therm. Anal. Calorim.*, 110:1511, 2011.

[99] R.A. Brand. *Normos 90-Mößbauer Fitting Program.* Universität Duisburg, Duisburg, Germany, 2007.

[100] D. Massiot, F. Fayon, M. Capron, I. King, S. Le Calvé, B. Alonso, J.O. Durand, B. Bujoli, Z. Gan, and G. Hoatson. Modelling one- and two-dimensional solid-state nmr spectra. *Magn. Reson. Chem.*, 40:70, 2002.

[101] A.E. Bennett, R.G. Griffin, J.H. Ok, and S. Vega. Chemical shift correlation spectroscopy in rotating solids: Radio frequency-driven dipolar recoupling and longitudinal exchange. *J. Chem. Phys.*, 96:8624, 1992.

[102] P. Kubelka and F. Munk. An article on optics of paint layers. *Z. Tech. Phys.*, 12:593, 1931.

[103] J. Tauc, R. Grigorovici, and A. Vancu. Optical properties and electronic structure of amorphous germanium. *Phys. Status Solidi*, 15:627, 1966.

[104] J. Tauc. Optical properties of amorphous semiconductors. *J. Mater. Res. Bull.*, 3:37, 1968.

[105] J.P. Perdew, K. Burke, and M. Ernzerhoff. Generalized gradient approximation made simple. *Phys. Rev. Lett.*, 77:3865, 1996.

[106] K. Koepernik and H. Eschrig. Full-potential nonorthogonal local-orbital minimum- basis bandstructure scheme. *Phys. Rev. B*, 59:1743, 1999.

[107] I. Opahle, K. Koepernik, and H. Eschrig. Full-potential band-structure calculation of iron pyrite. *Phys. Rev. B*, 60:14035, 1999.

[108] R. Dovesi, R. Orlando, A. Erba, C.M. Zicovich-Wilson, B. Civalleri, S. Casassa, L. Maschio, M. Ferrabone, M. De La Pierre, P.D. Arco, Y. Noel, M. Causa, M. Rerat, and B. Kirtman. Crystal14: A program for the ab initio investigation of crystalline solids. *Int. J. Quantum Chem.*, 114:1287, 2014.

[109] S. Grimme. Semiempirical gga-type density functional constructed with a long-range dispersion correction. *Journal of Computational Chemistry*, 27(15):1787, 2006.

[110] J.P. Perdew and Y. Wang. Accurate and simple analytic representation of the electron-gas correlation energy. *Phys. Rev. B*, 45:13244, 1992.

[111] A.V. Krukau, O.A. Vydrov, A.F. Izmaylov, and G.E. Scuseria. Influence of the exchange screening parameter on the performance of screened hybrid functionals. *J. Chem. Phys.*, 125:224106, 2006.

[112] A.J. Karttunen, T.F. Fässler, M. Linnolahti, and T.A. Pakkanen. Structural principles of semiconducting group 14 clathrate frameworks. *Inorg. Chem.*, 50:1733, 2011.

[113] J. Rothballer, F. Bachhuber, F. Pielnhofer, S.M. Schappacher, R. Pöttgen, and R. Weihrich. Effect of in-sn ordering on semiconducting properties in insnco$_3$s$_2$- x-ray, [119]sn moessbauer spectroscopy, and dft studies. *Eur. J. Inorg. Chem.*, page 248, 2013.

[114] K. Doll and H. Stoll. Ground-state properties of heavy alkali halides. *Phys. Rev. B*, 57: 4327, 1998.

[115] A. Kokalj. Xcrysden-a new program for displaying crystalline structures and electron densities. *J. Mol. Graphics Modell*, 17:176, 1999.

[116] A. D. Becke and K. E. Edgecombe. A simple measure of electron localization in atomic and molecular systems. *The Journal of Chemical Physics*, 92(9):5397, 1990.

[117] B. Silvi and A. Savin. Classification of chemical bonds based on topological analysis of electron localization functions. *Nature*, 371:683, 1994.

[118] G Kresse and J Hafner. Norm-conserving and ultrasoft pseudopotentials for first-row and transition elements. *J. Phys.: Condens. Matter*, 6(40):8245, 1994.

[119] G. Kresse and J. Furthmüller. Efficiency of ab-initio total energy calculations for metals and semiconductors using a plane-wave basis set. *Comput. Mater. Sci.*, 6:15, 1996.

[120] G. Kresse and J. Furthmüller. Efficient iterative schemes for ab initio total-energy calculations using a plane-wave basis set. *Phys. Rev. B*, 54:11169, 1996.

[121] P.E. Blöchl. Projector augmented-wave method. *Phys. Rev. B*, 50:17953, 1994.

[122] K. Momma and F. Izumi. Vesta 3 for three-dimensional visualization of crystal, volumetric and morphology data. *J. Appl. Crystallogr.*, 44:1272, 2011.

[123] L. Li, Y. Yu, G.J. Ye, Q. Ge, X. Ou, H. Wu, D. Feng, X.H. Chen, and Y. Zhang. Black phosphorus field-effect transistors. *Nat. Nano*, 9(5):372–377, 2014.

[124] K. Terashima, T. Katsumata, F. Orito, T. Kikuta, and T. Fukuda. Electrical resistivity of undoped gaas single crystals grown by magnetic field applied lec technique. *Jpn. J. Appl. Phys.*, 22(6):L325, 1983.

[125] W. Shockley and H.J. Queisser. Detailed balance limit of efficiency of p?n junction solar cells. *J. Appl. Phys.*, 32(3):510, 1961.

[126] N. Youngblood, C. Chen, S.J. Koester, and M. Li. Waveguide-integrated black phosphorus photodetector with high responsivity and low dark current. *Nat. Photonics*, 9:247, 2015.

[127] T. Low, A.S. Rodin, A. Carvalho, Y. Jiang, H. Wang, F. Xia, and A.H. Castro Neto. Tunable optical properties of multilayer black phosphorus thin films. *Phys. Rev. B*, 90: 075434, 2014.

[128] M. Freitag, T. Low, F. Xia, and P. Avouris. Photocurrent in graphene harnessed by tunable intrinsic plasmons. *Nat. Photonics*, 7:53, 2013.

[129] M. Buscema, J.O. Island, D.J. Groenendijk, S.I. Blanter, G.A. Steele, H.S.J. van der Zant, and A. Castellanos-Gomez. Photocurrent generation with two-dimensional van der waals semiconductors. *Chem. Soc. Rev.*, 44:3691, 2015.

[130] T. Hong, B. Chamlagain, W. Lin, H.J. Chuang, M. Pan, Z. Zhou, and Y.Q. Xu. Polarized photocurrent response in black phosphorus field-effect transistors. *Nanoscale*, 6:8978, 2014.

[131] L. Li, G.J. Ye, V. Tran, R. Fei, G. Chen, H. Wang, J. Wang, K. Watanabe, T. Taniguchi, L. Yang, X.H. Chen, and Y. Zhang. Quantum oscillations in a two-dimensional electron gas in black phosphorus thin films. *Nat. Nano*, 10:608, 2015.

[132] X. Chen, Y. Wu, Z. Wu, Y. Han, S. Xu, L. Wang, W. Ye, T. Han, Y. He, Y. Cai, and N. Wang. High-quality sandwiched black phosphorus heterostructure and its quantum oscillations. *Nat. Commun.*, 6:7315, 2015.

[133] N. Gillgren, D. Wickramaratne, Y. Shi, T. Espiritu, J. Yang, J. Hu, J. Wei, X. Liu, Z. Mao, K. Watanabe, T. Taniguchi, M. Bockrath, Y. Barlas, R.K. Lake, and C.N. Lau. Gate tunable quantum oscillations in air-stable and high mobility few-layer phosphorene heterostructures. *2D Mater.*, 2:011001, 2015.

[134] Z. Luo, J. Maassen, Y. Deng, Y. Du, R.P. Garrelts, M.S. Lundstrom, P.D. Ye, and X. Xu. Anisotropic in-plane thermal conductivity observed in few-layer black phosphorus. *Nat. Commun.*, 6:8572, 2015.

[135] Q. Guo, A. Pospischil, M. Bhuiyan, H. Jiang, H. Tian, D. Farmer, B. Deng, C. Li, S.J. Han, H. Wang, Q. Xia, T.P. Ma, T. Mueller, and F. Xia. Black phosphorus mid-infrared photodetectors with high gain. *Nano Lett.*, 16:4648, 2016.

[136] F. Xia, H. Wang, and Y. Jia. Rediscovering black phosphorus as an anisotropic layered material for optoelectronics and electronics. *Nat. Commun.*, 5:4458, 2014.

[137] H. Liu, Y. Du, Y. Deng, and P.D. Ye. Semiconducting black phosphorus: synthesis, transport properties and electronic applications. *Chem. Soc. Rev.*, 44:2732, 2015.

[138] J. Nelson. *The Physics of Solar Cells.* Imperial College Press, London, 2003.

[139] S.L. Chuang. *Physics of Photonic Devices.* John Wiley & Sons, New Jersey, 2009.

6 Appendix
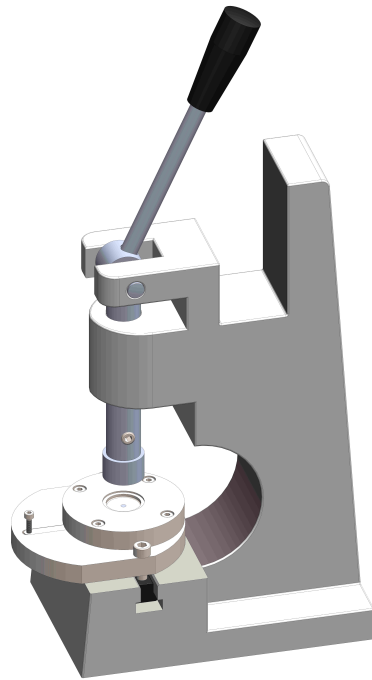
Figure 6.1: Schematic overview drawing of the coin cell press built in the course of this work.
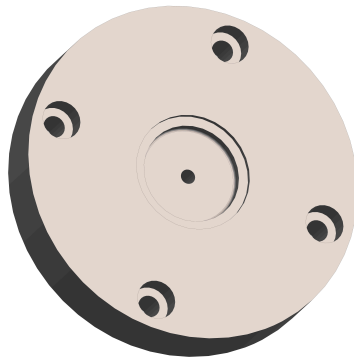
Figure 6.2: Schematic drawing of the manufactured lower part of the extrution die fitting the exact dimensions of CR2032 coin cells.
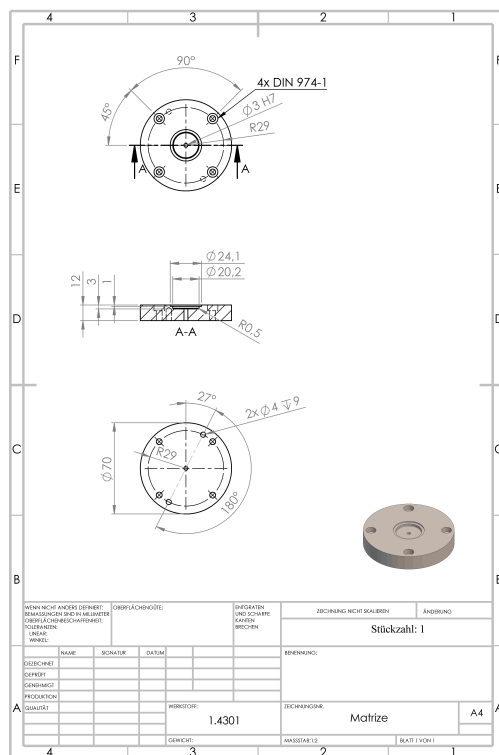
Figure 6.3: Measurements of the manufactured lower part of the extrution die fitting the exact dimensions of CR2032 coin cells.

Figure 6.4: Schematic drawing of the manufactured upper part of the extrution die fitting the exact dimensions of CR2032 coin cells. The metal die was lines with Teflon$^®$ to avoid short circuit.
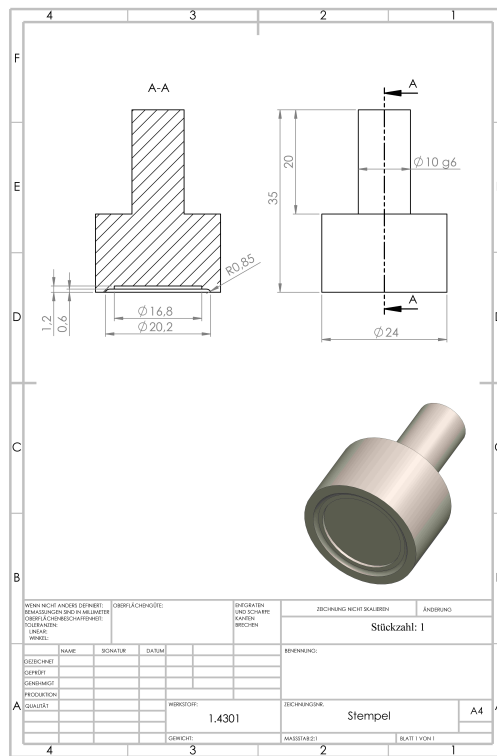
Figure 6.5: Measurements of the manufactured upper part of the extrution die fitting the exact dimensions of CR2032 coin cells. The metal die was lines with Teflon$^®$ to avoid short circuit.
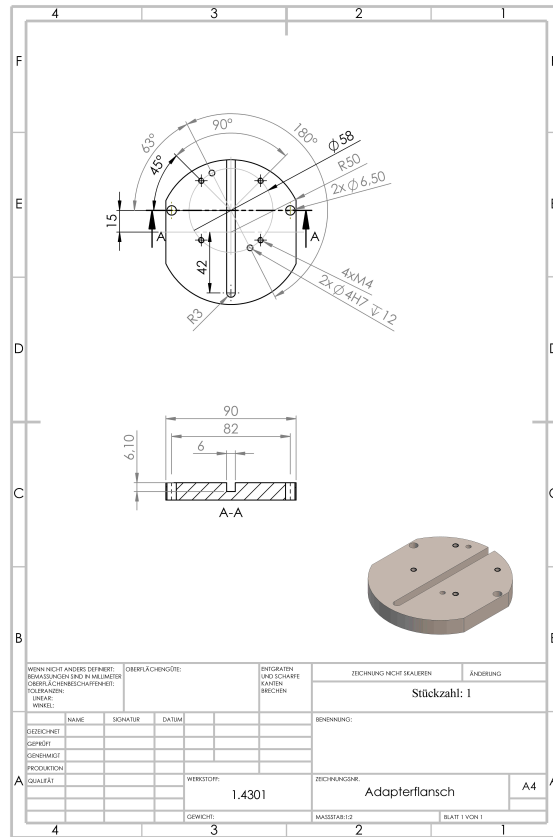
Figure 6.6: Schematic drawing of the manufactured of the attatment for the extrution die.
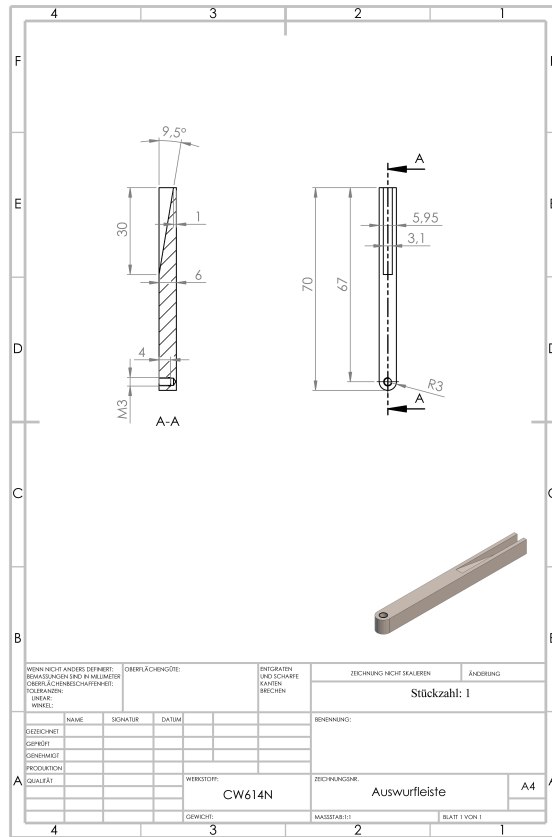
Figure 6.7: Schematic drawing and dimensions of the ejection mechanism for CR2032 coin cells.

List of Figures

List of Tables

Eidesstattliche Erklärung

Ich erkläre an Eides statt, dass ich die bei der promotionsführenden Einrichtung

_____

der TUM zur Promotionsprüfung vorgelegte Arbeit mit dem Titel:

_____

_____

_____

in _____

    Fakultät, Institut, Lehrstuhl, Klinik, Krankenhaus, Abteilung

unter der Anleitung und Betreuung durch: _____

ohne sonstige Hilfe erstellt und bei der Abfassung nur die gemäß § 6 Ab. 6 und 7 Satz 2 angebotenen Hilfsmittel benutzt habe.

☐ Ich habe keine Organisation eingeschaltet, die gegen Entgelt Betreuerinnen und Betreuer für die Anfertigung von Dissertationen sucht, oder die mir obliegenden Pflichten hinsichtlich der Prüfungsleistungen für mich ganz oder teilweise erledigt.

☐ Ich habe die Dissertation in dieser oder ähnlicher Form in keinem anderen Prüfungsverfahren als Prüfungsleistung vorgelegt.

☐ Die vollständige Dissertation wurde in _____

veröffentlicht. Die promotionsführende Einrichtung

_____

hat der Veröffentlichung zugestimmt.

☐ Ich habe den angestrebten Doktorgrad noch nicht erworben und bin nicht in einem früheren Promotionsverfahren für den angestrebten Doktorgrad endgültig gescheitert.

☐ Ich habe bereits am _____ bei der Fakultät für _____

_____

der Hochschule _____

unter Vorlage einer Dissertation mit dem Thema _____

_____

die Zulassung zur Promotion beantragt mit dem Ergebnis: _____

_____

Die öffentlich zugängliche Promotionsordnung der TUM ist mir bekannt, insbesondere habe ich die Bedeutung von § 28 (Nichtigkeit der Promotion) und § 29 (Entzug des Doktorgrades) zur Kenntnis genommen. Ich bin mir der Konsequenzen einer falschen Eidesstattlichen Erklärung bewusst.

Mit der Aufnahme meiner personenbezogenen Daten in die Alumni-Datei bei der TUM bin ich

☐ einverstanden,   ☐ nicht einverstanden.

_____

Ort, Datum, Unterschrift